

2007

INVESTIGATION OF OCEAN ACOUSTICS USING AUTONOMOUS INSTRUMENTATION TO QUANTIFY THE WATER-SEDIMENT BOUNDARY PROPERTIES

<https://hdl.handle.net/2144/1376>

Boston University

BOSTON UNIVERSITY
COLLEGE OF ENGINEERING

Dissertation

**INVESTIGATION OF OCEAN ACOUSTICS
USING AUTONOMOUS INSTRUMENTATION TO
QUANTIFY THE WATER-SEDIMENT
BOUNDARY PROPERTIES**

by

JASON DAVID HOLMES

B.S., Boston University, 2003

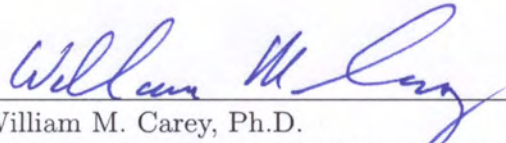
Submitted in partial fulfillment of the
requirements for the degree of
Doctor of Philosophy

2007

© Copyright by
JASON DAVID HOLMES
2006

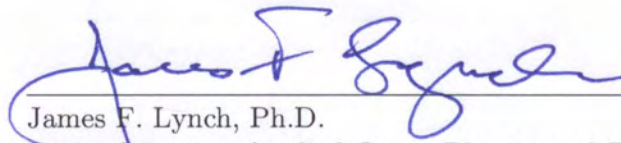
Approved by

Advisor:



William M. Carey, Ph.D.
Professor, Aerospace and Mechanical Engineering

Second Reader:



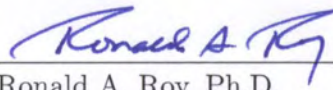
James F. Lynch, Ph.D.
Senior Scientist, Applied Ocean Physics and Engineering
Woods Hole Oceanographic Institution

Third Reader:



Allan D. Pierce, Ph.D.
Professor, Aerospace and Mechanical Engineering

Fourth Reader:



Ronald A. Roy, Ph.D.
Professor, Aerospace and Mechanical Engineering

This dissertation is dedicated
to Grandpa for inspiring me to think,
to Lisa for inspiring me to fight,
and to Kate for inspiring me to love.

Acknowledgments

It was once explained to me that an expert is someone who knows more and more about less and less until they know everything about nothing. As a doctor of philosophy, I am expected to be an expert in my field, but my grandfather offered me a piece of advice concerning this adage. He said, "Let your dissertation be an example of what you can do when you apply yourself, but not all that you can apply yourself to." While I strive to take this to heart, I realize now that without the help of others, I would not have succeeded. The rest of this document is meant to show my expertise in the field, but it is in this section that I get to acknowledge the support that I received along the way.

First, to my major advisor Prof. William Carey, the gratitude I owe is difficult to put on paper. Through my entire career at Boston University, he has been an advisor, a mentor, a foundation, and a friend. He recognized my potential and gave me exposure and connections in the professional world which are simply invaluable. The same can be said for Dr. James Lynch at the Woods Hole Oceanographic Institution. Dr. Lynch served as my WHOI advisor and offered continuous support, advice, funding, and access to the amazing facilities. I thank Prof. Ronald Roy for his support, both academic and personal, and Prof. Allan Pierce for his wisdom and assistance with theory. To Professors Glynn Holt and Gregory McDaniel I owe thanks for the support through both my undergraduate and graduate educations.

I would like to thank my fellow students at Boston University. I would especially like to thank the members of the Physical Acoustics and Underwater Acoustics Labs: Zach Waters, Jed Wilbur, Caleb Farney, Parag Chitnis, and Tianming Wu. To my predecessor at BU, Preston Wilson, I owe thanks for the countless pieces of advice. From the other side of my life at Boston University, I owe thanks to Laura DeVeau, Daryl Healea, all of the resident assistants, and the rest of the staff at the Office of Residence Life.

At WHOI I owe an incredible debt of gratitude to Amy Kukulya who helped with the

experiments and all of the operations of the REMUS vehicle. To Greg Packard, Ben Allen, and all of the other members of the Ocean Systems Lab at WHOI I also owe thanks. Arthur Newhall was a personal friend, professional asset, and reliable helping hand throughout my time at WHOI. I thank the captain and crew of the R/V Tioga, Ken Houtler, and Ian Hanley for their time and assistance during the Nantucket Sound experiments. Phillip Abbot and Dave Morton of OASIS, inc, also contributed greatly to the at-sea experiments.

For funding, I thank Boston University, the College of Engineering Dean's Graduate fellowship, the National Defense Science and Engineering Graduate Fellowship through the American Society for Engineering Education, the Office of Naval Research, and the Woods Hole Oceanographic Institution. I also thank the ONR program managers Tom Curtin, for his support of AUV programs, and Ellen Livingston, for her support of our project, especially with the environmental impact statement.

In addition to the professional side of my life, I owe much gratitude to the people in my personal life. To Dr. Vincent Ho and R.N. Kate Fisher of the Dana Farber Cancer Institute, thank you. In my family, I could always count on the support, guidance and love of Nana and Papa. The eternal admiration that I have for Dede and Grandpa will always keep me inspired. My parents, step mother, siblings, and step siblings have been a huge support, without which I would not have been able to complete my education. My wife's father and brothers have also accepted me as a part of the family and offered enormous encouragement.

Finally, above all else, I must thank my wife. Without her I don't know where I would be. She suffered through a long distance relationship, living in the city, and dealing with my late nights working on my dissertation. Her love for me has exemplified the vow "In good times and in bad, in sickness and in health, 'til death do us part."

**INVESTIGATION OF OCEAN ACOUSTICS USING AUTONOMOUS
INSTRUMENTATION TO QUANTIFY THE WATER-SEDIMENT
BOUNDARY PROPERTIES**

(Order No.)

JASON DAVID HOLMES

Boston University, College of Engineering, 2007
Major Professor: William M. Carey, Professor
of Aerospace and Mechanical Engineering

ABSTRACT

Sound propagation in shallow water is characterized by interaction with the oceans surface, volume, and bottom. In many coastal margin regions, including the Eastern U.S. continental shelf and the coastal seas of China, the bottom is composed of a depositional sandy-silty top layer. Previous measurements of narrow and broadband sound transmission at frequencies from 100 Hz to 1 kHz in these regions are consistent with waveguide calculations based on depth and frequency dependent sound speed, attenuation and density profiles. Theoretical predictions for the frequency dependence of attenuation vary from quadratic for the porous media model of M.A. Biot to linear for various competing models. Results from experiments performed under known conditions with sandy bottoms, however, have agreed with attenuation proportional to $f^{1.84}$, which is slightly less than the theoretical value of f^2 [Zhou and Zhang, J. Acoust. Soc. Am. 117, 2494]. This dissertation presents a reexamination of the fundamental considerations in the Biot derivation and leads to a simplification of the theory that can be coupled with site-specific, depth dependent attenuation and sound speed profiles to explain the observed frequency dependence. Long-range sound transmission measurements in a known waveguide can be used to estimate the site-specific sediment attenuation properties, but the costs and time associated with such at-sea experiments using traditional measurement techniques can be prohibitive.

Here a new measurement tool consisting of an autonomous underwater vehicle and a small, low noise, towed hydrophone array was developed and used to obtain accurate long-range sound transmission measurements efficiently and cost effectively. To demonstrate this capability and to determine the modal and intrinsic attenuation characteristics, experiments were conducted in a carefully surveyed area in Nantucket Sound. A best-fit comparison between measured results and calculated results, while varying attenuation parameters, revealed the estimated power law exponent to be 1.87 between 220.5 and 1228 Hz. These results demonstrate the utility of this new cost effective and accurate measurement system. The sound transmission results, when compared with calculations based on the modified Biot theory, are shown to explain the observed frequency dependence.

Contents

1	Introduction	1
1.1	Background	1
1.1.1	The Importance of Shallow Water Propagation	3
1.1.2	Motivation	6
1.2	Historical Prospective	7
1.2.1	Attenuation in Sediments	7
	Theory and review literature	7
	Types of attenuation measurements	8
	A summary of at sea measurements	10
1.2.2	Autonomous Underwater Vehicles	14
1.2.3	Towed Arrays	16
1.3	The Problem Statement	18
1.4	Roadmap for the Dissertation	18
2	Theory	20
2.1	Sediment Theory	20
2.1.1	Biot Theory	21
2.1.2	Simplified Biot Theory	26
2.1.3	Reflection from a Biot Bottom	30
2.2	Propagation Theory	36

2.2.1	Normal Modes	37
2.2.2	Propagations Effects with Biot Theory	40
2.2.3	Sources of Attenuation	42
2.3	Array Theory	43
2.3.1	Wave Guide Characterization	43
2.3.2	Synthetic Aperture Methods	47
2.3.3	Measurements with AUVs	51
	Long range transmission loss	51
	Single path	52
3	System Characterization	56
3.1	Array Calibration	57
3.2	Vehicle Noise	58
3.2.1	Tethered Measurements	61
3.2.2	Array Measurements	75
3.3	Towing Characteristics	76
3.3.1	Control Characteristics	77
3.3.2	Drag	85
3.3.3	Array Motion	88
4	The Experiment and Apparatus	91
4.1	Experimental Technique	91
4.2	The Nantucket Sound Site Survey	94
4.2.1	Historical Data	99
4.2.2	Precision Depth Recorder	100
4.2.3	Grab Sample Data	105
4.2.4	Geoacoustic Profiles	107
4.3	Experimental Description	114

5	Nantucket Sound Experiment	117
5.1	Numerical Modeling	117
5.2	September Experiment	118
5.2.1	Signal Processing	119
	Array gain	120
	Overlap processing	132
5.3	December Experiment	141
5.3.1	Signal Processing	142
	Array gain	142
	Overlap processing	149
5.3.2	Hankel Transforms	150
	Range error	150
	Range dependence	157
5.3.3	Attenuation Profiles	164
5.4	Frequency Dependence of Attenuation	169
5.5	Error Analysis	196
6	Summary and Conclusions	201
6.1	The System and Experiment	201
6.2	Future Directions	205
	Appendices	208
	Appendix A - Matlab Codes	208
	Appendix B - Linear array beamformer	258
	Appendix C - Noise on an array	262
	Appendix D - Design of recording system	279
	Appendix E - Pressure, range and time	296
	Appendix F - Acoustic Sources	300

Bibliography	304
Curriculum Vitae	315

List of Tables

1.1	Summary of experiments showing non-linear attenuation	13
2.1	Summary of propagation modes in a Sediment	33
3.1	Qualitative likelihood of cavitation	59
4.1	Summary of reported archival sediment properties	101
4.2	Summary of the measured sediment size distribution from sieving.	107
4.3	Exact latitude and longitude of the source in each experiment.	114
5.1	Source frequencies and levels for 10 DEC 2005	142
5.2	Measured wavenumbers in different range sections for 220.5 Hz, 10 DEC 2005.	158
5.3	Measured vs. Calculated modal eigenvalues for 220.5-635 Hz.	159
5.4	Modal attenuation coefficients measured and calculated	168
5.5	Summary of results for best fit n for each attenuation profile.	176
D.1	Summary of REMUS 100 Specifications	280

List of Figures

1.1	An early U.S. Navy listening device	2
1.2	Sound propagation in the ocean	5
1.3	Shepard's Sediment Triangle	11
2.1	Effect of frequency on angle dependent reflection coefficient	34
2.2	Comparison of angle dependent reflection coefficient for fluid and Biot models	34
2.3	Comparison of angle dependent reflection coefficient for solid and Biot models	35
2.4	Diagram of the Lynch-Frisk-Rajan experiment.	48
2.5	Conventional vs. synthetic aperture processing	51
2.6	Overlap processing used on an AUV towed array	52
2.7	Long-range sound transmission experiment geometry	53
2.8	Diagram of the subsystems of the towed array system	53
2.9	Single path sound transmission experiment geometry	54
2.10	Single path sound transmission from an AUV experimental geometry	55
3.1	Configuration of Radiate Noise Test	61
3.2	Radiated noise from two different vehicles	64
3.3	Ambient noise at test range SEP 2004	65
3.4	Load ADCP noise broadside of vehicle	66
3.5	Radiated noise from REMUS as a function of RPM	69
3.6	Radiated noise from the REMUS used for the towed array	70

3.7	Ambient noise at test range DEC 2004	71
3.8	Directionality of noise averaged over different frequency bands	72
3.9	Directionality of different peaks in the noise spectrum	73
3.10	The effect of the propellor on the radiated noise	74
3.11	Spectrogram of vehicle noise compared to RPM	76
3.12	Photograph of vehicle with unbalanced array attachment	78
3.13	Free body diagrams of different array attachments	79
3.14	Photograph of vehicle with more stable array attachment	80
3.15	Mission timeline showing motor faults	81
3.16	Vehicle path during tow test 08 DEC 2004	83
3.17	Mission timeline showing a stable tow	84
3.18	Effects of drag and currents on vehicle velocity	86
3.19	Vehicle power as a function of estimated velocity with and without the array	87
3.20	Time lag as a function of array position and time	89
3.21	Estimated array shape from signal time lag	90
4.1	Experimental configuration for Nantucket Sound Experiment	92
4.2	Wiring diagram for the source on the ship	93
4.3	Chart of Nantucket Sound showing potential experiment sites	95
4.4	Map showing the precision depth recorder tracks	96
4.5	Map showing the grab sample locations	97
4.6	Map showing the relative position of site 2 to Cape Cod	98
4.7	Results of inversion from Frisk, Lynch and Rajan	100
4.8	Precision depth recorder output for the proposed course at 33kHz	103
4.9	Precision depth recorder output for the proposed course at 200kHz	104
4.10	Photograph of the setup of the sediment vacuum filtering apparatus	106
4.11	Measured sediment size distribution for Nantucket Sound	108

4.12	Image capture of Nantucket Sound sediment sample as seen under a microscope.	109
4.13	Measured salinity, temperature and sound speed as a function depth in December 2005	111
4.14	Geo-acoustic profile for Nantucket Sound as determined by the pre-experiment site survey.	113
4.15	Map showing the experimental geometry for the September 2005 experiment.	115
4.16	Map showing the experimental geometry for the December 2005 experiment.	116
5.1	Relative array signal gain during the 15 SEP 2005 Experiment.	128
5.2	Path of vehicle during the synthetic aperture trial, 15 SEP 2005	129
5.3	Schematic of a curved array.	129
5.4	Relative array noise gain for the 15 SEP 2005 experiment	130
5.5	Synthetic aperture beamformer output compared to average conventional beamformer output from the 15 SEP 2005 Experiment.	131
5.6	Received signal level vs. range and estimated wave number spectrum for 635 Hz, 15 SEP 2005	135
5.7	Received signal level vs. range and estimated wave number spectrum for 823 Hz, 15 SEP 2005	136
5.8	Received signal level vs. range and estimated wave number spectrum for 1031 Hz, 15 SEP 2005	137
5.9	Received signal level vs. range and estimated wave number spectrum for 1228 Hz, 15 SEP 2005	138
5.10	Bathymetry reported by the AUV for 15 SEP 2005.	139
5.11	Transmission loss measured compared to RAM for 15 SEP 2005	140
5.12	Relative array signal gain during the 10 DEC 2005 Experiment (outbound).	145
5.13	Relative array signal gain during the 10 DEC 2005 Experiment (inbound). .	146

5.14 Synthetic aperture beamformer output compared to average conventional beamformer output from the 10 DEC 2005 Experiment (outbound).	147
5.15 Synthetic aperture beamformer output compared to average conventional beamformer output from the 10 DEC 2005 Experiment (inbound).	148
5.16 Comparison to results with and without overlap processing	150
5.17 Comparison of the estimated wave number spectrum on the outbound and inbound leg of the 10 DEC 2005 experiment without range correction.	151
5.18 Bathymetry for the 10 DEC 2005 Experiment as reported by the vehicle.	155
5.19 Comparison of the estimated wavenumber spectrum for 635 Hz on the outbound and inbound leg of the 10 DEC 2005 experiment with range correction determined by doppler estimation.	156
5.20 Transmission loss and estimated wavenumber spectrum for 220.5 Hz.	160
5.21 Transmission loss and estimated wavenumber spectrum for 415 Hz.	161
5.22 Transmission loss and estimated wavenumber spectrum for 635 Hz.	162
5.23 Horizontal wavenumber spectrum at 220 Hz as reported by Frisk et. al.	163
5.24 Waterfall plot of estimated horizontal wave number spectrum at 415 Hz vs. range	165
5.25 Example of estimated mode amplitude vs. range showing a clear modal attenuation coefficient by fitting.	167
5.26 Example of estimated mode amplitude vs. range showing a noisy fitting used to determine the modal attenuation coefficient.	167
5.27 Comparison of measured transmission loss to calculated transmission loss for 220.5 Hz.	179
5.28 Comparison of measured transmission loss to calculated transmission loss for 415 Hz.	180
5.29 Comparison of measured transmission loss to calculated transmission loss for 635 Hz outbound.	181

5.30 Comparison of measured transmission loss to calculated transmission loss for 635 Hz inbound.	182
5.31 Comparison of measured transmission loss to calculated transmission loss for 823 Hz.	183
5.32 Comparison of measured transmission loss to calculated transmission loss for 1031 Hz.	184
5.33 Comparison of measured transmission loss to calculated transmission loss for 1228 Hz.	185
5.34 Schematic of the 3 layer geo-acoustic model used for a Biot bottom.	186
5.35 Comparison of measured and calculated transmission loss for 1000-2000m range, 10 DEC 2005.	187
5.36 Comparison of measured and calculated transmission loss for 3000-3000m range, 10 DEC 2005.	188
5.37 Comparison of measured and calculated transmission loss for 2600-3600m range, 10 DEC 2005.	189
5.38 Flow chart depicting the iterative determination of the frequency dependent attenuation.	190
5.39 Comparison of measured and calculated transmission loss assuming an mod- ified Biot profile with varying frequency dependence, 10 DEC 2005.	191
5.40 Slope of best fit between measured and calculated range averaged trans- mission loss assuming a modified Biot profile as a function of power law exponent, 10 DEC 2005.	192
5.41 Attenuation in silty-sand sediments from 16 locations around the world, reported by Zhou and Zhang.	193
5.42 Schematic of the 4 layer geo-acoustic model used for a Biot bottom with an underlying constant Q layer.	193
5.43 Comparison of measured and calculated transmission loss assuming a quadratic bottom over a linear bottom with varying layer thickness, 10 DEC 2005. . .	194

5.44	Slope of best fit between measured and calculated range averaged transmission loss assuming a quadratic bottom over a linear bottom as a function of layer thickness, 10 DEC 2005.	195
5.45	Estimated standard deviation of the received signal levels as a function of range and frequency.	197
A.1	Diagram showing flow of data in the computations.	209
B.1	Plane wave linear array geometry	258
C.1	Sources of noise on a ship towed array	265
C.2	Frequency dependence of TBL convection velocity	268
C.3	Geometry of the Problem	269
C.4	Calculated flow noise spectrum on a rigid cylinder	275
C.5	Calculated frequency dependence of eddie convection velocity	276
C.6	Towed array hose transfer function $k - \omega$ plane	278
D.1	Diagram of the subsystems of the towed array system	279
D.2	Photograph of the REMUS 100 AUV used in the experiments	281
D.3	Details of array construction	285
D.4	Photograph of wired hydrophone group	286
D.5	Photograph of hydrophone group in mesh sleeve	286
D.6	Photograph of mesh sleeve tie off	287
D.7	Photograph of connector on the front of the array	287
D.8	Wiring schematic for internal array components	288
D.9	Engineering drawing of array front termination	289
D.10	Engineering drawing of array back termination	290
D.11	Engineering drogue connector	291
D.12	Schematic of conditioning and timing board	293
D.13	Schematic of conditioning and timing board	294
D.14	Photograph of recording system	295

E.1	Navigation and acoustic time scales	297
E.2	Interpolation of range and time	297
F.1	Wiring diagram for the source on the ship	301
F.2	Properties of the XF-4 Flex-tensional source.	302
F.3	Properties of the HX-188 Omni-directional source.	303

Chapter 1

Introduction

1.1 Background

Since the earliest times in human history the ocean has provided food, protection, a means for transportation, and trade routes. The earliest accounts of the ocean depict it as an infinite expanse filled with unknown dangers. In the Epic of Gilgamesh, the earliest known recorded literature, Gilgamesh is told by the tavern-keeper, “Gilgamesh, there never has been a way across, nor since olden days can anyone cross the ocean. ... The crossing is perilous, its way full of hazard, and midway lie the Waters of Death, blocking the passage forward.” [1] Because of the great perils associated with simply navigating the ocean, much of man’s earliest interests in studying the oceans focused on mapping. One of the earliest tools for surveying the ocean consisted of a weight on the end of a line with knots at regular intervals. Sailors could drop the weight into the water and count the number of knots that were submerged in order to measure the depth of the water. When sailing in deep water, a similar tool that was 100 fathoms long was hung over board. When the line began to drag on the bottom, the mariners knew that the coast was near; they had encountered what is now referred to as the shelf break.

While ocean mapping is still an active area of ocean research, throughout history other ocean related disciplines have developed including the study of the creatures that live there,

the influence of the ocean and atmosphere on climates, and ocean acoustics. During the 15th century, Leonardo Da Vinci is credited with noting “If you cause your ship to stop, and place the head of a long tube into the water, and place the other extremity to your ear, you will hear ships at a great distance from you.”[2] This is probably the earliest reference to long range sound propagation in the ocean, the phenomenon which is exploited in modern sonar systems. The next major advance in sonar technology did not happen until the early 20th century when two listening devices were attached to the end of a rotating shaft, thus providing a sense of the direction of the sound. A photograph of one of these early listening devices is shown in figure 1.1. Coincidentally, this was about the same time the United States purchased its first military submarine, the U.S.S. Holland.



Figure 1.1: A crewman of the USS H-5 seen with an early sonar listening device.[3] The use of two transducers on a rotating shaft provided directionality and was perhaps the first major advance in sonar technology since Da Vinci.

Since World War I, sonar technology has rapidly progressed. Active systems were developed to detect enemy vessels at long ranges and as electronic and computing capability increased, so did on board sonar signal processing capability. Systems advanced from having two sensors, to multiple sensors on a single line, and then to multiple lines of multiple sensors which gave directionality in bearing as well as depth. These systems were adapted by the Navy for surveillance and detection as well as by the surveying industry

for oil exploration [4].

By combining the field of underwater acoustics and the study of the structure and mechanics of the ocean, acoustical oceanography was born. Presently, underwater acoustic technology has advanced to the point where the weighted depth lines of ancient sailors have been replaced with electronic precision depth sounders which enable the captain of a vessel to not only know the depth of the water below his keel, but to know the structure of the ocean bottom. This thesis is a demonstration of the next generation of technology in a progression of acoustic oceanography and bottom measurements that started with the ancient desire to know “what’s down there”.

1.1.1 The Importance of Shallow Water Propagation

Oceans cover approximately 70% of the earth’s surface. The majority of the ocean is deeper than 2000 m, but navigation in the continental margins is important for commercial, military, and personal ocean traffic. These continental margins are regions extending out to (on average) 70 km which surround the continental land mass in which the water depth is shallow. They consist of the continental shelf, the continental slope and the continental rise. Water depths are typically less than 200 m¹ on the shelf out to the shelf break where the continental slope starts and the bottom drops off steeply down to the deep ocean depths. [5]

In the deep ocean, sound propagation is characterized by refraction due to the depth dependence of the speed of sound in the water. Typically the sound speed profile contains a minimum allowing for total refraction of sound by what is known as the deep sound channel or SOFAR (sound fixing and ranging) channel. Although there is interaction of sound with the surface or bottom, the major influences on long range sound propagation are the sound speed profile, volume scattering and the intrinsic attenuation of sea water.

In contrast, in the shallow water areas of the continental margins, sound propagation is characterized by multiple surface and bottom reflections. In this case, the physical mecha-

¹Charts actually mark the shelf by the 100 fathom line which is approximately 200m.

nisms involved in volume, surface and bottom interactions must be understood in order to predict sound propagation and the performance of sonar systems. Thus, the importance of shallow water research is to pave the way for the development and applications of sonar technology in shallow water.

Figure 1.2 details the distinction between deep water sound propagation and shallow water sound propagation. In shallow water the properties of the bottom layers become exceedingly important and multiple interactions with the bottom produce significant scattering losses. In general the geoacoustic profile, which details the acoustic parameters as a function of depth and geological parameters, is required to predict sound transmission.

Starting in World War I and continuing through World War II, shallow water coastal defense was a key issue due to advances in submarine technology. Active sonar was developed to detect enemy vessels and in order to predict the performance of these active systems, shallow water propagation was heavily researched. After 1950 the primary military interest in underwater acoustics shifted to deep water passive systems in order to covertly detect and track deep water nuclear submarines. Since the end of the Cold War, there has been an renewed interest in both active and passive shallow water acoustics for coastal monitoring and defense and clandestine littoral warfare. This includes the protection of domestic harbors as well as the detection of mines and acoustic surveillance in enemy waters.

In addition to the military importance of shallow water acoustics, there are scientific and commercial applications in shallow water acoustics. Since electromagnetic waves attenuate extremely rapidly underwater, instrumentation and systems used for shallow water oceanographic measurements often rely on acoustic communications to relay information. Further, the commercial and private vessel traffic in the continental margins often use acoustic depth sounders (termed fathometers by the Submarine Signal Company [2]), side scan sonars, and acoustic sub-bottom profilers. Also, the entire field of acoustic oceanography depends on using acoustics to quantify the ocean environment.

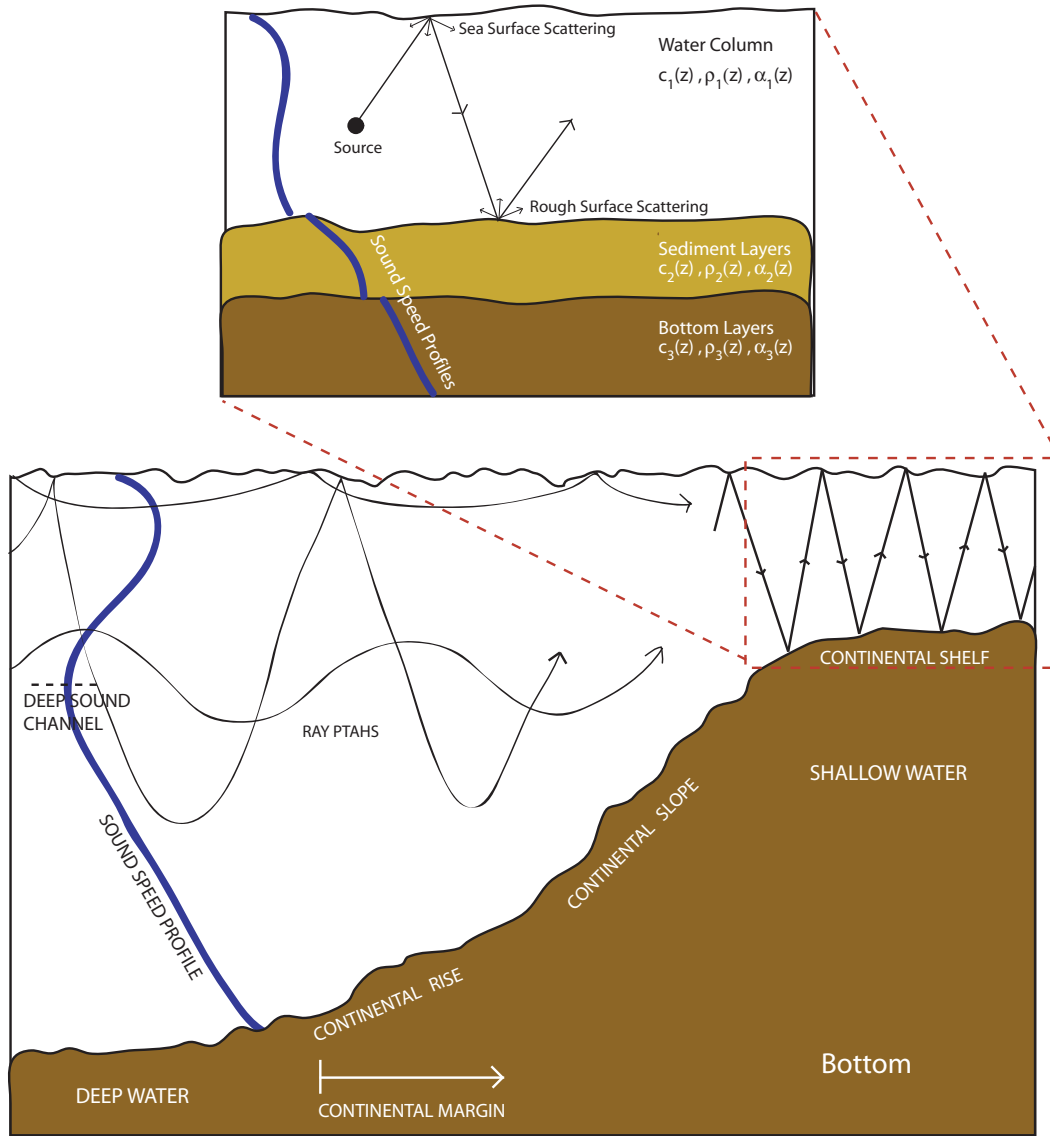


Figure 1.2: A schematic diagram detailing various propagation regimes in the ocean. Inspired from [6].

1.1.2 Motivation

Currents and tides in the continental margin act like a grain size filter for sediment transport, since smaller particles have a lower settling speed. In areas formed by glacial movement, where sediments are originally unsorted and particles range from fine clays to large rocks, the sediments are eventually sorted into regions of similar characteristic size. This is also true in areas with significant run off from the land. Since sands and silts have particles larger than clay particles, and since settling speeds decrease with size, the shallow coastal regions with high current speeds will often contain silty-sands whereas the regions with less current and the deeper ocean will typically have silty-clay bottoms. This means that many areas formed by glacial movements, such as Nantucket sound, as well as areas with land run off, such as the East China Sea, will often be characterized by a critical angle (sound speed greater than water) bottom with sandy-silty depositional sediment layers.

In addition to the East China Sea, many critical areas around the world including the Northeast coast of the United States, the Northern Indian Ocean, and the straits of Korea have sandy-silty bottoms. In order to accurately predict propagation, the geo-acoustic characteristics of the sediments must be fully understood. In general, the depth of penetration into the bottom changes with frequency, which inherently couples frequency and depth dependence of geo-acoustic parameters when measured in-situ. While there has been significant work investigating the bottom interaction [7], the required site specific frequency dependent attenuation in the sonar frequency range (<10 kHz) is not fully quantified and a theoretical treatment of the dispersive characteristic not completed. At-sea measurements of sound transmission are required to characterize site-specific parameters. These at-sea measurements have typically involved multiple ships and moored assets, both of which can be prohibitively expensive. This motivates the need to be able to make rapid, accurate and cost effective measurements of the frequency dependent sound transmission. If autonomous instrumentation were developed that could accomplish this with results that were comparable or better than previous ship based experiments, then the need would be

satisfied.

1.2 Historical Prospective

1.2.1 Attenuation in Sediments

Theory and review literature

Between 1941 and the late 1970's Maurice Biot wrote a series of papers describing the mechanics of porous materials [8–16]. Of particular importance were two papers concerning the theory of propagation of elastic waves in porous solids in the low and high frequency limits [17,18]. In these papers, Biot used a continuum approach with composite fields and dashpot-like damping to derive the relevant mechanics. Later, Stoll reformulated Biot's [19] work which often leads researchers to refer to Biot's theory as the "Biot-Stoll" theory. In the 1970's and 80's Hamilton published a sequence of experimental review papers discussing semi-empirical results for the geo-acoustic characteristics of sediments including the attenuation [20–32]. In the model which Hamilton presents for a broad range of sediments based on experiments, the quality factor, Q , is assumed constant, which leads to the predication of a linear frequency dependence of attenuation. This is contrary to Biot's theory which predicts a quadratic frequency dependence at low frequency. As pointed out by Stoll [33], a constant Q is seldom the case in a water saturated sediment.

In addition to Biot's model and Hamilton's constant Q model, several other theoretical models have been developed. Hovem [34] gives a brief description of three of the major models including Hamilton and Biot. Other models that have been proposed to explain broad band data are the "effective grain model" [35], an effective density fluid model variant of Biot theory [36], a grain shearing model [37], and a Biot model variant with contact squirt flow and shear drag [38]. There are also a plethora of other papers discussing approximations to the full Biot theory, which typically has up to 13 independent parameters defining the properties of the sediment. Many of the mentioned newer theories include just

as many parameters, many of which have large error bounds because they are difficult, if not impossible, to measure and are frequently unphysical. In order to avoid this, focus will be placed here on a derivation of Biot’s original theory which leads to a low frequency approximation applicable at typical sonar frequencies of interest ($\sim 1kHz$).

While theoretical papers provide insight into the mechanics associated with attenuation, review papers provide an important link between theory and experiment. Hamilton wrote one of most referenced review papers which discussed how to model the geo-acoustic parameters in the bottom based on semi-empirical results [30]. A general linear frequency dependence of attenuation was given. Later, Kibblewhite [7] added new data at the lower frequencies and provided an extensive discussion of linear versus non-linear frequency dependent attenuation. Rozenfeld added to Kibblewhite’s data and presented a review of non-linear measurements with new measurements that gave an average exponent of 1.8 [39]. Another review by Holmes and Dediu compared the frequency dependent exponent and critical angles reported by various measurements over silty-sands as well the experimental methods used [40]. More recently, Zhou reviewed many previous at sea experimental works and found that some used incorrect depth dependence, thus resulting in incorrect frequency dependence [41]. Zhou corrected the mistakes and came up with a best fit for sandy-silty sediments of

$$\alpha(z) = 0.34 \left(\frac{f}{f_0} \right)^{1.84} [dB/m] \quad (1.1)$$

where Zhou took the reference frequency f_0 to be 1 kHz. This is also very close to the results reported by Rozenfeld [39].

Types of attenuation measurements

There are essentially four main experimental techniques for in-situ measurement of the frequency dependence of the attenuation in ocean sediments. These are:

Modal Techniques: Modal techniques usually incorporate a vertical or horizontal hydrophone array and take advantage of dispersion or wave number analysis to separate

modes (for example see reference [42]). Comparison of measured mode properties to forward models while adjusting the bottom properties reveals the best fit bottom model.

Transmission Loss Techniques: Transmission loss techniques use transmission loss versus range measurements as data. Determination of frequency dependence is, again, accomplished by using a forward model based on a geoacoustic profile with a variable frequency dependence to determine the best fit to data (for example references [43,44]).

Inversion Techniques: Inversion schemes are also used and encompass many techniques such as genetic algorithms or perturbative inversions. These methods often use multi-parameter fitting for the geoacoustic profile and attenuation (for example see reference [45]).

Reflection Coefficient Techniques: Measurement of the angle dependent reflection coefficient, while more commonly used for higher frequencies because of the ease in forming a directional source, has been used with some success in slow bottoms. This method often makes use of the fact that the sub-critical angle reflection loss depends on the sediment attenuation. For the case of a slow bottom, it has been performed by examining the reflection coefficient at the angle of intromission for the thin top layer (for example see reference [46]).

In addition to these classical measurement techniques, there have been some new approaches to in-situ measurement as well as many laboratory experiments. One recent in-situ experiment involved using the noise from an airplane flying over a known hydrophone location and utilizing the propeller noise harmonics, doppler shift and mode theory to infer the bottom properties[47]. A similar technique was also applied which makes use of ship propellor noise [48].

At higher frequencies, laboratory measurements are often simple time of flight experiments in which the time delay between transmission and reception indicates the sound speed and the decrease in amplitude indicates the attenuation. One experiment by Simpson and Houston [49] used a synthetic hydrophone aperture in the lab to measure the bottom reflection properties in the time, frequency-wavenumber and two dimensional spatial domains. At the lower frequencies of interest, similar laboratory techniques are often impossible due to mutli-path and time spread effects as well as long wavelengths. An attempt was made to use a water filled impedance tube to classify sediments at lower frequencies with mixed results [50,51]. Another recent low frequency laboratory measurement utilized the resonant characteristics of a thin walled cylindrical vessel filled with sediment [52]. By measuring the modal structure within the cylinder and comparing it to a model, the characteristics of the sediment are recovered.

A summary of at sea measurements

While the literature contains data for various sediment types, it is important to note that sediment characteristics are dependent on the grain size distribution. For sediments which are silty-sands, there is a significant amount of evidence that the Biot theory holds and low frequency attenuation scales as the square of frequency. In order to compare results between experiments, consistent semantics must be used. According to the American Geophysical Union Sediment Classification System (AGUSCS) sediments are composed of sand, silt, and clay [53,54], each characterized by a range of particle sizes. The distinction between sand, silty-sand, clay, sandy-silty-clay etc. can thus be made simply by comparing the relative percent of each constituent to the limits given in the triangle diagram by Shepard shown in figure 1.3. [55]. Sediment particles can also be classified by their origins as lithographic (derived from rocks), biogeneus (derived from organisms) or hydrogeneous (derived from reactions in the sea water) [5].

By using the AGUSCS and origin classifications, proper comparisons can be made between experimental results. In general, different sediment mixtures behave differently. The sed-

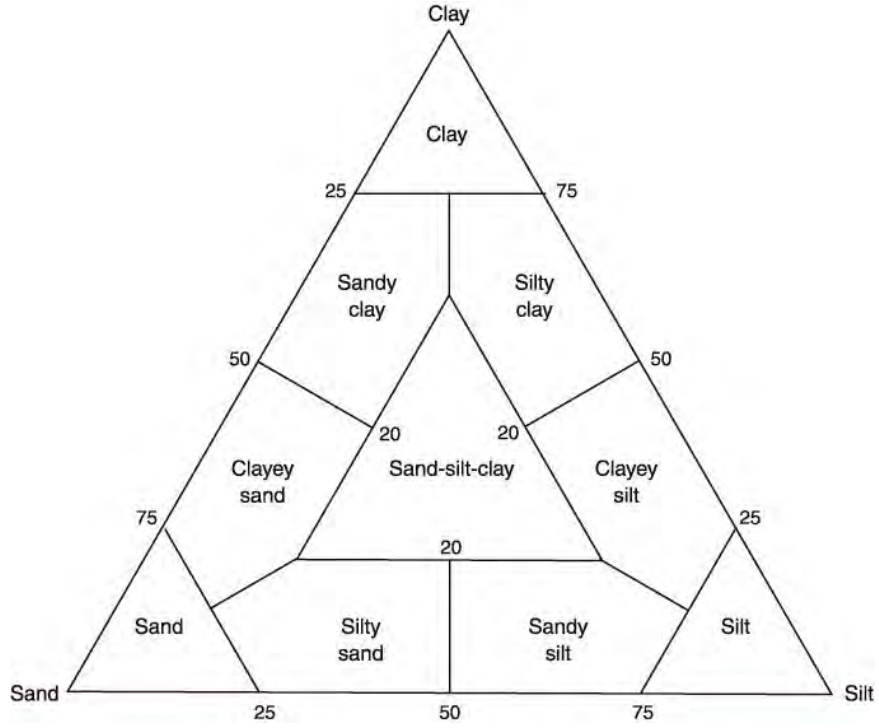


Figure 1.3: Triangle diagram used to classify sediments based on the relative percent of sand, silt and clay as given in [55]

iments considered in this work are generally in the lower left hand side of the sediment classification triangle, and are predominantly sandy silty sediments. Therefore it would be improper to compare results that were predominantly clay and silt as frequency dependence in these sediments may be governed by different power laws.

As with the sediment classification, the frequency dependent attenuation as determined in experiments should be expressed in a uniform fashion as

$$\alpha(z) = \alpha(f_0) \left(\frac{f}{f_0} \right)^n \quad (1.2)$$

where f_0 is a reference frequency (often 1 kHz), n is the frequency dependent exponent, and $\alpha(f_0)$ is the attenuation at the given reference frequency in dB/m. By expressing the results of all experiments in this consistent fashion, with a common reference frequency, common units, and common sediment classification scheme, a consistent basis for comparison can

be made.

Despite recent interest in the matter, nonlinear frequency-dependent sediment attenuation factors are not a new finding in shallow water waveguides with fast sandy bottoms. In 1973, Ingenito [42] observed a nonlinear dependence between 400 and 750 Hz. Nine years later, for two sites with medium to coarse sand, Beebe [43] found exponents between 1.57 and 1.83. In the mid 1980s, Rogers and Zhou [45] summarized several previous experiments [56,57] in the Yellow Sea and observed that the frequency dependent attenuation factor ranged between 1.6-1.9. Tappert [58] found in his 1993 analysis of the Act I experiment on the West Coast of Florida, Urick's Site, that $n = 2$ was the best fit parameter consistent with the Biot porous medium model. Chizhik and Tattersal (1992-1993) [59,60] used the Biot theory to compute sediment parameters for a fluid bottom and an elastic bottom; they also used a fast field program calculation with a geoacoustic bottom. Calculations using the fast field program and a multipath expansion code were found to agree with measured transmission over the 100 Hz to 8 kHz range when the Biot bottom was used. That is to say that one sees a frequency dependent attenuation coefficient with an $n = 2$ power for frequencies less than 1 kHz and another dependence above this frequency [17]. Additionally, the Act III experiment modeled by Rozenfeld [39] was found to require a frequency dependent factor of $n = 1.8$ to describe both narrowband and broadband transmission loss in the complex Strait of Korea, which compared favorably with previous work. Results from experiments in the East and South China Seas conducted by the Office of Naval Research in 2003 reported by Peng and Zhou [61] and Zhou and Zhang [57] showed dependencies between 1.6 and 1.63 while the results of Knobles et al. [62] (2005) showed a power dependence of 2. Table 1.1 provides a chronological summary of this previous work on the frequency dependence of attenuation including the bottom type, the type of experiment, and the estimated critical angle of the bottom as a basis of comparison. From the results shown in Table 1.1 it is clear that there is substantial evidence that for sandy-silty bottoms in the frequency range of 100 Hz to 1 kHz attenuation in the sediments follows a non-linear frequency dependence with $1.5 < n < 2.0$.

Table 1.1: Summary of non-linear dependent attenuation factors for various sediments from previous works using different measurement techniques

Author, Date, Reference	Frequency Range (Hz)	Bottom Type (in accordance with [22])	Estimated Critical Angle (degrees)	Frequency Dependent Exponent (n) following af^n	Experimental Technique ^a
Ingenito, 1973, [42]	400-750	Sand	19	1.75	M
Beebe et al., 1982, [43]	100-600	Medium to Coarse Sand	29	1.76	TL
Beebe et al., 1982, [43]	25-250	Coarse Sand with Gravel	35	1.57	TL
Zhou 1985, [63]	80-800	Sand-Silt-Clay	19	1.84	M
Zhou et al. 1987, [56]	100-1000	Fine Sand and Silt	21	1.6	INV
Tattersall and Chizhik, 1992-93, [59,60]	100-8000	Medium Sand	24	2.0 ^b	TL
Tappert, 1993, [58]	50-800	Sand-Silt-Clay	19	2.0	TL
Carey and Evans, 1998, [44]	500-1000	Sand-Silt-Clay	18	1.5	TL
Rozenfeld et al. , 2001 , [39]	47-604	Sand-Silt	23	1.8	TL
Peng et al. , 2004, [61]	100-500	Very Fine Sand	21	1.65	TL
Zhou et al. , 2004 , [57]	100-700	Very Fine Sand	22	1.63	INV
Knobles et al. , 2005, [64]	25-800	Fine Sand	21	2.0	TL

^aM=Modal, TL=Transmission Loss, INV=Inversion

^bPaper actually reports agreement with Biot theory, which gives $n = 2.0$ in the 100-1000 Hz range.

1.2.2 Autonomous Underwater Vehicles

A common misconception by the public is that Autonomous Underwater Vehicles (AUVs) are synonymous with Remote Operated Vehicles (ROV) or Unmanned Underwater Vehicles (UUV). The one word in common with the three is “vehicle,” which is in general an instrument by which an object is transported from one point to another. In this case the vehicles transport instrumentation and sensors, not people, as is explicitly indicated with UUVs. The meaning of the word “underwater” is obvious and indicates that, whether they be propeller driven submarines or crawling robots with legs, these vehicles are designed to operate while submerged in water. The term ROV is a more general term and applies to land based vehicles as well, but they must be remotely operated by a human. This brings about the distinction. While UUV is usually all encompassing for any underwater vehicle without a human on board, an AUV differs from an ROV in that it can make intelligent decisions using information from its surroundings, without the intervention of a human, but based on decision making rules given to it by a human before its mission. This makes AUVs very attractive for performing underwater research because it is often difficult, expensive, or undesirable to have a human on station, connected to the vehicle in order to operate it.

Given the definition of an AUV, probably the earliest example of an AUV is the torpedo, which as early as World War II could determine when they were in proximity to a ship and were not merely impact projectiles.² Shortly afterwards, torpedos were given the ability to acoustically sense a ship and steer towards a target.

After the first use of autonomy in torpedoes, there have been a number of AUV’s developed for various purposes. Richard Blidberg of the Autonomous Undersea Systems Institute gave a very good history of AUV development including what has already been discussed [65]. Although few papers were published at the time, AUV technology was

²Another interesting misconception is that modern torpedos detonate into the side of ships. During World War I it was determined that because of the armor on ships it was much more effective to detonate an explosive device below a ship, causing a large shock wave and inertially collapsing gas bubble which break the ship in half.

originally investigated in the 1960's. The 1970's and 80's saw an increase in research in the field with several platforms constructed by academia and the military. Small, low power computers helped propel the advancement of AUV technology through the 90's with many new proof of concept systems with complex software and control algorithms. As the technology became more robust and reliable in the late 90's the first routine operational platforms were in service and in the early part of the new millennium AUVs have become a commercially available product.

Even though the history of AUVs is relatively short, there have been a number of different types of AUVs developed. The means for propulsion of vehicles ranges from battery powered electric motors with propellers to diesel powered engines to bouyancy driven gilders [66]. Gliders have better endurance than propeller driven systems, but docking stations and solar powered AUVs have recently been developed to increase mission times. The current state of AUV technology sees advances in materials, power systems, control, communications, propulsion and on board transducers occurring at an astounding pace. Still, advances in acoustics onboard AUVs have been primarily limited to high frequency active sensors such as the typical side scan sonar system, due to the noise radiated by the vehicle and the physical aperture that a low frequency array would require. One solution would be to tow a sensor to minimize hull born noise contamination and then use synthetic aperture processing to attain the necessary array aperture.

There is only one previous case of an AUV towing a hydrophone array; a communications array deployed on a Florida Atlantic Ocean Explorer vehicle with the purpose of increasing the signal to noise ratio for acoustic communications in the 2-4 kHz range [67]. This system was not utilized to perform ocean acoustic experiments.

Two instances of AUV's utilizing a hydrophone array system that was slightly removed from the hull yet not towed have also been published. The first was a small 8 channel array mounted on the nose of a Massachusetts Institute of Technology vehicle in a mine detection experiment [68,69]. This system was not entirely isolated from the vehicle and operated in a bi-static active sense with broad band pulses emitted from a parametric source with a

source level of 201 dB re 1 μPa @ 1m. The goal was to be able to image buried and proud mines at a distance of 10-20 meters away from the source. In essence the noise level seen at the array from the AUV was unimportant because of the high level of the transmitted signal. Further, the vehicle navigated by long base line (LBL) and the signal from the LBL transducer had to be interleaved with the experimental signal to avoid interference. This allowed for only a 7 m long synthetic aperture with an 8 kHz center frequency signal.

The other published case of a hydrophone array slightly removed from the hull was a passive volumetric array mounted on a Florida Atlantic University Ocean Explorer II. This was a targeting system, but it required the vehicle to land on the ocean bottom and keep station to operate. By stopping, the problem of vehicle noise was virtually eliminated [70].

It is clear that of the two major problems associated with low frequency sound measurements with AUV's, sensor aperture and hull born vehicle noise, the problem of aperture size seems to have only one viable solution: synthetic aperture. Hull born noise, on the other has been mitigated by simply using a loud source, separating the hydrophones from the hull, or stopping the vehicle. The other obvious solution to this problem is to design a quieter vehicle. Acoustic and vibrational noise levels recorded on a hull mounted array were decreased by 20 to 50 dB across the 20 Hz to 10 kHz band in one case [71], but the hull mounted array still suffered from performance degradation due to the acoustic field created by scattering off the vehicle body. These results indicate that a combination of a quiet vehicle and a carefully designed towed hydrophone array could be the optimal solution.

1.2.3 Towed Arrays

Deemed as critical technology, much of early towed array work was classified and only available in classified journals. In 2002 a special issue of the Journal of Oceanic Engineering was published in which several archival papers on towed array technology and towed array history were published [72,73,4]. The first towed array system was devised by Dr. Harvey Hayes in 1917. It had two 12 element arrays and was capable of detecting a submarine at 2000 yards. After this development, towed array work was mostly dormant until the 1950's

when the Chesapeake Instrument Corporation (CIC) was asked by the Office of Naval Research (ONR) to resurrect the technology in order to solve the “hindsight” problem; the bow mounted sonar systems on submarines simply could not see aft. Improved cable design, quiet transistors, and an oil filled hose assemble decreased the noise level on the array and contributed to the the success of the early arrays, but they were not integrated into the fleet because of two prototypes, one design was deemed too expensive and the other was sail mounted and might interfere with missile launch.

Having been rejected from the submarine fleet, towed array technology was implemented on surface ships. When a new CIC array showed almost 20 dB gain over the expected detection threshold values, towed array technology began to become much more accepted. As Soviet submarines became quieter, longer towed array systems were built and implemented into the submarine fleet. Slow speed surveillance arrays and high speed tactical arrays were built in the 1970’s, but flow noise was still an issue. In the 1980’s application of new theoretical work led to decreased flow noise and thinner arrays that could be stored in the ballast tanks of submarines. By the 90’s high and low frequency arrays were common in the fleet and multi-line arrays which eliminated directional ambiguity were being used for oil exploration from surface ships. The latest technology in unclassified military towed array systems includes fiber optic data transmission and multi-line submarine systems.

Synthetic aperture techniques were originally developed for radar, but were later applied to sonar. Synthetic aperture processing is the process by which the spatial resolution of a short aperture sensor is enhanced by incorporating the motion of the sensor into the spatial-temporal processing and signal model. In 1984 Yen and Carey were able to beamform a passive synthetic aperture over long ranges to track the bearing of sources [74] and a good review of synthetic aperture processing was presented by Sullivan, Carey and Stergiopolis [75]. With the maturation of this discipline, shorter and thinner arrays have been emerging in the past decade. The “thinarray” is one example of an ultra thin towed array meant to be used from a small ship of opportunity without special deck equipment [76]. Another recent development has been the use of a vector sensor. This sensor is in fact a hydrophone

coupled with a tri-axis accelerometer which eliminates the left-right ambiguity inherent in single line towed arrays. The drawback of vector sensors is that they are quite large compared to hydrophones, requiring a larger array with higher drag [77].

1.3 The Problem Statement

In section 1.1.2, a motivation for this work was presented. Recapping, there is a need to be able to make rapid and cost effective measurements of the geo-acoustic profiles in the ocean bottom, especially focusing on the depth and frequency dependent attenuation. Since ship costs are prohibitive, the desire is to accomplish this with a single coastal ship rather than multiple large, deep water platforms. Inspired by advances in AUV technology and partially motivated by the proven performance of towed array systems, it was hypothesized that this goal can be accomplished using an AUV towed hydrophone array. This thesis focuses on the problem of developing such a device and testing it in a proof of concept experiment in which the frequency dependent attenuation is measured in-situ .

1.4 Roadmap for the Dissertation

The remainder of this dissertation will focus on the development and testing of and results obtained with a prototype AUV towed hydrophone array system. This work was performed in collaborative effort between Boston University and the Woods Hole Oceanographic Institution (WHOI). REMUS³ was the chosen AUV because of its availability as a test platform and because it is the smallest and least powerful of the readily available vehicles. Thus, if the system could be developed to work on this limiting case vehicle, it could easily be implemented on larger, more powerful vehicles. In chapter 2 of this dissertation, the requisite theory for sediment propagation, a simplified Biot theory, propagation theory, and array theory will be presented. The requirements and theoretical basis for two experiments

³REMUS is a trade name for a vehicle developed at WHOI that is commercially available from Hydroid Inc., Pocasset, MA. The name stands for Remote Environmental Monitor UnitS.

using the prototype system are also discussed. In chapter 3 the characteristics of the prototype system are presented and the experimental geometry and site survey information for a long-range transmission loss experiment are discussed in chapter 4. Results from the at-sea experiment conducted in Nantucket Sound are presented in chapter 5 including error analysis. Finally, conclusions are given in chapter 6.

Chapter 2

Theory

2.1 Sediment Theory

In Chapter 1, table 1.1 focused on measurements that have exhibited a non-linear frequency dependence of attenuation for sandy-silty sediments. While measurements are useful by themselves, theory provides a basis for explanation and extrapolation of the measurements. As discussed in section 1.2.1, there are several theoretical models that predict the attenuation of sound in sediments.

In general, an acoustical-mechanical system can be described in terms of its quality factor, Q , as Hamilton did [30]. The derivation of the quality factor representation of a system starts with assuming complex Lamé constants

$$\lambda = \lambda_R + i\lambda_I, \quad (2.1)$$

$$\mu = \mu_R + i\mu_I. \quad (2.2)$$

Applying linear stress-strain relations, one finds a phase between stress and strain given by

$$\theta = \frac{\lambda_I + 2\mu_I}{\lambda_R + 2\mu_R}. \quad (2.3)$$

The ratio of successive time series peaks (the natural logarithm of which is the logarithmic decrement) for a lumped-constant oscillating system is the same as the amplitude variation with range in wavelengths for any traveling waves. White [78] showed that, when the attenuation coefficients are small,

$$\theta = \frac{1}{Q} = \frac{aV}{\pi f} \quad (2.4)$$

where a is the attenuation coefficient, Q is the quality factor (or $1/Q$ is the specific attenuation factor), V is the wave velocity, and f is the frequency. Inspection of equation 2.4 shows that when Q is considered to be independent of frequency, which Hamilton approximates in [20], then attenuation is linearly related to frequency.

2.1.1 Biot Theory

A frequency independent Q is seldom the case for water saturated sediments. Biot adopted a different approach and considered a fluid saturated porous media by first considering two displacement fields, one for the fluid (\mathbf{U}) and one for the solid (\mathbf{u}). Averaging of properties is considered over a volume cell which is small compared to a wavelength but large compared to the characteristic pore size. The stress and strain in the solid are given by ¹

$$\tilde{\sigma}_s = \begin{bmatrix} \sigma_{x_s} & \tau_{xy_s} & \tau_{xz_s} \\ \tau_{yx_s} & \sigma_{y_s} & \tau_{yz_s} \\ \tau_{zx_s} & \tau_{zy_s} & \sigma_{z_s} \end{bmatrix} \quad (2.5)$$

$$e_{ij} = \frac{1}{2} \left(\frac{\partial u_i}{\partial x_j} + \frac{\partial u_j}{\partial x_i} \right) \quad (2.6)$$

$$\tilde{e}_s = \begin{bmatrix} e_{x_s} & \gamma_{xy_s}/2 & \gamma_{xz_s}/2 \\ \gamma_{yx_s}/2 & e_{y_s} & \gamma_{yz_s}/2 \\ \gamma_{zx_s}/2 & \gamma_{zy_s}/2 & e_{z_s} \end{bmatrix} \quad (2.7)$$

¹The author chooses here to use a tilde (\sim) over a quantity to designate that quantity as a tensor.

The stress in the fluid is given by,

$$\tilde{\sigma}_f = \begin{bmatrix} s & 0 & 0 \\ 0 & s & 0 \\ 0 & 0 & s \end{bmatrix}. \quad (2.8)$$

Since there are no off-diagonal terms in the fluid, we can simply consider the dilatation rather than the strain,

$$\epsilon_f = \frac{\partial U_i}{\partial x_i}. \quad (2.9)$$

The reader is reminded that the index summation convention is being used. Further, the stresses and strains with the subscript ‘‘s’’ denote the solid, those with the subscript ‘‘f’’ denote the fluid, and those with no subscript denote the aggregate. Potential energy density in the aggregate is given by strain energy as [79]

$$W = \frac{1}{2} \sigma_{ij} e_{ij} \quad (2.10)$$

when expressed as a function of the aggregate stress and strain. The constitutive equation relating stress and strain is given by

$$\sigma_{ij} = c_{ijkl} e_{kl}. \quad (2.11)$$

An important feature of the strain energy is that only the products of stresses and strains in the same direction contribute to energy even though the stress in one direction is dependent on all of the strains. Thus, the strain energy can be expressed in terms of the seven components of stress and strain in the fluid and solid

$$W = \frac{1}{2} [\sigma_{x_s} e_{x_s} + \sigma_{y_s} e_{y_s} + \sigma_{z_s} e_{z_s} + \tau_{xy_s} \gamma_{xy_s} + \tau_{xz_s} \gamma_{xz_s} + \tau_{yz_s} \gamma_{yz_s} + s_f \epsilon_f]. \quad (2.12)$$

The constitutive equation between the solid and fluid stresses and strains is then

$$\begin{bmatrix} \sigma_{x_s} \\ \sigma_{y_s} \\ \sigma_{z_s} \\ \tau_{xy_s} \\ \tau_{xz_s} \\ \tau_{yz_s} \\ s_f \end{bmatrix} = \tilde{D} \begin{bmatrix} e_{x_s} \\ e_{y_s} \\ e_{z_s} \\ \gamma_{xy_s} \\ \gamma_{xz_s} \\ \gamma_{yz_s} \\ \epsilon_f \end{bmatrix} \quad (2.13)$$

where \tilde{D} is a 7×7 symmetric matrix which relates the stresses to the strains as c_{ijkl} did in the aggregate. In general, this gives 28 independent coefficients required to define the system. If the system is statistically isotropic², then the principal stresses and principal strains align. Further, symmetry about any point means that each principal stress in the solid and fluid must depend on its corresponding principal strain as well as the other principal strains in exactly the same manner. Therefore,

$$\sigma_{1_s} = Ae_{1_s} + Be_{2_s} + Be_{3_s} + C\epsilon_f \quad (2.14)$$

$$\sigma_{2_s} = Ae_{2_s} + Be_{1_s} + Be_{3_s} + C\epsilon_f \quad (2.15)$$

$$\sigma_{3_s} = Ae_{3_s} + Be_{1_s} + Be_{2_s} + C\epsilon_f \quad (2.16)$$

$$s_f = D\epsilon_f + Ee_{1_s} + Ee_{2_s} + Ee_{3_s} \quad (2.17)$$

or

$$\begin{bmatrix} \sigma_{1_s} \\ \sigma_{2_s} \\ \sigma_{3_s} \\ s_f \end{bmatrix} = \begin{bmatrix} A & B & B & C \\ B & A & B & C \\ B & B & A & C \\ E & E & E & D \end{bmatrix} \begin{bmatrix} e_{1_s} \\ e_{2_s} \\ e_{3_s} \\ \epsilon_f \end{bmatrix} \quad (2.18)$$

²By statistically isotropic it is meant that when averages are taken over regions large compared to the particle sizes, there is symmetry about any given point. That is, there is not preferred direction in the stress-strain relations.

In order for a strain energy to exist, the matrix in (2.18) must be symmetric and therefore $E = C$ which gives only 4 distinct elastic coefficients required to define the system. Further, while equation (2.18) considers the principal stresses and strains, the problem is more realistically defined using the stresses and strains relative to some natural cartesian coordinate (for example z increases with depth into the sediment, x is to the right according to the viewer and y is according to the right hand rule). The principal stresses and strains give the stresses and strains in the actual coordinate system by means of a rotational transformation which simply introduces the off-diagonal terms in a predictable way [79]. Using this and introducing new constants N , A , Q and R , gives

$$\begin{aligned}
\sigma_{x_s} &= 2Ne_{x_s} + Ae_s + Q\epsilon_f & \tau_{yz_s} &= N\gamma_{yz_s} & s_f &= Qe_s + R\epsilon_f \\
\sigma_{y_s} &= 2Ne_{y_s} + Ae_s + Q\epsilon_f & \tau_{xz_s} &= N\gamma_{xz_s} & & \\
\sigma_{z_s} &= 2Ne_{z_s} + Ae_s + Q\epsilon_f & \tau_{yz_s} &= N\gamma_{yz_s} & e &= e_{x_s} + e_{y_s} + e_{z_s}
\end{aligned} \tag{2.19}$$

The coefficients are chosen in this manner to be identical to standard elastic theory coefficients [17]. In contrast to equation (2.18), equation (2.19) is now in the coordinate system defined relative to the sediment geometry and includes shear explicitly. Here the σ_s terms are the normal stresses associated with the solid field, the τ_s terms are the shear stresses associated with the solid field, the e_s terms are the solid field strains, the s_f term is the fluid field stress, and ϵ is the fluid field dilatation. A and N are the familiar Lamé coefficients, A being the bulk modulus and N the shear modulus. R is a measure of the diffusive nature of the fluid and Q is a volume change coupling term which relates changes in the volume of the solid to changes in the volume of the fluid.

Equation (2.19) is the constitutive equation in terms of the fluid and solid stresses and strains. To form energy arguments, the kinetic and potential energy densities must be explicitly found. The kinetic energy of the system per unit volume for the isotropic case is the sum of densities times velocities squared including cross terms involving the relative

motion between fields:

$$T = \frac{1}{2}\rho_{11}[u_i u_i] + \rho_{12}[\dot{U}_i u_i] + \frac{1}{2}\rho_{22}[\dot{U}_i \dot{U}_i]. \quad (2.20)$$

Dots are used to represent time derivatives. The nature of ρ_{ij} is such that $\rho_{11} + 2\rho_{12} + \rho_{22} = (1 - \beta)\rho_s + \beta\rho_f = \rho$, the total mass of the fluid-solid aggregate per unit volume where β is the porosity. Further,

$$\rho_{12} = -\rho_a < 0, \quad \rho_{11} > 0, \quad \rho_{22} > 0, \quad \tilde{\rho} = \begin{bmatrix} \rho_{11} & \rho_{12} \\ \rho_{12} & \rho_{22} \end{bmatrix}. \quad (2.21)$$

where $\tilde{\rho}$ is positive definite, ρ_{11} is the total effective mass of the solid, ρ_{22} is the total effective mass of the fluid, and ρ_a effective added mass coupling term [17]. Using (2.19) with (2.10) gives the potential energy expression.

$$W = \frac{1}{4}N \sum_{ij} \left(\frac{\partial u_i}{\partial x_j} + \frac{\partial u_j}{\partial x_i} \right)^2 + \frac{1}{2}A(\nabla \cdot \mathbf{u})^2 + Q(\nabla \cdot \mathbf{u})(\nabla \cdot \mathbf{U}) + \frac{1}{2}R(\nabla \cdot \mathbf{U})^2. \quad (2.22)$$

Equations (2.20) and (2.22) are identical to equations 3 and 4 of [80] (making note of a difference in convention for ρ_{ij} from Biot and Pierce.³) The Lagrangian density is $\mathcal{L} = T - W$ and, by Hamilton's principle, satisfies the Lagrange-Euler equations given by

$$\frac{\partial}{\partial t} \left(\frac{\partial \mathcal{L}}{\partial(\partial U_i / \partial t)} \right) + \frac{\partial}{\partial x_j} \left(\frac{\partial \mathcal{L}}{\partial(\partial U_i / \partial x_j)} \right) = \mathfrak{f}_i, \quad (2.23)$$

$$\frac{\partial}{\partial t} \left(\frac{\partial \mathcal{L}}{\partial(\partial u_i / \partial t)} \right) + \frac{\partial}{\partial x_j} \left(\frac{\partial \mathcal{L}}{\partial(\partial u_i / \partial x_j)} \right) = \mathfrak{f}_i. \quad (2.24)$$

The terms on the right hand side of (2.23) and (2.24) are the equal and opposite forces per unit volume exerted on the fields. Biot [17] took the the forces per unit volume exerted

³Pierce uses ρ_{11} to denote the fluid density and ρ_{22} solid density where as Biot assumes the opposite. Biot's convention is followed here.

by the solid on the fluid and vice-versa to be similar to a dashpot and proportional to the relative velocity. Thus,

$$\mathfrak{F}_i = -f_i = -b(\dot{U}_i - \dot{u}_i). \quad (2.25)$$

Applying (2.25) as well as (2.20) and (2.22) to (2.23) and (2.24), with extensive algebraic manipulation yields the classic coupled equations of Biot

$$N\nabla^2 \mathbf{u} + \nabla [(A + N)e + Q\epsilon] = \frac{\partial^2}{\partial t^2}(\rho_{11}\mathbf{u} + \rho_{12}\mathbf{U}) + b\frac{\partial}{\partial t}(\mathbf{u} - \mathbf{U}), \quad (2.26)$$

$$\nabla [Qe + R\epsilon] = \frac{\partial^2}{\partial t^2}(\rho_{12}\mathbf{u} + \rho_{22}\mathbf{U}) - b\frac{\partial}{\partial t}(\mathbf{u} - \mathbf{U}). \quad (2.27)$$

Here b is related to Darcy's coefficient of permeability by $b = \mu\beta^2/k$ where μ is the fluid viscosity, β is the porosity, and k is the permeability. N , A , Q and R are as before and represent the bulk modulus, shear modulus, diffusion effects, and coupled volume changes. Solution of these coupled equations will yield an attenuated wave. The solution is often carried out numerically but requires the definition of at least 8 parameters ($A, Q, N, R, \rho_{11}, \rho_{12}, \rho_{22}, b$). Relation of the equations' parameters to measurable quantities requires the knowledge of up to 13 independent parameters, as presented in Stoll's extension of Biot theory[19].⁴

2.1.2 Simplified Biot Theory

In 2005, Pierce *et al.* offered a simplification of the Biot Theory [80]. The relevant portions are briefly re-derived here. The goal (as is usual with coupled partial differential equations) is to simplify the problem into a single partial differential equation. Longitudinal compressional waves are irrotational so solutions to Biot's Equations (2.26), (2.27) for which

⁴The 13 parameters from Stoll's extension of Biot's theory are: porosity β , fluid density ρ_f , grain density ρ_s , fluid bulk modulus K_f , grain bulk modulus K_s , viscosity η , permeability κ , pore size a , tortuosity τ , the real and imaginary frame shear modulus $\mu = \mu_r + i\mu_i$, and the real and imaginary frame bulk modulus $K = K_r + iK_i$.

the curl is zero are considered. Introducing displacement scalar potentials as

$$\mathbf{U} = \nabla\Phi \quad (2.28)$$

$$\mathbf{u} = \nabla\Psi \quad (2.29)$$

gives

$$\frac{\partial^2}{\partial t^2}(\rho_{22}\Phi + \rho_{12}\Psi) - Q\nabla^2\Psi - R\nabla^2\Phi = -b\frac{\partial}{\partial t}(\Phi - \Psi), \quad (2.30)$$

$$\frac{\partial^2}{\partial t^2}(\rho_{12}\Phi + \rho_{11}\Psi) - (A + 2N)\nabla^2\Psi - Q\nabla^2\Phi = b\frac{\partial}{\partial t}(\Phi - \Psi). \quad (2.31)$$

For the zeroth order low frequency approximation one imagines that the displacement fields (and thus potentials) are equivalent. Equating Φ and Ψ in (2.30) and (2.31) gives

$$\frac{\partial^2}{\partial t^2}[(\rho_{22} + \rho_{12})\Phi] - (Q + R)\nabla^2\Phi = 0, \quad (2.32)$$

$$\frac{\partial^2}{\partial t^2}[(\rho_{12} + \rho_{11})\Phi] - (A + 2N + Q)\nabla^2\Phi = 0. \quad (2.33)$$

Adding these,

$$\frac{\partial^2}{\partial t^2}[(\rho_{11} + 2\rho_{12} + \rho_{22})\Phi] - [A + 2N + 2Q + R]\nabla^2\Phi = 0. \quad (2.34)$$

Rearranging,

$$(A + 2N + 2Q + R)\nabla^2\Phi = (\rho_{11} + 2\rho_{12} + \rho_{22})\frac{\partial^2}{\partial t^2}\Phi. \quad (2.35)$$

This gives the approximation

$$\nabla^2 \rightarrow \frac{\rho}{\lambda} \frac{\partial^2}{\partial t^2}. \quad (2.36)$$

Where ρ is the effective medium density given by $\rho = \rho_{11} + 2\rho_{12} + \rho_{22}$ and λ is the effective medium Lamé constant, chosen here to be the effective bulk modulus, given by

$\lambda = A + 2N + 2Q + R$. Using this approximation in (2.30) and (2.31) gives

$$\frac{\partial^2}{\partial t^2} \left(\rho_{22} - R \frac{\rho}{\lambda} \right) \Phi + \frac{\partial^2}{\partial t^2} \left(\rho_{12} - Q \frac{\rho}{\lambda} \right) \Psi \approx -b \frac{\partial}{\partial t} (\Phi - \Psi), \quad (2.37)$$

$$\frac{\partial^2}{\partial t^2} \left(\rho_{12} - Q \frac{\rho}{\lambda} \right) \Phi + \frac{\partial^2}{\partial t^2} \left(\rho_{22} - (A + 2N) \frac{\rho}{\lambda} \right) \Psi \approx b \frac{\partial}{\partial t} (\Phi - \Psi). \quad (2.38)$$

A first order correction is obtained by considering a difference in displacement fields only in the forcing term. Then (2.37) becomes

$$\frac{\partial^2}{\partial t^2} \left[\left(\rho_{22} + \rho_{12} - (R + Q) \frac{\rho}{\lambda} \right) \Phi \right] = -b \frac{\partial}{\partial t} (\Phi - \Psi). \quad (2.39)$$

Which is rearranged as

$$\frac{\partial}{\partial t} \left\{ \frac{\partial}{\partial t} \left[\left(\rho_{22} + \rho_{12} - (R + Q) \frac{\rho}{\lambda} \right) \Phi \right] + b(\Phi - \Psi) \right\} = 0. \quad (2.40)$$

Thus, the term in the braces is a constant

$$\left[\rho_{22} + \rho_{12} - (R + Q) \frac{\rho}{\lambda} \right] \frac{\partial \Phi}{\partial t} + b(\Phi - \Psi) = C. \quad (2.41)$$

Shortly it will be shown that this constant is only seen in derivatives where it vanishes and is thus unimportant, but it will be kept for the time being for correctness. Extensive algebra on (2.41) yields

$$C - D \frac{\partial \Phi}{\partial t} = b\lambda(\Phi - \Psi) \quad (2.42)$$

where $D = (\rho_{12} + \rho_{22})(A + 2N + Q) - (\rho_{11} + \rho_{12})(R + Q)$. This leads to the approximation

$$\Psi \rightarrow \Phi + \frac{D}{b\lambda} \frac{\partial \Phi}{\partial t} - \frac{C}{b\lambda}. \quad (2.43)$$

It is now clear that D describes the slippage between the fields. Summing (2.30) and (2.31) gives

$$\frac{\partial^2}{\partial t^2} [(\rho_{22} + \rho_{12})\Phi + (\rho_{11} + \rho_{12})\Psi] - (A + 2N + Q)\nabla^2\Psi - (R + Q)\nabla^2\Phi = 0. \quad (2.44)$$

Using (2.43) in (2.44) gives

$$\begin{aligned} & (\rho_{12} + \rho_{22})\frac{\partial^2}{\partial t^2}\Phi + (\rho_{11} + \rho_{12})\frac{\partial^2}{\partial t^2}\left[\Phi + \frac{D}{b\lambda}\frac{\partial\Phi}{\partial t} - \frac{C}{b\lambda}\right], \\ & -(A + 2N + Q)\nabla^2\left[\Phi + \frac{D}{b\lambda}\frac{\partial\Phi}{\partial t} - \frac{C}{b\lambda}\right] - (R + Q)\nabla^2\Phi = 0. \end{aligned} \quad (2.45)$$

Dropping the C terms because they are all in derivatives and rearranging,

$$\rho\frac{\partial^2}{\partial t^2}\Phi + (\rho_{11} + \rho_{12})\frac{D}{b\lambda}\frac{\partial^3\Phi}{\partial t^3} - \lambda\nabla^2\Phi - (A + 2N + Q)\nabla^2\left[\frac{D}{b\lambda}\frac{\partial\Phi}{\partial t}\right] = 0. \quad (2.46)$$

Now applying (2.36) to the last term gives

$$\rho\frac{\partial^2}{\partial t^2}\Phi - \lambda\nabla^2\Phi + (\rho_{11} + \rho_{12})\frac{D}{b\lambda}\frac{\partial^3\Phi}{\partial t^3} - (A + 2N + Q)\frac{D}{b\lambda}\frac{\rho}{\lambda}\frac{\partial^3\Phi}{\partial t^3} = 0 \quad (2.47)$$

but,

$$\rho_{11} + \rho_{12} - (A + 2N + Q)\frac{\rho}{\lambda} = \frac{D}{\lambda}. \quad (2.48)$$

Thus the acoustic potential equation (noting that c is given by $c = \sqrt{\lambda/\rho}$), is given by

$$\nabla^2\Phi - \frac{1}{c^2}\frac{\partial^2}{\partial t^2}\Phi = \frac{-\tau_B}{c^2}\frac{\partial^3}{\partial t^3}\Phi. \quad (2.49)$$

where τ_B is the ‘‘Biot Time Constant’’ and is given by

$$\tau_B = \frac{D^2}{b\lambda^2\rho}. \quad (2.50)$$

Equation (2.49) is now a wave equation with a dissipation term completely characterized by the sound speed and a term with units of time which has been named the Biot time constant. Thus, for low frequency sound in porous media, one should be able to characterize the sediment by a sound speed, density and this time constant. Assuming plane wave propagation in (2.49), the dispersion relationship is,

$$-\rho\omega^2 + \lambda k^2 - i\omega^3 \frac{D^2}{b\lambda^2} = 0 \quad (2.51)$$

which yields

$$k = \frac{\omega}{(\lambda/\rho)^{1/2}} \left[1 + i\omega \frac{D^2}{\rho b \lambda^2} \right]^{1/2}. \quad (2.52)$$

Since the second term in the brackets is small, a binomial expansion is used to get

$$k = \frac{\omega}{c} + i\alpha, \quad \alpha = \frac{\tau_B}{2c} \omega^2. \quad (2.53)$$

The value of expressing the theory in terms of the Biot time constant is that it results in a simple model that describes the dispersion. If measurements for attenuation are made at higher frequencies, which is often easier, then this theory together with the measured Biot time constant could be used to extrapolate the attenuation down to lower frequency. Carey *et al.* [81] showed that the Biot time constant as calculated by Hamilton's 1 khz attenuation constant and other non-linear attenuation measurements are consistent and on the order of microseconds.

2.1.3 Reflection from a Biot Bottom

Biot's coupled field equations are given by (2.26),(2.27). The simplified Biot theory uses low frequency approximations to these coupled equations to derive a single third order linear partial differential equation describing the acoustic mode in a saturated porous medium. This considered only irrotational disturbances in the sediment in which the fluid and solid motions were approximately equal at low frequencies. Some insight into the nature of the

sediment may be gained from looking at the problem of reflection from a water-sediment interface considering all possible types of disturbances. Starting from Biot's coupled field equations, (2.26),(2.27), rearranging using the definition of e and ϵ , and using a useful vector field identity⁵, Biot's couple equations are rewritten as

$$-\frac{\partial^2}{\partial t^2}(\rho_{11}\mathbf{u} + \rho_{12}\mathbf{U}) + \nabla [(A + 2N)\nabla \cdot \mathbf{u} + Q\nabla \cdot \mathbf{U}] - \nabla \times (N(\nabla \times \mathbf{u})) = b\frac{\partial}{\partial t}(\mathbf{u} - \mathbf{U}) \quad (2.54)$$

$$-\frac{\partial^2}{\partial t^2}(\rho_{12}\mathbf{u} + \rho_{22}\mathbf{U}) + \nabla [Q\nabla \cdot \mathbf{u} + R\nabla \cdot \mathbf{U}] = -b\frac{\partial}{\partial t}(\mathbf{u} - \mathbf{U}). \quad (2.55)$$

Written in this form, the terms in (2.54) are easy to recognize by comparison to familiar partial differential equations. The first term is an inertial term, the second term is a normal stress term as seen in a wave equation, the third term is a shear stress term as seen in a wave equation and the last term is a dash-pot term.

If different terms are determined to be insignificant compared to the remaining terms, different propagation modes can be identified. The assumption made in the earlier derivation was that at low frequencies the fields are in phase and approximately equal. Thus the dash-pot term is small. If the field is also irrotational the shear term is identically zero and (2.54) and (2.55) reduce to a compressional wave propagation equation. On the other hand, if the field is non-dilatational, the normal stress term is zero and the relevant mode is a shear wave. If the fields were actually out of phase, then the inertial term becomes insignificant compared to the dash-pot term. An irrotational field would thus reduce to a diffusion law mode.

In general, a vector field can be represented by the sum of a scalar potential field and a vector potential field. With this the fluid and solid fields are defined as

$$\mathbf{u} = \nabla\phi_u + \nabla \times \psi_u \quad (2.56)$$

$$\mathbf{U} = \nabla\phi_U + \nabla \times \psi_U \quad (2.57)$$

⁵ $\nabla \times (\nabla \times \mathbf{u}) = \nabla(\nabla \cdot \mathbf{u}) - \nabla^2\mathbf{u}$

The field component represented by the scalar potential necessarily has a curl of zero and is thus irrotational. Likewise, the field component represented by the vector potential has a divergence of zero and is thus non-dilatational. While the form of the coupled equations in (2.54) and (2.55) reveal the different propagation modes by the easily recognizable terms, the form given in (2.26) and (2.27) is easier to apply potentials to. Applying the scalar potential to the coupled equations of Biot and taking the sum and difference of the equations we have

$$\frac{\partial^2}{\partial t^2} [(\rho_{12} + \rho_{22})\Phi + (\rho_{11} + \rho_{12})\Psi] - (A + 2N + Q)\nabla^2\Psi - (Q + R)\Phi = 0 \quad (2.58)$$

$$\frac{\partial^2}{\partial t^2} [(\rho_{12} - \rho_{22})\Phi + (\rho_{11} - \rho_{12})\Psi] - (A + 2N - Q)\nabla^2\Psi - (Q - R)\Phi - 2b\frac{\partial}{\partial t}(\Phi - \Psi) = 0 \quad (2.59)$$

Assuming plane waves of the form $e^{i(\omega t - \mathbf{k} \cdot \mathbf{r})}$, gives the dispersion relationship

$$\begin{vmatrix} -\omega^2(\rho_{12} + \rho_{22}) + k^2(Q + R) & -\omega^2(\rho_{11} + \rho_{12}) + k^2(A + 2N + Q) \\ -\omega^2(\rho_{12} - \rho_{22}) + k^2(Q - R) - 2ib\omega & -\omega^2(\rho_{11} - \rho_{12}) + k^2(A + 2N - Q) + 2ib\omega \end{vmatrix} = 0 \quad (2.60)$$

From this, the phase velocity defined as $v = \omega/k$ has two roots. That is, there are two irrotational propagation modes. One of these roots yields a velocity close to the sonic velocity and the other has a slower speed. These are the disturbances termed the first and second dilatational waves by Biot and often referred to as the acoustic wave and slow wave, or acoustic mode and Darcy mode.

Applying the vector potential to the coupled equations of Biot in a similar way yields another dispersion relationship which only has one root in v . Thus there is one rotational wave, the shear wave.

Therefore, a saturated porous medium supports three disturbance modes each of which simplifies to a different partial differential equation at low frequencies [82]. The characteristics of these modes are summarized in table 2.1.

In general, the three modes of propagation are uncoupled, but at the fluid-solid interface the following boundary conditions exist for each field which couple the fields[83]:

Table 2.1: Summary of propagation modes predicted in a sediment by the Biot theory

Mode	Low frequency Approx.	Field Type	Related PDE
Acoustic	$\mathbf{u}_{ac} \approx \mathbf{U}_{ac}$	Dilatational	$\nabla^2 \mathbf{u}_{ac} - \frac{1}{c_{ac}^2} \frac{\partial^2}{\partial t^2} \mathbf{u}_{ac} = \frac{\tau_B}{c_{ac}^2} \frac{\partial^3}{\partial t^3} \mathbf{u}_{ac}$
Shear	$\mathbf{u}_{sh} \approx \mathbf{U}_{sh}$	Rotational	$\nabla^2 \mathbf{u}_{sh} - \frac{1}{c_{sh}^2} \frac{\partial^2}{\partial t^2} \mathbf{u}_{sh} = \frac{(\rho_{22} + \rho_{12})^2}{Nb} \frac{\partial^3}{\partial t^3} \mathbf{u}_{sh}$
Darcy	Inertial term negligible	Dilatational	$\nabla^2 \mathbf{u}_D = \kappa_D \frac{\partial \mathbf{u}_D}{\partial t}$

1. Continuity of fluid displacement
2. Equilibrium of normal traction
3. Equilibrium of fluid pressure
4. Equilibrium of tangential traction

Stoll and Kan solved numerically for the reflection coefficient as a function of angle of incidence for a water-sand interface including all three modes [83]. The results showed a frequency and permeability dependence of the reflection coefficient. While one could model the sediment in a simple way as a fluid having a loss tangent (constant complex moduli) [6, pp. 42-48] Stoll and Kan showed that there is a difference between this assumption and using all three acoustic modes in the Biot theory. Chizhik and Tattersall [59] later numerically modeled the reflection coefficient from a sand bottom using Biot's theory and compared it to an effective fluid and an effective solid model. Figures 2.1 through 2.3 are taken from reference [59] and show that Biot's model leads to a frequency dependent reflection coefficient that differs from the fluid and solid models. This difference is especially pronounced at low grazing angles. These plots show that the measured angle dependent reflection coefficient, when compared to theory, can differentiate models. However, the differences in reflection coefficient between models are on the order of 0.5 dB, which may be difficult to discern in a reflection experiment.

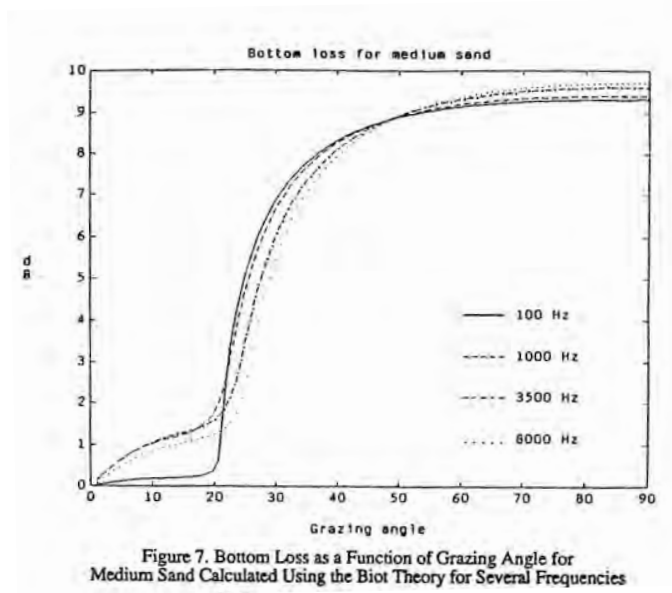


Figure 2.1: The effect of frequency on the reflection coefficient as a function of angle as reported by [59]

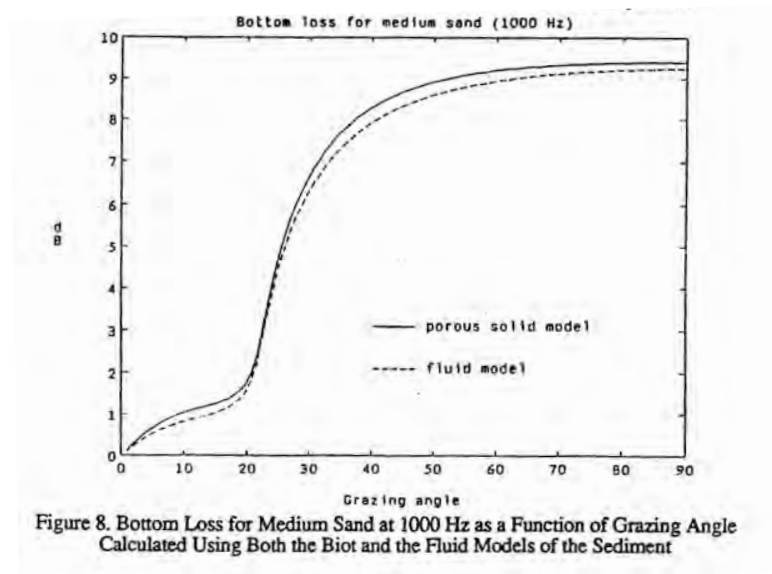


Figure 2.2: A comparison of angle dependent reflection coefficient for fluid and Biot models as reported by [59]

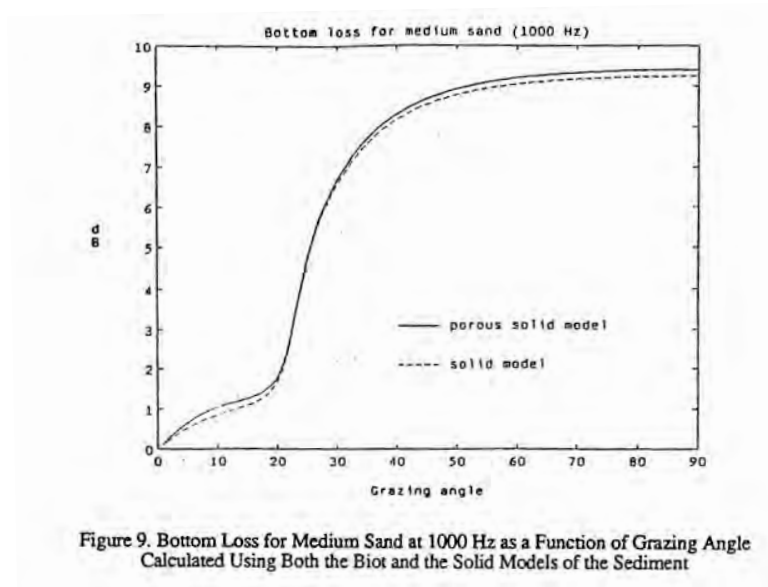


Figure 2.3: A comparison of angle dependent reflection coefficient for solid and Biot models as reported by [59]

2.2 Propagation Theory

Several models exist to predict the phenomena experienced in ocean acoustic propagation. In the high frequency limit, the wave equation can be solved by an expansion into the ray series which results in the eikonal equation and ray methods [6]. For horizontally stratified media (i.e. range independent problems) the wave equation can be easily solved by means of an integral transform. The transform space is the wavenumber and integration must be performed on this space to find the inverse transform and thus the pressure. Methods using an integral transform are thus termed wavenumber integration techniques and computer programs based on them are often referred to as “fast field programs” because of the use in some routines of the fast Fourier transform (FFT) to perform the transforms [6].

By considering only singularities in the wavenumber space, one would essentially have a finite sum of contributions to the pressure field due to Cauchy’s residue theorem. This is equivalent to the normal mode solution to the wave equation which considers the weighted sum of propagating modal functions, each of which satisfies the depth separated wave equation [84].

If the functional form of the pressure field is assumed to be a product of a depth envelope function which is slowly varying in range and a Hankel function, the cylindrical wave equation reduces to an elliptic equation in the far field. By making a small angle paraxial assumption, this reduces to a standard parabolic equation (PE). An added convenience is that slowly varying range dependence is simple to model by including it in the envelope function.

Each model of ocean acoustic propagation has inherent assumptions and thus differing regions of applicability. The full wave equation with depth and range variations can be solved by some numerical methods such as finite differences, but these methods may be time consuming. By determining what parameters are most important for a particular region of interest, models with appropriate assumptions can be used. Often the important parameters are handled correctly by different models, and thus these models should con-

verge in their regions of applicability. For a critical angle bottom, the results in the far field should converge for the normal mode solution and the PE solution if there is no range dependence. The solution from the wavenumber integration routine contains contributions from the residues corresponding to normal modes as well as contributions from the integration contour in the complex plane corresponding to lateral waves and the evanescent field. Thus, if a receiver is not close enough to the bottom interface to measure these fields the wavenumber integration routine should also converge with the normal mode solution in the far field.

While most common numerical codes allow for the modeling of fluid-fluid interfaces as well as fluid-solid interfaces, the ability to include shear waves in the bottom is often not important at long range. The effect of shear is predominantly evident in the reflection loss at grazing angles above critical, where loss is already quite high [6, p. 47]. Thus, at long ranges in shallow water shear is not very important.

2.2.1 Normal Modes

The derivation of the normal mode solution to the wave equation starts with the wave equation with density and sound speed dependence derived from conservation of mass, Euler's equation (Newton's second law) and the linear adiabatic equation of state.

$$\rho \nabla \cdot \left(\frac{1}{\rho} \nabla p \right) - \frac{1}{c^2} \frac{\partial^2 p}{\partial t^2} = 0. \quad (2.61)$$

Taking the Fourier transform in time gives the Helmholtz equation.

$$\rho \nabla \cdot \left(\frac{1}{\rho} \nabla p \right) + \frac{\omega^2}{c^2} p = 0. \quad (2.62)$$

Expressing this in cylindrical coordinates with no azimuthal dependence and considering a sound speed and density which depend only on depth, z , gives

$$\frac{1}{r} \frac{\partial}{\partial r} \left(r \frac{\partial p}{\partial r} \right) + \rho(z) \frac{\partial}{\partial z} \left(\frac{1}{\rho(z)} \frac{\partial p}{\partial z} \right) + \frac{\omega^2}{c^2(z)} p = 0. \quad (2.63)$$

A point source can be included at a depth $z = z_0$ and range $r = 0$ by including a monopole source term

$$\frac{1}{r} \frac{\partial}{\partial r} \left(r \frac{\partial p}{\partial r} \right) + \rho(z) \frac{\partial}{\partial z} \left(\frac{1}{\rho(z)} \frac{\partial p}{\partial z} \right) + \frac{\omega^2}{c^2(z)} p = \frac{-\delta(r)\delta(z - z_0)}{2\pi r} \quad (2.64)$$

where $\delta(x)$ is a Dirac delta function. Separation of variables assumes

$$p(r, z) = R(r)Z(z). \quad (2.65)$$

Substituting (2.65) into (2.63) and dividing by RZ yields

$$\frac{1}{R} \left[\frac{1}{r} \frac{\partial}{\partial r} \left(r \frac{\partial R}{\partial r} \right) \right] + \frac{1}{Z} \left[\rho(z) \frac{\partial}{\partial z} \left(\frac{1}{\rho(z)} \frac{\partial Z}{\partial z} \right) + \frac{\omega^2}{c^2(z)} Z \right] = 0. \quad (2.66)$$

The terms in the brackets of (2.66) are each dependent only on r or z . The only way this can be true is if each component is equal to a constant. Letting this constant be equal to k_n^2 gives the modal equation

$$\rho(z) \frac{\partial}{\partial z} \left[\frac{1}{\rho(z)} \frac{\partial Z_n(z)}{\partial z} \right] + \left[\frac{\omega^2}{c^2(z)} - k_n^2 \right] Z_n(z) = 0 \quad (2.67)$$

where Z_n is the particular function (mode) which satisfies the modal equation for k_n given a set of boundary conditions at the surface and bottom. The modal equation is a classic Sturm-Liouville problem and thus the solution, Z_n , has certain properties. Some of the important properties are:

1. There are an infinite number of solutions satisfying the equation.

2. Each solution (eigenfunction) Z_n is termed a mode and has a corresponding k_n , termed a modal number or eigenvalue.
3. Each k_n is distinct.
4. The modes are orthogonal and can be scaled such that

$$\int_0^D \frac{Z_n(z)Z_m(z)}{\rho(z)} dz = \delta_{nm} \quad (2.68)$$

where δ_{nm} is the Kronecker delta function.

$$\delta_{nm} = \begin{cases} 1 & n = m \\ 0 & n \neq m \end{cases} \quad (2.69)$$

5. The modes form a complete set allowing the representation of any function by choice of appropriate modal amplitudes. Thus,

$$P(r, z) = \sum_{n=1}^{\infty} R_n(r)Z_n(z). \quad (2.70)$$

Substitution of 2.70 into 2.64 yields

$$\sum_{n=1}^{\infty} \left\{ \frac{1}{r} \frac{\partial}{\partial r} \left(r \frac{\partial R_n(r)}{\partial r} \right) Z_n(z) + R_n(r) \left[\rho(z) \frac{\partial}{\partial z} \left(\frac{1}{\rho(z)} \frac{\partial Z_n(z)}{\partial z} \right) + \frac{\omega^2}{c^2(z)} Z_n(z) \right] \right\} = \frac{-\delta(r)\delta(z - z_0)}{2\pi r}. \quad (2.71)$$

Making use of the modal depth equation, (2.67), gives

$$\sum_{n=1}^{\infty} \left\{ \frac{1}{r} \frac{\partial}{\partial r} \left(r \frac{\partial R_n(r)}{\partial r} \right) Z_n(z) + k_n^2 R_n(r) Z_n(z) \right\} = \frac{-\delta(r)\delta(z - z_0)}{2\pi r}. \quad (2.72)$$

By use of the orthogonality condition in (2.68) and the properties of the delta function the equation for each range function can be extracted from the sum

$$\frac{1}{r} \frac{\partial}{\partial r} \left[r \frac{\partial R_n(r)}{\partial r} \right] + k_n^2 R_n(r) = \frac{-\delta(r) Z_n(z_0)}{2\pi r \rho(z_0)}. \quad (2.73)$$

(2.73) is a standard Bessel equation and its solutions are thus given by

$$R_n(r) = \frac{i}{4\rho(z_0)} Z_n(z_0) H_0^{(1)}(k_n r) \quad (2.74)$$

where the Hankel function of the first kind has been chosen to allow for only outward propagating energy. Using this solution for the range dependence with (2.70) gives the standard normal mode solution to the wave equation in shallow water

$$P(r, z) = \frac{i}{4\rho(z_0)} \sum_{n=1}^{\infty} Z_n(z_0) Z_n(z) H_0^{(1)}(k_n r) \quad (2.75)$$

where the Z_n 's are given by solution of the mode equation using boundary conditions.

2.2.2 Propagations Effects with Biot Theory

The complex pressure as function of range in shallow water wave guide with a sandy-silty bottom will be governed at long range by the modal propagation solution given in the preceding section with bottom properties described by the Biot theory. A comparison of (2.49) to (2.61) shows that if the density profile in the sediment were constant, the wave equation in the bottom would be identical to that used in the normal mode derivation except for the dissipative Biot time constant term. The addition of this term makes this problem an improper Sturm-Liouville problem. Assuming a seperable solution in cylindrical coordinates as before, the modal depth separated portion of the solution to 2.49 is

$$\rho \frac{\partial}{\partial z} \left(\frac{1}{\rho} \frac{\partial Z}{\partial z} \right) + \left(\frac{\omega^2}{c^2} + i \frac{\tau_B}{c^2} \omega^3 - k^2 \right) Z = 0. \quad (2.76)$$

Multiplying by the complex conjugate of the depth function, integrating and rearranging, results in the Rayleigh quotient,

$$k_n^2 = \frac{\int \frac{\partial}{\partial z} \left(\frac{1}{\rho} \frac{\partial Z_n}{\partial z} \right) Z_n^* dz + \int \left[\frac{\omega^2}{c^2} + \frac{i\tau_B}{c^2} \omega^3 \right] \frac{Z_n^2}{\rho} dz}{\int \frac{Z_n^2}{\rho} dz}. \quad (2.77)$$

Integrating the first term in the numerator by parts, and satisfying the radiation conditions gives

$$k_n^2 = \frac{\int \left[\frac{\omega^2}{c^2} + \frac{i\tau_B}{c^2} \omega^3 \right] \frac{Z_n^2}{\rho} dz - \int \frac{1}{\rho} \left(\frac{\partial Z_n}{\partial z} \right)^2 dz}{\int \frac{Z_n^2}{\rho} dz}. \quad (2.78)$$

The complex modal wave number is given by

$$k_n^2 = \left[\frac{\omega}{v_{ph,n}} + i\alpha_n \right]^2 \approx \frac{\omega^2}{v_{ph,n}^2} + 2i\alpha_n \frac{\omega}{v_{ph,n}} \quad (2.79)$$

where α_n is the modal attenuation coefficient and $v_{ph,n}$ is the phase velocity of the n^{th} mode. Equating the imaginary components of 2.78 and 2.79,

$$\alpha_n = \frac{v_{ph,n} \omega^2}{2} \frac{\int \frac{\tau_B}{\rho c^2} Z_n^2 dz}{\int \frac{Z_n^2}{\rho} dz} = v_{ph,n} \frac{\int \frac{\alpha(\omega)}{\rho c} Z_n^2 dz}{\int \frac{Z_n^2}{\rho} dz} \quad (2.80)$$

which makes use of (2.53). From this, it is clear that the modal attenuation coefficient depends on the intrinsic attenuation in the sediment as a function of depth and can be described by considering mode functions and the depth dependent profiles. Rather than having profiles for sound speed, density, porosity, etc. (13 Biot parameters), the problem in the low frequency range can potentially be solved using profiles for only the sound speed, density, and Biot time constant. This also means that the measured effective attenuation will be site specific and since lower frequency modes penetrate deeper into the sediment, making more consolidated deeper layers an increasing factor, the measured exponent, n , in $\alpha = \alpha_0(f/f_0)^n$ is often below 2, as reported in table 1.1 [85].

2.2.3 Sources of Attenuation

When low to mid frequency sound is propagated through sediment, sound energy is lost through a number of mechanisms. Intrinsic attenuation is treated above, but it is only one mechanism. Sheriff summarizes the possible mechanisms which include [86]

1. Intrinsic attenuation - This is the attenuation caused by conversion of acoustic energy to heat as a wave passes through a material. This is of primary interest here.
2. Transmission through boundaries - Whenever sound propagates through a discontinuity, some energy is reflected and some transmitted. Boundaries can cause enhancement of a signal or degradation and shear wave conversion can occur at the boundaries as indicated in section 2.1.3.
3. Boundary roughness - Acoustic energy can be focused or defocused due to boundary curvature. Also, bottom roughness can cause sub-critical penetration into the sediment. Rough surface and interface scattering is also a loss mechanism.
4. Scattering by inhomogeneities - Inhomogeneities such as shells, large rocks, or bubbles in sediment can cause sound energy to scatter.

If more than one of these effects is present and of similar importance, then the measured attenuation in situ will be an effective attenuation instead of solely the intrinsic attenuation. Kuperman and Inginito treat the case of an intrinsic attenuation in the bottom with an additional attenuation term due to interface roughness at the surface and bottom in a perturbational approach [87]. Evidence of the combination of several effects causing an effective attenuation in the sediment, limiting the ability to measure intrinsic attenuation, is present in a measurement made in the Barents Sea where there is a high density of scatterers in the sediment [88]. In order to avoid these problems in an experiment, an experimental location can be chosen with the help of a high frequency sub-bottom profiler such that the surface roughness is small compared to a wavelength and the sediment layer is relatively homogenous.

2.3 Array Theory

In section 1.3 it was hypothesized that an AUV towed hydrophone array could be used to measure the sound transmission effects seen in the preceding sections. In order to accomplish this, linear array theory must be explored. While the derivations of array gain and a beamformer algorithm are important, they are rather mundane and are given in appendix B.

2.3.1 Wave Guide Characterization

The basis for the wave number integration technique for prediction of propagation is that the solution of the inhomogeneous wave equation

$$\left[\frac{1}{r} \frac{\partial}{\partial r} \left(r \frac{\partial}{\partial r} \right) + \rho \frac{\partial}{\partial z} \left(\frac{1}{\rho} \frac{\partial}{\partial z} \right) + \frac{\omega^2}{c(z)^2} \right] p(r; z, z_0) = \frac{-\delta(r)\delta(z - z_0)}{2\pi r} \quad (2.81)$$

can be expressed by the zero-order Hankel transform pair of the depth dependent Green's function

$$p(r) = \int_0^\infty g(k_r) J_0(k_r r) k_r dk_r \quad (2.82)$$

$$g(k_r) = \int_0^\infty p(r) J_0(k_r r) r dr \quad (2.83)$$

where r is the range, k_r is the horizontal wave number, and J_0 is the Bessel function of order 0. The Green's function satisfies

$$\left(\frac{\partial^2}{\partial z^2} + \frac{\omega^2}{c(z)^2} - k_r^2 \right) g(k_r; z, z_0) = \frac{\delta(z - z_0)}{2\pi} \quad (2.84)$$

as well as the boundary conditions at the surface and bottom. Inspection of (2.84) reveals that it is independent of range. Wave number integration techniques take advantage of this and solve (2.84) for $g(k_r; z, z_0)$ using the boundary conditions and then use (2.82) to

find the pressure. This is often done by assuming the asymptotic transform pair

$$p(r) \approx \frac{e^{-i\pi/4}}{\sqrt{2\pi r}} \int_0^\infty g(k_r) e^{(ik_r r)} \sqrt{k_r} dk_r, \quad (2.85)$$

$$g(k_r) \approx \sqrt{\frac{2\pi}{k_r}} e^{i\pi/4} \int_0^\infty p(r) e^{(-ik_r r)} \sqrt{r} dr. \quad (2.86)$$

Noticing that (2.85) and (2.86) are simply the Fourier transform of $g(k_r)\sqrt{k_r}$ and $p(r)\sqrt{r}$ respectively yields the fast field approximation by which the transforms can be calculated efficiently using the FFT.

Using the normal mode and wave number integration solutions to the wave equation in shallow water, the pressure field can be represented as a function of range as

$$p(r; z, z_0) = i\pi \sum_{n=1}^N a_n Z_n(z_0) Z_n(z) H_0^{(1)}(K_n r) + I(r) \quad (2.87)$$

This differs from the equation shown in section 2.2.1 in that the modal normalization is incorporated into the mode amplitude a_n and the eigenvalues K_n are made complex ($K_n = k_n + i\alpha_n$) to include the modal attenuation predicted in section 2.2.2. Also, $I(r)$ is included to represent the continuum contribution to the field given from the wave number integration contour, but is readily neglected because the trapped mode sum dominates in the far field. Further, the modal sum is limited to include only the number of propagating modes predicted by modal cutoff. The eigenvalues and eigenfunctions must still satisfy the modal equation and the boundary values so the sound transmission problem is a classic boundary value waveguide problem. This means that the long-range sound transmission in the water column contains information about the bottom and thus so does the transform $g(k_r)$.

Using the asymptotic form of $H_0^{(1)}$

$$H_0^{(1)}(K_n r) \approx \sqrt{\frac{2}{\pi K_n r}} e^{-i\pi/4} e^{ik_n r - \alpha_n r} \quad (2.88)$$

gives

$$p(r) \approx \sqrt{2\pi} e^{i\pi/4} \sum_{n=1}^N a_n Z_n(z_0) Z_n(z) \frac{e^{ik_n r - \alpha_n r}}{\sqrt{K_n r}}. \quad (2.89)$$

If $p(r)$ is measured as a function of range for a given source and receiver depth, then the measured horizontal wavenumber spectrum is given by the transform in (2.83)⁶. This yields

$$g(k_r) \approx \frac{2\pi i}{\sqrt{k_r}} \sum_{n=1}^N \frac{a_n}{\sqrt{K_n}} Z_n(z_0) Z_n(z) \times \int_0^R e^{-i(k_r - k_n - i\alpha_n)r} dr. \quad (2.90)$$

If an infinite aperture was realized with no attenuation, perfect resolution would be achieved and at each eigenvalue, k_n , the measured horizontal wavenumber spectrum would give a peak of infinite height and zero width. Lynch, Frisk and Rajan [89] showed that on a finite aperture R , the measured horizontal wave number spectrum becomes

$$g(k_r) \approx \frac{-2\pi}{\sqrt{k_r}} \sum_{n=1}^N \frac{a_n}{\sqrt{k_n + i\alpha_n}} Z_n(z_0) Z_n(z) \left(\frac{e^{-i(k_r - k_n - i\alpha_n)R} - 1}{k_r - k_n - i\alpha_n} \right). \quad (2.91)$$

This gives first order poles at wave numbers corresponding to the modal eigenvalues $k_r = k_n + i\alpha_n$. The finite aperture gives modal peaks in the spectrum with a finite height and the attenuation gives the peaks a finite width. By L'Hopital's rule, it can be shown that the amplitude of each modal peak is proportional to the modal amplitude times a function dependent only on R^2 [89]. Thus, the transform of $p(r)$ over a finite aperture allows for the estimation of the modal amplitudes.

While this analysis is carried out here using the asymptotic approximation, modern computing allows for the calculation of (2.83) in its full form numerically either by quadrature integration or the Fourier-Bessel series [89,90].

Since $g(k_r)$ depends on the boundary conditions, it contains all of the necessary information to determine how the sediment properties affect propagation. It has been shown by many analyses that the measured values of the eigenvalues from the horizontal wave

⁶It is noted that "horizontal wavenumber spectrum" is used when referring to the transform given by (2.83) when applied to measured data. This is because the "Green's function" requires an infinite measurement with no attenuation and no measurement noise.

number spectrum permits the determination of $c(z)$, $\rho(z)$, and $\alpha(z)$ by various inversion techniques [89,91–94]. An addition to these techniques comes from the previous section of propagation effects with a Biot bottom. If a sliding window finite aperture in range is used, then the modal amplitude as a function of window range can be measured. This should be of the form

$$A_n(r) = a_n e^{-\alpha_n r}. \quad (2.92)$$

Fitting measured amplitudes to (2.92) gives the modal attenuation coefficient α_n which we know from section 2.2.2 is

$$\alpha_n = v_{ph,n} \frac{\int \frac{\alpha(\omega)}{\rho c} Z_n^2 dz}{\int \frac{Z_n^2}{\rho} dz}. \quad (2.93)$$

$Z_n(z)$ is primarily affected by $c(z)$, so if a sound speed profile is known, the modal equation gives $Z_n(z)$, which can be numerically calculated. To determine the attenuation profile from modal attenuation values, we start by rearranging (2.93) to be

$$\int_z \frac{\alpha(z, \omega)}{\rho c} Z_n^2 dz = \frac{\alpha_n}{v_{ph,n}} \int_z \frac{Z_n^2}{\rho} dz. \quad (2.94)$$

The left side of (2.94) is a function of the unknown profile $\alpha(z)$ and the right side contains only measured values. Letting the right side be represented by d_n gives

$$\int_z \frac{\alpha(z, \omega)}{\rho c} Z_n^2 dz = d_n. \quad (2.95)$$

Taking the ratio of (2.95) for two modes, n and m , gives

$$\frac{\int_z \frac{\alpha(z, \omega)}{\rho c} Z_n^2 dz}{\int_z \frac{\alpha(z, \omega)}{\rho c} Z_m^2 dz} = \frac{d_n}{d_m}. \quad (2.96)$$

If the attenuation profile is assumed to be a frequency dependent attenuation times a depth

dependent envelope, $\alpha(\omega)\kappa(z)$, (2.96) reduces to

$$\frac{\int_z \frac{\kappa(z)}{\rho c} Z_n^2 dz}{\int_z \frac{\kappa(z)}{\rho c} Z_m^2 dz} = \frac{d_n}{d_m}, \quad (2.97)$$

$$\frac{G_n(\kappa(z))}{G_m(\kappa(z))} = \frac{d_n}{d_m}. \quad (2.98)$$

Using this, the best fit of the measured data to an assumed model can be found numerically using standard optimization algorithms and the ratio of measured quantities. Unlike previous approaches to finding the depth dependence of attenuation [95] there is no requirement for an assumption for the form of $\alpha(\omega)$ which allows for the independent determination of depth and frequency dependence.

2.3.2 Synthetic Aperture Methods

In ocean acoustics space and time are often treated as independent random variables and ergodicity is assumed. Synthetic aperture methods make use of the fact that with a moving source-recipient pair, space and time are not independent and a space-time processor can increase gain and resolution. Carey and Moseley [96] give a good review of space time processing as well as the environmental and acoustic effects of spatial coherence and angular spread.

In a shallow water waveguide there have been two major applications of synthetic aperture processing: waveguide characterization and target tracking [75]. In either case the idea is to use space-time processing to generate a long spatial aperture using a small physical sensor by exploiting the motion of the sensor. The advantage, as shown in appendix B, is that by increasing the aperture of the array the resolution in the transform space is enhanced.

Waveguide characterization using the Hankel transform as presented in the previous section requires apertures on the order of kilometers. Frisk, Lynch, and Rajan [91] realized that such an aperture could be achieved using a synthetic aperture formed by a source

and receiver pair moving apart at drift velocities. Their experiments took place off Corpus Christi, TX and in Nantucket sound and took hours to complete, which allowed for changes in currents, water column sound speed profiles, and tidal depths over the course of the experiments. Figure 2.4 shows a diagram of their experimental configuration. By using an AUV towed hydrophone array the goal is to perform this type of synthetic aperture Hankel transform experiment much faster and more accurately.

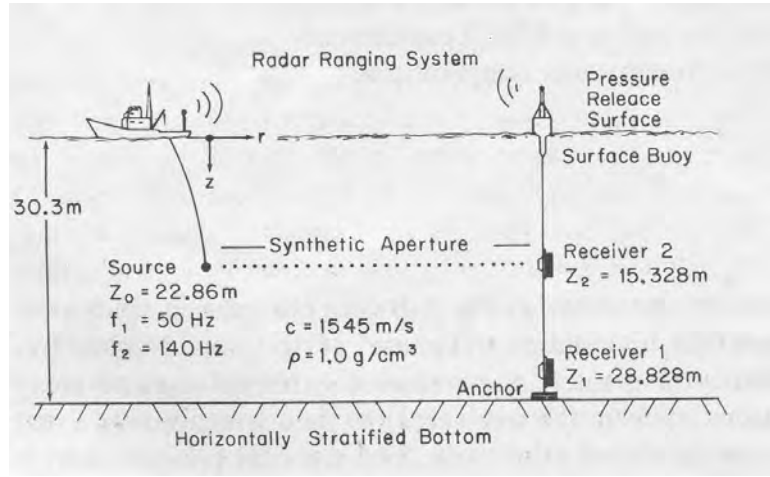


Figure 2.4: Diagram of the Lynch-Frisk-Rajan drift velocity experiment taken from [89].

The difference between physical aperture processing and synthetic aperture processing can be readily seen in the beamforming solution. The standard beamformed output of a line array is given by (from appendix B)

$$b(k, \theta, t) = \sum_{j=1}^N \langle p_j(\omega) \rangle e^{[\frac{\omega}{c} x_j \sin \theta]} W_j \quad (2.99)$$

where $\langle p_j(\omega) \rangle$ is the complex pressure on the j^{th} sensor at the frequency ω given by a Fourier transform, x_j is the position of the j^{th} sensor relative to the array center, θ is the steering angle, and W_j is the shading of the j^{th} sensor. The sum is taken over the N

sensors in the physical aperture. The extension to the synthetic aperture case is

$$b(k, \theta, t, \phi_i) = \sum_{i=1}^M \sum_{j=1}^N \langle p_{ij}(\omega') \rangle e^{[\frac{\omega}{c} x_j \sin \theta - \phi_i]} W_{ij} \quad (2.100)$$

where now $\langle p_{ij}(\omega') \rangle$ is the pressure on the j^{th} sensor of the i^{th} sub-aperture at the doppler frequency given by $\omega' = \omega (1 \pm (v/c) \sin \theta_s)$. ϕ_i is the phase compensation term needed to account for the time between measurements and the random motions of the array. Yen and Carey showed in their derivation that this is equivalent by the product theorem of arrays [2] to the beamformed output of the sub-aperture times the beamformed output considering an array of sensors with positions at the the sub-aperture centers [74]. For a stable, straight tow,

$$\phi_i = \omega t_i \quad (2.101)$$

where t_i is the time at which the i^{th} sub-aperture sample is measured relative to the time at which the first sub-aperture sample is taken.

Thus far the analysis assumes knowledge of the relative velocity V between the source and receiver and the source frequency. If the relative velocity and frequency are not well known, a more general beamformer integrating beam power over several frequency bands can be used as derived in appendix B. Also, Sullivan showed theoretically that by posing the problem as a joint detection problem with frequency and bearing in a Kalman filter the variance of the output can be reduced [97].

Assuming perfect array stability, the synthetic aperture phase correction term is given by (2.101). In reality the array often experiences some oscillations and more robust methods of estimating the phase correction are needed. Sullivan and Stergiopolis developed an overlap correlation technique where the array is moved forward only a fraction of its total length between each measurement allowing overlap of hydrophone samples between successive measurements. Correlation of the signal on the overlapped channels allows for an estimation of the phase compensation term.

Other means for estimating the phase term are using the the vehicle velocity with an accurate clock along (which inherently assumes a stable tow and that (2.101) is valid), putting a reference source of known position and frequency in the water, and using a high frequency, high band-width acoustic pinger for shape estimation and motion compensation. These methods can be arranged in decreasing order of required array stability as

1. Use only the navigational and clock information from the vehicle.
2. Use a reference source with a known position and frequency.
3. Use high frequency pingers for shape and motion compensation.
4. Use overlap correlation between sub-apertures to estimate the phase term.

While the preceding arguments are formed for the target tracking (angle space) application of synthetic aperture, Frisk *et al.* [98] showed that beamforming for wave guide characterization is equivalent and one can transform the wave number space to an angle space. Thus these methods can be applied to the wave guide characterization problem.

The difference between conventional array processing and synthetic array processing is shown schematically by figure 2.5. The most important difference is of course the phase correction term which, in this case, is given by vehicle information.

Even if overlap correlation is not used to find the phase correction term, overlap processing can improve the signal to noise ratio and provide a measure of the signal variance. Figure 2.6 shows the overlap processing scheme used by an AUV towed hydrophone array in which the vehicle data is used for phase compensation and measurements are taken for every advance d of the array where d is the sensor spacing in the array. By doing this, N independent measurements of the complex pressure at each range are obtained where N is the number of sensors in the array. Averaging of the N measurements improves the signal to noise in the same manner that an array achieves gain: exploiting the coherent gain of the signal over the incoherent noise gain. This allows for improved performance of the towed array system as compared to the single source-receiver used by Frisk *et al.* .

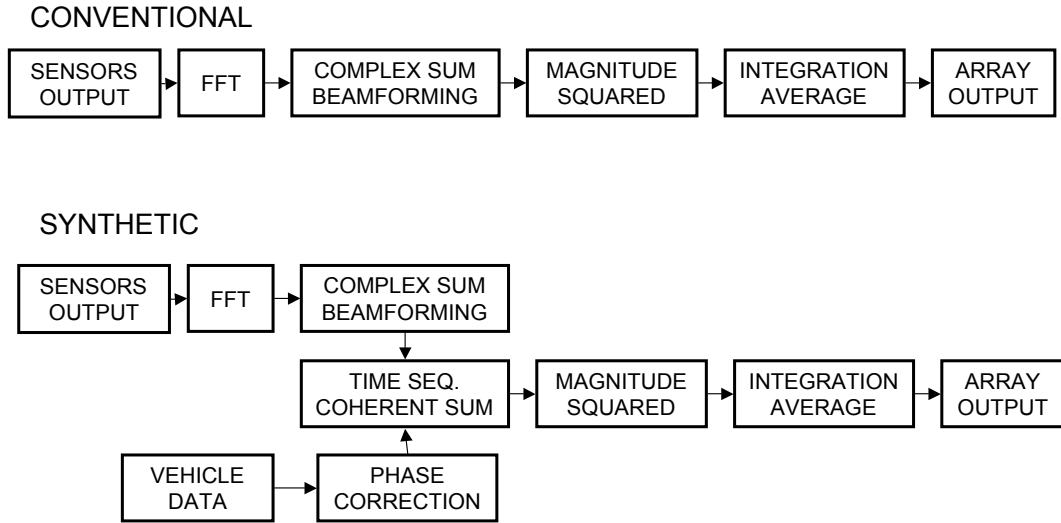


Figure 2.5: Schematic comparison of conventional and synthetic aperture processing

2.3.3 Measurements with AUVs

Long range transmission loss

In a long range transmission loss experiment, the sound transmission as a function of source and receiver depth, frequency, and range is measured. The intent of this technique to perform the measurement done in the Corpus Christi or Nantucket experiments described in section 2.3.2 but to perform it more rapidly and more accurately by using an AUV. The experimental setup is as shown in figure 2.7 and involves an AUV towed hydrophone array moving radially outward from a source on a moored support ship. A more realistic depiction of the AUV towed array system described in appendix D is shown in figure 2.8. Deployment of the AUV is performed by the same ship that the source is on. By using a source with multiple narrow band tones, sound transmission is measured as a function of frequency on the array and by having the AUV navigate radially out and back the experiment is immediately repeated else the source frequencies are changed on the return leg and the data set expanded. The intent is to measure $p(r; z, z_0)$ and thus characterize the waveguide by means of the synthetic aperture Hankel transform technique described

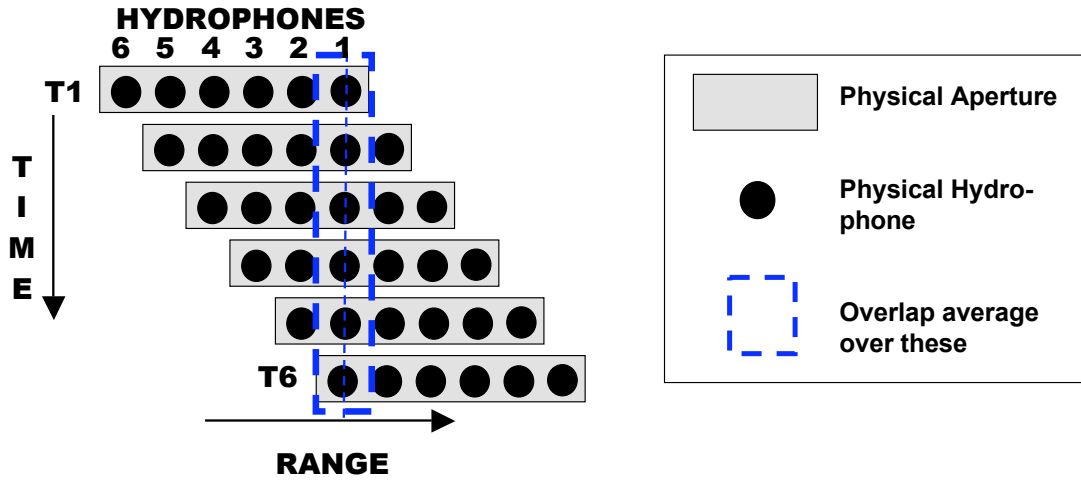


Figure 2.6: Schematic of overlap processing used on an AUV towed hydrophone array to improve the signal to noise ratio

in section 2.3.1.

Single path

Another experiment besides the long range sound transmission experiment makes use of the theory of reflections from a Biot bottom (section 2.1.3) as well as beamforming into an angle space. Figure 2.9 shows a diagram of the experimental setup for this experiment as originally proposed. By using a directional parametric source the intent was to measure a single path reflection off the bottom or surface and measure the direct path transmission with no surface interactions. By doing this with an array the reflection coefficient as a function of angle off the bottom could be measured by adjusting the parametric source angle. From the diagram it is clear that the source is deployed from the stationary ship and thus only a single patch of the bottom is ensonified. Early static tests of this technique performed at the Naval Surface Warfare Center, Panama City Florida indicated that the unknown ripple on the sediment interface introduced too much error into the received signal angle for this method to be useful.

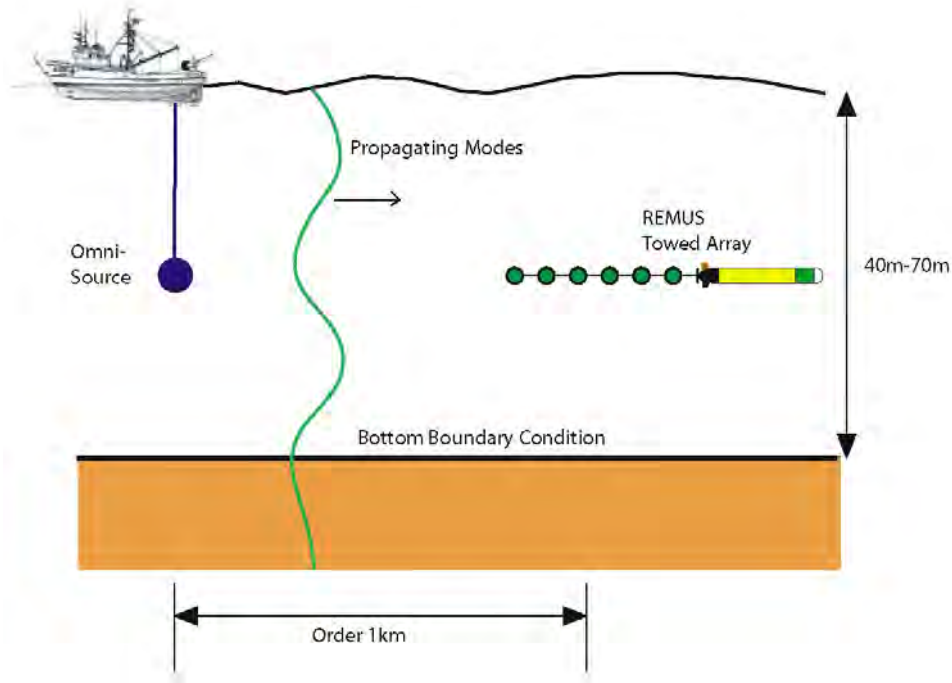


Figure 2.7: Geometry of the long-range sound transmission experiment used with the synthetic-aperture-Hankel transform waveguide characterization method

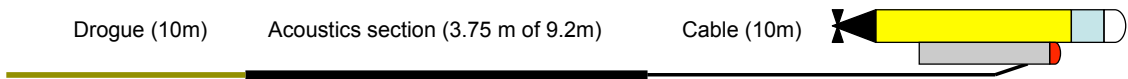


Figure 2.8: Diagram of the subsystems of the towed array system. The vehicle is shown towing the array with the recording canister strapped to the bottom.

Currently, sound sources are inefficient and require the power available on board a ship. If smaller, more efficient sources could be made to operate at these low frequencies such that they could be mounted directly on the AUV, then a new single path experimental setup can be used. A schematic for this experiment is shown in figure 2.10. By mounting a source directly on the vehicle, the ship is no longer needed. Further, by having the vehicle use its on board sensors to keep it at a height h above the sea floor then the angle from the source to the array is given by

$$\theta = \tan^{-1} \left(\frac{2h}{L} \right) \quad (2.102)$$

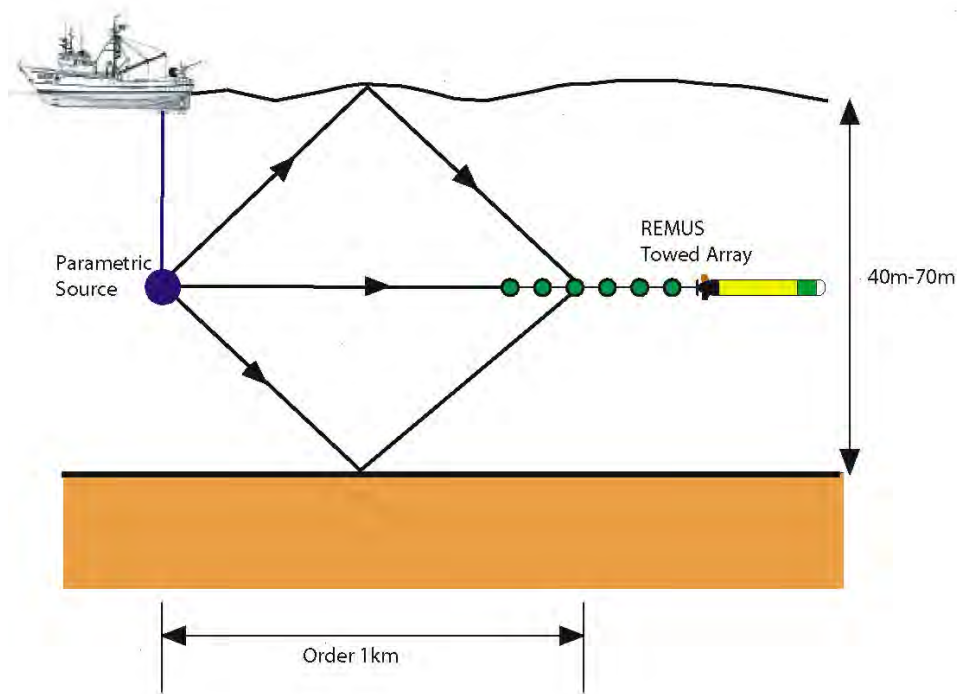


Figure 2.9: Geometry of the single path sound transmission experiment as originally proposed to measure the angle dependent reflection loss from a saturated sediment in-situ

where L is the distance between the vehicle source and the array center. By navigating in straight paths at different heights above a flat bottom and beamforming the array in the direction of θ , the angle dependent reflection loss can be measured in-situ. The motion of the source with the array allows for ripple effects to be averaged out over time.

While this experiment may allow for the measurement of the propagating field as well as the evanescent field, it requires the development of an AUV based low frequency source which may prove difficult given the power constraints on a vehicle. Also, this experiment relies on the measurement of the reflection loss from a single reflection off the bottom. The difference between models for a single reflection can be very small and thus signal to noise problems are of primary concern. Due to these concerns, it was determined that the synthetic aperture Hankel transform experiment was the best method for characterizing the sediments with the current technology and is thus used in this work.

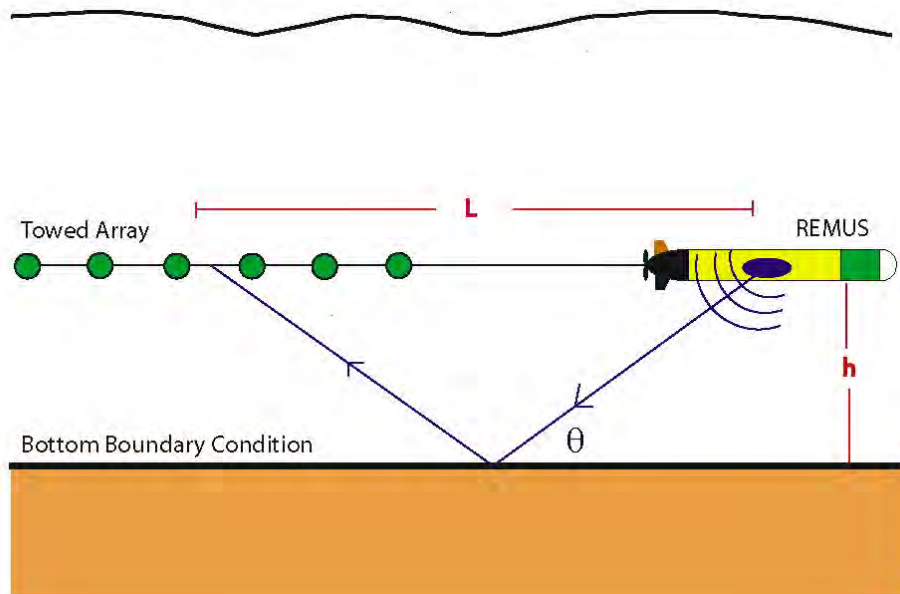


Figure 2.10: Geometry of the single path sound transmission experiment as proposed with an AUV mounted source to measure the angle dependent reflection loss from a saturated sediment in-situ

Chapter 3

System Characterization

In order to perform the synthetic aperture Hankel transform experiment described in section 2.3.3, a small AUV towed hydrophone array system was designed and constructed. In Appendix D section 1 the characteristics of the vehicle chosen to tow the array are presented. Of particular importance are the 1kw-hr battery capacity, the 5 knot maximum speed with no added drag, and the propulsion system characteristics. These characteristics imposed constraints that the array be optimized to have low drag and consume little power. Further, for the array to be useful for the experiment, the entire system, including the array, the vehicle, and the recording system, had to be low noise. By utilizing known array design methods and adapting them to the problems associated with towing an array by a small AUV, a simple yet elegant design emerged. Details of the system design and construction are given in appendix D and motivated by the discussion of towed array noise in appendix C. The system consisted of a slightly modified REMUS vehicle towing an approximately 30 m long neutrally buoyant array. The array consisted of a 10 m long cable, a 9.2 m long, 2.8 cm diameter oil filled acoustic section with 6 hydrophone channels spaced 0.75 m apart, and an approximately 10m long high drag drogue to keep the array straight. In order to rapidly interface the array to the vehicle, an external canister was clamped to the vehicle and a recording system consisting of off the shelf components was designed and fabricated. This recording system used audio quality mini-disc recorders which were

limited to 90 minutes of uncompressed data.

In order to determine the operating characteristics of the components of the system, i.e. the vehicle, the array, and the recording system, a series of engineering tests were performed. Since the recording system was composed of off the shelf components, it needed only to be calibrated, which was done by recording a known signal and determining the calibration constant to convert the recorded data to voltages seen at the input. The results of this calibration are given in appendix D. Before performing an at-sea experiment, the vehicle and array required more detailed characterization, which is the focus of the remainder of this chapter.

3.1 Array Calibration

For the array to be used to make accurate measurements, it first required calibration. This calibration was performed on a floating test platform in a pond with a thick mud bottom¹. The bottom reflection coefficient at the facility is low which makes the test range a low noise test range. Before calibrating the array, the range was characterized by putting a calibrated H-52 hydrophone [99] at a known distance from a J-9 reference source [99]. Known pulses with center frequencies between 300 Hz and 10 kHz were transmitted through the source and recorded on the reference hydrophone. The hydrophone array was then hung vertically in the water with a weight at the end keep it vertically straight and positioned such that the first channel was in the same position that the reference hydrophone originally was. Sine wave pulses were recorded on the array at the same frequencies used for calibrating the reference. This was repeated for each hydrophone channel and the response on each channel compared to the reference hydrophone response. The results of this calibration showed that every channel had a sensitivity of -174 ± 1 dB re $1V/\mu Pa$ from 300 Hz to 5 kHz and -174 ± 2 dB re $1V/\mu Pa$ from 5 kHz to 10 kHz.

Calibration stability with temperature changes was a concern. Pre-amplifiers and hy-

¹The test facility was the U.S. Navy's Dodge Pond Acoustic Test Facility in Niantic CT.

drophones can change sensitivity with a temperature change. More importantly, the properties of the array hose and fill oil can change due to temperature, causing a stiffening of the material and a change in the transfer function to the hydrophones. The calibration was first conducted in water that was approximately 24°C . When this calibration was repeated 3 months later in the same fashion with water at 6°C , the results showed good stability with a calibration over all channels of -173.5 ± 1.5 dB re $1\text{V}/\mu\text{Pa}$ over 300 Hz to 10 kHz.

3.2 Vehicle Noise

The radiated noise from the vehicle towing the hydrophone array is one of the major sources of noise in the system. A discussion of this and other noise mechanisms can be found in appendix C. Measurements of the radiated noise are required to characterize the system and an understanding of the mechanics of the relevant noise sources is necessary if quieting is required.

Donald Ross gives a very thorough treatment of the radiated noise from vehicles [100]. For an AUV, the potential sources of radiating noise are internal components such as hard drives and motor controllers radiating through the hull, propulsion system noise, and other sensor noise. Other sensors on the vehicle which emit noise are the acoustic modem, the ADCP, and the side scan sonar. The side scan sonar operates at a much higher frequency than the intended operating frequency of the array and has a narrow beam broad side of the vehicle. Thus very little side scan noise would be picked up by the array which is directly aft of the vehicle. Regardless, since the side scan sonar is not being used while the towed array is being used, it is not an issue. The ADCP is used to navigate when the array is in use and it transmits very broadband clicks which could interfere with the array acoustics. Fortunately, the ADCP is also very directional and transmits predominately in the upward and downward directions. Likewise, it is expected that any internal component noise would radiate through the thin hull, not the thick tail section, and thus be predominately directed radially outward from the vehicle, not behind it.

Table 3.1: Qualitative relationship between tip cavitation index and likelihood to cavitate.

K_T Range	Likelihood of cavitation
$K_t > 5$	Cavitation unlikely
$2 < K_t < 5$	Inception in poor wakes (blunt body)
$1 < K_t < 2$	Inception in good wakes (streamlined body)
$0.5 < K_t < 1$	Inception in uniform flow
$0.2 < K_t < 0.5$	Moderate cavitation probable
$K_t < 0.2$	Heavy cavitation probable

Before performing the experiment, it was expected that the major noise source contribution would be thruster noise. Noise radiated from the thruster is caused by cavitation, oscillating thrust on the blades, vortex interactions, rotor-stator interactions, and bearing noise. All of these noise sources can radiate noise directly or excite hull or propellor motion which then radiates. Each of these noise mechanisms has its own characteristics.

Cavitation is the formation of gas bubbles on the propellor due to high dynamic pressures. Bubbles form and collapse on the propellor face generating very broad band noise, but an aggregate bubble cloud is also formed in the wake. The bubble cloud is excited by bubble collapse and oscillates as a whole with natural frequencies of tens to hundreds of hertz. The clearest evidence of cavitation noise is thus the presence of bubbles in the propellor wake, concurrent with broad band radiated noise.

For a submarine, Ross gives a tip cavitation index to indicate the likelihood of cavitation as

$$K_t = \frac{2}{3} \frac{h + 9}{\left(\frac{N}{100}\right)^2 D^2} \quad (3.1)$$

where h is the depth of submergence in meters, N is the rotational speed of the propellor in RPM, and D is the propeller diameter in meters [100]. The relationship between the qualitative likelihood of cavitation and tip index is then given in table 3.1.

Using the diameter of the propellor on the vehicle and a typical operating RPM of 1350 at a depth of 3 meters gives $K_t \approx 2.2$. Since the vehicle is streamlined, it is thus unlikely

that the vehicle will cavitate, but at it's highest RPM near the surface cavitation inception could occur.

Table 3.1 suggests that cavitation will not be present until the cavitation index drops below some inception value, after which its effects will be noticed. Equation (3.1) reveals that the cavitation index is inversely proportional to the propeller RPM squared. Thus, cavitation will not be present until some critical RPM, beyond which it will generate a great deal of noise. Oscillating thrust on the blades, bearing noise, and rotor-stator interaction, on the other hand, would be RPM dependent in a more smoothly varying manner. As the RPM increases, these noise mechanisms will have a characteristic frequency and level, both of which increase with RPM. This gives the characteristic blade lines shown in Urick's figure 10.10 [2]. These lines appear at frequencies proportional to the product of the shaft RPM and the number of balls in the bearing, blades on the propellor, or other mechanical discontinuities which are relevant for each rotating part. At high ka (that is the acoustic wave number times a characteristic length scale for the vehicle) , thruster noises are expected to have a component due to loading noise caused by oscillating flow on the blades with a main lobe long the axis of the vehicle, and another component due to the blade motion with a main lobe along the plane of rotation of the blade. At low ka , however, all of these noises will be omnidirectional.

Finally, hull and propellor resonances have a characteristic frequency which is fixed by geometry. The build up of total energy because of excitations will produce larger and larger oscillations between potential and kinetic energy of the resonator. In mechanical systems this usually means an increase in displacement and velocity resulting in radiation. Thus. if a noise source exists at the resonator's resonant frequency and can excite the resonator, a louder noise at that resonant frequency will be radiated. If the driving noise is RPM dependent, this will be characterized by a particular noise line in the frequency domain which is persistent, but changes level with changing RPM.

To characterize the noise of the vehicle used in the system, the approach taken was to first measure the radiated noise versus RPM and bearing in two experiments, and then

determine the relevant mechanisms.

3.2.1 Tethered Measurements

The first radiated noise test of the vehicle was a test of the vehicle at bollard, that is tethered to the end of a test shaft. This was performed at the same location as the array calibration with a floating test platform on a quiet lake. The test platform has a test shaft capable of positioning a 5 ton object vertically at any given depth below the platform and rotating the object with a 0.1° rotational accuracy. 13 meters away from this test shaft, three hydrophones were hung below the platform. The configuration for this test is shown in figure 3.1. In order to calibrate the test range, a calibrated source was first attached

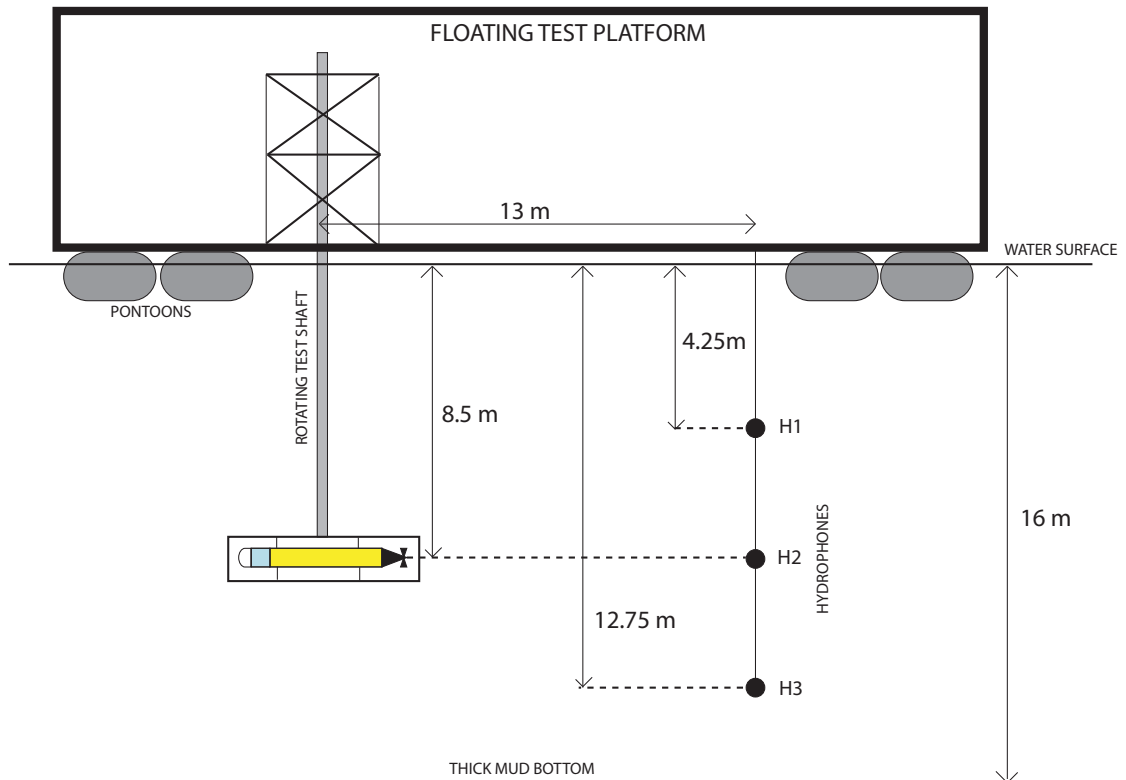


Figure 3.1: Diagram showing the experimental configuration for measuring the radiated noise from a REMUS vehicle while at bollard.

to the test shaft at the location where the vehicle is shown in figure 3.1. 6 ms continuous wave (CW) pulses were transmitted from the source and recorded on each hydrophone at frequencies of 300, 500, 1000, 5000, and 10000 Hz. This allowed for the characterization of multi-path effects, which ranged from +3 dB of constructive interference to - 3 dB of destructive interference depending on frequency as is expected for a shallow water waveguide. The measured results from this calibration can be analyzed in three ways.

- First, one could use the measured interference effects to correct the measured radiated noise levels. A range corrected source level could then be given for the source level at 1m. This is difficult because the multi-path effects were only measured at discrete frequencies.
- Second, the constructive and desctructive interference effects as measured in the calibration can be used as error bounds on the measurements. That is, one could correct for distance and report a source level at 1 m, but apply error brackets to that source level due to the multi-path interference effects. This is probably more reasonable to do with the measurements taken but would place error bounds that are larger than reality on the radiated noise.
- Finally, the approach taken here, is to realize that the measurements were made with the vehicle at a typical operational depth in a typical water column with the calibrated hydrophone the same distance away as the hydrophone channels in the towed array. Thus, the measurements are characteristic of what will be experienced operationally. Using this method, it would be improper to range correct the measured noise levels but the noise levels experienced by the array would be given without further calculations.

The vehicle was lowered on the rotating shaft and the radiated noise was measured on the the center hydrophone shown in figure 3.1. Measurements were taken with the vehicle rotated every 10° to determine the directionality of the radiated noise. A heading of 180°

was defined to be aft of the vehicle, 90° was broadside of the vehicle, and 0° was forward of the vehicle. The radiated noise was recorded for 10 seconds at a sampling rate of 2^{15} samples per second. Power spectral densities were found using an FFT of 2^{15} points with a 50% overlap, resulting in 1 Hz band output. Since the hydrophones were 13 meters away from the vehicle, the reported levels are not range corrected and represent the levels expected on an array towed by the vehicle.

Two tests were performed using this setup, one in September of 2004 and the second in December of 2004. In the first test, two vehicles were used in order to get a sense of the variation between vehicles. Figure 3.2 shows the radiated noise from these two vehicles as a function of frequency directly aft of the vehicle at 13 meters. While the exact frequency structure varied between vehicles, the major features were the same. The loudest noise component was a peak in the spectrum slightly above 1 kHz and there were less prominent features near 600 Hz and closer to 2 kHz. Figure 3.3 shows the ambient noise for the September tests, which indicates that the radiated noise measurements were ambient noise limited below 400 Hz and above 8 kHz. Measurements taken at different vehicle bearings in this test showed that the radiated noise was primarily omni-directional. The one exception to this was at broadside to vehicle where broadband, high frequency pulses from the ADCP are experienced. A time series waveform of the noise as recorded in this direction is shown in figure 3.4. An expanded view of a single pulse in the sequences is also shown. It was determined that these were ADCP noise because the clicks were not present when the ADCP was turned off and were only measurable within 5 degrees of broad side when in the 0 degree plane in elevation.

While noise sources on ships are often directional, the fact that the radiated noise is omnidirectional is not a surprising result if the vehicle components are compared to a radiating piston. Assuming a radiating part of the vehicle can be approximated by a piston with a constant face velocity, the directionality is [100]

$$D(\theta) = 1 - \frac{(ka \sin \theta)^2}{8} + \frac{(ka \sin \theta)^4}{192} \quad (3.2)$$

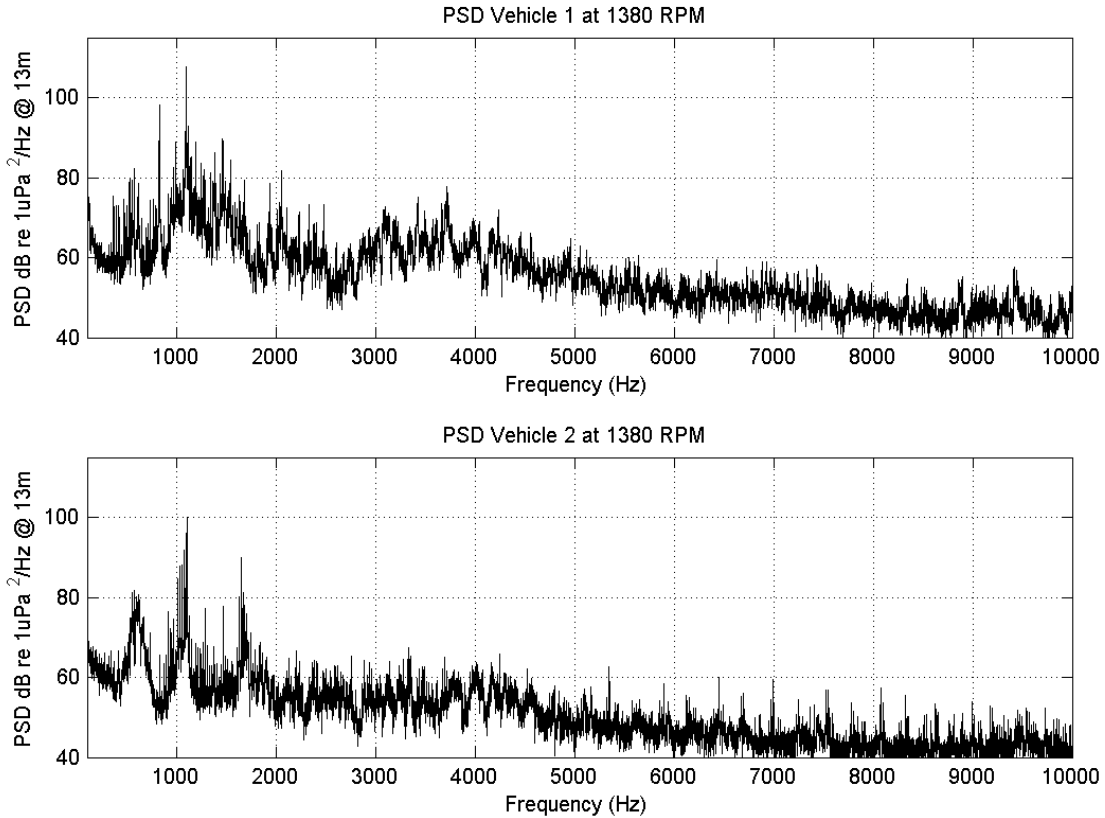


Figure 3.2: Measured power spectral density of the radiated noise from two different vehicles. The first vehicle was a newer REMUS with an inertial navigation unit. The second was an older REMUS with standard sensors.

For a frequency of 1 kHz, ka becomes significant only for a part on the order of 40 cm long. Since most of the radiating noise comes from the propulsion system and the propellor is only 14 cm in diameter, omnidirectional noise is not unlikely.

At each bearing the vehicle thruster RPM was also adjusted to be 25%, 50%, 75% and 100% of the achievable RPM at bollard. 100% corresponded to 1380 RPM, above which the vehicle would enter a current fault state in which the thruster is turned off by the vehicle's processor to protect the components against high currents in the motor. The radiated noise as a function of RPM is shown in figure 3.5. As the motor rate is increased, the narrow peaks characteristic of rotating components shift up in frequency and more become evident. Also, the predominant peak slightly above 1 kHz does not shift in frequency

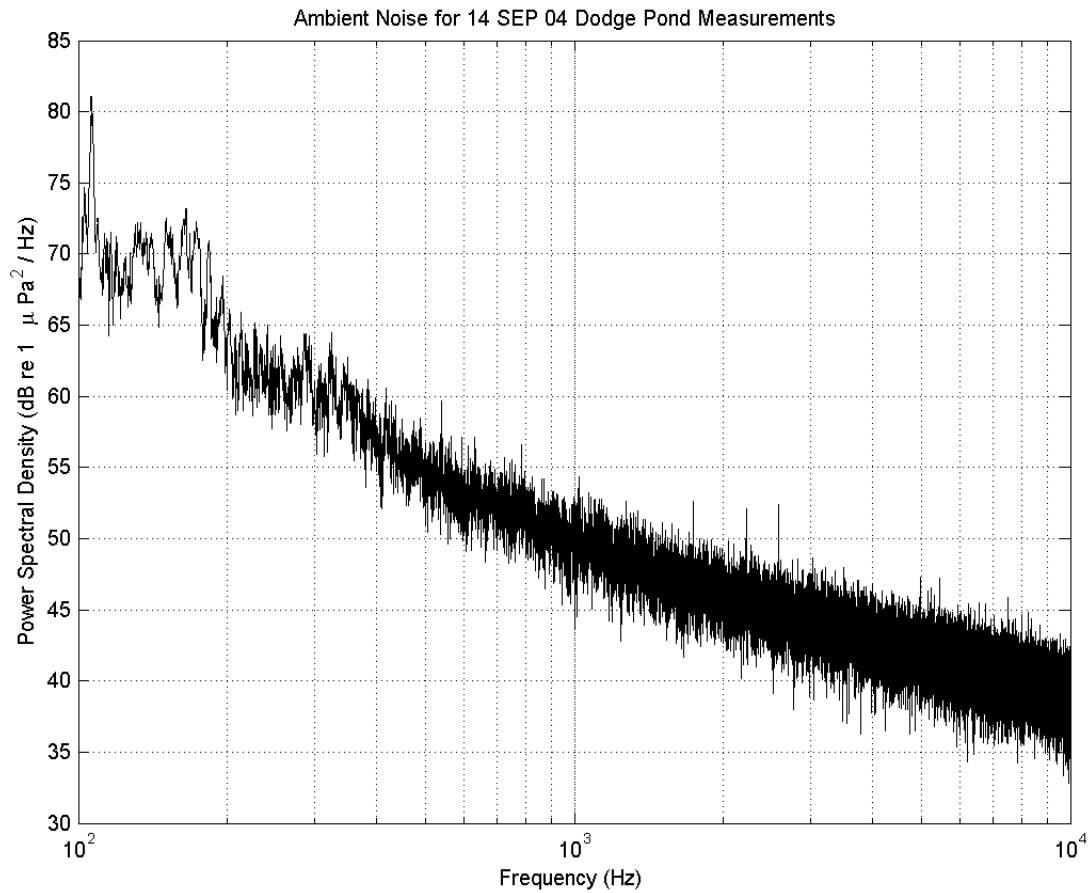


Figure 3.3: Measured power spectral density of the ambient noise at the test platform in September 2004.

but increases in level as the rotation speed of the thruster is increased. These results are indicative of different rotating parts both radiating noise and coupling into a resonance near 1kHz. The lines which shift with frequency are rotating parts radiating noise, and the peak which remains near 1 kHz is indicative of these rotating parts driving a resonance. It is interesting to note that at all but the lowest RPM the noise from an excited resonance is the loudest component of the radiated noise.

In December 2004 the REMUS vehicle used in all of the subsequent experiments was tested. The radiated noise from this vehicle exhibited very similar structure to the two vehicles tested in September. Figure 3.6 shows the power spectral density of the radiated

Broadband Click Experience Broadside to Vehicle 14 SEP 2004

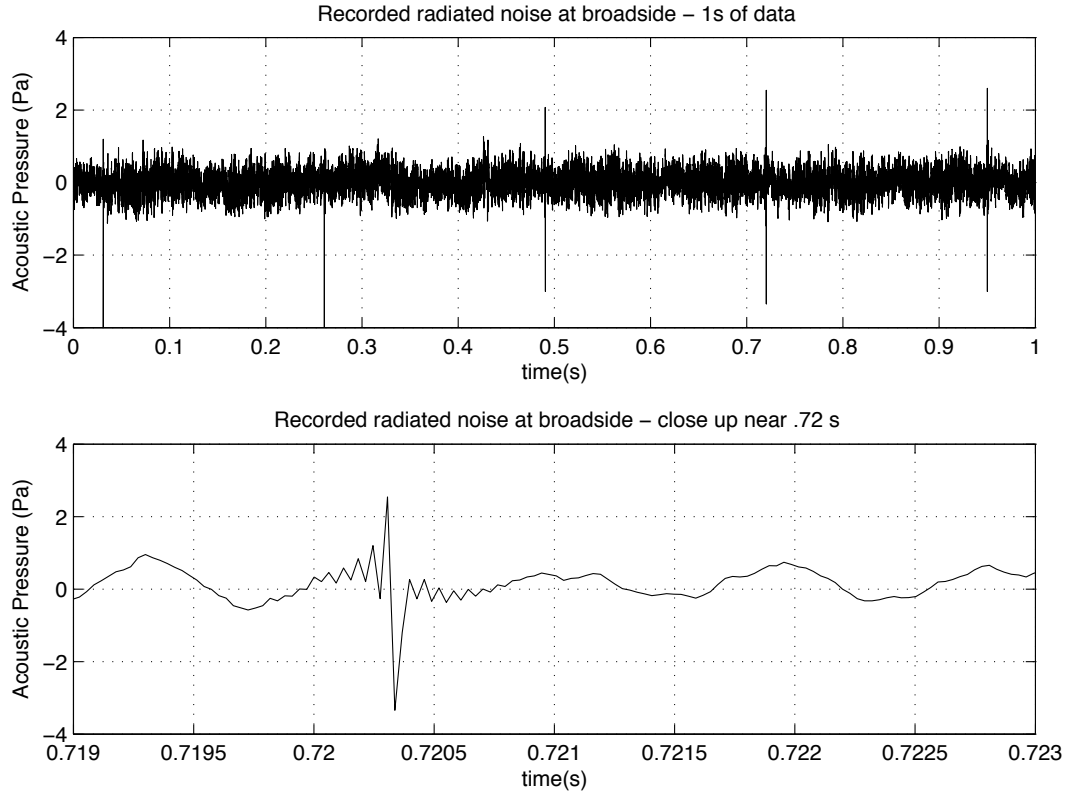


Figure 3.4: Measured time series of the noise radiated from a REMUS vehicle at 90° due to the acoustic doppler current profiler.

noise from this vehicle and figure 3.7 shows the ambient noise of the test pond at the time the measurement was made. The ambient noise shown is much higher than the ambient noise experienced in September because there was a light rain during the December test. Also, there was much more noise contamination from the floating measurement platform as indicated by the 60 Hz harmonics at 120, 180, 240, 300, and 360 Hz. The measured vehicle radiated noise was ambient noise limited below 400 Hz and above 7 kHz.

While the radiated noise was not expected to be caused by cavitation per the tip cavitation index and the lack of significant broadband signatures, it was still necessary to rule out cavitation. This was done while the vehicle was mounted on the test shaft by inspecting the propeller with an underwater video camera as the thruster was started

and accelerated to full RPM. Video footage revealed a stream of bubbles ejected from the propellor axle housing when the thruster was started, but not afterwards. Stopping the thruster and restarting it did not recreate this situation so it was determined that the initial stream was due to air entrained during submersion and that the propellor did not cavitate.

By rotating the vehicle the directionality of radiated noise was again measured. Considering average levels in the noisiest frequency bands the noise again appears omnidirectional. This is shown in figure 3.8 for six different frequency bands. Focusing on smaller frequency bands around the major noise peaks reveals that there is a slight directional nature to the noise with a main lobe facing the aft of the vehicle. This is expected since the assumption of parts behaving like rigid pistons is not perfect and the vehicle body places a mass between the receiver and the thruster in the forward direction. The measured bearing dependence for these peaks is shown in figure 3.9. In the level vs. bearing plots here, the levels are generally lower at 0° then they are at 180° . While this may be construed as a dipole radiation pattern, the results do not show significant nulls near 90° . This means that the effect is more likely explained by the effect of the vehicle body which scatters the radiated noise of the thruster. The geometry of the vehicle scatters sound produced at the tail away from the forward direction and toward the aft direction. Thus, the level forward is lower, the level aft is greater, and the level broadside the same as expected from a monopole.

Tapping the propellor underwater with the vehicle off gave a radiated noise with a ring down frequency of 1.1 kHz which indicated that the propellor resonance could be the source of the major resonance feature. To determine the effect of the propellor, it was removed and the noise test was repeated with a bare propellor shaft spinning at the same RPM. When the propellor was removed, the resonant peaks in the radiated noise spectrum essentially disappeared, showing that the propellor resonances were in fact the cause of much of the noise. The radiated noise power spectral density is shown for 1380 RPM with and without a propellor in figure 3.10. When the entire thruster armature including bearings was removed there was no radiated noise below 10 kHz measured at 13 meters

from the vehicle. Thus, the noises that drive the propellor are caused by the armature and bearings. After cleaning the bearings in the thruster assembly by flushing them with fresh water, peak noise levels dropped by approximately 3-6 dB.

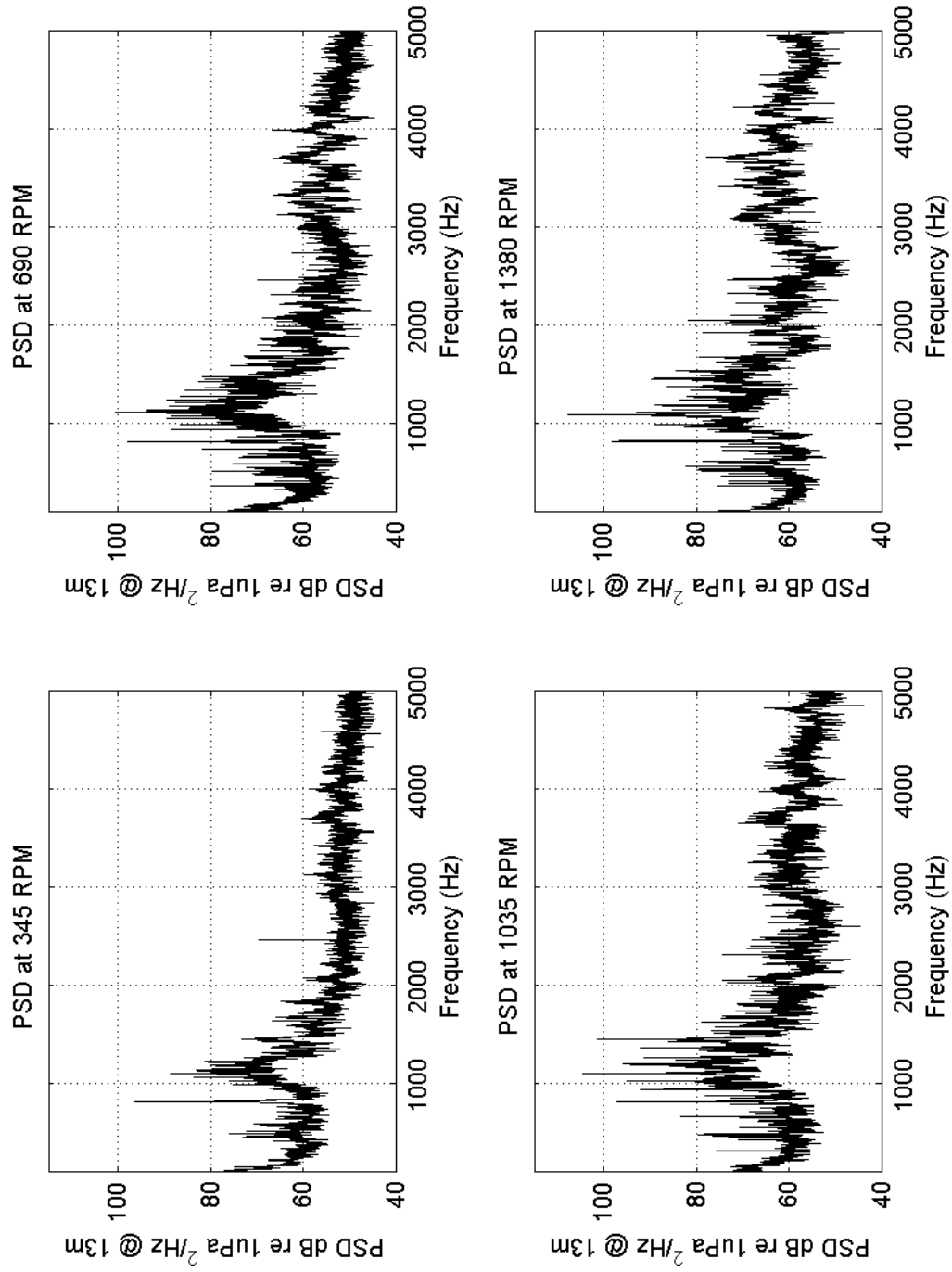


Figure 3.5: Measured power spectral density of the radiated noise from a REMUS vehicle at four different thruster RPM's.

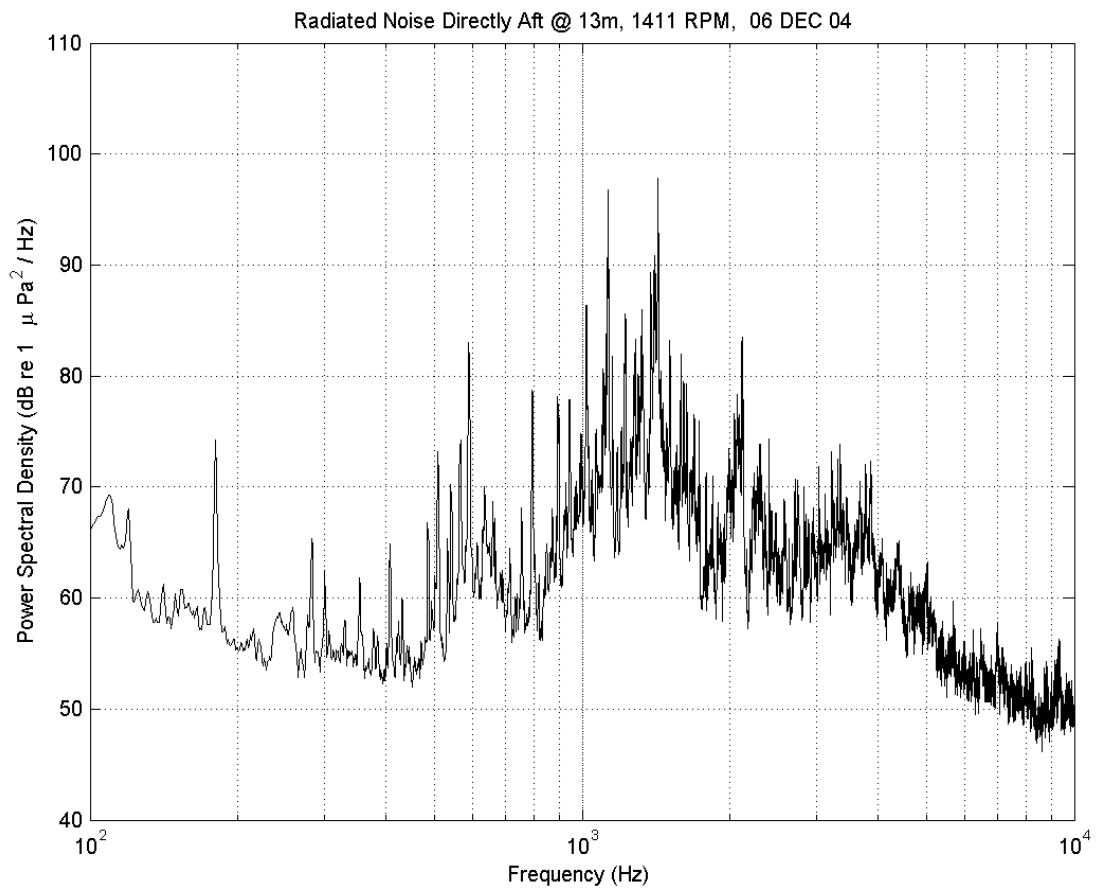


Figure 3.6: Measured power spectral density of the radiated noise from the vehicle used to tow the hydrophone array.

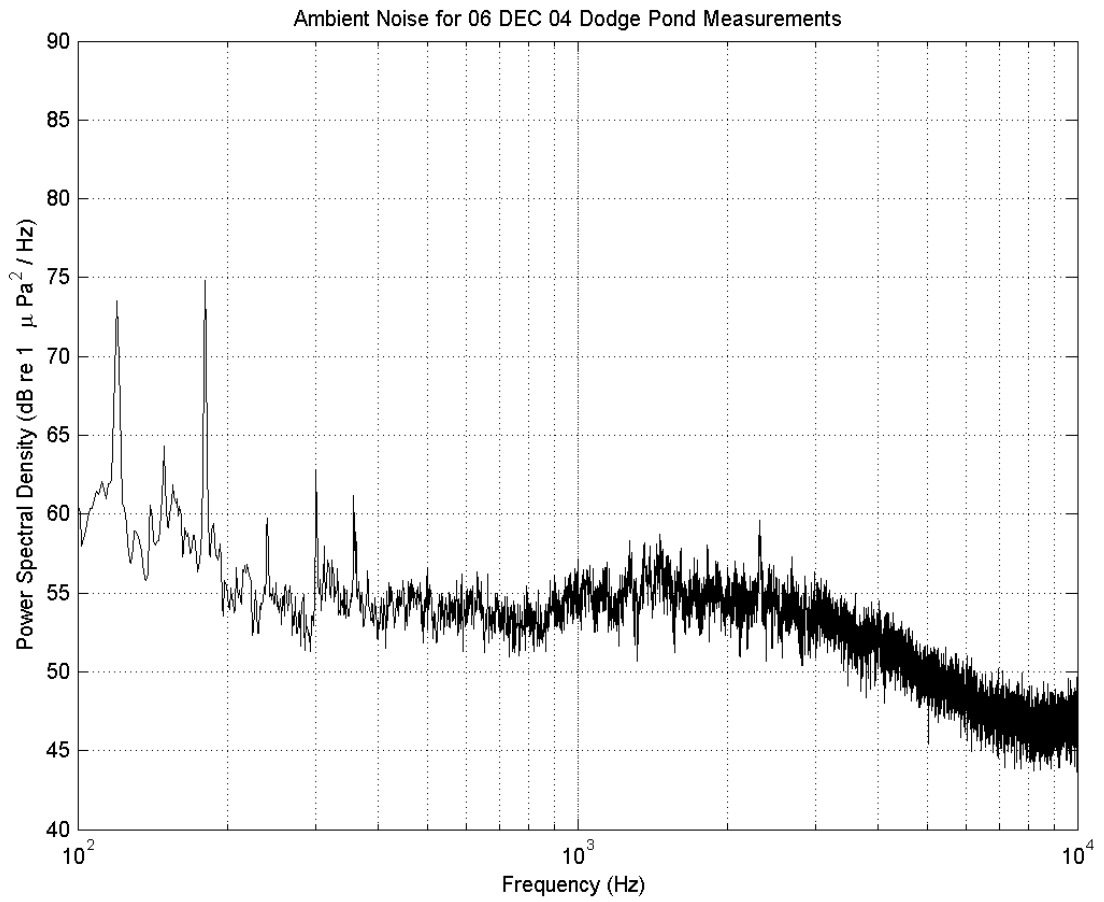


Figure 3.7: Measured power spectral density of the ambient noise at the test platform in December 2004.

Measured Directionality of Radiated Noise 06 DEC 04

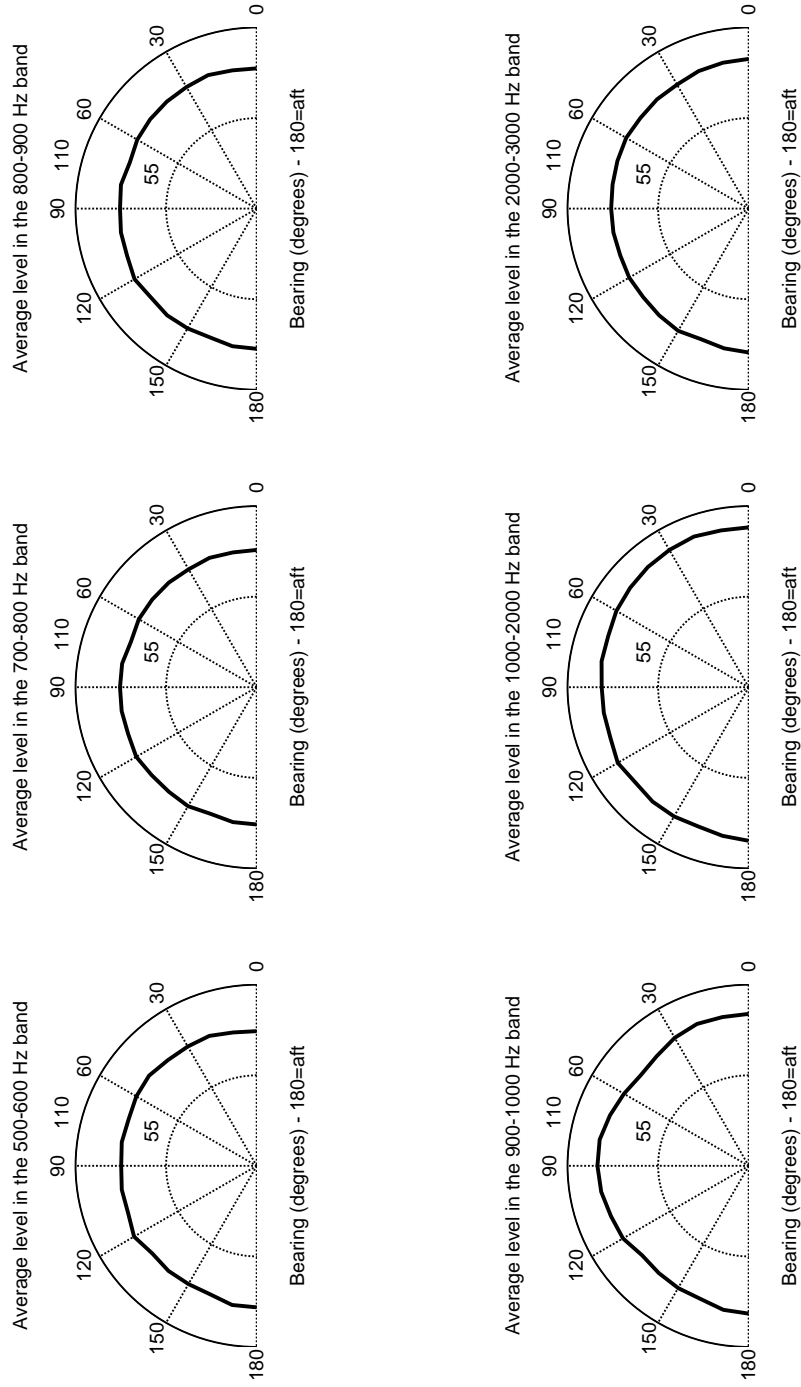


Figure 3.8: Measured average level of radiated noise in different frequency bands as a function of vehicle bearing to indicate noise directionality.

Measured Directionality of Radiated Noise at Peaks 06 DEC 04

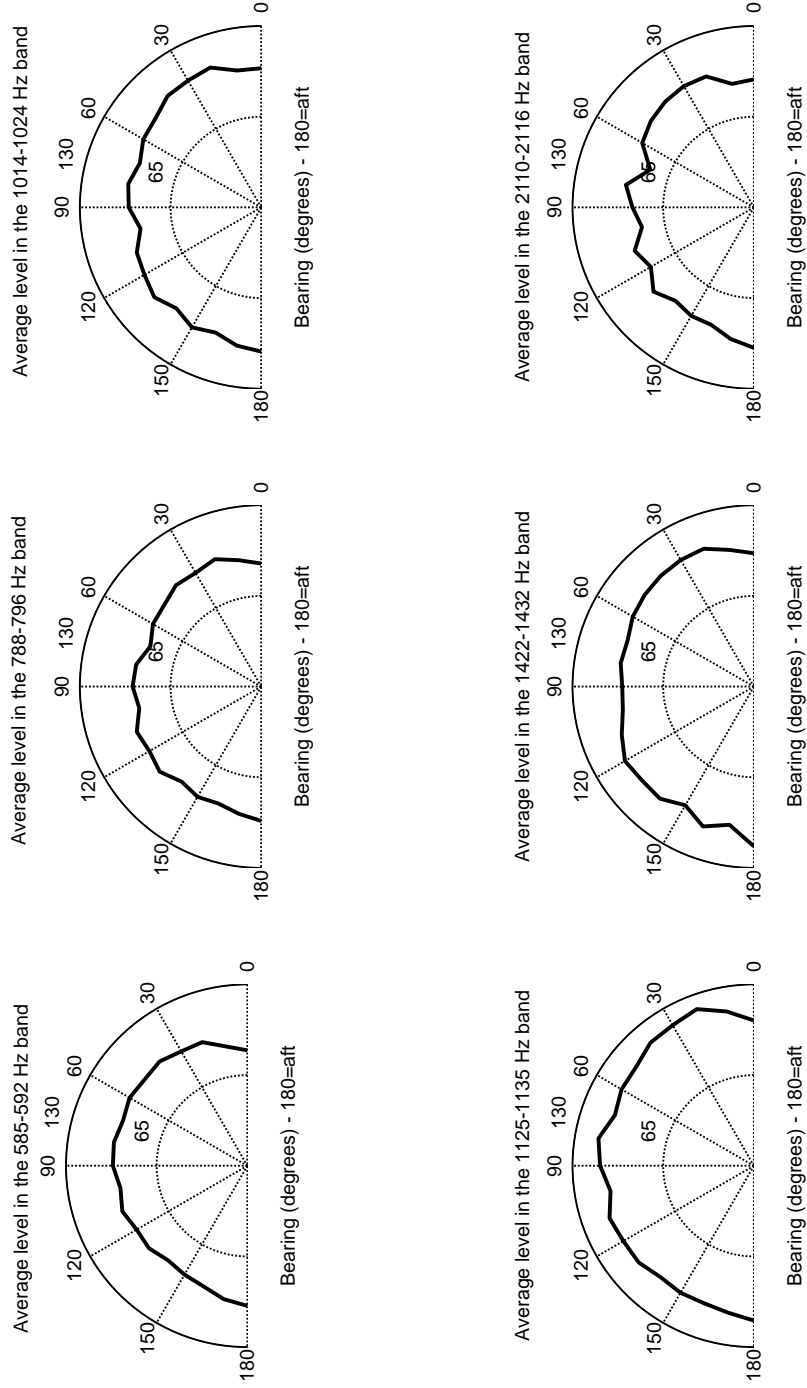


Figure 3.9: Measured level of radiated noise of different peaks in the radiated noise spectrum as a function of vehicle bearing to indicate noise directionality.

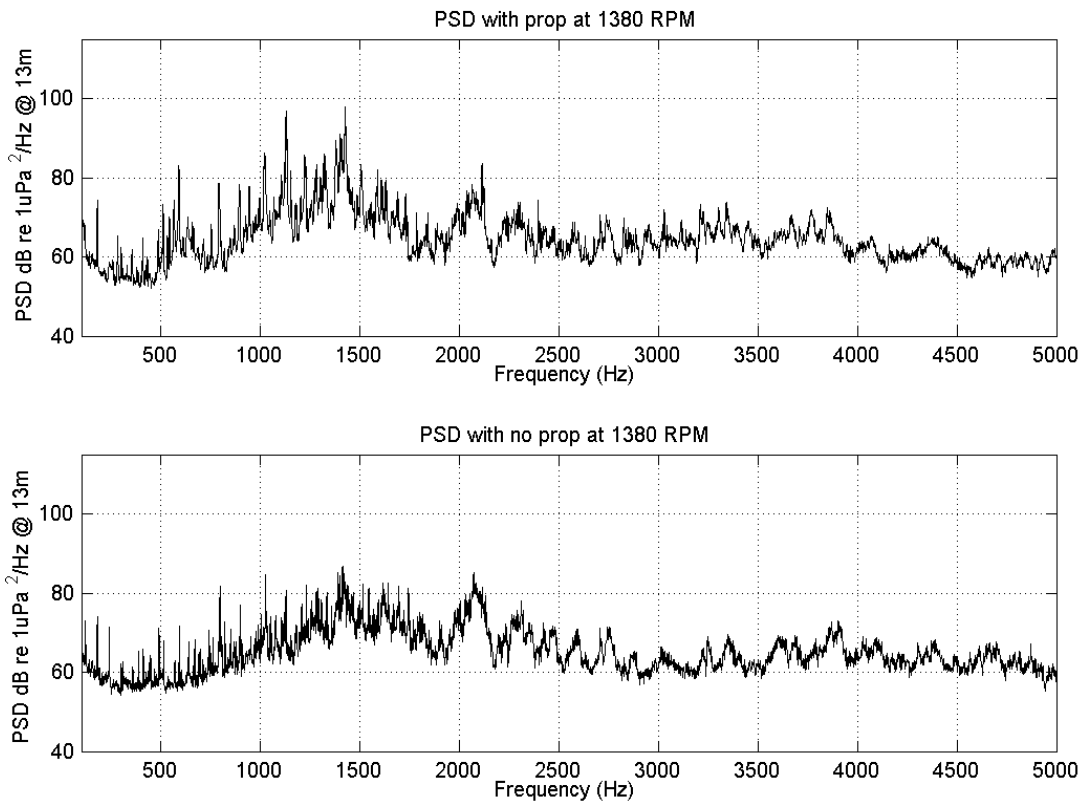


Figure 3.10: Power spectral density of the measured radiated noise directly aft of the vehicle with and without a propellor.

3.2.2 Array Measurements

In addition to measuring the radiated noise from the vehicle attached to a shaft, the towed array was utilized as a convenient measurement tool to measure the radiated noise of the vehicle. After removing the vehicle from the test shaft and calibrating the hydrophone array, the array was attached to the vehicle to perform a tow test. During this first tow test the vehicle experienced several current faults which stopped the thruster for a brief moment. Since the vehicle records the thruster RPM as function of time, the power spectral density seen on the first hydrophone which is 12 meters behind the vehicle, when combined with the vehicle data, revealed the RPM dependent noise characteristic.

Figure 3.11 shows the power spectral density of the signal received on the first array hydrophone vs. time with a time scale coincident with the RPM data reported by the vehicle. At approximately 18 seconds on the time scale the vehicle RPM drops from roughly 1500 RPM to 0. The vehicle data is sampled approximately every second, so what appears to be a gradual change in RPM over 1 second at this time is in fact an abrupt shut off. Before this shut off, the radiated noise spectrum is constant with time as the RPM is roughly constant with time. Shortly after 19 seconds on the time scale the vehicle thruster turns back on and the revolution rate steadily increases over the next 6 seconds. As the rotation rate of the thruster increases, the spectrum clearly shows several noises with frequencies that are some multiple of the revolution rate and some distinct noise components that have a constant frequency even though they are only present when the thruster is rotating. These effects are explained by RPM dependent bearing, armature and blade noises, which track the thruster rotation rate, superimposed with resonant features. The resonant feature near 1100 Hz increases the radiated noise when the rotating parts have driving frequencies coincident with resonant frequency. This explains the very loud noise at 1100 Hz shortly before 25 seconds on the time scale.

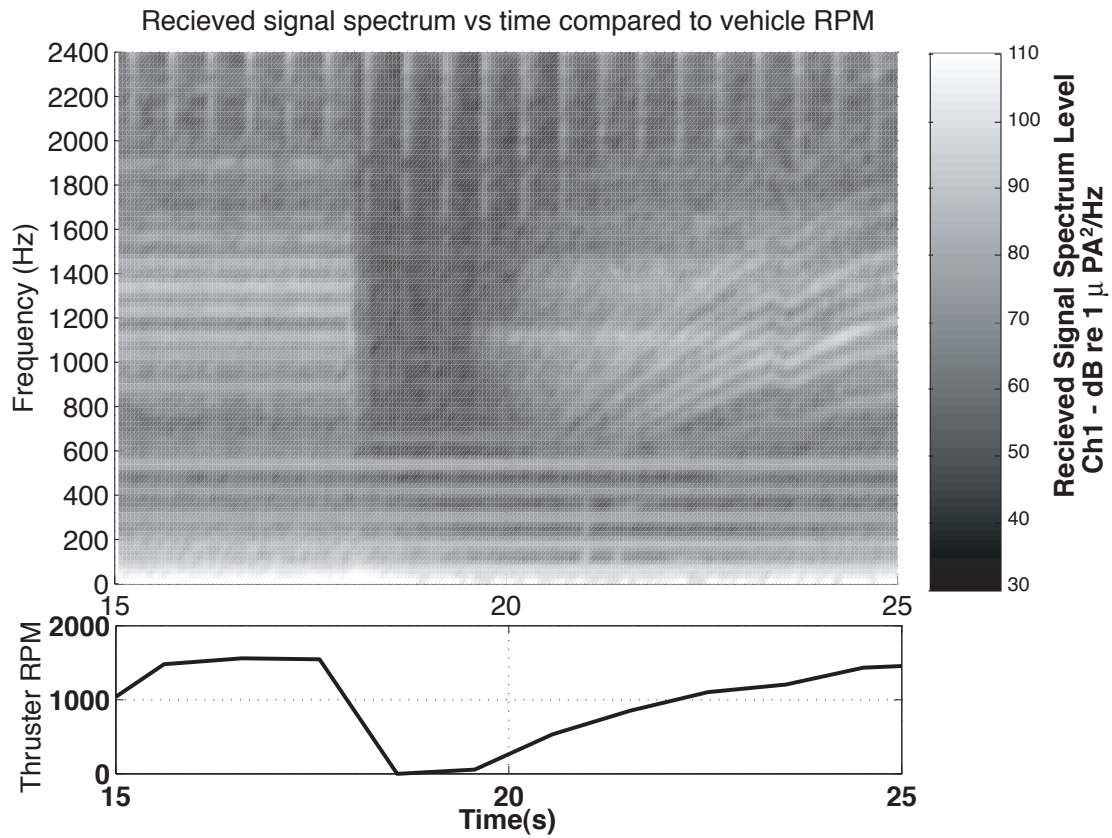


Figure 3.11: Power spectral density of the radiated noise directly aft of the vehicle vs. time as measured on the first channel of the towed array compared to the thruster RPM reported by the vehicle. The measurement is taken as the thruster faults in drops to zero RPM during the long straight course shown in figure 3.16

3.3 Towing Characteristics

Of primary concern is the dynamics of the system when in motion. Proper acoustic beam-forming requires that the array be towed in a stable path with little motion. In order for the vehicle to be able to do this, it must have enough control to be able to maintain a steady course. The drag on the array must be optimized because additional drag on the drogue will tend to keep the array straight, but the vehicle control system was not designed to control the tow of a high drag body.

3.3.1 Control Characteristics

The REMUS vehicle relies on forward motion for control since it is not a thrust vectoring vehicle. Control is provided by 4 coupled fins at the tail of the vehicle. The vehicle is also positively buoyant as a fail safe in case of power failure. Thus, at the surface it must first attain forward motion and then use fin control to overcome the buoyancy and dive. With the added drag of the array the vehicle had a difficult time doing this because it was not able to accelerate to its maximum possible speed and then pitch down. At lower speeds when the vehicle first tries to pitch down, the propeller comes near the surface and air becomes entrained near the propeller, reducing its effectiveness and thus reducing the forward motion of the vehicle. This causes it to stall at the surface. In order to aid the vehicle in diving, weight was added to the front of the vehicle to help it pitch down. In the ocean the vehicle was sometimes started into the waves to allow waves to crest over the tail during the start of the mission which prevented air from getting entrained in the propeller.

When the system was first tested, the array was attached to the bottom of the vehicle near the canister. A photograph of this attachment is shown in figure 3.12. With the array attached in this way, once moving the vehicle would dive uncontrollably until on the bottom. The reason for this can be seen in the free body diagrams shown in figure 3.13. Attaching the array on the same side as the canister is an unbalanced configuration because all of the extra sources of drag are on the same side of the center of gravity. Once the vehicle started moving forward, the array drag and canister drag imparted an unbalanced torque on the vehicle which was too great for the control surfaces to overcome. This was in part caused by the large moment arm created when mounting the array not only on the same side of the vehicle as the canister, but far from the center line of the vehicle as seen in figure 3.12.

Considering the free body diagrams, the balanced case is much more stable because the array drag and canister drag impart opposing moments about the center of gravity. The



Figure 3.12: Photograph of vehicle with unbalanced array attachment

thrust line nearly goes through the center of gravity and center of buoyancy and thus does not impart a moment. Additionally, mounting the array closer to the hull provides a smaller moment arm and thus less torque for the control surfaces to overcome. A photograph of this more stable attachment point is shown in figure 3.14.

The relative spacing in the horizontal and vertical directions of the center of gravity and the center of buoyancy is also important. If the center of gravity is displaced along the axis of the vehicle from the center of buoyancy, the vehicle will have a tendency to naturally orient itself to put the center of gravity below the center of buoyancy. This will generate a torque that will pitch the vehicle and must be overcome by the control surfaces. Further, in the vertical direction, the center of buoyancy must be above the center of gravity for the vehicle to have a righting tendency. This ensures that the vehicle's natural orientation is upright. If the center of buoyancy is too far above the center of gravity, the the righting tendency would be too great for the control surfaces to overcome and the vehicle would not be able to maneuver. When properly ballasted, the center of buoyancy is directly above the center of gravity, separated by about 2 cm. Ballast on the vehicle is changed by adding or removing weights in different locations on the vehicle and the test for correct ballast is an at rest attitude measurement of the vehicle.

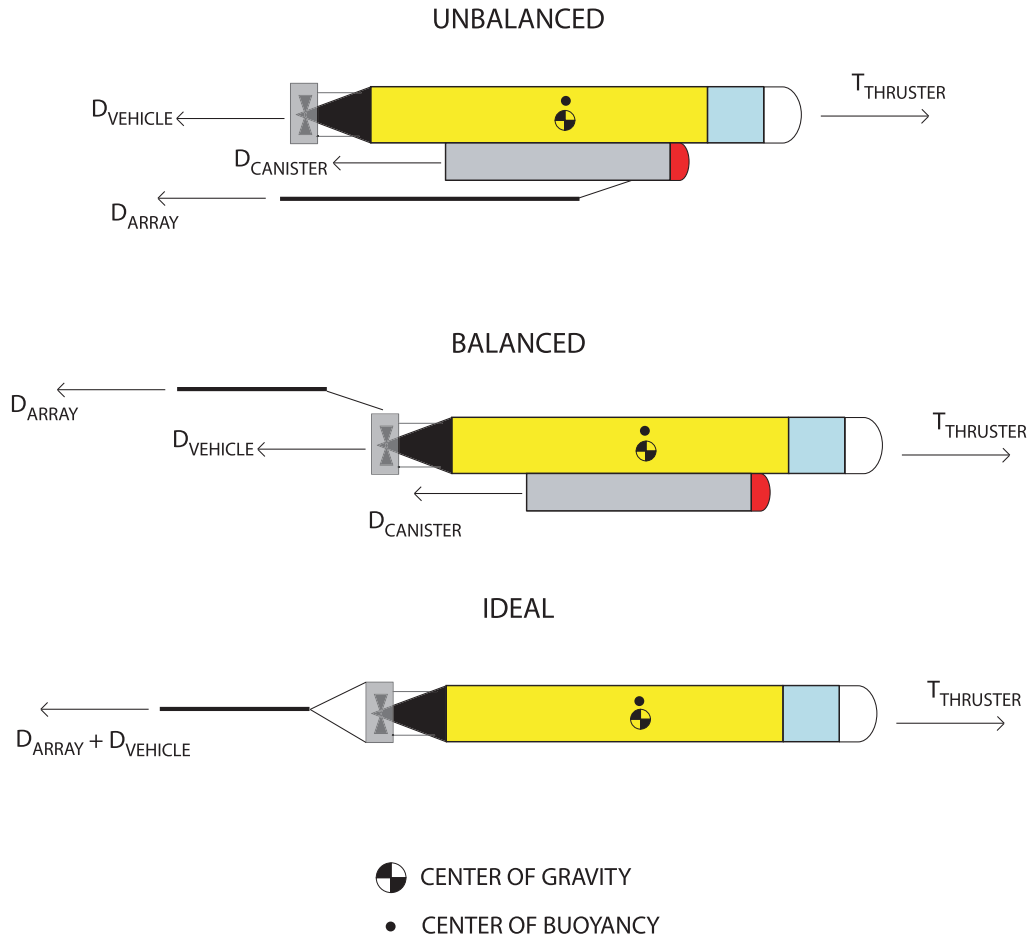


Figure 3.13: Free body diagrams of different array attachments. The separation between the center of gravity and the center of buoyancy is exaggerated here. In reality the center of buoyancy is approximately 2 cm above the center of gravity.

At depth, the vehicle ordinarily relies on forward motion and body lift to maintain depth with little control surface involvement. At lower speeds, due to array drag, the vehicle cannot do this, and requires more control surface influence. This in turn adds more drag and slows the vehicle down more. If the total added drag of the array plus the control surface drag required to keep the vehicle down becomes too great, the current required by the thruster will exceed a safety threshold and the control software will indicate a fault. This fail-safe was included in case the vehicle were ever stuck in a net or seaweed and ensures that the motor does not get damaged by excess current. When the thruster



Figure 3.14: Photograph of the vehicle with a more stable array attachment. The vehicle is on its side in its cradle with the top to the right. The lifting bail, recording canister, and shroud are clearly seen.

faults, it temporarily turns off and then restarts, causing a jerking motion in the tow and a sawtooth depth profile. This is seen in the experimental timeline of the first successful deployment of the system in a confined pond shown in figure 3.15. This timeline is taken from the straight section of the mission path shown in figure 3.16 between recorder times 22 and 24 minutes.

To correct this problem, weight was added to make the vehicle less positively buoyant and horizontal at rest in the water. This allowed the vehicle to stay down with less control surface control and thus less drag. Operationally speaking, this is a problem since reserve buoyancy is intentionally included to allow for the vehicle to surface under the no power condition even with the largest water density change possible in the ocean . This largest density change would be if the vehicle entered a halocline. The difference in density between

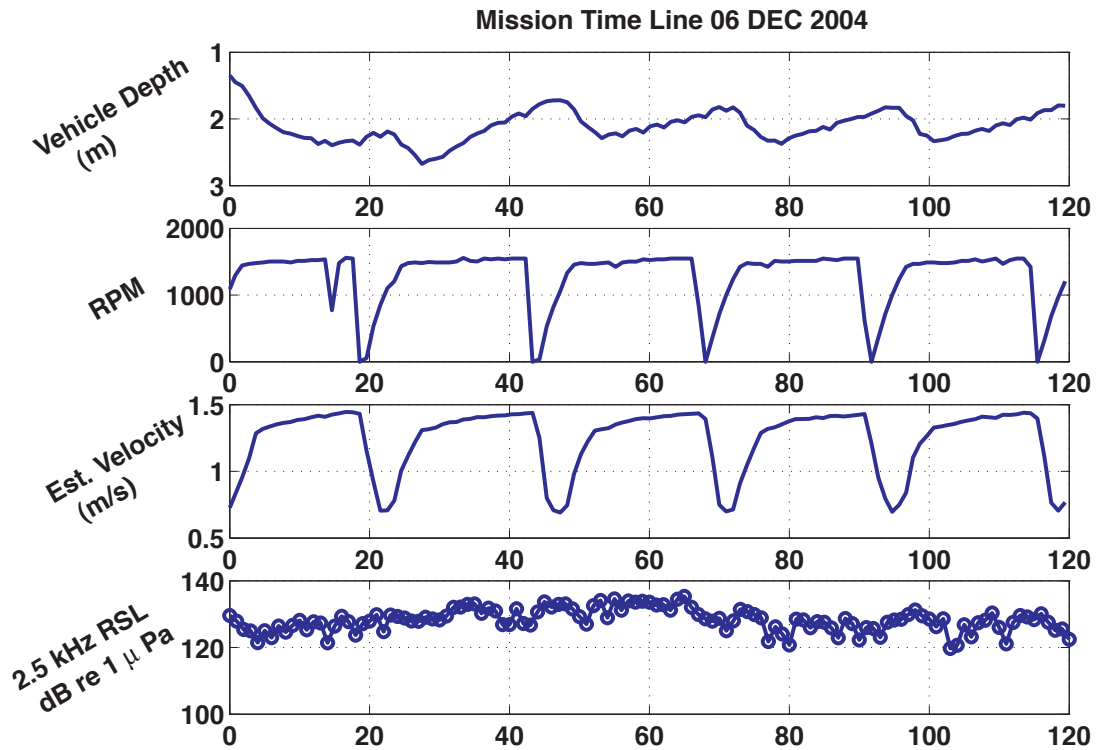


Figure 3.15: Mission timeline showing motor faults.

salt water and fresh water is approximately 3%, so a reserve buoyancy of at least 3% of the weight of the vehicle is required to satisfy this. The weight added to the front of the vehicle left the vehicle approximately 1-2 lbs. positively buoyant, which was less than the suggested safe reserve, but it allowed the vehicle to control its depth well. The thruster current threshold was also increased to help avoid motor faults. A typical feedback control response in depth was achieved after these changes were implemented and is shown in figure 3.17. A single overshoot and small steady state error in the step response in depth indicate that while the vehicle control system was not designed for towing a body, it is still a well tuned controller if the array is attached in a stable configuration.

The last free body diagram in figure 3.13 is labeled “ideal” and represents the ideal case where the action of the body and array drag are both along the same line as the thruster which goes through the center of gravity. The center of buoyancy is near and above the

center of gravity and thus the vehicle has no uncontrolled moments about its center of gravity. It is then easily controlled. Ideally the center of gravity would be automatically adjustable with a trim and ballast control. Adjustment of the trim and ballast is especially necessary when operating in coastal waters where the density of the water is variable.

While not shown in the diagram, the ideal attachment of the array would be able to pivot in front of the control surfaces to increase the vehicle's ability to turn. If the array attachment pivot point is at the center of gravity, the turning capability of the vehicle is unaffected by the array and the vehicle's turn radius is unaffected. As the attachment point moves back behind the control surfaces, the turn radius of the vehicle becomes larger and the vehicle must thus make much wider turns. As shown in figure 3.14, in this case the array was attached to the vehicle at the convenient attachment point provided by the aluminum propellor shroud, near the control surfaces. The turning radius in this configuration was approximately 15 m while the turning radius of the vehicle alone is approximately 5 m.

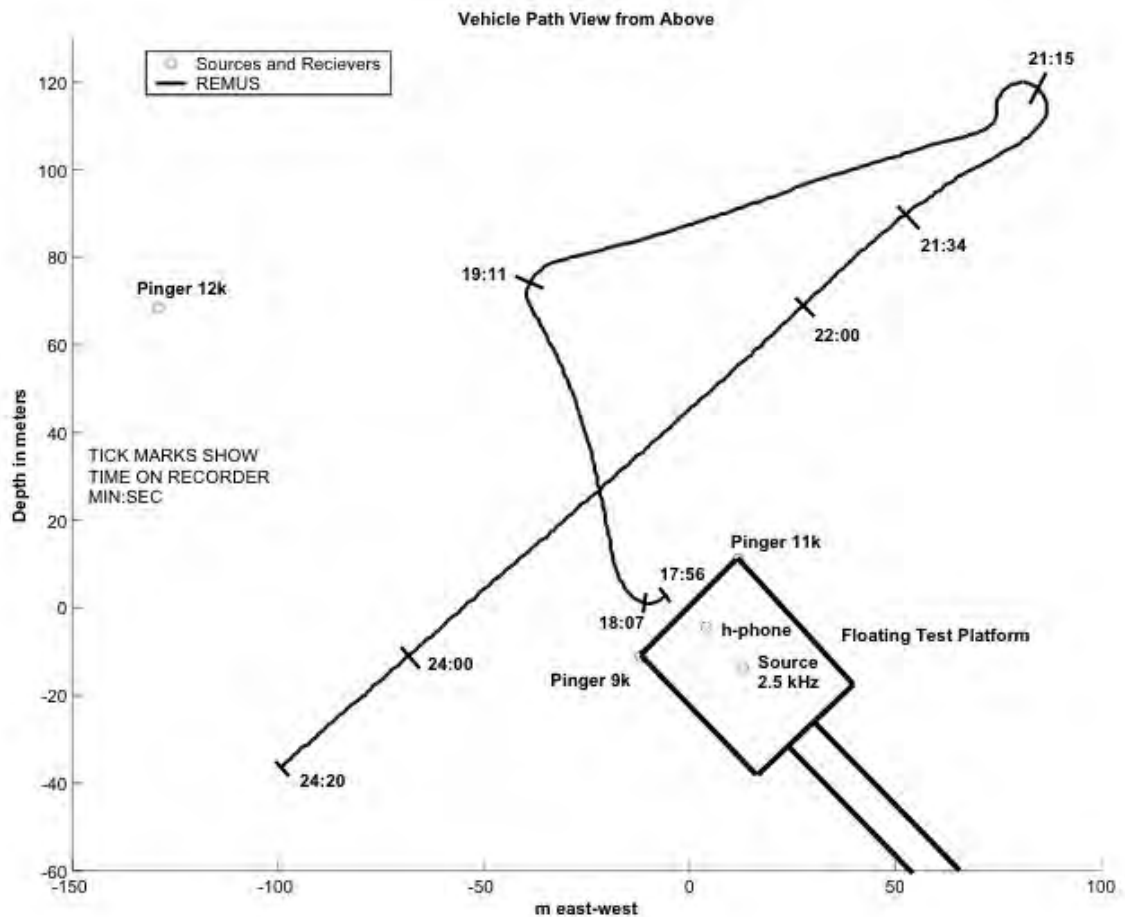


Figure 3.16: Vehicle path showing the layout of equipment during the Decemer 2004 Dodge Pond Tow test as well as the path the vehicle took. The floating test platform is seen with its ramp in the lower right. Below the platform are a reference hydrophone, a 2.5 kHz , 50% duty cycle source, a 20 cycle, 4.5 second repetition rate 9 kHz pinger and a 20 cycle 4.4 second repetition rate 11 kHz pinger. All of these were at 6m depth. Approximately 100m away from the platform on a mooring was a 20 cycle, 4 second repetition rate 12 kHz ping at 4 meters deep. The tick-marks show the time scale on the acoustic recorders in minutes and seconds.

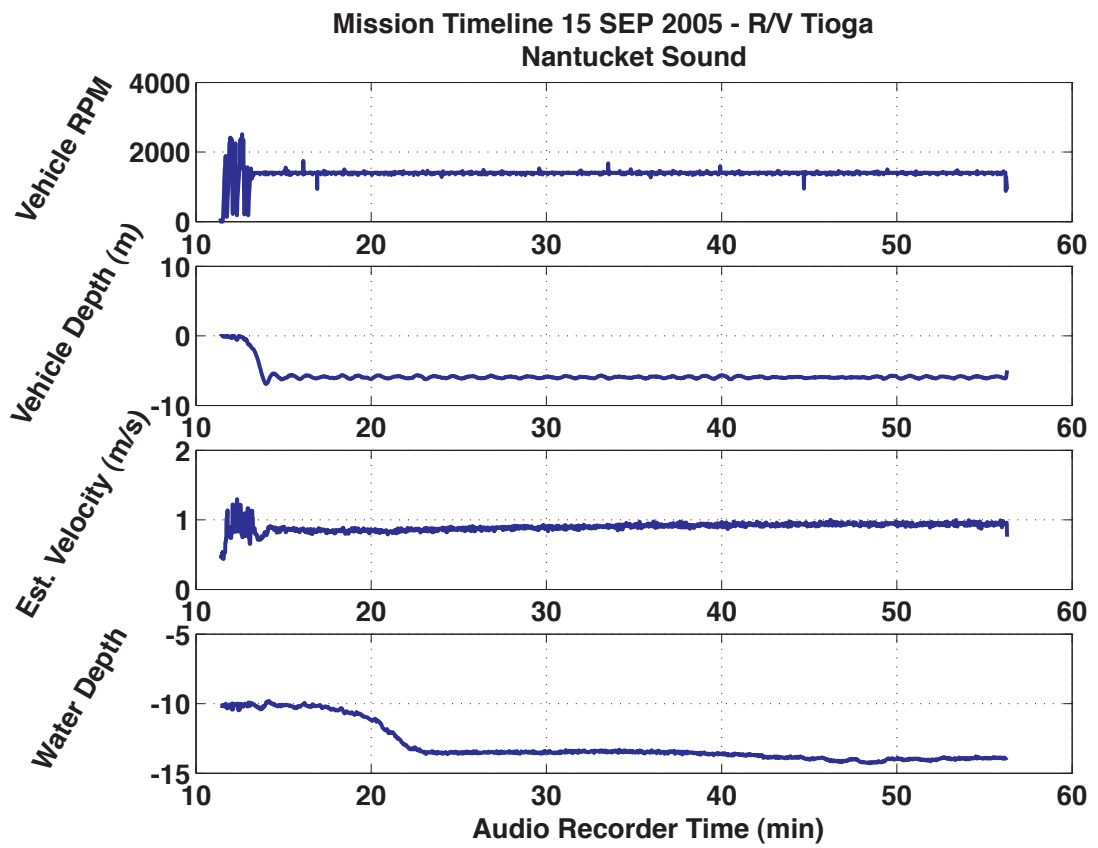


Figure 3.17: Mission timeline showing a stable tow

3.3.2 Drag

From the previous section it is clear that the drag from the array greatly affects the control of the vehicle. Figure 3.15 shows that without adding weight to the front of the vehicle the drag limits the forward velocity of the vehicle to below 1.5 m/s before the current in the motor gets dangerously high. This was in a test pond with no currents. In the ocean, where currents exist, this velocity limit is of larger concern because currents can be on the order of this maximum velocity. Adding weight to maintain depth improves the control characteristics, but the vehicle is still limited to a maximum velocity relative to the water below the 2.5 m/s rated vehicle maximum. This is evident in figure 3.18 in which the vehicle turns around at time 58 minutes. At the start of this mission the tide was high and currents were small. As time progressed the currents increased in the direction of the vehicle until it turned around and was then fighting an increasing current. As the current increased the vehicle was capable of an increasingly lower velocity relative to ground.

Determination of the effect of array drag on the vehicle and the desire to be able to optimize the drag in the future requires the measurement of the drag characteristics of the array. Conveniently the vehicle records both the current from and the voltage across the batteries. Thus, the power usage of the vehicle can be determined by the product of current and voltage.

$$P = IV \tag{3.3}$$

Power is consumed by various sources on the vehicle including the central processor, hard drives, sensors, and most importantly, the thruster. If all other operating characteristics are held constant, the difference in power consumption for a vehicle with and without an array must be due to the drag of the array and any additional control surface drag needed to control the vehicle with the array attached. While it is not possible to separate these effects, the control characteristics of the vehicle with the array mounted in a stable tow configuration indicate that the added drag of the control surfaces is much smaller than the drag of the array. The vehicle was thus run with only the recording canister attached

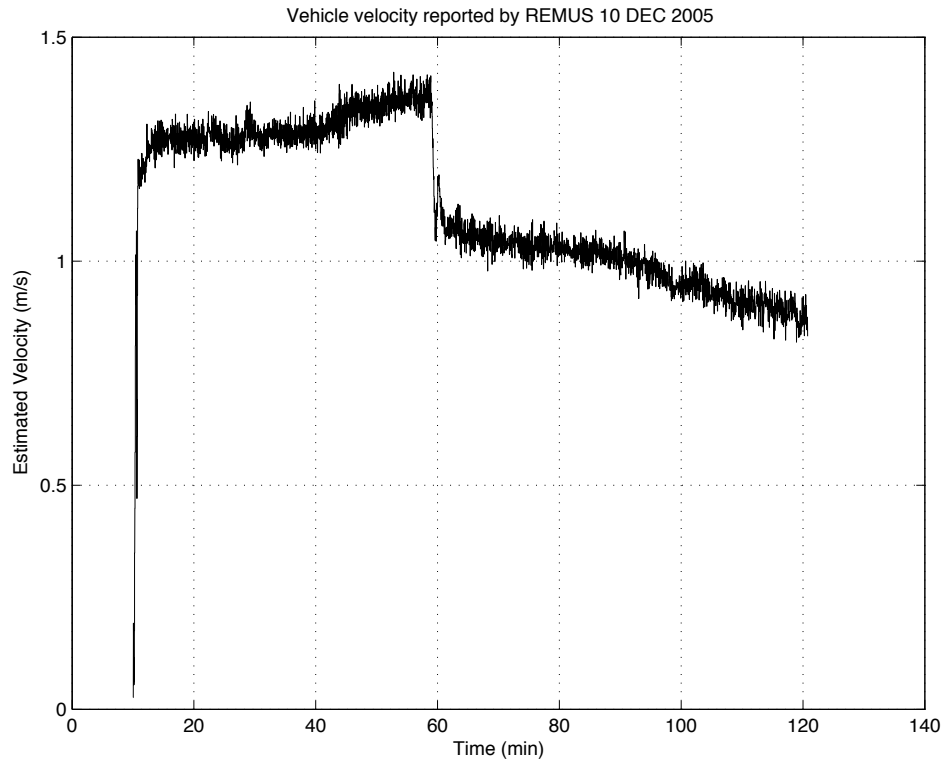


Figure 3.18: Plot of estimated speed over ground reported by the vehicle which shows the effects of array drag and local currents.

to the vehicle and then the recording canister and the array attached. Figure 3.19 shows the power reported by the vehicle as a function of estimated velocity at each time sample. Adding the array slowed the vehicle down, but the power-velocity trends are evident and it is clear that the power difference at 1.4 m/s is approximately 20 W. Using the relationship between power, force, and velocity for an object in steady motion,

$$P = F \cdot V \tag{3.4}$$

gives the estimated force of drag as 14.3 N. For comparison, a standard coefficient of drag table [101] gives the coefficient of drag as 0.9 for a cylinder with a similar aspect ratio.

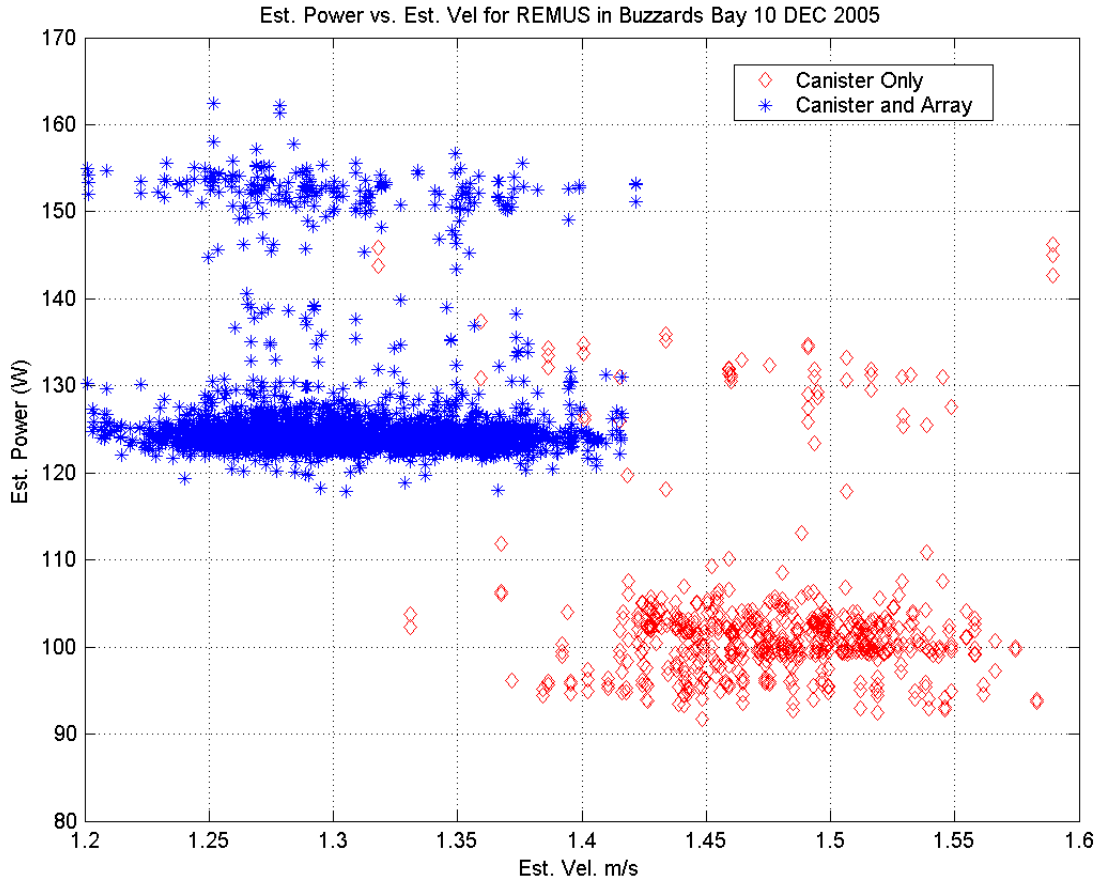


Figure 3.19: Vehicle power as a function of estimated velocity reported by the vehicle both with and without the array attached.

Using

$$D = \frac{1}{2} \rho v^2 A C_D \quad (3.5)$$

where ρ is the density of water, v is the array velocity, A is the cross sectional area, and C_D is coefficient of drag gives a drag of 11.5 N at 1.4 m/s. Measurements on similar towed arrays indicate that the expected drag at 1.4 m/s would be about 11.2 N if the entire array was made from the 2.8 cm diameter array hose used in the acoustic section [102]. This indicates that the extra drag is most likely due to (in order of assumed decreasing importance) the high drag nature of the drogue, the changes in diameter between the tow cable, acoustic section, and drogue, and the control fins.

3.3.3 Array Motion

The signal processing techniques presented in chapter 2 require a straight, stable array tow. Qualitatively, the motions of the array must be small compared to a wavelength in order to be unimportant. Transverse motion on the order of $\lambda/4$ or smaller will most likely have little importance and motions smaller than $\lambda/10$ certainly will not be of importance. To determine if advanced array shape and motion compensation were required, the array shape and motion were estimated in the tow test shown in figure 3.16.

As shown in the figure, a 2.5 kHz source was deployed from the floating test platform as were 9,11, and 12 kHz broad band pingers. The 2.5 kHz source had a 50% duty cycle and a repetition rate of 1 s. The time lag of the 2.5 kHz signal between channel 1 of the array and every other channel was calculated by cross correlation of the channels and used to estimate the shape of the array. To do this, the time lags were calculated for many consecutive 1 second time segments and plotted as a function of hydrophone position behind channel 1. This is shown in figure 3.20. The time lags vs. position along the array increased in slope as the array drove past the source. Theoretically the line connecting the time lags should be a straight line with a slope given by $\sin(\theta)/c$ where θ is the bearing to the source.

For each time lag vs. array position curve the line of best fit is found. This is considered to be the line of time lags if the array were perfectly straight. A difference between this line and the actual data indicates that a particular hydrophone is displaced within the plane formed by the line of the array and the source. To find the maximum possible vertical displacement of the hydrophones the fact that the hydrophones are physically connected is used. A physical connection requires that the distance between hydrophones never changes, only the apparent distance with reference to the incoming wave. Thus,

$$X_{apparent} = X_{hydrophone} - c\Delta t \quad (3.6)$$

where $X_{apparent}$ is the apparent position of the hydrophone, $X_{hydrophone}$ is the known position of the hydrophone along the array, c is the speed of sound and Δt is a difference

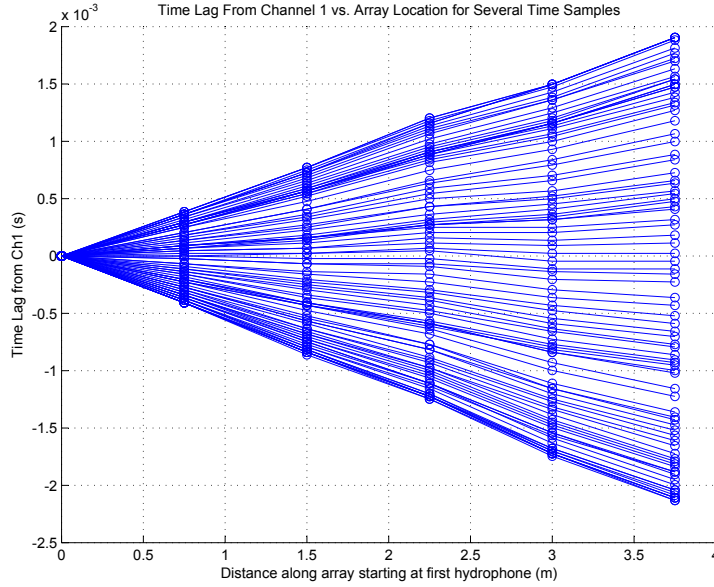


Figure 3.20: Time lags between channel 1 and each other channel on the array for the 2.5 kHz as a function of array position for many consecutive pulses.

between the line of best fit and a measured time lag. The maximum possible vertical displacement, which is also the maximum possible conical displacement, of the hydrophone is then given by

$$Z = \sqrt{X_{hydrophone}^2 - X_{apparent}^2} \quad (3.7)$$

$$Z = \sqrt{X_{hydrophone}^2 - (X_{hydrophone} - c\Delta t)^2} = \sqrt{2X_{hydrophone}c\Delta t - (c\Delta t)^2}. \quad (3.8)$$

Applying this to the time lags given in figure 3.20 gives the average maximum vertical array displacement as shown in figure 3.21. The error bars in the figure show the standard deviation of the hydrophone positions, indicating the motion of the array. It is thus concluded that the acoustic section was slightly bowed due to uneven ballasting with a bow depth of 25 cm over the 375 cm of the acoustic section. Further, the motion of the array was on the order of plus or minus 7 cm or less. This motion of the array is approximately $\lambda/10$ for 2 kHz.

After this particular tow test the array was re-ballasted and then used in at sea experiments. In order to characterize the array shape visually, divers were placed in the water

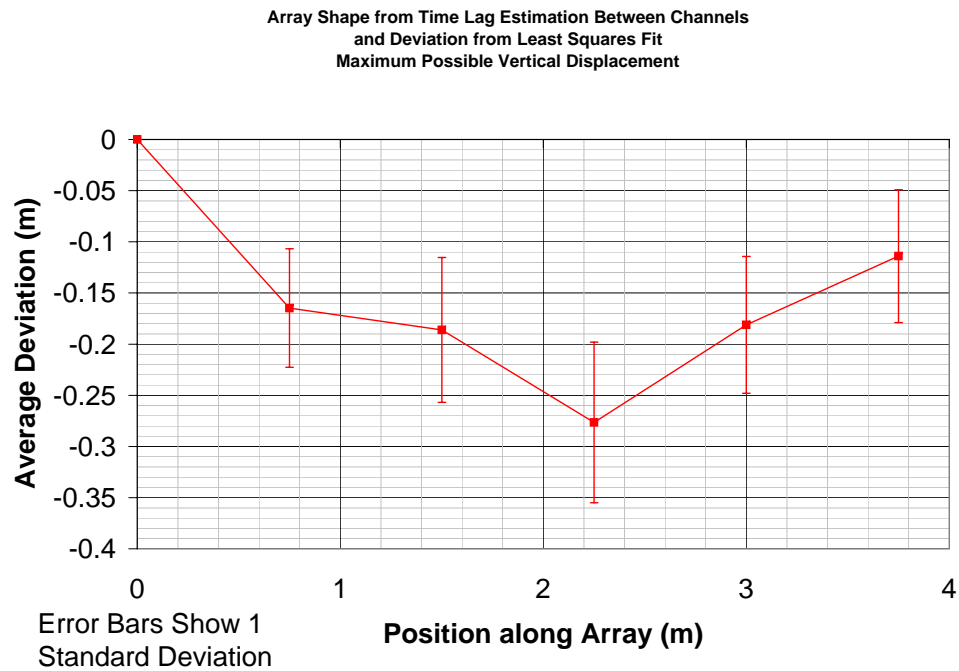


Figure 3.21: Estimated array shape determined from cross correlation of the received signal on each channel and comparison to a least squares fit.

with the array. The divers were able to observe and describe the motion of the array as well as record the motion of the array at the start of a mission on an underwater video recorder. The video showed no visible waving or flapping of the array and the divers reported that once the vehicle gained speed and the drag on the array increased the array straightened from its slack state and there was almost no visible bow.

Chapter 4

The Experiment and Apparatus

4.1 Experimental Technique

The long range transmission experiment described in section 2.3.3 was performed in September 2005 and repeated in December of the same year . Both experiments were conducted at the same site in Nantucket Sound and the major difference between the two was the maximum source to receiver range. In September the AUV towed the array 2 km radially away from the source. The range was extended in December when the vehicle traveled out 4 km radially from the source and back.

The purpose of the experiments was to use the long range transmission loss to infer the frequency dependence of the intrinsic attenuation in the bottom using a synthetic aperture. The coherent processing limits of synthetic aperture using an AUV towed array were to be examined as well. To minimize the measurement error and place firm brackets on the properties of the bottom, an effort was made to determine all other geo-acoustic parameters from means other than the long range transmission measurements. This would avoid the need for a multi-parameter inversion. Thus, the experimental technique included scientific instrumentation on board the coastal support ship such as a conductivity-temperature-depth sensor (CTD), acoustic doppler current profiler (ADCP), and precision depth profiler. The standard configuration AUV sensors were also used during the experiment and included

a separate CTD, ADCP, and bottom profiler mounted on the vehicle. Figure 4.1 shows the experimental configuration including the scientific sensors used on board the research ship.

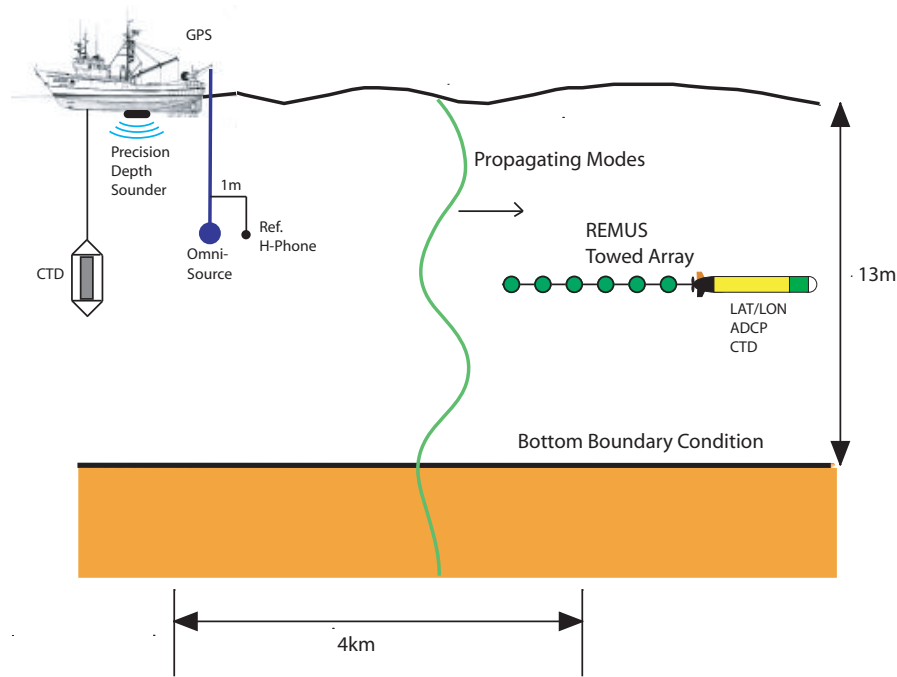


Figure 4.1: The configuration of the Nantucket Sound Experiment including instrumentation on board the support ship.

During a pre-experiment survey of Nantucket Sound, an acoustic doppler current profiler (ADCP) was used to measure the local currents and a precision depth recorder (PDR) was used to measure the depth variation of the bottom as well as provide some idea of the composition of the upper layers of the sediment. Physical samples of the sediment were also obtained by means of a grab sampler. These measurements helped determine an acceptable location to perform the experiment.

Once a location was decided upon, the ship was able to leave and return to the same location via GPS in order to conduct the acoustics experiment at a later date. When at the correct location for anchorage, the ship entered a three point mooring for stability. A conductivity, temperature, and depth (CTD) sensor was lowered to the bottom and

the data obtained was converted to salinity, temperature and sound speed as a function of depth by standard tables. The source and reference hydrophone were then lowered off the aft of the ship and the towed array system put in the water. Output from a function generator capable of superimposing up to four tones was put through a McIntosh MC 2500 amplifier which drove the source. Drift on the signal generator was reduced by synchronizing it to a rubidium clock. A digital audio tape recorder recorded the output of the signal generator as well as the calibrated reference hydrophone. Coupled with the measured transmit-voltage-response of the source, the reference hydrophone enabled the science crew on the ship to accurately set the signal source level for each tone. A wiring diagram for the source setup is shown in figure 4.2

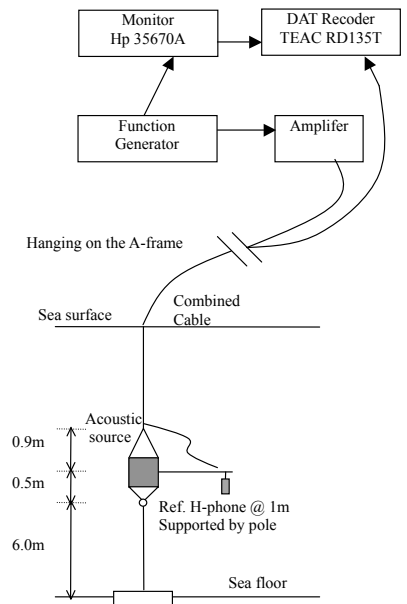


Figure 4.2: Wiring diagram for the source on the ship. In this case the source is attached to a heavy anchor to prevent sway. Later the anchor was removed and the weight of the source alone was found sufficient to prevent sway.

A GPS receiver was attached to the aft of the ship to indicate the source latitude and longitude and a depth sensor was attached to the source to monitor source depth. Latitude and longitude of the vehicle was determined on the surface by GPS and while submerged

by dead reckoning. The relative source-receiver range was later determined by comparison of the vehicle latitude and longitude to that of ship.

4.2 The Nantucket Sound Site Survey

As mentioned in the previous section, a survey of Nantucket sound was performed using ADCP and PDR data. The purpose of this survey was to find the best site to perform the intended long-range transmission loss experiment. In section 2.2.3 the importance of site selection was discussed. Since different mechanisms contribute to the overall attenuation of the transmitted signal, it was important to find a site that had a relatively smooth bottom interface with few inhomogeneities such as shells and few sub-bottom interfaces. Further, since the frequency dependent attenuation in silty-sands was of key interest, it was important that the sediment at the experimental site was classified as a silty sand.

The chart in figure 4.3 shows two possible sites for performing the experiment as well as the location of the Frisk-Lynch-Rajan (FLR) experiments [91] which inspired the present experimental method. For comparison reasons, a site close to the FLR site was desirable. The potential environmental impact of the source on local marine mammals and recreational swimmers, however, prevented the use of that particular site due to its proximity to the shore. The other two potential sites were then proposed because of their constant bathymetry, distance from shore, and relative proximity to the FLR site.

The site survey was performed in August, 2005 and consisted of making precision depth recorder, acoustic doppler velocity profiler, and conductivity-temperature-depth sensor measurements coupled with obtaining samples from the bottom with a grab sampler. Figure 4.4 shows the path that the ship took while taking PDR measurements during the site survey and figure 4.5 shows the locations of grab samples. The relative position of the second proposed site relative to Cape Cod is indicated in figure 4.6 for a frame of reference. The anchorage point indicated in the plots is a proposed spot to place the ship in a three point anchorage to perform an experiment at site 2.

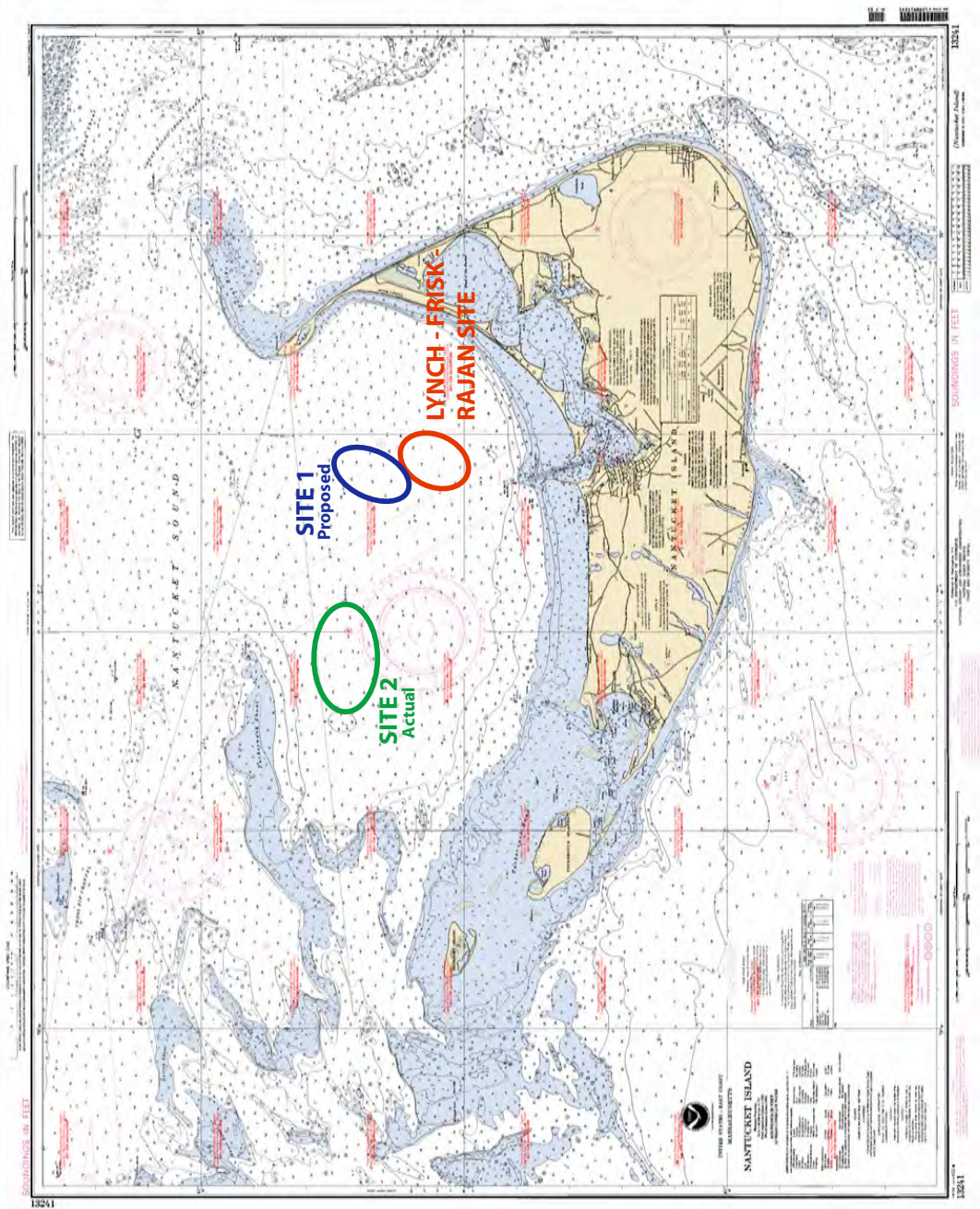


Figure 4-3: Chart of Nantucket Sound showing potential experiment sites as well as the site of the Frisk-Lynch-Rajan experiment [91,103].

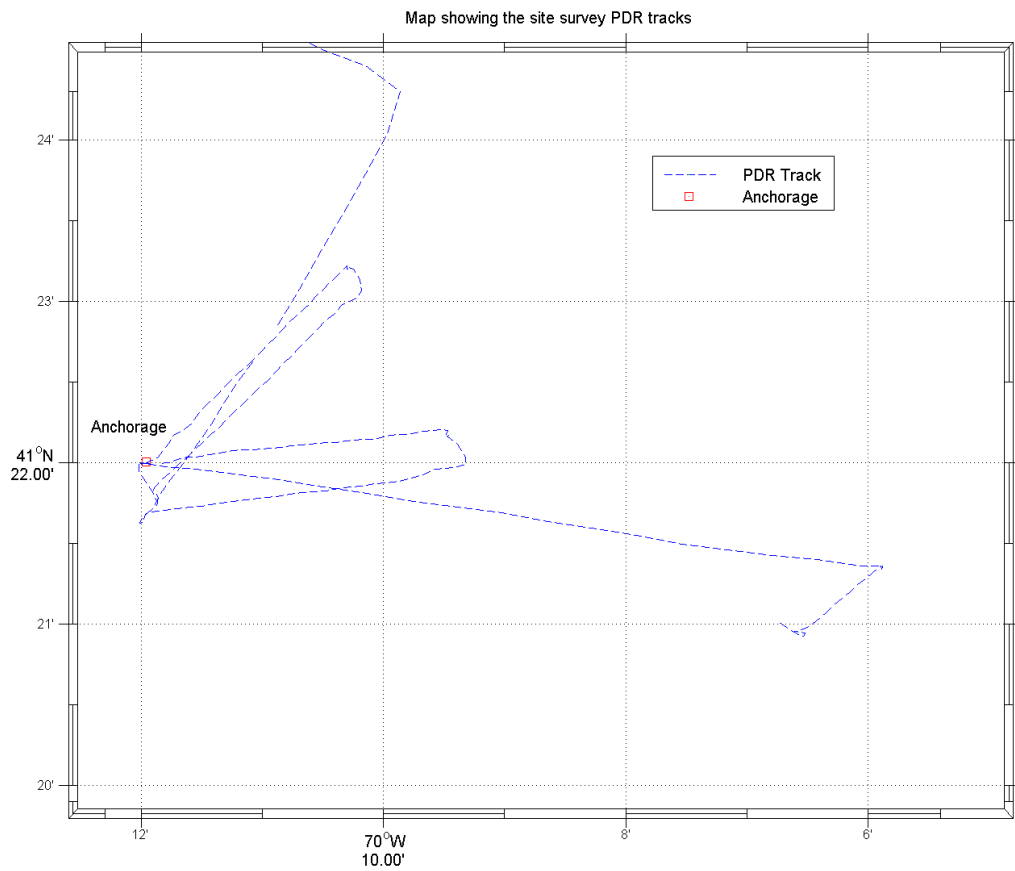


Figure 4.4: Map showing the precision depth recorder tracks for the site survey.

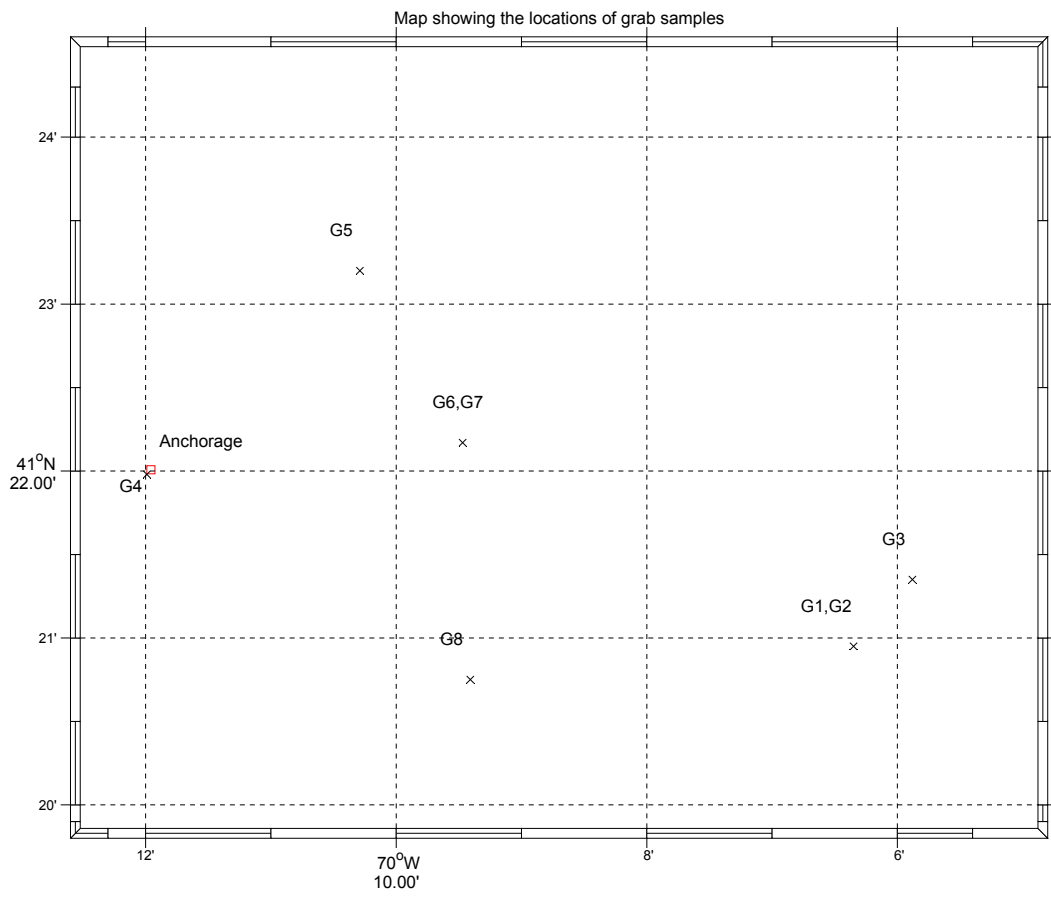


Figure 4.5: Map showing the grab sample locations for the site survey.

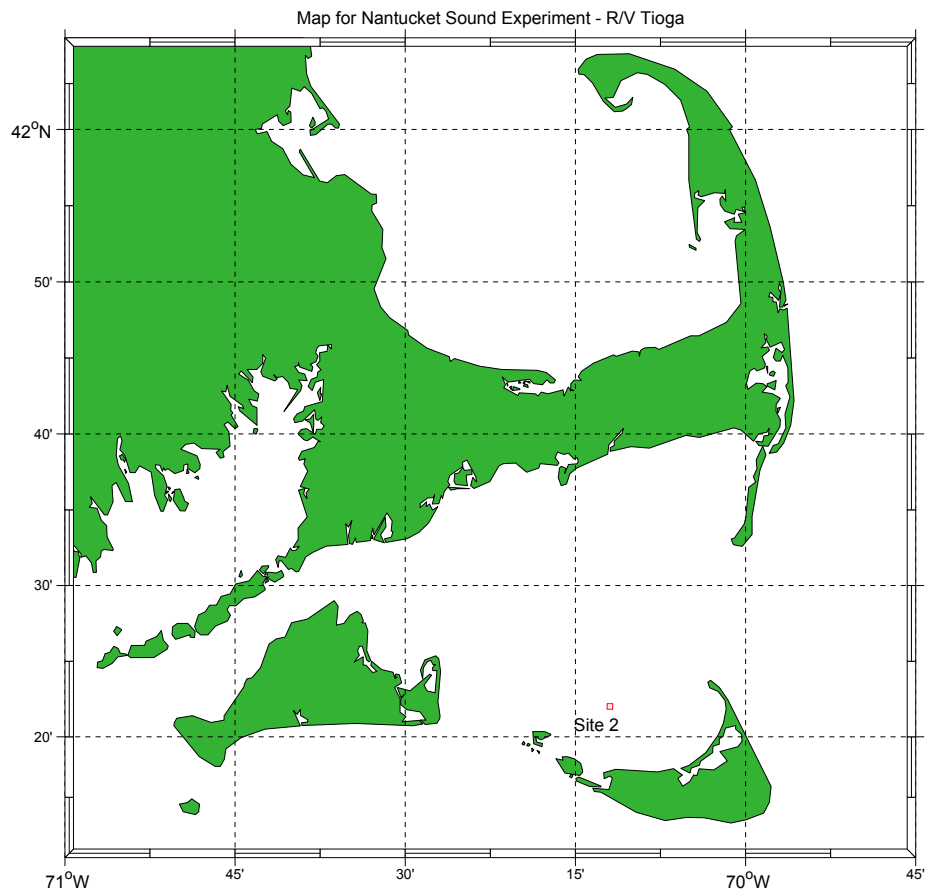


Figure 4.6: Map showing the relative position of site 2 to Cape Cod.

4.2.1 Historical Data

Cape Cod and Nantucket Sound were formed by glacial movement of the Laurentide ice sheet during the last stage of the Pleistocene Epoch, some 50,000 to 70,000 years ago. [104,105]. Two positions of ice standstill during the retreat of the ice formed the northern edges of what are now the islands Martha's Vineyard and Nantucket and the main land of Cape Cod. As they retreated, mechanical wear between the glaciers and the underlying tertiary and cretaceous rocks left a poorly sorted sediment with many different grain sizes [5]. Since the end of the glacial era, sediment transport has sorted the sediments because different grain sizes have different fall velocities.

Bedrock scouring from the movement of the glaciers also formed many depressions in the deep layers below the sediments which are evident by sub-bottom profiling [106]. These scours were later filled in by settling sediment and appear as valleys in the sub-bottom geo-acoustic profile. In areas with high currents, and thus low sediment accumulation, the hard acoustic basement reflector is closer to the surface and thus multiple layers will affect the acoustic transmission [107]. This is especially evident in the shoals of the sound. The irregular character of the bottom layers due to scouring and the effect of multiple interfaces is not ideal, so areas of known, thick, sandy-silty sediment layers were sought for the experiment.

The area inside of Tuckernuck shoal, coincident with site 2 here, is shown on a chart by O'hara and Oldale [108] to have a sandy-silty bottom. Further, the ongoing Cape Wind energy project investigated the area around Tuckernuck shoal as a potential site for a wind park and published sub-bottom profiling records with coincident bottom core samples which showed a 30 m thick silty-sand bottom layer over a hard sub-bottom reflector [107].

Frisk, Lynch and Rajan cited "archival data" which suggested a bottom density of 1.7 g/cm^3 and a sound speed in the deep bottom of 1800 m/s . [91]. While it is not clear what is meant by "archival data", they also published their inverted sound speed profiles, which are shown in figure 4.7. More than likely, this archival data was taken from the

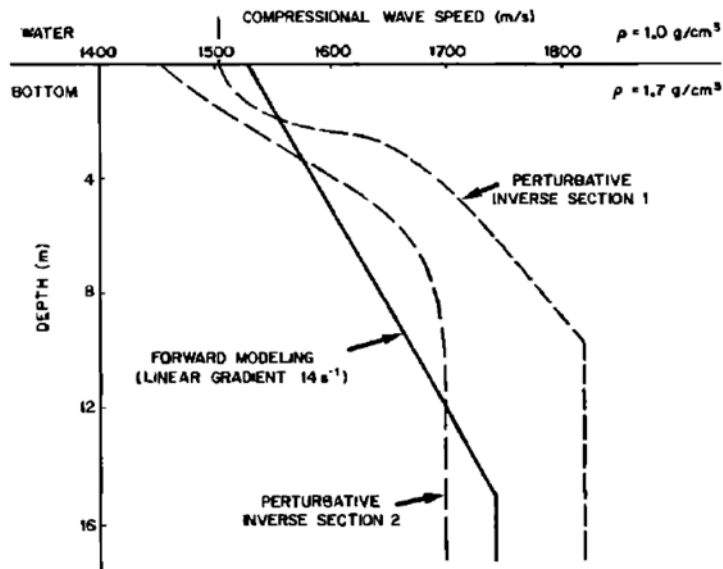


Figure 4.7: Results of bottom property inversion in Nantucket Sound from Frisk, Lynch and Rajan [91].

Woods Hole Oceanographic Institution report 71-15 which reports sediment properties in Nantucket Sound [109] obtained by grab sample analysis. In that report, there is one particular data point that was coincident with site 2 and had the properties listed in table 4.1.

After reviewing the historical data, it was quite clear that there was more data about the bottom at site 2. Further, the ADCP on board the ship indicated what was expected by the surrounding bathymetry at site 2: the currents were lower and the surface waves were less severe when compared to the first proposed site. Because of these reasons, and the fact that the precision depth recorder showed a thick, homogeneous sediment layer (discussed in the next section), site 2 was chosen as the location for the acoustics experiment. The remaining site survey data back up this decision and quantify the bottom properties.

4.2.2 Precision Depth Recorder

Data from the PDR as the ship moved from the location of grab sample 4 to the location of grab samples 6 and 7 are shown in figures 4.8 and 4.9. The transducer used by the

Table 4.1: Summary of reported archival sediment properties at site 2 from [109].

Sample Property	Value
Date taken	04 April 1964
Research Vessel	Asterias
Sample method	Smith-McIntyre grab sample
Latitude	41° 22.6' N
Longitude	70° 10.7' W
Composition (grain size)	85% Sand / 15% Silt
Composition (grain origin)	97% Quartz/ 1% Glauconite/ 1% Dark mineral/ 0.5% Mica/ 0.5% Foraminifara ^a
Mean grain size	3.38 ϕ (96 μm)
First distribution mode	3.25 ϕ (105 μm)
Second distribution mode	3.60 ϕ (82 μm)
Final description ^b	Silty-Sand

^aGlauconite is a green mineral which is chemically a hydrous silicate of iron and potassium and forms from the salts in the water. Foraminifara are single-celled organisms with shells.

^bNote: The original description upon recovery of the sample was “ Clayey silt, dark greenish-brown on top, dark grey below”.

Knudsen 320 echo-sounder PDR system was a dual frequency transducer emitting pulses with frequencies of 33 kHz and 200 kHz. The lower frequency penetrates deeper into the sediment since its attenuation is lower, but the transducer is more directional and the pulse shorter for the higher frequency. This means that the low frequency data set reveals more sub-bottom structure, but the higher frequency has a better resolution of the interface.

The low frequency data from the PDR was also susceptible to more noise. A precision depth recorder works by emitting a broad band pulse and operating in a mono-static configuration. That is the emitter also acts a receiver. After each pulse is emitted the system records the received signal for a certain amount of time. Using the time of arrival of each reflection recorded in the received signal and knowing the speed of sound in the water column allows determination of the depth of interfaces by time of flight. In figure 4.8

the vertical axis is a depth axis determined by the speed of sound and the time of arrival of each pulse. The grayscale image is then the received signal level as a function of time in the vertical axis. If the noise level is low, only the reflection from the bottom would show up as a dark line. The vertical striations in the figure are actually noise caused by the wake of the ship as it moves along the profile path. Approximately 3/4 of the way down the figure is a uniform dark line which is the return from the bottom. From this the bottom is roughly 13 m deep and has few returns from inhomogeneities. These would appear as strong clutter in the first few meters of the bottom. The output also shows that path is relatively range independent with only a slight variation of depth with range. Further, the echo strength reported by the depth recorder was consistent with a sound speed ratio between the water and bottom of $C_{bottom}/C_{water} \approx 1.1$.

PRECISION DEPTH RECORDER OUTPUT 33kHz
24 AUG 2005 - 18:05 LOCAL TIME START

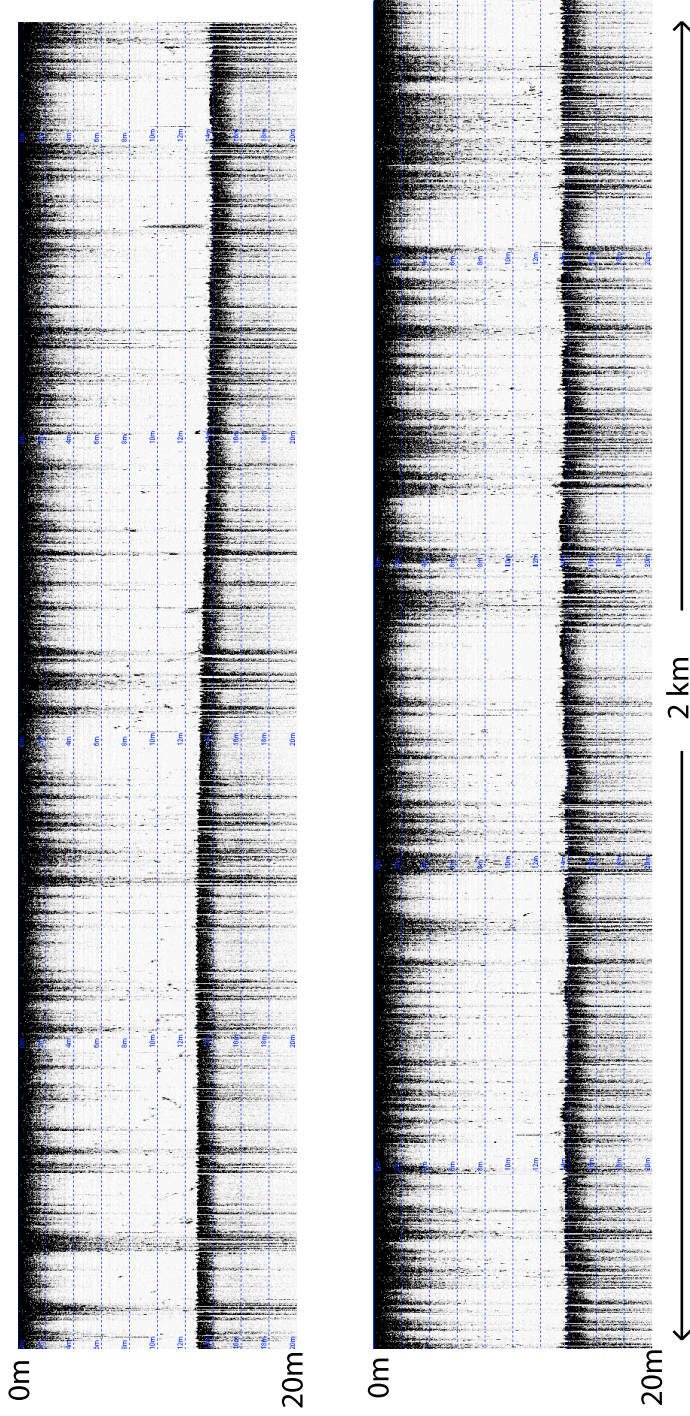


Figure 4.8: Precision depth recorder output at 33kHz. The lower frame is a continuation of the upper frame and the two frames combined correspond to the path from grab sample 4 to grab sample 6 and 7.

PRECISION DEPTH RECORDER OUTPUT 200KHZ
24 AUG 2005 - 18:05 LOCAL TIME START

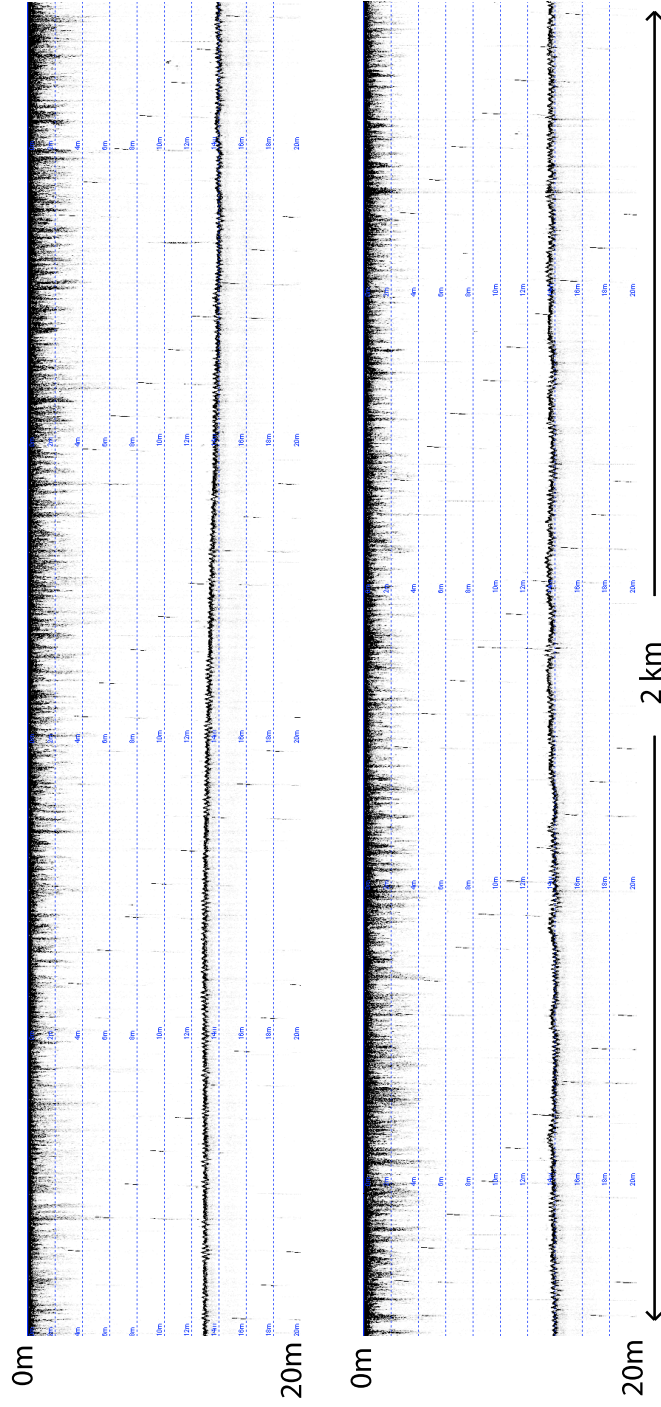


Figure 4.9: Precision depth recorder output at 200kHz. The lower frame is a continuation of the upper frame and the two frames combined correspond to the path from grab sample 4 to grab sample 6 and 7.

4.2.3 Grab Sample Data

Approximately 1 kg of sediment was retrieved at each of the grab sample locations shown in figure 4.5. Grab samples 1,2, and 3 from site 1 had some small shells. All of the samples were generally described as “grey mud” when recovered. Small, sealed plastic bottles were used to preserve the sediment as it was retrieved, without drying out, to be analyzed on shore in the laboratory.

The density of the sediment samples was measured by measuring the mass of a 100 cm^3 sample in a graduated test tube. This resulted in an average density of 1.7 g/cm^3 . The composition of the sediment was then measured by using a set of standard sieves. Each sieve had different opening sizes and the sieves were stacked such that the opening sizes decrease down the stack. Below the stack was a clean 5 gallon bucket. A sample of 100 g of sediment sample was placed in the top sieve and starting from the top, distilled water in a spray bottle was used to rinse the sediment until all of the grains smaller than the opening in that sieve had passed through the openings. As each sieve was satisfactorily rinsed, the sieve was removed from the stack and the grains that were trapped in the sieve were rinsed into a clean beaker. The sediment and rinse water caught in the beaker were then filtered by a vacuum drawn on a filter flask with a Buchner funnel in its stopper. Filter paper capable of filtering particles larger than 20 μm was used in the Buchner filter. This setup is shown in the photograph in figure 4.10. The mass of the filter paper was measured when dry before use and was removed and allowed to dry after filtering the sediment from the water. Once the filter with the sediment was dry, it was weighed again. The difference in measured mass before and after the vacuum filtering process was the mass of the sediment with the effective grain size associated with each sieve. To determine the effective grain size, the mean of the opening size was taken for each sieve and the sieve above it.

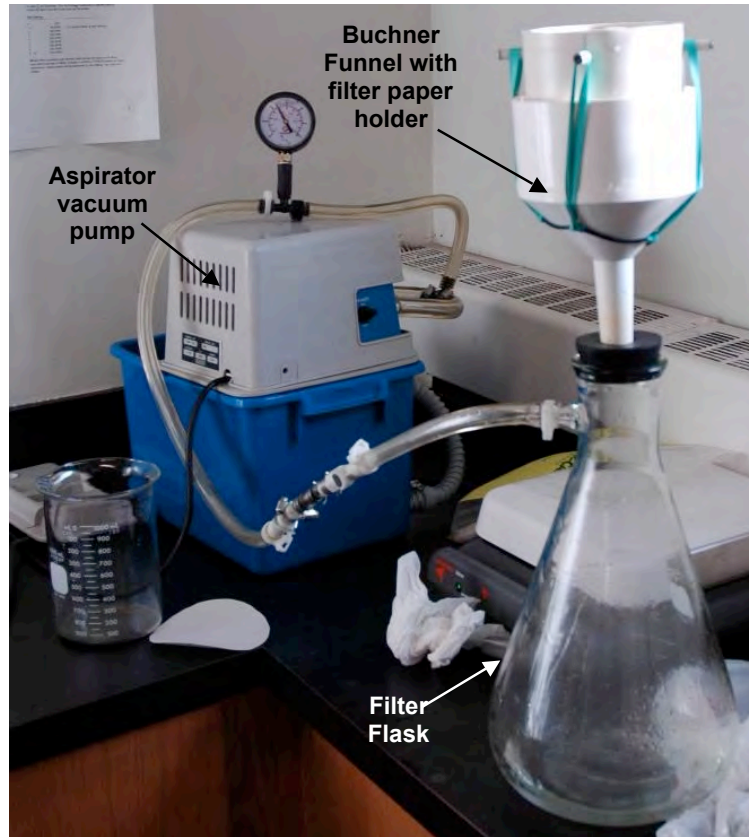


Figure 4.10: Photograph of the setup of the sediment vacuum filtering apparatus.

The average particle size was found using

$$(\text{Average particle size}) = \sum_n (\text{mass fraction})_n \times (\text{effective particlesize})_n \quad (4.1)$$

Where each n is a different sieve. Grain sizes are expressed in a logarithmic scale where $\phi = -\log_2(\text{grain diameter in mm})$. Table 4.2 summarizes the sieves used as well as the opening size, effective particle size, and mass fraction associated with each sieve for grab sample number 4, which was taken from site 2. The particles in the row labeled “> 400” are those that passed through all of the sieves into the bucket on the bottom. Figure 4.11 shows the grain size distribution graphically. The mean grain size was 0.115 mm. Measurement of the mass of the saturated sediment sample prior to filtering as well as the

Table 4.2: Summary of the measured sediment size distribution from sieving..

Sieve number	Sieve opening size (μm)	Effective particle size (μm)	Effective particle size (ϕ)	Mass fraction	Sediment description
35	500	> 500	1.00	0.0036	Coarse Sand
40	425	462.5	1.11	0.0024	Medium Sand
45	355	390	1.36	0.0040	Medium Sand
50	300	327.5	1.61	0.0092	Medium Sand
60	250	275	1.86	0.0141	Medium Sand
70	212	231	2.11	0.0193	Medium - Fine Sand
80	180	196	2.35	0.0149	Fine Sand
100	150	165	2.60	0.0326	Fine Sand
120	125	137.5	2.86	0.1090	Fine Sand
140	106	115.5	3.11	0.4854	Very Fine Sand
200	75	90.5	3.47	0.1510	Very Fine Sand
400	38	56.5	4.15	0.0667	Very Fine Sand - Coarse Silt
> 400	-	< 38	4.72	0.0879	Silt - Clay

dry filtered sediment allowed for the determination of porosity by

$$\beta = \frac{\text{Volume of water in sediment}}{\text{Volume of saturated sediment}} = \frac{(m_{sat.sed} - m_{dry sed})/\rho_{sea water}}{m_{sat.sed}/\rho_{sat.sed}} \quad (4.2)$$

This gave a porosity of 49%. Figure 4.12 shows a photographic capture of the sediment as seen through a microscope. The different grains sizes, geometries, and compositions are clear from this picture.

4.2.4 Geoacoustic Profiles

Based on the measurements made during the site survey and historical literature a geoacoustic profile to be used in analysis of the experiment was determined. One of the most comprehensive discussions of sediment modeling comes from Hamilton [30]. The best fit sound speed in a sandy sediment as a function of depth is given by Hamilton as

$$V_{Hamilton} = V_{1m} Z^{0.015} \quad (4.3)$$

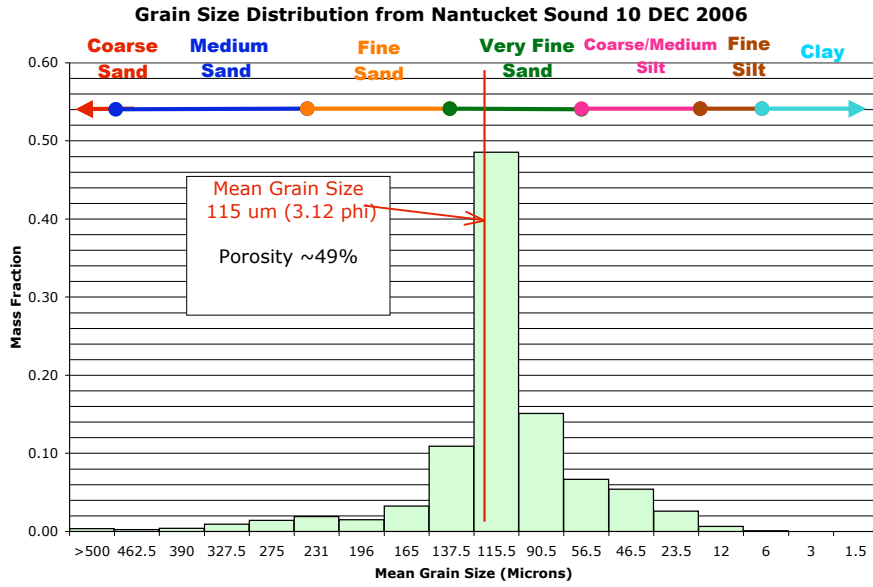


Figure 4.11: Measured sediment size distribution for Nantucket Sound as determined by sieving 100g of grab sample 4.

where Z is the depth below the sea floor and V_{1m} is the sound speed velocity 1m below the interface. This sound speed profile has a very large gradient near the surface and the difficulty with using this profile computationally is that the sound speed tends to zero at the interface. In order to avoid this problem, a sound speed profile of the form

$$c = c_{interface} + c_{diff}(1 - e^{-aZ}) \quad (4.4)$$

was assumed where $c_{interface}$ is the sound speed at the interface, c_{diff} is the difference between the interface sound speed and the deep sound speed, and a is some positive constant. Choosing $a = 0.3$ and $c_{diff} = 200$ gives sound speed gradients with depth near the surface similar to Hamilton's profile for a sandy bottom [32]. These parameters also give a sound speed profile with depth that is very similar in magnitude and gradient to the profile determined by Cederberg for a sandy sediment with a depth dependent porosity [110]. This selection of parameters is somewhat arbitrary other than the fact that it gives good agreement to historical data. The only remaining parameter to determine was the

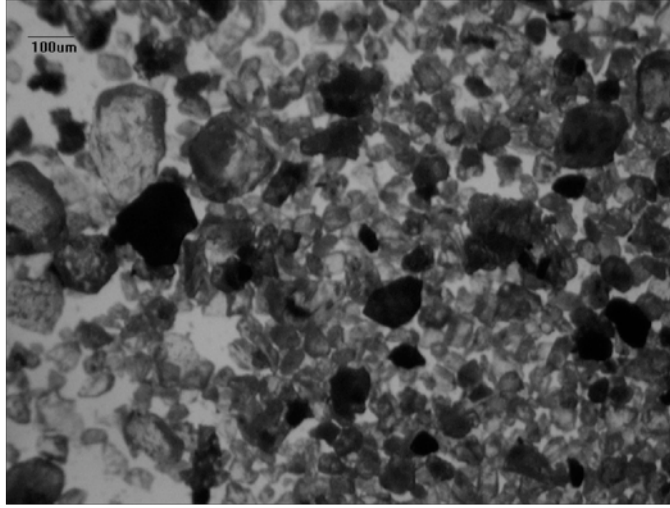


Figure 4.12: Image capture of Nantucket Sound sediment sample as seen under a microscope. For reference, the frame is approximately 1mm wide.

sound speed at the interface. Since the sound speed in the sediment depends on the sound speed in the water, and this changes with temperature and salinity, the best basis for comparison between experiments is the sound speed ratio given by [111]

$$\text{Ratio}_c = \frac{c_{\text{sediment}}}{c_{\text{water}}}. \quad (4.5)$$

Lynch, Frisk and Rajan give a velocity ratio of 0.97 to 1.02 near the surface from their inversions shown in figure 4.7 at the Nantucket Sound site shown in figure 4.3. Comparing the measured porosity from the grab sample data to the measurements given by Hamilton and Bachman [31] gives an expected velocity ratio at the present experimental site of 1.116, very similar to the approximated sound speed ratio from the precision depth recorder given earlier in this chapter. Using mean grain size instead to calculate the sound speed ratio based on the measurements gives an expected velocity ratio of 1.128. The measurements given by Hamilton and Bachman, as well as the PDR measurements in Nantucket Sound were, however, made at high frequencies (33 kHz or 200 kHz). The dispersive nature of sediments given by Biot theory predicts that the sound speed in the sediment is on the order 3% lower at 1kHz then it is at 33 kHz [59]. Thus, the sound speed ratio at the

surface was expected to be approximately 1.09. At frequencies near 1 kHz and below, a fine sand sediment is in the region where Wood's limit is applicable and thus a nearly constant sound speed as function of frequency is expected. This does not mean that there is not dispersion because as we know from causality, for a medium to have a complex wave number it must be analytic. Thus, by the Kramer-Kronigs relations the presence of attenuation at this frequency requires a dispersive sound speed. The change in sound speed over the frequency range used, however, is expected to be negligible. In the models used in the next chapter, a frequency independent sound speed profile is thus used.

During the September experiment the sound speed in the water column was nearly iso-velocity with a sound speed of 1522 m/s. Some digital data for the sound speed profile near the bottom was lost, and the vehicle only recorded the sound speed down to 6 m, but handwritten logs taken from the CTD display of the profile near the bottom indicate that there was no significant change in the profile for the bottom several meters. During the December experiment, the water was well mixed due to storm the previous day and the sound speed profile was nearly iso-velocity at 1467.5 m/s as is shown in the CTD plot in figure 4.13. The sound speed profile used for modeling is thus

$$c_{sediment} = 1600 + 200(1 - e^{-0.3Z})[m/s] \quad (4.6)$$

below the interface and nearly constant above the interface, given by the CTD. From Hamilton [30] it is known that the density as a function of depth in a sandy sediment has a gradient of approximately $.001kg/m^3/m$. Frisk, Lynch and Rajan [91] noted that sound speed profiles below several meters deep mattered little, indicating that the penetration depth of acoustic energy was less than 10 m. With this, it is expected that any variation of the density with depth was small and the density profile is thus considered constant at $1.7 g/cm^3$.

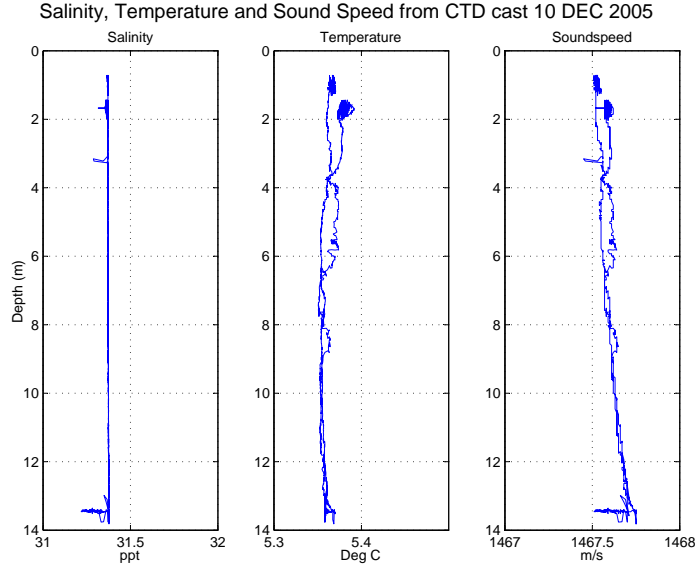


Figure 4.13: Measured salinity, temperature and sound speed as a function depth in December 2005 at experimental site 2 in Nantucket Sound.

Hamilton [30] also gives the attenuation as a function of depth as¹

$$\alpha(Z)_{Hamilton} = \alpha_{1m} Z^{-1/6}. \quad (4.7)$$

The problem with this attenuation profile is that it has a singularity at the interface. Computationally speaking, the best one could do is to define the attenuation at the interface as equal to the attenuation some small depth into the sediment, for example 10 cm.

If the Biot time constant is considered to be independent of depth, the the attenuation profile is given by

$$\alpha(Z)_{Simp.Biot} = \alpha_{interface}/c(z) \quad (4.8)$$

where the attenuation at the interface is given by $\alpha_{interface} = \tau_B \omega^2 / 2$ as is derived in chapter 2. This result also follows from a standard homogeneous medium approximation in which the sound speed is modeled as complex and the density is a real value. Although it

¹While Hamilton's empirical data are used here, the data from Stoll [19] could have also been used. Hamilton was simply chosen because much of Stoll's empirical work is based on Hamilton.

has been shown that an incorrect depth dependence assumption for attenuation will give an incorrect frequency dependence of attenuation [95], many previous experiments, including Frisk, Lynch, and Rajan, assumed a constant depth dependence. Since measurement of the attenuation characteristics is of primary concern, this portion of the geo-acoustic profile will not be exactly defined. Instead, these three attenuation profiles are proposed as potential profiles to be compared in the next chapter. As a reminder, in chapter 2 it was theoretically proposed that the modal attenuation coefficients can be used to discriminate the correct attenuation depth dependence.

In general, the geo-acoustic profile should include density, compressional wave velocity, compressional wave attenuation, shear wave velocity, and shear wave attenuation as a function of depth and location. The site survey indicates that a range independent model should be sufficient. Further, since the shear is relatively unimportant in long range propagation problems, as discussed in section 2.2, the shear wave velocity and attenuation are considered to be zero here. It should be noted that this is not to say that an effective fluid model of the sediment is being used. Instead, the recognition is that shear wave effects of the Biot model are not relevant for long range propagation. With this, the geo-acoustic profile defined by the site survey is given in figure 4.14 along with the CTD results given in figure 4.13.

Derived Geo-Acoustic Profile for Nantucket Sound Experiment

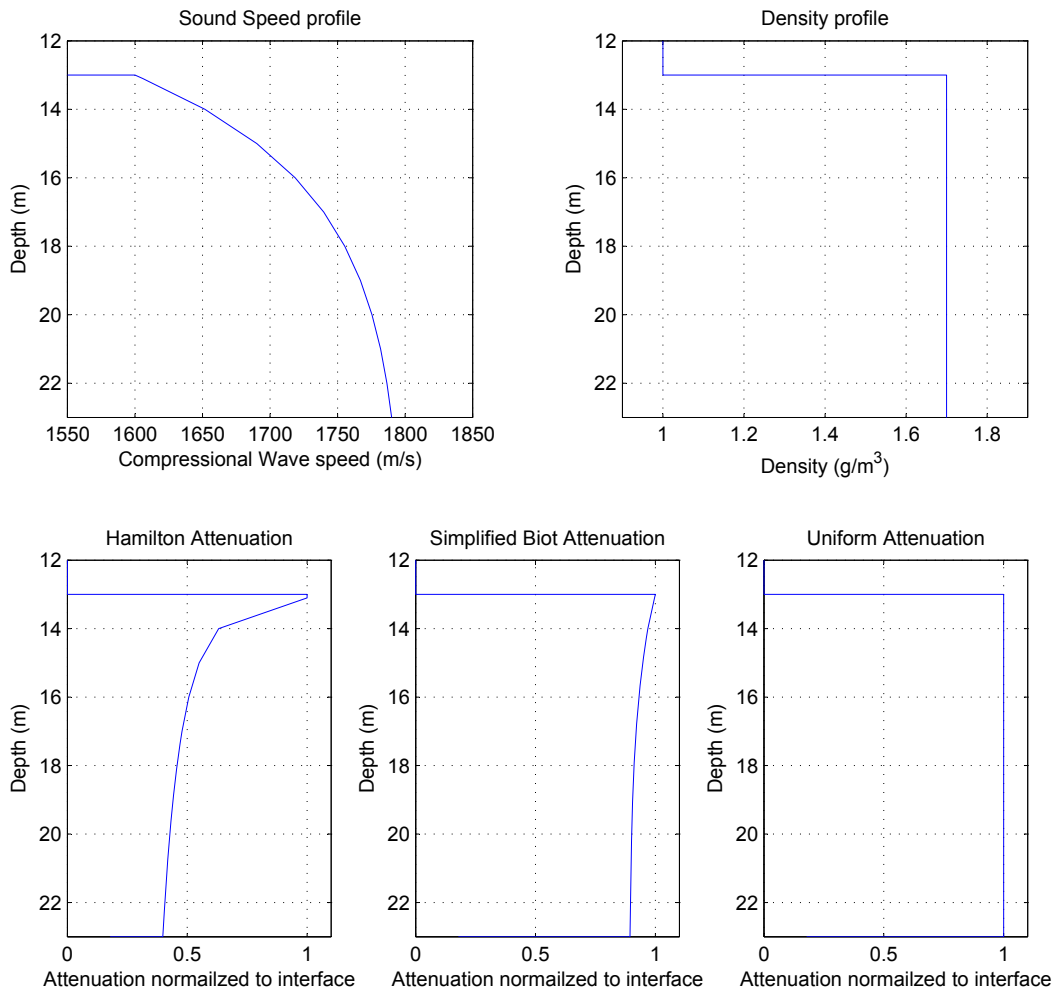


Figure 4.14: Geo-acoustic profile for Nantucket Sound as determined by the pre-experiment site survey. The three likely attenuation profiles are all shown.

4.3 Experimental Description

Experimental site 2 was chosen based on its protected characteristics, known sediment types, thick sediment layer, constant bathymetry and relative proximity to the Frisk-Lynch-Rajan site. The water depth in the area of this site was roughly 13 m. In order to strongly excite the first and higher order modes, the source depth was chosen to be mid-water-column at 6 to 6.5m. The towed array depth was chosen to be 6.0 m. The basic vehicle path was a straight course starting at $41^{\circ}22'N$, $70^{\circ}12'W$, moving out on a heading of 89° and returning to the start location. The September experimental path was meant to be a 2 km long outbound path and return trip. The source frequencies planned were 635, 823, 1031, and 1228 Hz on the outbound leg which would be switched to 220.5, 415, and 635 Hz on the inbound leg. A software fault in the vehicle prevented the return leg, but the outbound leg was successfully completed. The December experiment extended the maximum range out to 4km along the same track and the frequencies used were 220.5, 415, and 635 Hz on the outbound leg and 635, 823, 1031, and 1228 Hz on the inbound leg. Maps for these two experiments are shown in figures 4.15 and 4.16. The exact latitude and longitude of the source in each experiment is given in table 4.3.

Table 4.3: Exact latitude and longitude of the source in each experiment.

Experiment	Latitude	Longitude
September	$41^{\circ}22.041'N$	$70^{\circ}12.125'W$
December	$41^{\circ}22.008'N$	$70^{\circ}11.958'W$

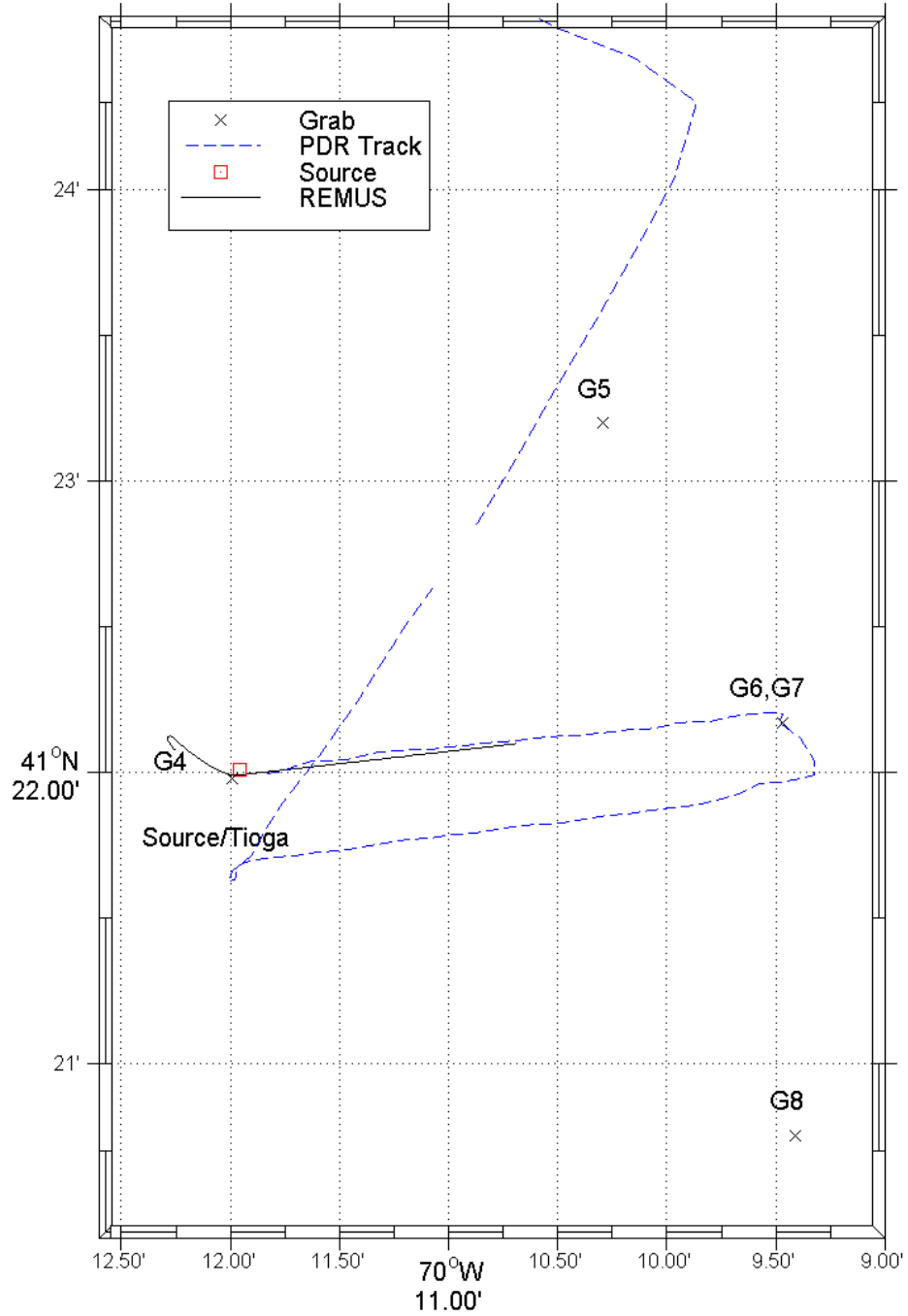


Figure 4.15: Map showing the experimental geometry for the September 2005 experiment.

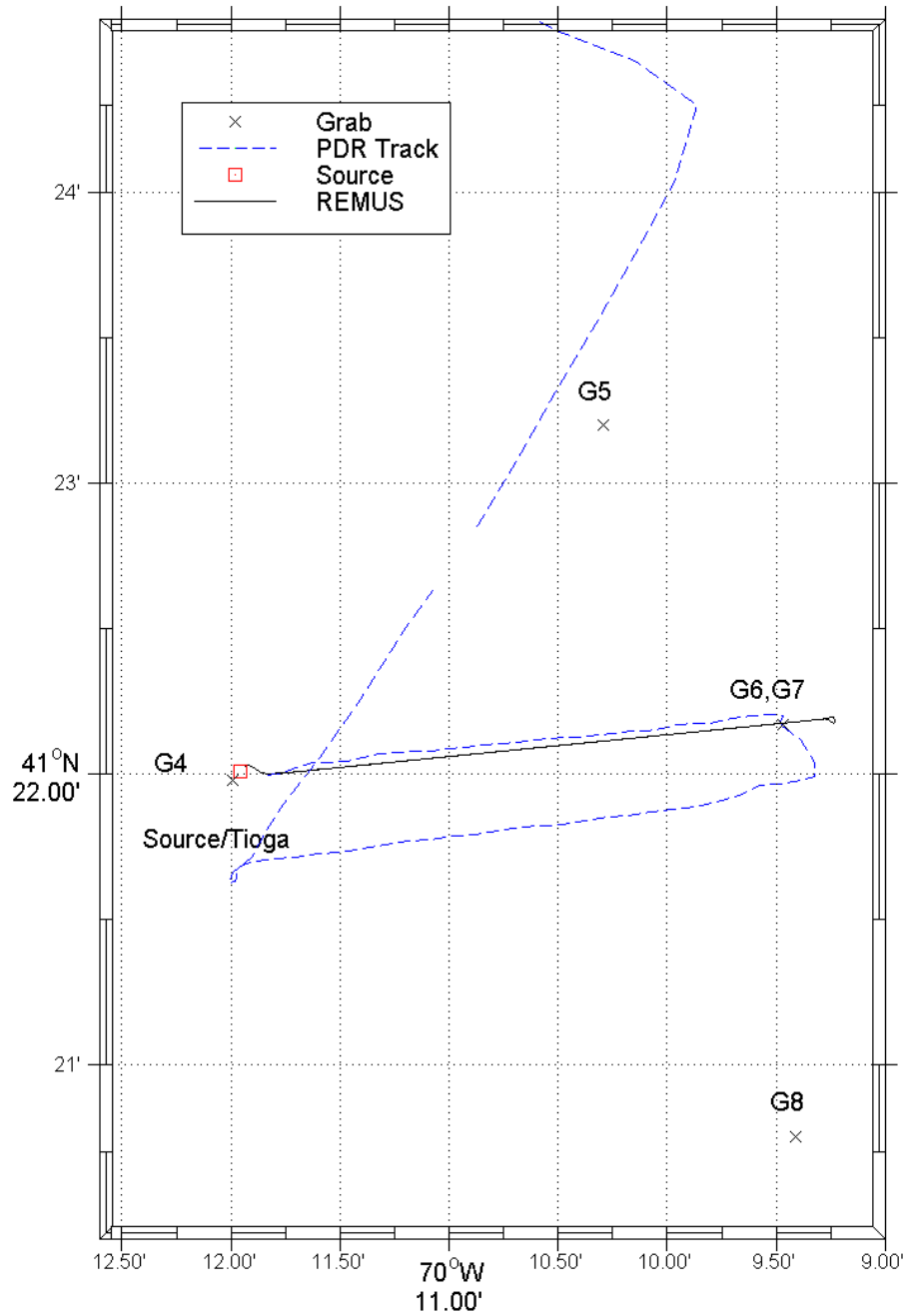


Figure 4.16: Map showing the experimental geometry for the December 2005 experiment.

Chapter 5

Nantucket Sound Experiment

5.1 Numerical Modeling

In the following sections numerical models of transmission in shallow water are used. It is convenient then to briefly discuss the models at this point. The models used were Kraken [112], a normal mode propagation program, RAM [113,114], a parabolic equation propagation program, and Safari [115], a wave-number integration program. The fundamental differences between these models were discussed in the Propagation Theory section of Chapter 2, but the important feature is that for a range-independent environment with a critical angle bottom and receivers away from the interfaces, their solutions should converge.

Ideally, any of the models could be used with equal accuracy. In reality, there are small range dependent affects. Safari cannot handle these affects. There are also interface waves and scattering, which Kraken and RAM do not handle well. For many calculations, such as those in section 2.3.1, it is necessary to determine the modal functions. Only Kraken explicitly calculates the modal functions. Thus, each program has its particular niche in this work

Appendix A gives a diagram of the flow of data in this work as well as all of the relevant computer programs written. One characteristic that the numerical models have in common is that they require a similar set of input data considering layered media properties. Since

each program requires the data in a slightly different format, subroutines were written to take the data given in the format for Kraken, add any missing data, and write input files for RAM and Safari. This also enabled the automation of the models so that they could be used in iterative loops comparing the output of the models to measured values, adjusting the input parameters, recalculating and repeating until convergence

5.2 September Experiment

The September Nantucket Sound Experiment took place on the 15th of September, 2005. The experimental geometry was as described in the previous chapter and is shown in figure 4.15. This was the first attempt at performing the long-range transmission loss experiment using an AUV towed hydrophone array and there were some problems experienced during the experiment. First, the source was deployed with an anchor such that the source was 6.5 meters off the bottom. On the chart shown in figure 4.3 it is clear that if the support ship were to drift off its anchorage slightly it could end up over a small area of shallower water. This indeed happened, and thus the source depth was 4.5 m instead of 6 m as planned. Further, the anchor applied a tension to the flex-tensional source which may have reduced the source level. It was also later discovered that salt water entered the sealed portion of the source at some point, which may have affected the source level. Additionally, the vehicle was not capable of making its return trip due to a software malfunction. Therefore the source levels had large errors and sampling of the entire range of frequencies was not achieved. These problems made the errors associated with making an accurate transmission loss measurement large. The experiment did, however, provide accurate information concerning the stability of the array, the ability to perform synthetic aperture signal processing and the ability to measure a received signal level which compared well qualitatively to calculated values. ¹.

¹While accurate transmission loss measurements require accurate knowledge of the source levels, accurate received signal level measurements only require a stable, low noise receiver.

5.2.1 Signal Processing

In the experimental setup in figure 4.1 it was explicitly shown that the experiment consists of a towed hydrophone array moving radially out from a source on a ship, which has onboard instrumentation to characterize the water column. The array data was recorded on an external recording system attached to the bottom of the vehicle. On-board sensors on the vehicle also recorded the local environmental data. Therefore there are essentially three sets of data: the ship data, the acoustic data on three separate mini-discs, and the AUV data. By synchronizing the data sets with known signals and using the synthetic aperture signal processing techniques described in section 2.3.2, the performance of the system is enhanced compared the previous single transducer pair system of Lynch, Frisk, and Rajan [91,89].

The formation of a synthetic aperture requires the knowledge of the positions of the hydrophones in space and time. Ideally one would use array shape and motion estimation algorithms as well as precise navigation data to correct for errors in assuming the array follows a straight path. However, if stability and motion of the array can be controlled, the complicated element motion and displacement compensation may not be needed. The idea with the prototype system was to attempt to form a synthetic aperture using the least advanced method, i.e. phase compensation based on the vehicle navigation data assuming the array exactly follows the path of the vehicle, and to then progress to more advanced methods as required. Thus, in this case, the phase compensation was given by

$$\phi_i = \omega t_i. \tag{5.1}$$

Where t_i is the time at which the i^{th} sub-aperture is evaluated and ω is the source frequency. The method for determining the range at which the received complex pressure is evaluated is given in appendix E. The range as a function of time is then used to find the locations of the hydrophones at each t_i . This synthetic aperture phase compensation method requires a stable tow in which the motion of the array is insignificant in comparison to a wavelength.

Array gain

The beamformer gain is dependent on the coherence of the acoustic field in addition to the array stability. Improvements by more advanced phase compensation techniques, therefore, can only extend the synthetic aperture to a length determined by the coherence of the acoustic field. In general the acoustic field can be considered as a deterministic signal with a known phase rate variation and a random phase component. This random phase component determines the coherence of the field and is affected by the water column, bottom, and interfaces. Statistical antenna theory shows that arrays have the characteristic that if the array is shorter than the coherence length of the acoustic field, an increase in array length will increase the gain according to $20 \log_{10}(N)$. Here N is the number of sub-apertures. After a coherence length is surpassed, an increase in the array length will tend to increase the array gain according to $10 \log_{10}(N)$. Thus, the array gain as a function of the number of sub-apertures will increase like a coherent signal for small arrays, and like an incoherent signal for arrays much longer than the coherence length (See appendix B for details). The transition from completely coherent to incoherent is a smooth transition.

By this reasoning, the gain achieved by the synthetic aperture as a function of number of sub-apertures serves as indicator to the performance of the system. If the system achieves coherent gain with synthetic apertures on the order of coherence lengths in the ocean, the indication is that the motion of the array is truly insignificant and advanced motion compensation is not needed. If, instead, the array gain behaves like the incoherent case even for small synthetic apertures, then more advanced techniques are required.

To determine the gain achieved by synthetic aperture processing, the output from the synthetic aperture beamformer is compared to the average conventional beamformer output of the sub-apertures. The computer programs used to perform these calculations are given in appendix A. Each sub-aperture is exactly a physical aperture of the towed array, that is 6 channels spaced at 0.75 m. The synthetic aperture is then formed by N sub-apertures each displaced 4.5 m from the previous. Thus, the sensor spacing in

the synthetic aperture is exactly the same sensor spacing in the sub-apertures. Aliasing characteristics of the sub-apertures and the synthetic aperture are therefore identical and additional sub-apertures will only affect the beam-width of the beamformer and the relative array signal gain. Relative array signal gain is found by the peak output of the synthetic aperture beamformer minus the peak of the mean of the conventional beamformer outputs of the sub-apertures.

$$RASG = \max(b_{SA}(\theta)) - \max\left(\frac{1}{N} \sum_{i=1}^N b_{conv_i}(\theta)\right) \quad (5.2)$$

where b is a beamformer output and θ is the beamformer bearing. Since there is no meaningful peak in the beamformed output for noise, the relative array noise gain is computed by taking the mean of the output of the synthetic aperture minus the mean of the average conventional beamformed sub-aperture output:

$$RANG = \frac{1}{M_\theta} \sum_{j=1}^{M_\theta} b_{SA}(\theta_j) - \frac{1}{M_\theta} \sum_{j=1}^{M_\theta} \left(\frac{1}{N} \sum_{i=1}^N b_{conv_i}(\theta_j)\right) \quad (5.3)$$

where M_θ is the number of points in the bearing space. Appendix B gives a detailed derivation of the relative array signal gain and relative array noise gain.

Figure 5.1 shows the relative array signal gain achieved as a function of the number of sub-apertures during a portion of the 2 km outbound leg of the September experiment. Since the wavelength at the lower frequencies is much longer, the motion of the array is less significant at lower frequencies than at higher frequencies. This is evident in the fact that the the relative array signal gain falls off at a much higher rate for 1228 Hz than for 635 Hz. Inspection of the gain achieved for the four frequencies shows that gain decreases the most at distinct aperture lengths that are the same for all frequencies. These decreases occur at 5, 12, and 75 sub apertures and are most evident in the 1228 Hz data. Figure 5.2 shows the locations of the hydrophones used to form the synthetic aperture. The array follows the path of the vehicle, which maintains course using a feedback control system.

Thus the vehicle deviates from a straight line due to controller steady state oscillations. In particular, there were curves in the array path near 65, 70, 85, and 97 meters north where the coordinate system is relative to the source location.

Comparing the positions of the decreases in relative array signal gain to navigational data from REMUS, it is clear that the decreases in gain coincide with deviations from a straight path of the vehicle. The one exception is the curve in the path near 85 m North. This curve, however, has a much larger radius of curvature than the other variations. Since the beamformer requires a deterministic phase rate to achieve beamformer gain, any error in signal phase on the elements will cause a reduction in gain.

Deviations from a straight path without the use of shape estimation or motion compensation will introduce phase errors in two ways. The first is that sudden heading compensation by the vehicle can generate a displacement wave that propagates down the array much like a classic vibrating string problem. The displacement of the hydrophones causes a phase error on the received signals and decreases the gain of the beamformer. This would be corrected using motion compensation.

The other loss of gain comes from a more gentle change in direction. Since the beamforming algorithm is based on the phases of a linear array, not a curved array, the hydrophone element phases will have an error even for smooth curves which do not excite array displacement waves. Corrections to this problem would be shape estimation corrections.

The fact that the curve near 85 m North does not affect the gain significantly while the other curves do characterizes the limits of synthetic aperture processing when using the vehicle data alone for phase compensation. The curves near 65 m and 70 m North have a radius of curvature of approximately 150 m. The curve near 85 m North has a radius of curvature on the order of 400 m, and the curve at 97 m North has a radius of curvature on the order of 50 m. It is expected that the effect of the radius of curvature should be related to the acoustic wavelength by the ratio of the chord height, d , to the acoustic wavelength. A schematic of a curved array is shown in figure 5.3 and the ratio of the chord height to

the acoustic wavelength is clearly given by

$$\frac{d}{\lambda} = \frac{r - \sqrt{r^2 - \frac{L_A^2}{4}}}{\lambda} \quad (5.4)$$

where r is the radius of curvature, L_A is the length of the array that is curved, and λ is the acoustic wavelength. This equation holds for radii of curvature large compared to the array length and shows that a longer wavelength (lower frequency) is less affected by curvature. Further, if a critical value of d/λ is determined, above which the gain will drop 1 dB, one can quantify the limit of array curvature permissible given the frequency of interest. The gain at 635 Hz is affected only by the curve with radius 50 m. This gives a chord height to wavelength ratio of .015. At 1031 Hz the effect of the 150 m radius is seen giving a chord height to wavelength ratio of 0.010. It is expected, therefore, that a chord height to wavelength ratio of below .010 will show little effect in the measured gain of the beamformer when no motion or shape compensation is used. At 1228 Hz, when the radius of curvature is 400 m, $c/\lambda = 0.004$ and the effect of the array curvature is not seen.

A random phase error causes two main effects in the synthetic aperture beamformer output. These are

1. A decrease in the maximum gain of the main beam
2. Broadening of the main beam

In reference [96] Carey and Moseley discuss these effects. A derivation of the array gain as a function of coherence length is presented in reference [116] and gives that, on average, a 2 dB degradation in array gain from the theoretical limit corresponds to an array that is approximately 2 correlation lengths long. This derivation was carried out assuming that the incident signal was arriving at broadside, which simplifies the integral equation of the expected beamformer output to the easily evaluated form

$$\langle |b(0)|^2 \rangle = \int \int P_0^2 \exp(-\alpha(1 - R_\phi)) dx_1 dx_2. \quad (5.5)$$

Where $\langle \rangle$ denotes an ensemble average, P_0 is the deterministic incident pressure amplitude, α phase variance of the incident signal caused by random phase fluctuations, and R_ϕ is the phase correlation function which is assumed gaussian with a horizontal coherence length of L_H . Reexamination of the derivation, however, reveals that the integral equation is given as

$$\langle |b(\psi_s)|^2 \rangle = \int \int P_0^2 \exp(-\alpha(1 - R_\phi) + i\psi_s(x_1 - x_2)) dx_1 dx_2 \quad (5.6)$$

where ψ_s is infact the steered beam angle given by the difference of the steered beamformer angle and the signal direction,

$$\psi_s = \psi - \psi_0, \quad \psi = \pi L \sin \theta / \lambda, \quad \psi_0 = \pi L \sin \theta_0 / \lambda. \quad (5.7)$$

While the analysis presented was correct in stating that this simplifies for the broadside case where $\psi_s = 0$, in fact this is more generally true as long as the array is correctly steered. That is, in the direction of the incident signal, $\psi_s = 0$. This means that the analysis performed on the relative gain degradation holds for any direction as long as the array is steered in the direction of the incident sound. Therefore, a degradation of 2 dB in array gain from the theoretical limit of $20 \log_{10}(N)$ corresponds to an array which is approximately 2 coherence lengths long. The caveat is that if an array is moving radially out from a source, and the source is then in the end-fire direction, the acoustic field is passing through the same volume of water over the same portions of the boundaries in order to get to different portions of the array. Thus, the coherence length in this case is the longitudinal coherence length which can be close to the temporal coherence scale of the water. If there are no internal waves or strong current effects, this coherence length can be quite long. In the transverse case, where the array is steered to a source near broadside, the acoustic field is traveling through a different volume of water and over different sections of the boundary when traveling to different sensors. The transverse coherence length, for

which measurements were presented by Carey [116], is then expected to be shorter than the longitudinal coherence length.

Out to 70 sub apertures the gain for 635 Hz for the path shown in figure 5.2 stayed within 2 dB of the perfectly coherent limit of $20 \log_{10}(N)$ as is shown in figure 5.1. This is equivalent to an array that is about 135 wavelengths long and thus corresponds to a longitudinal coherence length of 67 wavelengths. This is, as expected, better than the transverse coherence length results on the order of 30λ for shallow water regions with similar range to water depth ratios reported by Carey [116] and indicates excellent performance of the array system.

The major difference between the synthetic aperture in the end-fire and broadside direction is the beamwidth as is explained in appendix B. This relates to the second effect of a random phase variation on the synthetic aperture output, the broadening of the main signal beam. Carey and Moseley [96] show that the acoustic field angular signal spread² due to random phase fluctuations is given in radians by $0.530\lambda/L_H$ if the variations are gaussian distributed. Since the response of the array is the convolution of the beam response of the array and the wave-number spectra of the field, a resolution criterion can be established by matching the 3-dB down width of the beam response to the angular spread in the field. Since the beam width is much longer at end-fire and proportional to $(\lambda/L_A)^{1/2}$, the length of the array for which the beam-width and angular spread is matched is much longer at end-fire than at broadside. While the length of the array corresponding to 2 coherence lengths is the same for broadside and end-fire as was discussed above, the distinction comes in the angular spread resolution criterion where the end-fire array must be longer to be resolution limited than the broad side case. Coupled with the fact that the longitudinal coherence length is longer than the transverse, this is why the synthetic aperture Hankel transform technique works so well; long coherent apertures can be formed in the end-fire direction without reaching the wave field angular spread resolution limit.

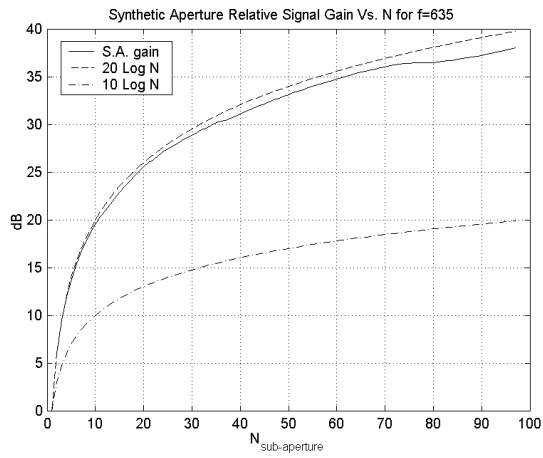
²The acoustic field angular spread can be thought of as the apparent smearing of the incident signal angle due to random phase fluctuations in the environment. This angular spread can not be avoided and is the limiting factor in synthetic aperture resolution.

To further characterize the performance of the array system, the ability to reject noise was investigated. If the array properly rejects noise, then the relative array gain for a frequency not emitted by the source should behave like $10 \log_{10}(N)$. During the experiment the source emitted narrow band tones at 635, 823, 1031, and 1228 Hz. Figure 5.4 shows the relative array gain for 750 Hz. The trend for this case of noise follows $10 \log_{10}(N)$, the theoretical result for the relative array noise gain.

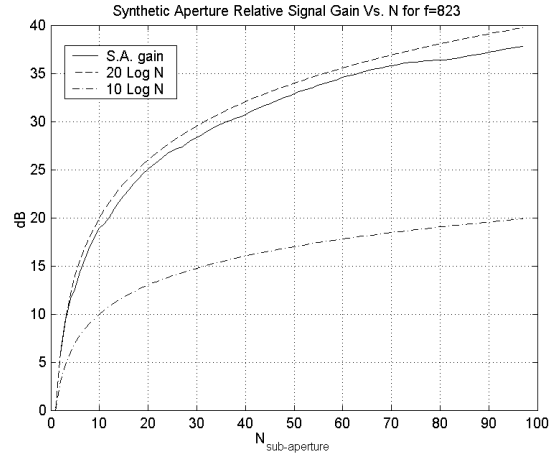
Figure 5.5 shows the synthetic aperture beamformer output for 100 sub-apertures (600 sensors) compared to the average conventional beamformer output for the 6 sensor sub-apertures. The vehicle was traveling radially outward from the source with the array behind it. Defining the array bearing to be 0° broadside, $+90^\circ$ in the forward direction, and -90° aft, this would put the expected source location for the outbound leg at -90° , the aft end-fire direction. Errors in the relative velocity of the array to the source when forming a synthetic aperture will cause the largest errors in end-fire direction [74]; a 10% error in velocity should cause a 20° bearing error near end-fire. In this case, the vehicle navigated by dead reckoning using the ADCP, which is prone to errors of 3-5%. While the results shown indicate an estimated bearing to the source of -85° , without the navigation correction described later in section 5.3.1, these results would indicate a bearing near -75° . The average conventional beamwidths and synthetic aperture beamwidths indicated by the 3 dB down points shown in figure 5.5 also correspond well to the beam width predicted by linear array theory in appendix B.

Figure 5.5a shows the beamformer output for 635 Hz with the peak representing the direction of the source. The average conventional beamformer output on the same plot shows that the conventional array can only locate the source within about 45° of end-fire. The synthetic aperture is much longer and therefore can resolve the direction within a few degrees. As frequency increases the length of the array compared to a wavelength increases for a fixed number of sub-apertures. Since angular resolution depends on the length of the array relative to a wavelength as is seen in appendix B, the resolution of the array improves with frequency as is seen in figures 5.5b,c, and d. At the higher frequencies

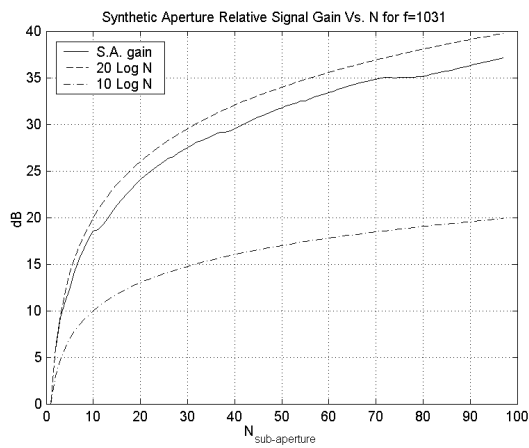
there are additional peaks which are evident due to aliasing. In figure 5.5d the peak at 47° is nearly as strong as the peak at -85° but is caused by the fact that the sensor spacing is greater than $\lambda/2$ for 1228 Hz. Thus the Nyquist criterion is violated and aliasing occurs. The other small peaks evident in 5.5b,c, and d, especially near -20° in figure 5.5c are due to aliasing effects caused by the sub-aperture spacing. In this case the sub-apertures are not overlapped and the phase centers are 4.5 m apart.



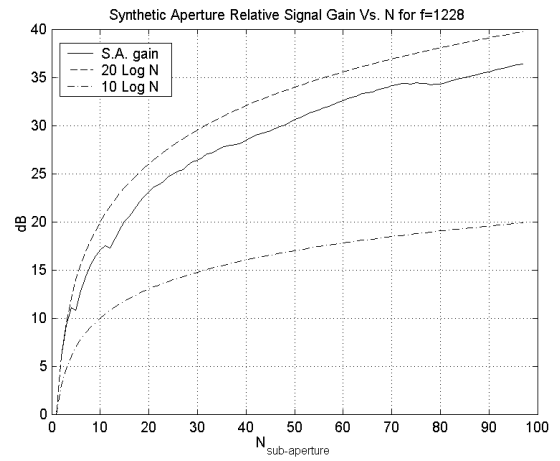
(a)



(b)



(c)



(d)

Figure 5.1: Relative array signal gain during the 15 SEP 2005 Experiment. (a) RASG for 635 Hz, (b) RASG for 823 Hz, (c) RASG for 1031 Hz, (d) RASG for 1228 Hz.

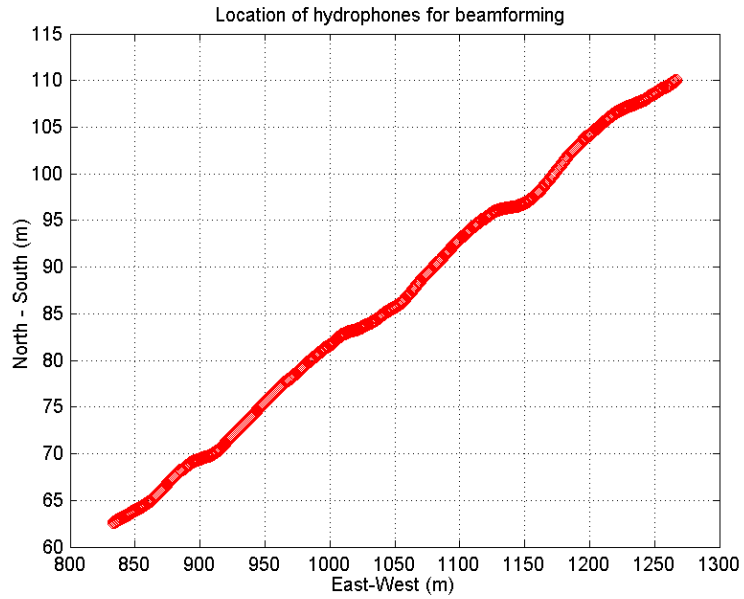


Figure 5.2: Path of the vehicle during the synthetic aperture trial on 15 SEP 2005 showing the locations of each hydrophone in the synthetic aperture with a circle. No overlap was used and the array progresses from lower left to upper right in time.

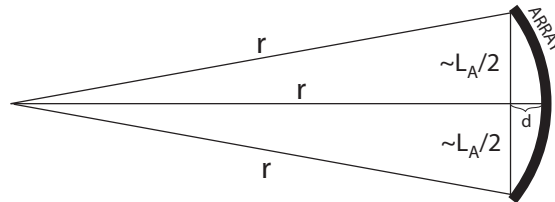


Figure 5.3: Schematic of a curved array showing the radius of curvature, r , chord height, d , and array length, L_a .

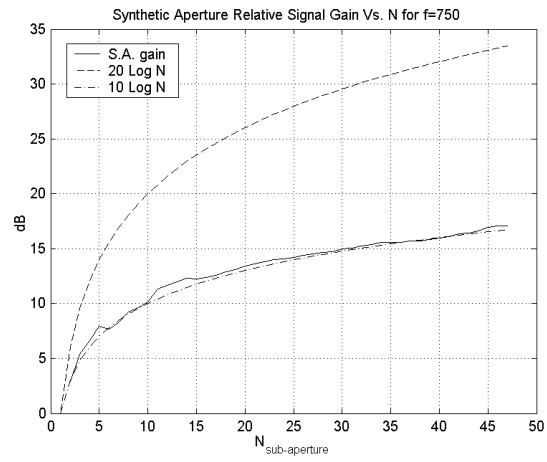
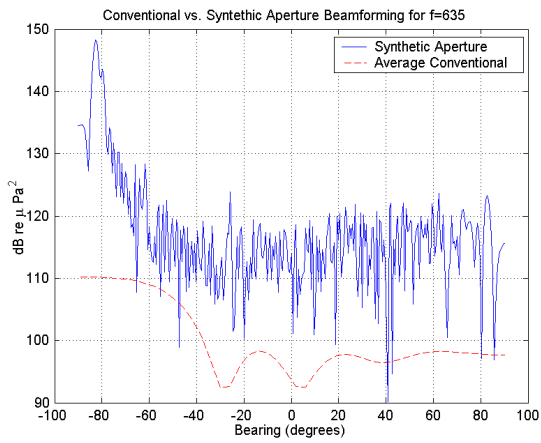
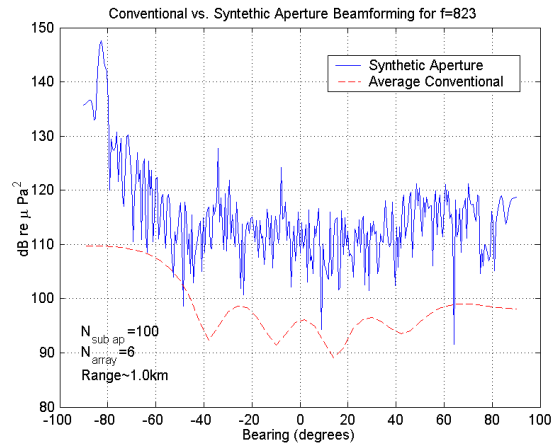


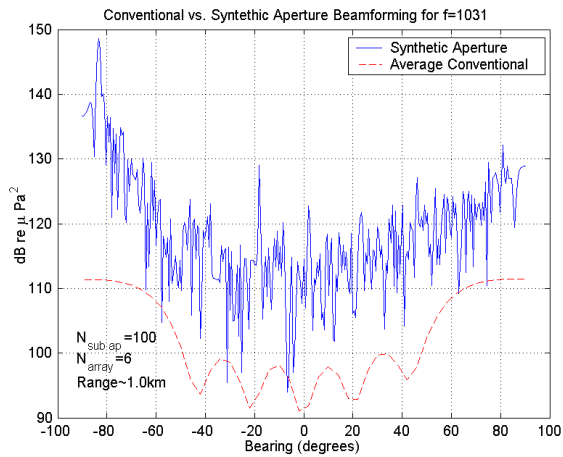
Figure 5.4: Relative array noise gain for the 15 SEP 2005 experiment as a function of number of synthetic aperture sub-apertures.



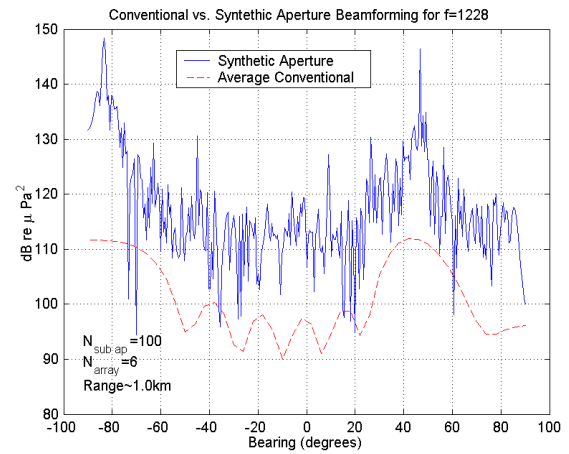
(a)



(b)



(c)



(d)

Figure 5.5: Synthetic aperture beamformer output compared to average conventional beamformer output from the 15 SEP 2005 Experiment. (a) 635 Hz, (b) 823 Hz, (c) 1031 Hz, (d) 1228 Hz.

Overlap processing

No overlap between sub-apertures was used in the beamforming results shown in the previous section. If an overlap is used as described in the synthetic aperture methods section, 2.3.2, with the method to determine the complex pressure as a function of range given in appendix E, then the received signal level as a function of range can be recovered. Figures 5.6 through 5.9 show for each of the signal frequencies the measured received signal level and the estimated wave-number spectrum. These wave-number spectra, as with all others in this work, are computed using a numerical quadrature approximation to the Hankel transform with the complex pressure data zero-padded to 6000 m. Details of the routine are given in the computer code in Appendix A. The reason for using a quadrature routine is that quadrature routines do not require a uniform spacing in range as Fourier routines do. If speed were critical, as is the case for on-board processing, the pressure vs. range would be interpolated onto a uniform grid and a fast Fourier transform (FFT) approximation to the Hankel transform would be used.

An important point to make is that the finite nature of the aperture in range results in the ability to resolve the modal amplitudes from the peaks in the Hankel transformed horizontal wavenumber output. This is derived in reference [89]. If the range were infinite and there were no noise sources, then the peaks in the spectra would extend to infinity and the measured output would be the Green's function as is given in equation (2.83). With a finite aperture, as the wavenumber approaches an eigenvalue of the modal equation ($k_r \rightarrow k_n$), the amplitude squared of the wave number spectrum approaches

$$|gg^*| = \left(\frac{(2\pi)^2 a_n^2 Z_n^2(z_0) Z_n^2(z)}{k_n} \right) \times R^2 \quad (5.8)$$

as is reported in section 2.3.1. Here R is the maximum range of the aperture. The component in the parenthesis is the modal amplitude squared and thus has units of pressure. Therefore, the units of the wavenumber spectrum output, $|gg^*|$ are $(Pa \cdot m)^2$. These are the units of a power spectral density with respect to the wavenumber. This is analogous to the

use of a power spectral density in the time domain with Fourier analysis. Normalizing by the range of the aperture will give the horizontal wavenumber spectrum in the units of Pa^2 and the spectrum is then a modal amplitude spectrum. For the remainder of this work the horizontal wavenumber spectra will be given as $|g(k)|$ to be consistent with previous works [89,91,98]. The units are then $Pa \cdot m$ and the peaks correspond to the modal amplitudes times the aperture range. The aperture range is explicitly given for each plot so that the reader can convert the results into units of pressure by simply dividing by the aperture range.

When the vehicle reached approximately 1860 m, the source was turned off but the system continued to record. Thus, the received signal level decreases to the ambient noise level at the end of the record. The results shown in figures 5.6 to 5.9 indicate that the signal to noise ratios out to 1900 m were nearly 10 dB. While these results indicate very quiet transmission measurements, the horizontal wave-number spectra are noisy and it is difficult to distinguish individual modal peaks within the spectra. Each of the figures includes the output horizontal wavenumber spectrum from the Safari wave number integration code using the geo-acoustic profile from Chapter 4 and a water depth of 13.5 m. In figure 5.6 it is clear that the individual modal peaks are correctly recovered, but each of the peaks is very broadly distributed about the value predicted by Safari.

Figure 5.10 shows the bathymetry reported by the vehicle for the this data set. At close ranges, as was mentioned in Chapter 4, the depth is 10.5 and quickly increases to the approximately flat 13.5 m depth. Since the modal eigenvalues are very strongly affected by the water column depth and since the source is in 10.5 m of water while the rest of the course is in 13.5m of water, it is expected that the measured wavenumbers will be an average of the wavenumbers for 10.5 m and 13.5m. The expected wavenumber from Safari for the first mode at 635 Hz is $2.605 m^{-1}$ in 10.5 m water, and $2.615 m^{-1}$ in 13.5 m of water. Thus, the broad peaks are caused by the range dependence of the bathymetry.

In addition to the change in wavenumber, the modal amplitudes are affected by a change in depth since the modal amplitudes are proportional to $Z(z)Z(z_0)$, the mode function at

the receiver times the mode function at the source. At the higher frequencies there are more propagating modes with closely spaced eigenvalues as is seen in the bottom panels of figures 5.7, 5.8, and 5.9. Changes in modal amplitudes and eigenvalues due to bathymetry thus causes the measured horizontal wavenumber spectral peaks to blend together and it is difficult to distinguish the modal amplitudes for the frequencies of 823, 1031, and 1228 Hz. This is seen in the center pane of figures 5.7, 5.8, and 5.9. An interesting observation is made in figure 5.8 where there is a peak in the spectrum near 4.37 m^{-1} . This peak is not aliasing and is in fact coherent noise contamination from vibrations of the vehicle propellor. In chapter 3 the noise from the vehicle was characterized and there was a peak in the radiated noise level near 1 kHz. This supports the measured noise contamination.

Despite the uncertainties in source level due to problems with the source and the range dependence caused by the local shallow region, figure 5.11 shows good qualitative agreement between the measurements and a parabolic equation model using a range dependent depth based on the bathymetry reported by the vehicle in figure 5.10. A low order mode beating pattern is easily observed while the finer interference patterns caused by higher modes seem to be lost. In this comparison the source levels were adjusted to get good agreement. Original source level estimates gave the source level as 148 dB re $1\mu\text{Pa}@1\text{m}$ for all frequencies. The adjusted source levels were 138.3, 138.5, 138.8, and 138.2 dB re $1\mu\text{Pa}@1\text{m}$ for 635, 823, 1031, and 1228 Hz respectively. The 10 dB discrepancy between reported and adjusted source levels can be explained by the fact that the flex-tensional source used here (see appendix F) was discovered during post-experiment calibration to be broken in such a way that the radiating components were not operating in phase. This could have caused the source to be directional. If the source were directional, the horizontal wavenumber estimates are further explained. At low frequencies, the dimensions of the transducer would limit the directionality and the results would be as expected. This is seen in figure 5.6. At higher frequencies, the source would become more directional which would result in some modes not being excited and other modes having unexpected modal amplitudes. This would explain the poor comparison between modeled and measured wavenumber spectra

Received signal level and horizontal wavenumber spectrum for 15 SEP 2005, $f=635$ Hz

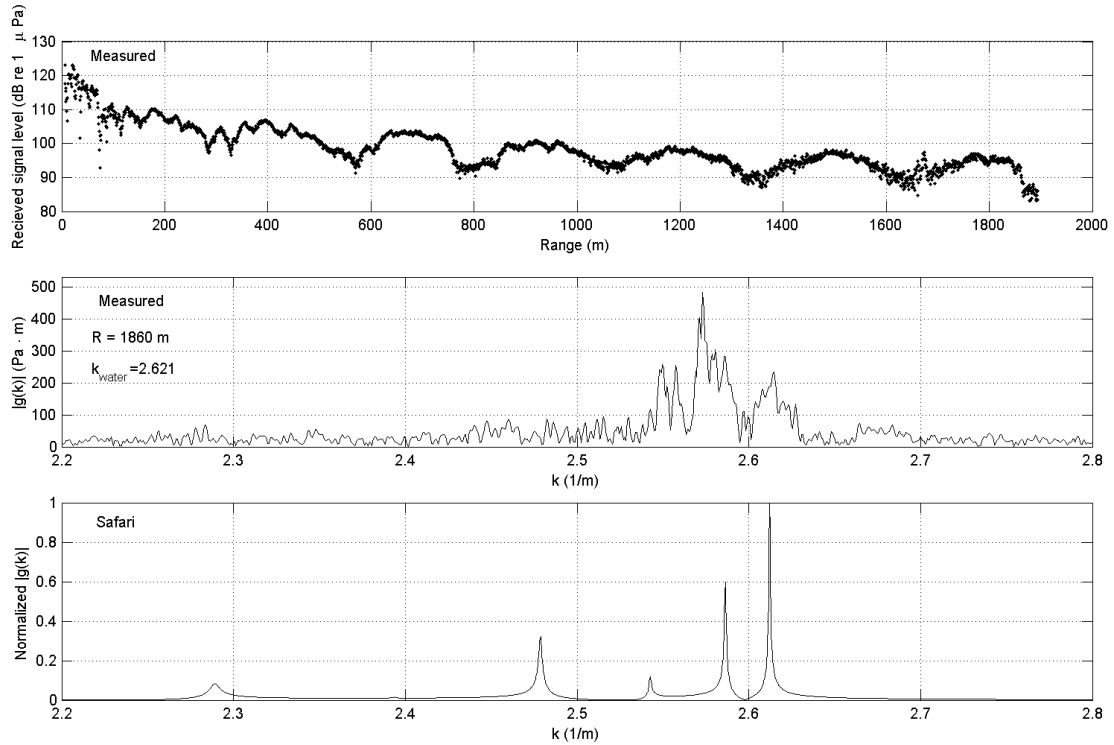


Figure 5.6: Received signal level vs. range and estimated wave number spectrum for 635 Hz, 15 SEP 2005. The top pane is the measured received signal level as a function of range. The center pane is the computed horizontal wavenumber spectrum from the measured pressure vs. range. The bottom pane is the horizontal wavenumber spectrum reported by Safari.

in figures 5.7 through 5.9 as well as the lack of higher mode interference patterns in figure 5.11.

Because the estimated source levels are based on agreement between measurement and calculation, and due to the short 2 km range, the range averaged transmission loss results from data set were not used for determining the attenuation. If a longer aperture were available, the relative decrease in level as a function of range beyond 1 km could have been used to infer the attenuation based on the work of Rozenfeld *et al.* [39].

Received signal level and horizontal wavenumber spectrum for 15 SEP 2005, $f=823$ Hz

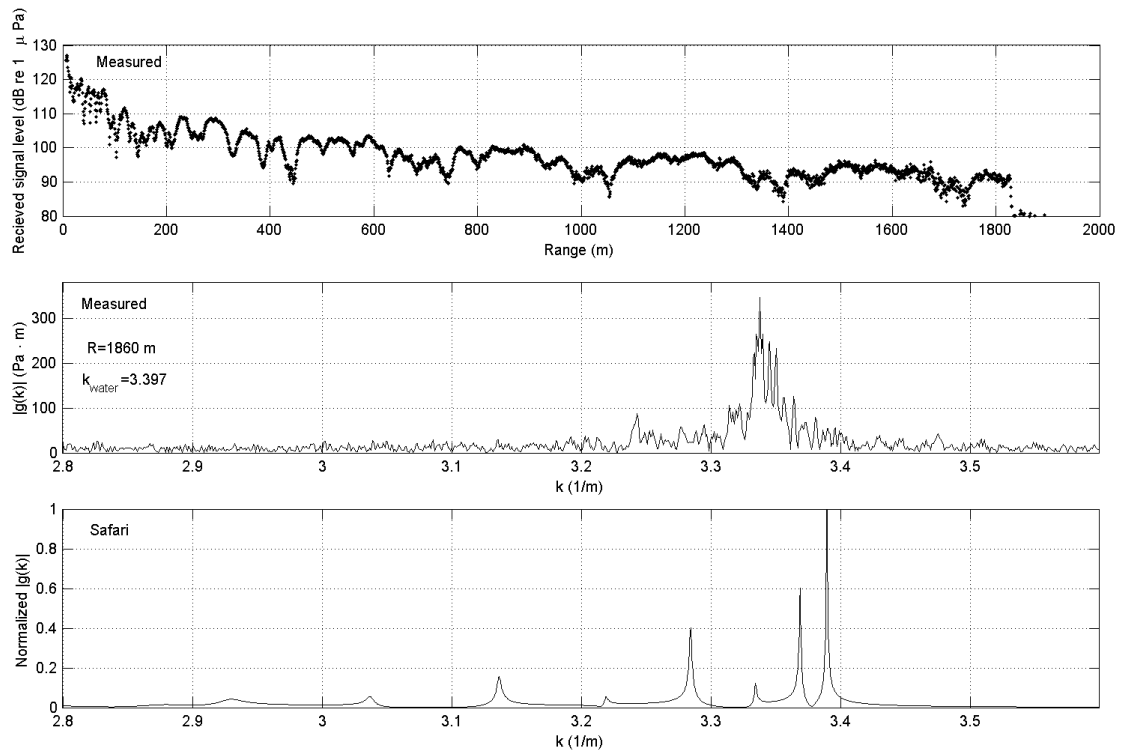


Figure 5.7: Received signal level vs. range and estimated wave number spectrum for 823 Hz, 15 SEP 2005. The top pane is the measured received signal level as a function of range. The center pane is the computed horizontal wavenumber spectrum from the measured pressure vs. range. The bottom pane is the horizontal wavenumber spectrum reported by Safari.

Received signal level and horizontal wavenumber spectrum for 15 SEP 2005, $f=1031$ Hz

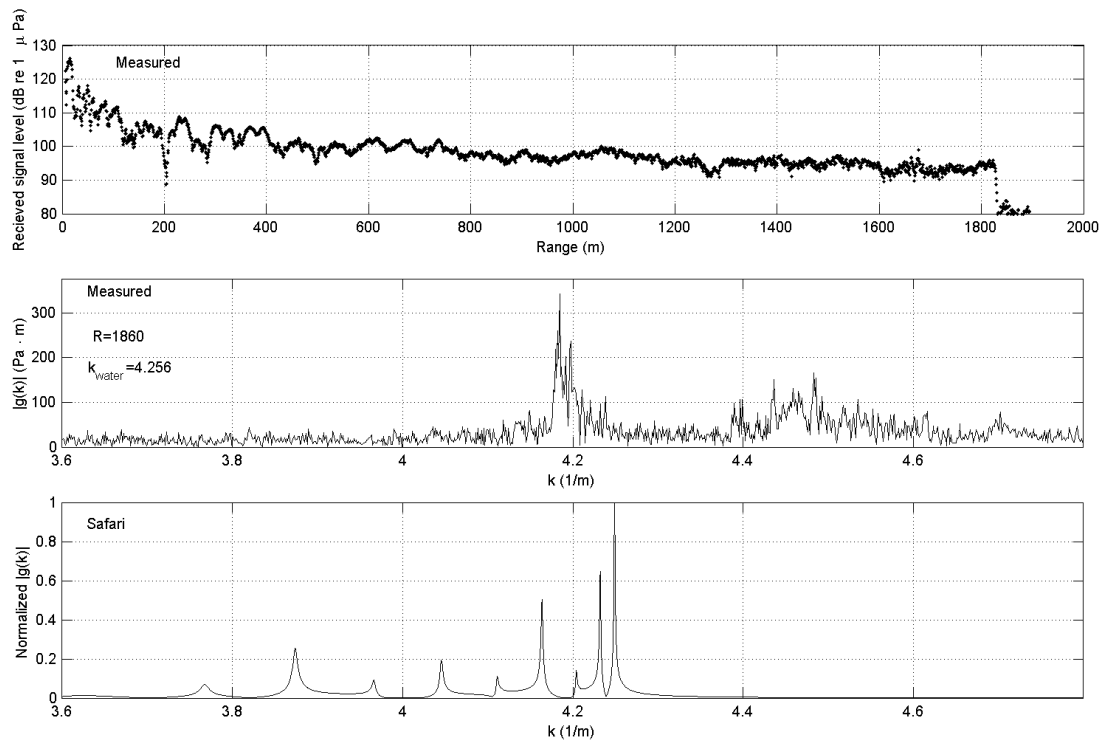


Figure 5.8: Received signal level vs. range and estimated wave number spectrum for 1031 Hz, 15 SEP 2005. The top pane is the measured received signal level as a function of range. The center pane is the computed horizontal wavenumber spectrum from the measured pressure vs. range. The bottom pane is the horizontal wavenumber spectrum reported by Safari.

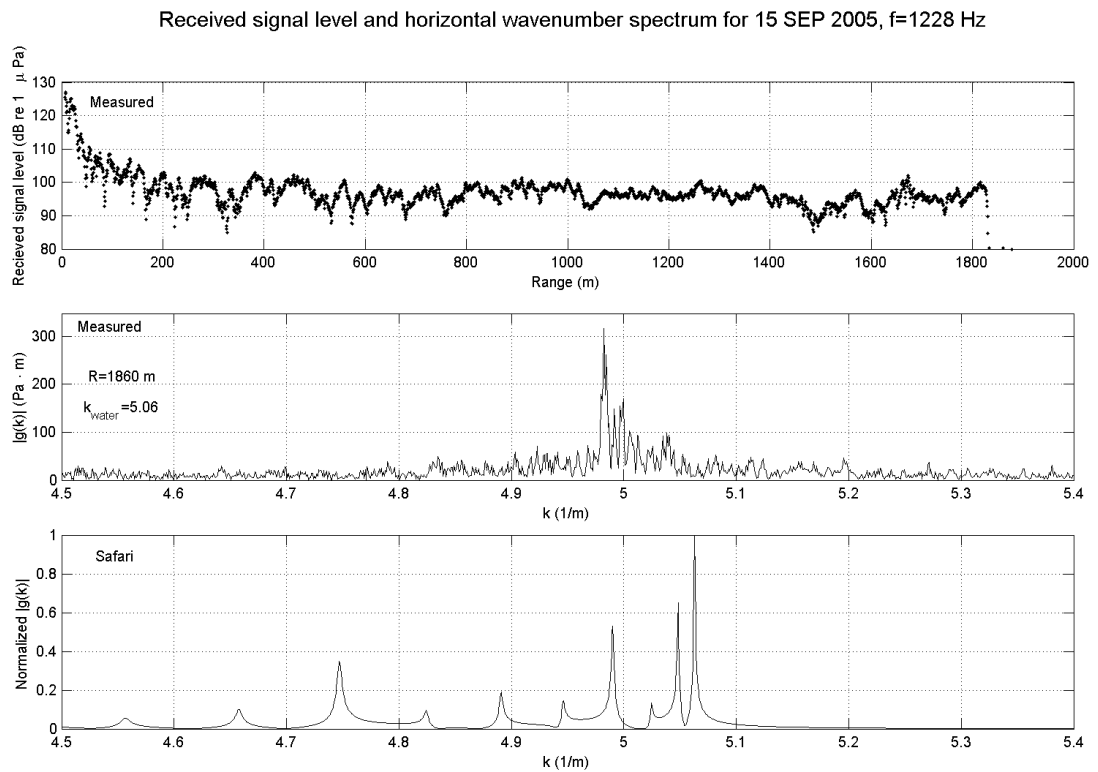


Figure 5.9: Received signal level vs. range and estimated wave number spectrum for 1228 Hz, 15 SEP 2005. The top pane is the measured received signal level as a function of range. The center pane is the computed horizontal wavenumber spectrum from the measured pressure vs. range. The bottom pane is the horizontal wavenumber spectrum reported by Safari.

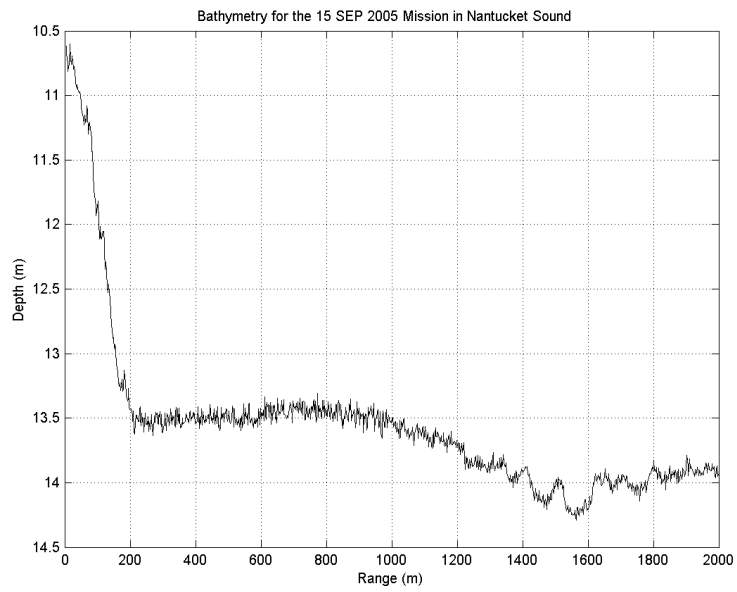


Figure 5.10: Bathymetry reported by the AUV for 15 SEP 2005.

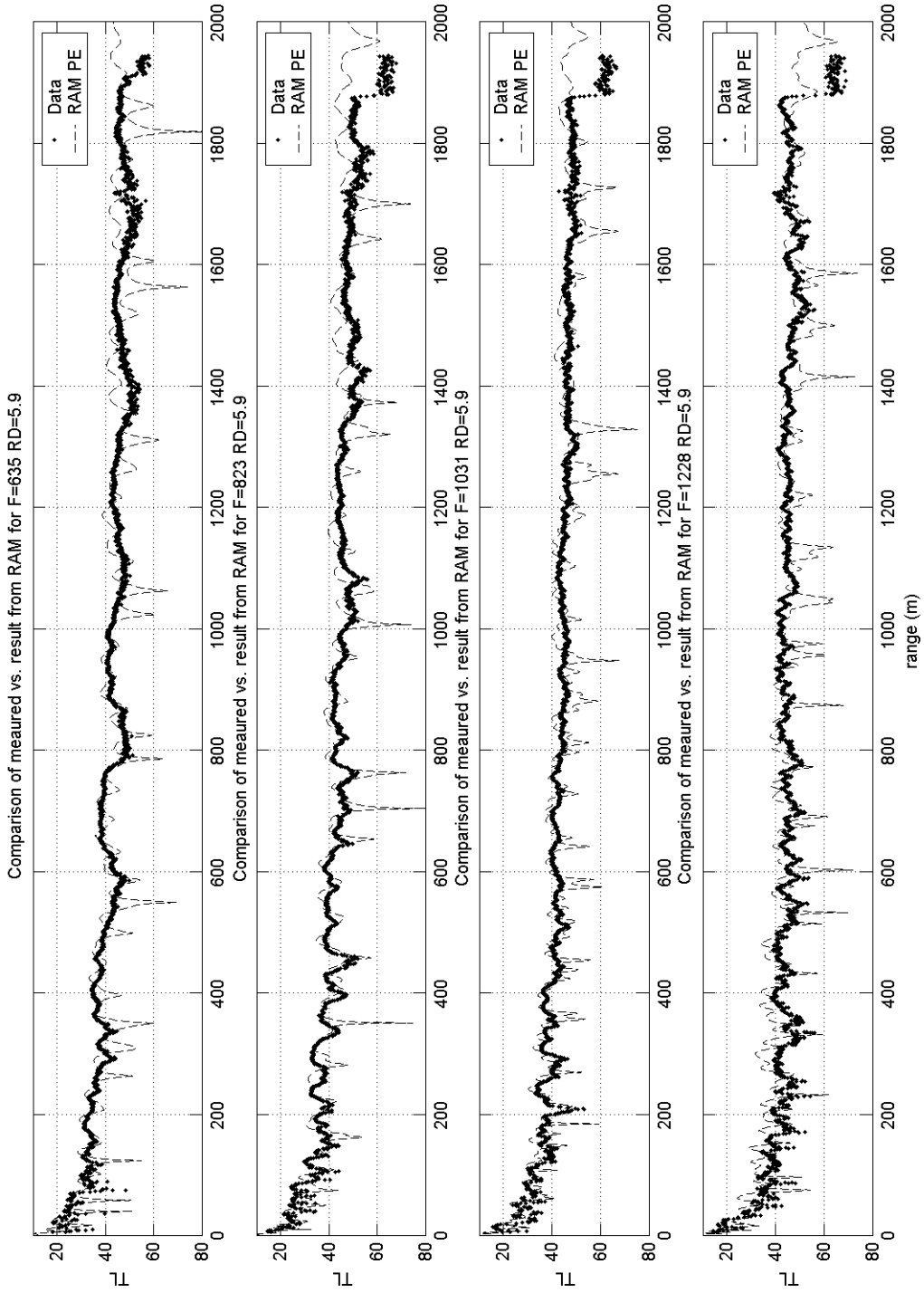


Figure 5.11: Transmission loss measured compared to RAM for 15 SEP 2005 for each frequency. The source levels were adjusted here due to source level uncertainties, but the qualitative agreement is good using a range dependent depth in RAM.

5.3 December Experiment

In December of 2005, the experiment was repeated at the same site with essentially the same path. The mission geometry is shown in figure 4.16. During this experiment, however, the problems associated with the September experiment were avoided. The source deployment and mooring were simplified in this experiment and the ship was moored in 13 m of water. This avoided the steep bathymetry feature seen in the September experiment. Further, the source was deployed without an anchor to eliminate the possibility of damaging the source due to anchor tension. The depth of the source was set by measuring the amount of cable payed out and a small depth recorder was attached to the the source to accurately monitor the source depth. Since the source was characterized as omni-directional (see appendix F), monitoring of the output from the reference hydrophone at 1 meter and the input voltage levels for each tone allowed for the accurate determination of the correct source levels when the calibrated transmit voltage response of the source was used. The software problem was fixed by vehicle optimization so the vehicle was able to complete the return trip. When the vehicle turned around and began its course back to the ship, the source operator was notified by an acoustic modem message from the vehicle. At this point the source frequencies were changed, but 635 Hz was kept as a control frequencies between both data sets.

The frequencies used and the source levels are given in table 5.1. During the Frisk-Lynch-Rajan experiment [91] the source frequencies were 140 Hz and 220 Hz. For comparison reasons, the intent was to use these frequencies and extend the data set to higher frequencies. Examination of table 5.1 shows that the source level at 220.5 Hz was about 10 dB lower then the source level at 415 Hz, and almost 20 dB lower then the source levels for all of the other frequencies. This was due to a fall off in the source response at low frequencies. For the same reason, use of 140 Hz was abandoned due to very low source level.

Table 5.1: Source frequencies and levels for 10 DEC 2005. The source was a Navy HX-188 source (see Appendix F) configured as shown in figure 4.2.

Frequency (Hz)	Vehicle Direction	SL (dB re $1\mu Pa@1m$)
220.5	Outbound	139.4
415	Outbound	149.8
635	Outbound	156.7
635	Inbound	159.4
823	Inbound	159.0
1031	Inbound	155.2
1228	Inbound	156.0

5.3.1 Signal Processing

Between the September and December experiments, the vehicle was optimized to maintain depth and course with less control surface contribution. The shape of the array was estimated in an earlier test described in section 3.3.3 and shown to have a slight curvature. As this could also affect the array performance, the array was also re-balleted between the experiments to be straighter under tow. The signal processing results were therefore expected to show improvement beyond the high quality already demonstrated in the September experiments.

Array gain

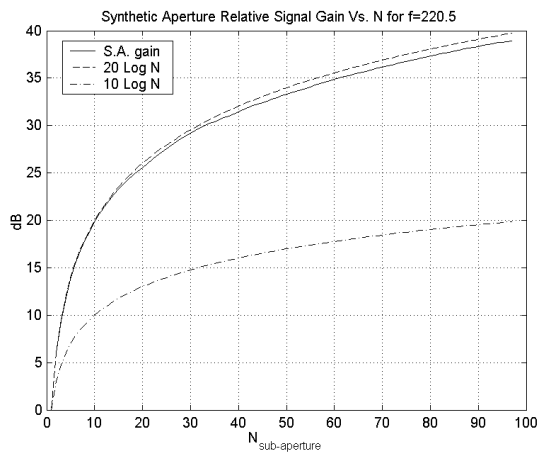
As was done in the previous section, the relative array signal gain was compared to the theoretical limits for a coherent and incoherent signal as a function of the number of sub-apertures on a synthetic aperture formed with no channel overlap. The results are shown in figure 5.12 for the outbound leg and figure 5.13 for the inbound leg. The gain results for the inbound leg show no decreases in gain like those seen in the September data set, which were shown to be caused by array motion. The gain degradation was less than 1 dB from the theoretical limit out to 100 sub-apertures. This corresponds to longitudinal coherence lengths longer than 33λ , 62λ , and 95λ for frequencies of 220.5 Hz, 415 Hz, and 635 Hz respectively at a range to depth ratio of approximately 100. For the inbound leg

the vehicle path over which the array was formed had some undulations which are evident in the reduction in achieved gain in figure 5.13. For the case where the gain is limited by array motion, the highest frequencies are affected the most. In this case the 1228 Hz gain output shows a 3 dB degradation in gain at 15 sub apertures. This corresponds to a synthetic aperture that is 55λ long for a physical aperture of 3λ . In fact, for all frequencies the achievable synthetic array length with 3 dB or less gain loss was on the order of at least 20λ .

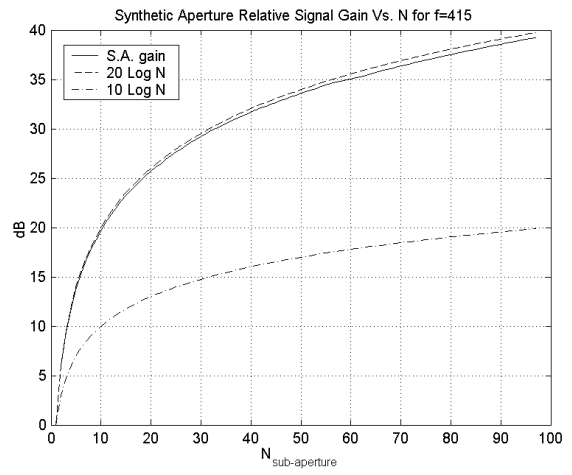
Figures 5.14 and 5.15 show the synthetic and conventional beamformer outputs for the same inbound and outbound tracks used in the gain plots. Again, these results use corrected navigation data and show the expected decrease in beam width with increased aperture. Bearings are defined such that behind the vehicle corresponds to -90° , broadside corresponds to 0° and forward corresponds to $+90^\circ$. Figure 5.14 shows the beamformer output for the case when the array is moving away from the source and the frequencies are 220.5, 415, and 635 Hz. In this case the source is nearly directly behind the vehicle and is tracked with the array as being at -85° . The peak of the synthetic output for 220.5 Hz is shown in 5.14a. In this case the signal to noise ratio was relatively low and random fluctuations of the phase due to noise broadened and distorted the main beam response which is shown at -80° . The synthetic aperture result shown in 5.14, however, shows remarkable improvement over the average conventional output in which the direction to the source is only identified within 60° to either side of endfire.

Figure 5.15 shows the beamformer output for the experimental leg in which the vehicle is moving towards the source and the frequencies are 635, 823, 1031, and 1228 Hz. In this case the source is nearly directly in front of the vehicle and should appear near $+90^\circ$. All frequencies on this inbound leg report the peak signal level at $+85^\circ$, the error being due to navigational error as discussed before. Figures 5.15c, and d show the results for 1031, and 1228 Hz, which exhibit strong grating lobes at -57° and -34° respectively. These grating lobes are due to the fact that the sensor spacing is 0.75 m. In this experiment the sound speed in the water was measured to be 1467 m/s while in September the sound speed

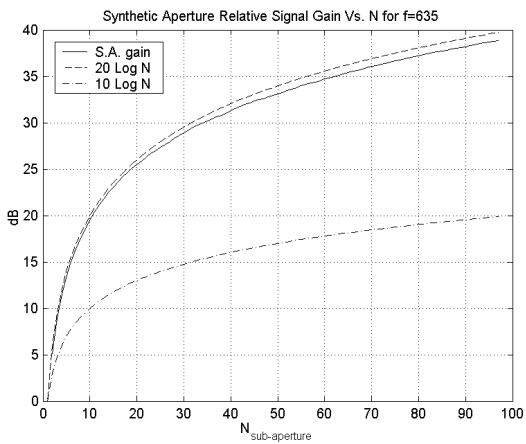
was approximately 1522 m/s. Because of this, the array response in December for 1031 Hz exhibited aliasing while in September the wavelength was close enough to the Nyquist criterion that aliasing was not seen. Figures 5.15 b,c, and d, also show the aliasing effects caused by the 4.5 m separation of the sub-apertures with smaller grating lobes. In 5.15b these are seen at roughly $+38^\circ$, $+14^\circ$, -9° , and -33° .



(a)

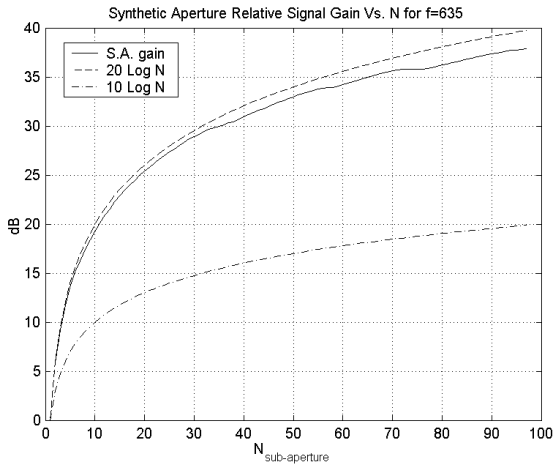


(b)

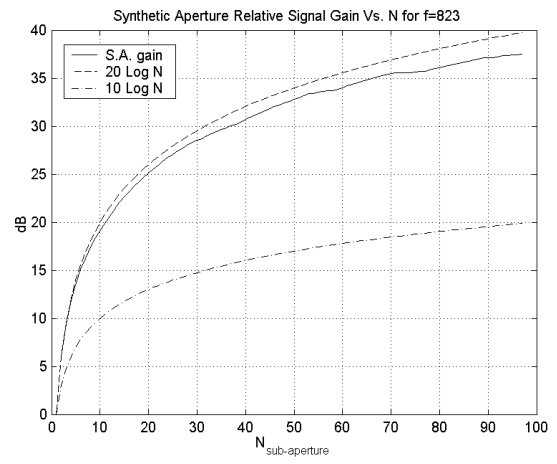


(c)

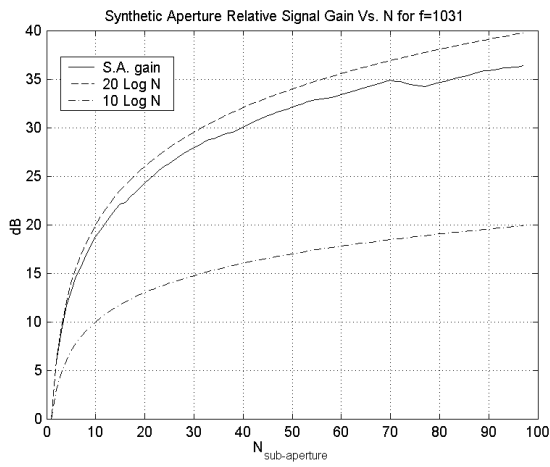
Figure 5.12: Relative array signal gain during the outbound leg of the 10 DEC 2005 Experiment. (a) RASG for 220.5 Hz, (b) RASG for 415 Hz, (c) RASG for 635 Hz.



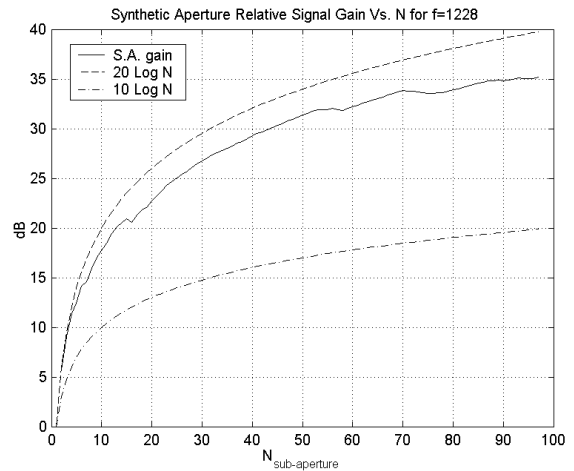
(a)



(b)

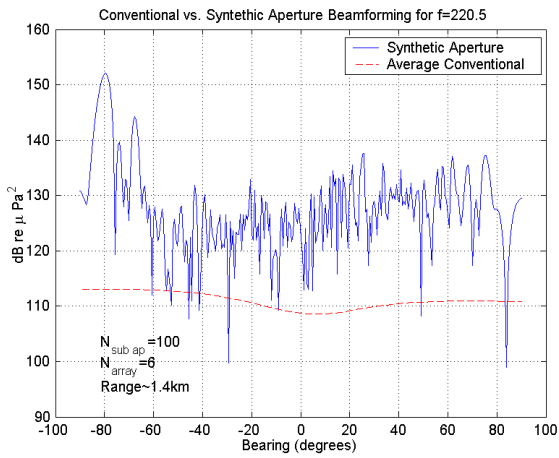


(c)

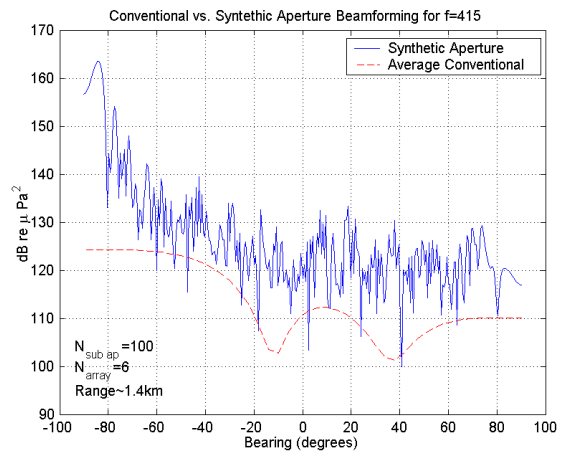


(d)

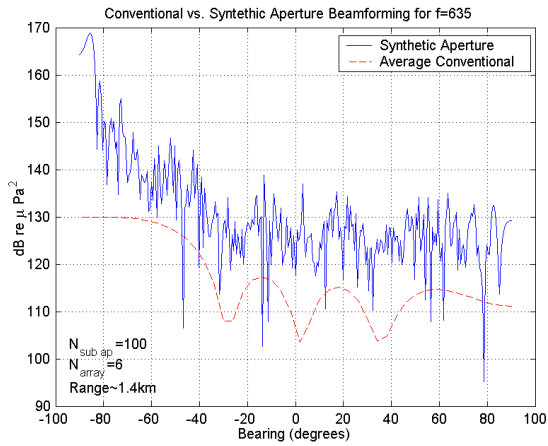
Figure 5.13: Relative array signal gain during the inbound leg of the 10 DEC 2005 Experiment. (a) RASG for 635 Hz, (b) RASG for 823 Hz, (c) RASG for 1031 Hz, (d) RASG for 1228 Hz.



(a)

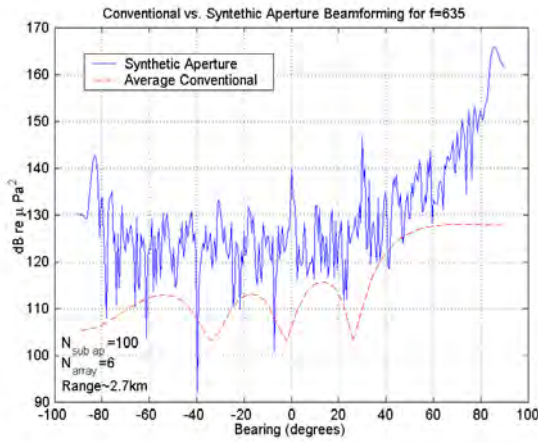


(b)

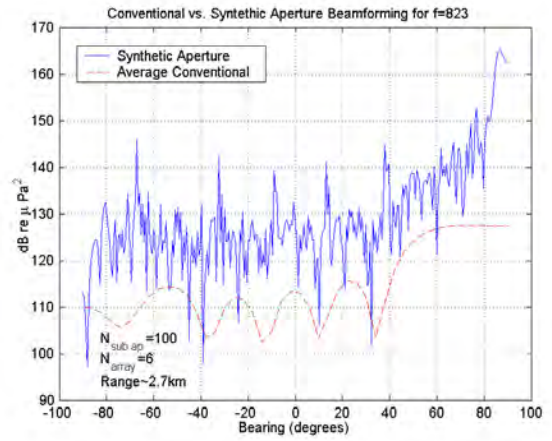


(c)

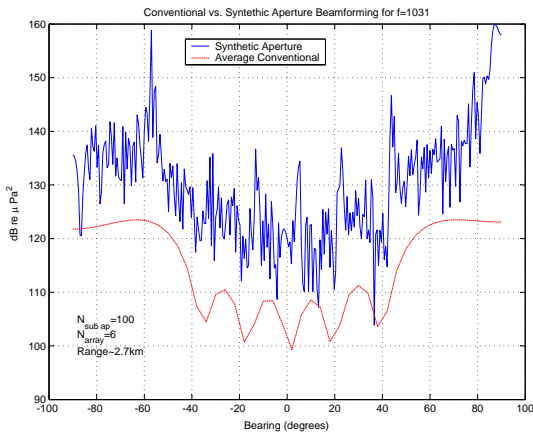
Figure 5.14: Synthetic aperture beamformer output compared to average conventional beamformer output from the outbound leg of the 10 DEC 2005 Experiment. (a) 220.5 Hz, (b) 415 Hz, (c) 635 Hz.



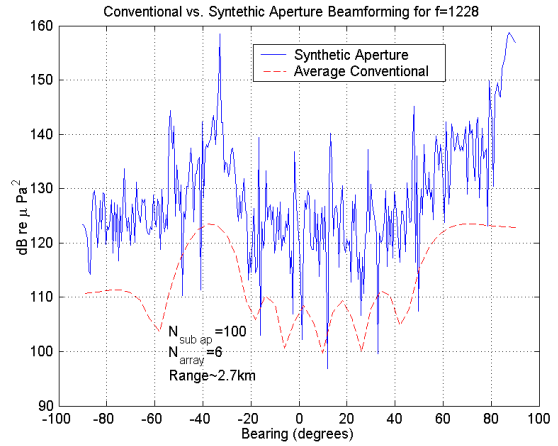
(a)



(b)



(c)



(d)

Figure 5.15: Synthetic aperture beamformer output compared to average conventional beamformer output from the inbound leg of the 10 DEC 2005 Experiment. (a) 635 Hz, (b) 823 Hz, (c) 1031 Hz, (d) 1228 Hz.

Overlap processing

Overlap processing was again used to find the complex pressure as a function of range. One of the advantages of overlap processing is that the signal to noise ratio is improved. At the higher frequencies, the signal to noise ratio was not a problem, but at 220.5 Hz the low source level caused the signal to noise ratio on any single channel to decrease to 0 dB near 1500 m away from the source. Overlap processing allowed for the reconstruction of the coherent signal out to 4 km as is shown in figure 5.16. In the top pane of the figure the received signal level as a function of range is plotted for the case where there is no overlap and thus each data point is taken from a single measurement on a single hydrophone. The bottom pane uses the overlap method shown in figure 2.6 for which each data point is the average of six measurements of the complex pressure on six different hydrophones as they pass through the same location. The improvement is clear and the modal interference pattern, which is not recognizable without overlap processing, is recovered. The increase in the received signal level near 2.2 km is the result of a passing high speed ferry.

The Frisk-Lynch-Rajan experiment [91] used only a single receiver at each location, so the improvement in measurement quality by the AUV system is made clear here. In addition to the improvement in the time to perform the experiment, the signal to noise ratios were improved from the single receiver method. This is shown explicitly for the 220.5 Hz case in which such an improvement was critical due to low source level, but the same improvement applies to all of the frequencies used. Since the signal to noise ratios were relatively good for all of the other frequencies, the comparison of non-overlapped to overlapped data for frequencies other than 220.5 Hz is not very illustrative and is therefore omitted. The transmission loss results ($TL = SL - RSL$) using overlap processing are shown later.

Comparison of complex pressure vs. range with and without overlap processing

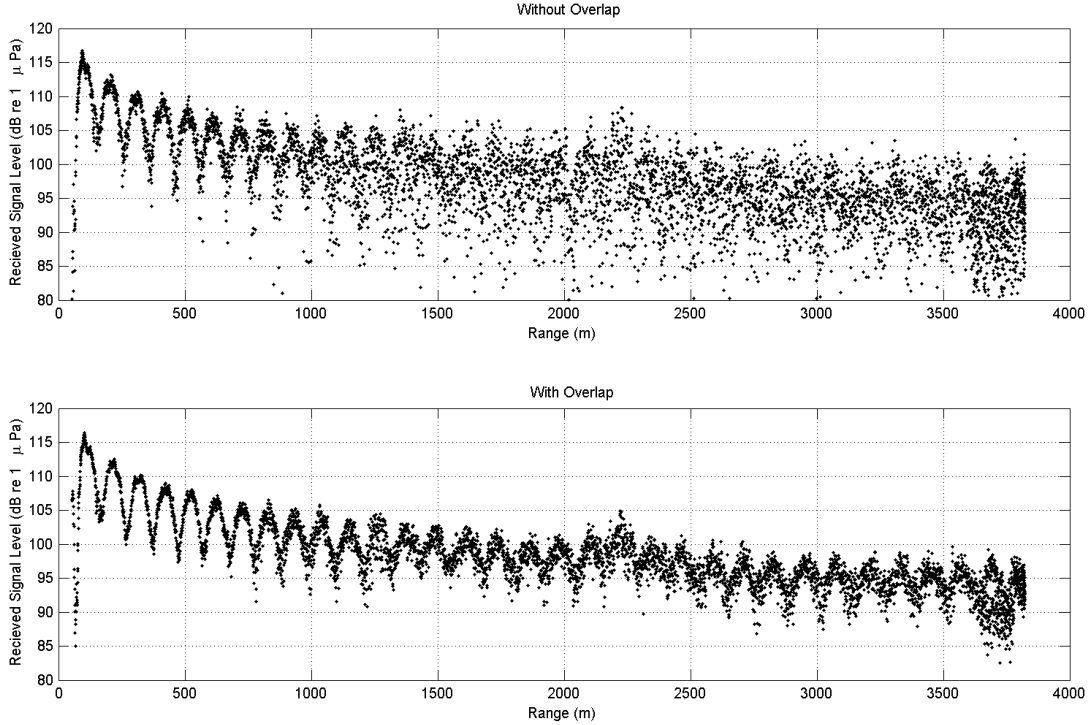


Figure 5.16: Measured received signal level vs. range at 220.5 Hz with and without overlap processing. The modal interference that is clearly visible with overlap processing is not recognizable without it.

5.3.2 Hankel Transforms

Range error

The waveguide characterization method described in section 2.3.1 requires that the horizontal wave-number spectrum be found for each frequency by implementation of the Hankel transform. The first test to make sure that the system was performing well was to take advantage of the fact that 635 Hz was used in the outbound and inbound leg and compute a Hankel transform for each direction. If the system were working properly and the waveguide was unchanged in the time between going out and coming back, then the modal eigenvalues would be identical for the two legs. Figure 5.17 shows the estimated wave-number spectra for 635 Hz outbound and inbound using the navigational data from the

vehicle and the source GPS. In both cases there appears to be a dominant first mode and some less dominant modes with lower wavenumbers, but the wavenumber associated with the first mode is clearly different for the two directions. In order to be able to compare the spectra, the complex pressure between 2500 m and 3700 m was used and zero padded down to 0 m and out to 6000 m. This range region was chosen because there is uncorrupted data for both the inbound and outbound course over this range. Since the data set is so far from the source, the higher order modal peaks are strongly attenuated and thus difficult to distinguish. The first mode is, however, obvious.

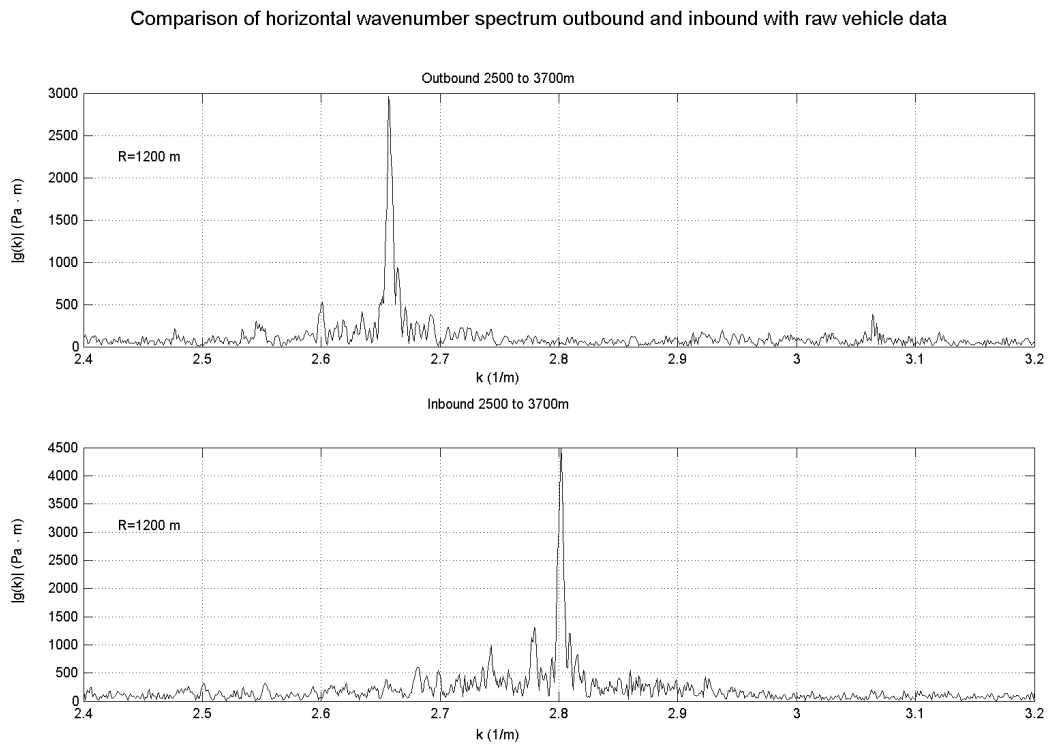


Figure 5.17: Comparison of estimated wave number spectrum for 635 Hz on the outbound and inbound leg of the 10 DEC 2005 experiment without range correction. The value of R given is the transform aperture.

One convenient property of the Hankel transform is that it, like all other integral transforms, is a linear operator. Thus, a small error in the range separation ΔR between points will cause a linear shift in the wavenumber space by the exact same percentage with

the opposite sign³. That is,

$$\frac{\Delta R}{R} = -\frac{\Delta k}{k}. \quad (5.9)$$

The modal eigenvalue for the first mode, however, changes little for a perturbational change in the bottom properties. It is much more sensitive to the water column properties, which are known. Therefore a normal mode program, Kraken in this case, could be used to estimate the expected wavenumber for the first mode and the navigational error could be estimated by comparing the measured to the calculated wavenumbers. While this is a simple and useful technique for performing long range navigational error corrections, it would not be appropriate to use the calculated wave-number spectra to correct the measured wave-number and then compare the measurements to calculations.

Four navigation correction schemes, including the wavenumber method, are as follows:

The wavenumber method: Since the Hankel transform is a linear operator and the water column properties are known, the percent error given by the measured wavenumber compared to the expected wave number will be the negative percent error in the range. This method requires that the system can record the complex pressure received for a known frequency as the system moves away.

The comparison method: If a more accurate navigation tool is available, the navigation data can be compared to this more accurate tool and corrected accordingly. In this case, when the vehicle is on the surface it can acquire its position by GPS. This information is not available while submerged due to the attenuation of electromagnetic waves in the water. While the vehicle is submerged it therefore navigates by another means, in this case the less accurate dead reckoning method. Comparing the estimated position by dead reckoning to the reported position by GPS at the beginning and end of the mission can give an estimate of the average navigation error. This method of course requires access to a more accurate navigation tool.

³The opposite sign comes from the fact that wavenumber and range are in a sense reciprocal.

The bathymetry method: If the vehicle retraces a path that it took earlier and has a system to measure the bathymetry, then comparison of the estimated position of known bathymetry features can yield an estimate of the navigation error. Features which depend on the exact water depth should be avoided due to tides, but features such as the location of the beginning of a slope, or the location of a ridge line can be useful. This method requires the ability to measure and record the bathymetry as well as the presence of distinguishing bathymetry features.

The doppler method If the vehicle is navigating in a known direction relative to a source of sound with a known frequency and the vehicle system has the capability to estimate the received signal frequency, then the true velocity can be determined according to

$$v = -c\left(\frac{\omega'}{\omega} - 1\right)/\sin(\theta) \quad (5.10)$$

where c is the speed of sound, ω' is the received frequency, ω is the source frequency and θ is the angle to target. In general the doppler frequency is given as

$$\omega' = \omega\left(1 \mp \frac{v}{c} \sin \theta\right) \quad (5.11)$$

where a minus is for a relative motion of the receiver away from the source and a plus is for a relative motion of the receiver towards the source. If, however, velocity is defined as positive for the motion away from the source, then (5.10) holds. If the vehicle is also navigating by dead-reckoning and thus integrating its estimated velocity, the percent error in the estimated velocity given by the vehicle compared to the velocity given by doppler will give the percent navigation error.

Conveniently, with this system and experimental geometry, the requirements of all four methods are satisfied. As shown earlier, the wavenumber spectra can be estimated from the measurements and the properties of the water column and approximate properties of the bottom are known. The same acoustic data used to find the wavenumber spectrum

can be used to estimate the doppler shift. Further, the vehicle has a GPS receiver and records the GPS as well as dead reckoning navigational data. Finally, the vehicle also doubles back on the same track during this experiment and records the bathymetry. This bathymetry is shown as a function of estimated range in figure 5.18. The vehicle starts at close range, proceeds on the outbound track to nearly 4 km, turns around and proceeds along the same track back to the origin. Clearly the depth of the shallow feature at a range close to the origin changed during the course of the experiment due to a tidal change. This tidal change is consistent with the data from the ship's depth sounder which reported a tidal depth variation of 0.1 m during the course of the experiment. The location of the peak near 600 m range and the trough near 1600 m range, however, should be the same for the inbound and outbound leg.

In figure 5.18 the bathymetry features appear to align well for the ranges beyond 2500 m. The reader is reminded, however, that the range error is an accumulating error and the vehicle turns around at 3700 m. Therefore, the traveled range between 2500 m outbound and 2500 m inbound is 2600 m. The percent error in navigation, however, has opposite signs for the inbound and outbound leg. Thus, the inbound and outbound portion in this range align well even though there is an error in the reported range. For this reason, it is desirable to use as many range corrections methods as possible to determine an average range error.

Using all four of these range correction methods, the average range error on the outbound leg was estimated to be 2.2 % of the range traveled. The error on the inbound leg was estimated to be 3.3%. Both errors were in the direction opposite to that of the vehicle motion and the true range could be determined by applying the errors to the accumulating range. More formally, if the range data set consists of range values r_i then one could construct a set of range differences,

$$\delta r_i = r_i - r_{i-1} \tag{5.12}$$

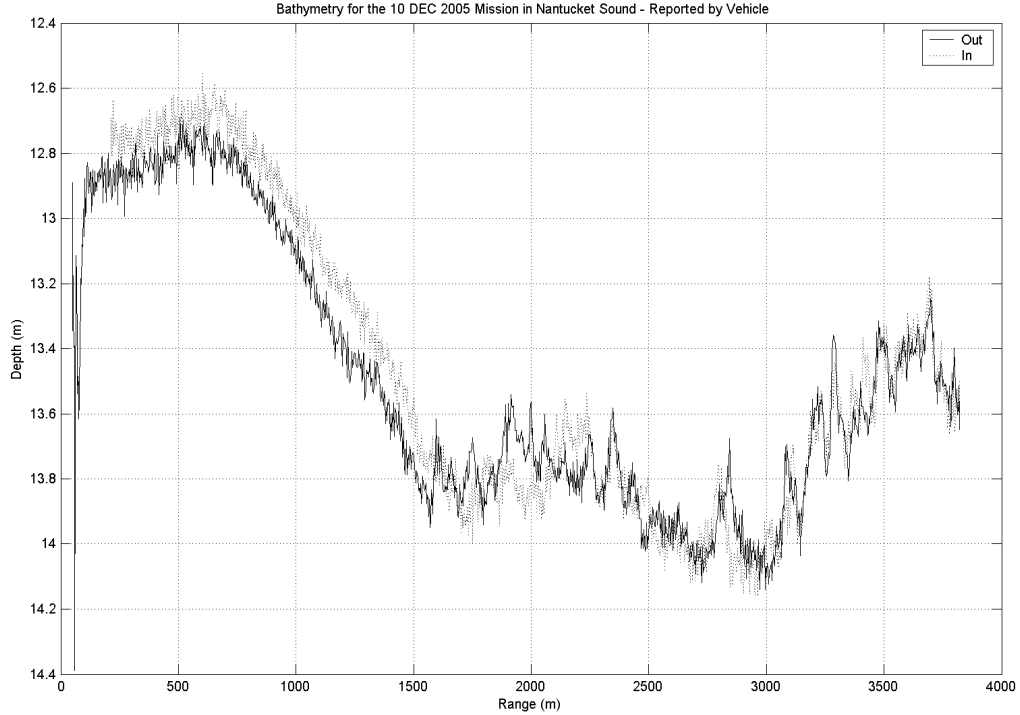


Figure 5.18: Bathymetry for the 10 DEC 2005 Experiment as reported by the vehicle. The features are not aligned on the outbound and inbound legs due to navigational error.

The true range, $r_{i\text{corrected}}$, is the sum of the corrected range differences,

$$r_{i\text{corrected}} = \sum_{j=1}^{j=i} \delta r_i (1 + p) \quad (5.13)$$

where $j = 1$ to $j = i$ and p is the percent error. In this case, $p = -.022$ for the outbound leg and $p = .031$ for the inbound leg.

The navigational correction mentioned earlier for the case of the beamformers can now be more formally addressed. Since a Fourier transform of the data was required for the beamforming operation, extension of the code to include an estimate of the Doppler shift was simple. This is done in the *get_array_p_quad_de2.m* routine given in appendix A. The routine simply returns the Doppler estimated velocity to be used in comparison to the vehicle estimated velocity.

Once the range corrections were applied to the range data, the Hankel transform was

again applied to the 635 Hz data set for both the inbound and outbound legs. The estimated wavenumber spectra using the corrected ranges are shown in figure 5.19. Clearly the modal wavenumber for the first mode is the same for both legs. Also, the higher order modes indicated by smaller peaks with lower amplitudes are visible and consistent between the legs.

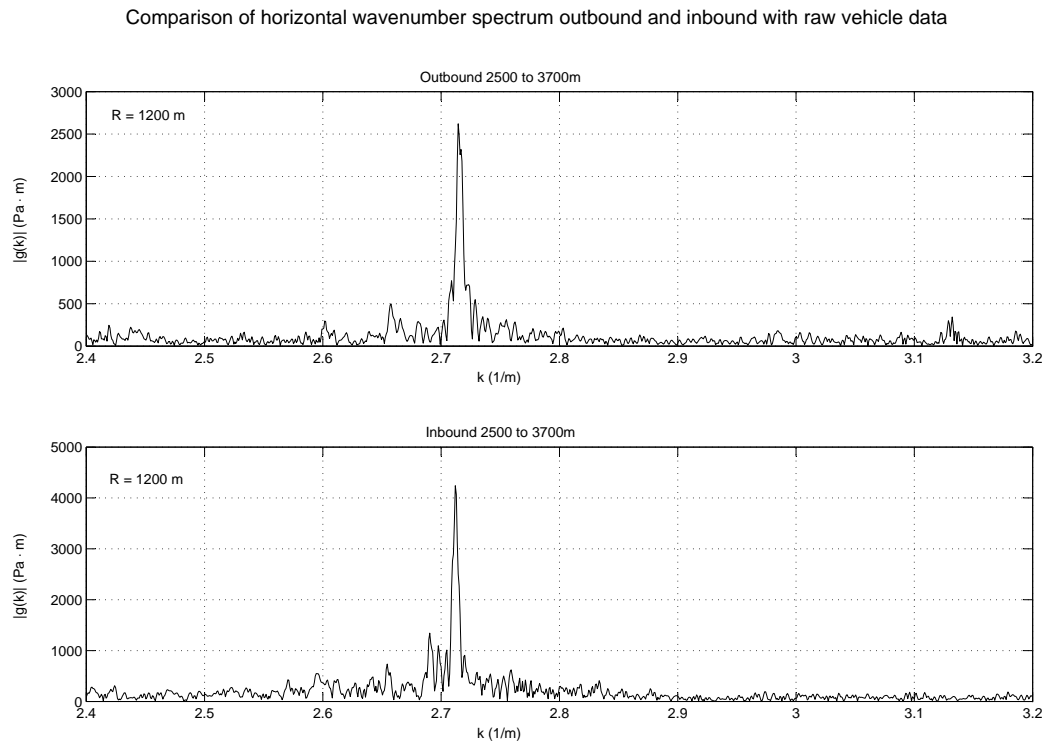


Figure 5.19: Comparison of estimated wavenumber spectrum on the outbound and inbound leg of the 10 DEC 2005 experiment with range correction. The value of R given is the transform aperture.

Range dependence

From the bathymetry plot in figure 5.18 it is clear that there is a slight range variation in the water column depth with range. To determine if this variation was reflected in the wavenumbers measured, the Hankel transform was performed on different sections of the data set. By using only the complex data in a range R_{min} to R_{max} , zero-padding the data out to 6 km, and performing a numerical Hankel transform, the wavenumber content for different regions can be measured. This was done for the case of 220.5 Hz and the results are shown in table 5.2. The regions chosen were based on the bathymetry data reported by the vehicle in figure 5.18 and coincide with regions of approximate constant depth and up and down sloping regions. From 0 to 700 m the depth is nearly constant, from 700 to 1700 m there is a gradual slope downward, from 1700 to 3000 m the depth is again nearly constant, and from 3000 to 3700 m the depth is gently decreasing. Measured wavenumbers are shown for the first and second mode and were determined by finding a local peak in the wave number spectrum. In regions such as 700 to 1700 m where the depth is continuously changing, the modal peaks split into several peaks due to the changing wavenumber with range. In these cases the reported wave number is the highest of the multiple peaks. Modal bifurcation caused by this bathymetry is shown later for the case of 415 Hz where it is easily visible.

The calculated values of the modal wavenumbers were determined using Kraken with the geo-acoustic profile given in Chapter 4. While there is a slight difference between the measured and modeled wavenumbers, the difference is roughly the same for all of the range intervals. Further, the case of 220.5 Hz had the worst signal to noise and thus the most effect of random phase fluctuations which would affect the resulting wave number estimates. The quality of the results using the geo-acoustic profile developed in Chapter 4 while changing only the bottom depth in the model indicates that the major range dependence in the experiment was caused by local depth variations and that the geo-acoustic model of the bottom should apply to all of the range intervals. Further, table 5.2 indicates that using

the mean depth value over the entire range from 0 to 3700 m is a reasonable approximation.

Table 5.2: Measured wavenumbers in different range sections for 220.5 Hz, 10 DEC 2005. The calculated wavenumbers are for the average depth in each range region. All depths and ranges are given in meters and wavenumbers are given in m^{-1} .

R_{min}	R_{max}	Bathymetry	Mean Depth	$k_{1,meas}$	$k_{2,meas}$	$k_{1,calc}$	$k_{2,calc}$
0	700	relatively flat	12.89	.9275	.865	.9247	.8593
700	1700	down slope	13.36	.9276	.871	.9258	.8644
1700	3000	relatively flat	13.84	.9296	.876	.9267	.8693
3000	3700	up slope	13.6	.9316	.877	.9263	.8669
0	Full Range	varying	13.5	.9296	.8772	.9261	.8659

Figures 5.20 to 5.22 show the measured transmission loss as a function of range as well as the estimated wavenumber spectrum from the measured data and the wavenumber spectrum calculated using Safari with the derived geo-acoustic model. All of the data sets were zero-padded out to 6 km and a quadrature Hankel transform routine was applied. Since peaks in the spectrum are difficult to pick out exactly, table 5.3 gives the estimated eigenvalues from the data as well as those computed using Kraken with the sediment profile described in Chapter 4. The eigenvalues computed using Kraken were compared to the peaks in the wavenumber spectrum calculated using Safari and the difference in calculated eigenvalues for the two programs were within rounding error. For reference, the transmission loss computed using Kraken is shown in the figures. These results indicate excellent agreement between the measured results and two range independent models (Safari and Kraken).

In figure 5.20 the noise of a passing ship is evident at 2.2 km. Even though the signal to noise ratio at 220.5 Hz was low, the overlap processing enabled the reconstruction of the interference pattern in the transmission loss curve. The fact that the horizontal wavenumber spectrum correctly reveals the modal eigenvalues indicates that the overlap processing technique also enabled proper phase measurement. For comparison, figure 5.23 shows the measured horizontal wavenumber spectrum for 220 Hz at 7.1 m from the Frisk-

Lynch-Rajan Nantucket Sound experiment in the same area. A single source-receiver pair was used in their experiment and the noise levels in the horizontal wavenumber spectrum are noticeably worse than the noise levels here.

Horizontal wavenumber spectra can also be calculated for the higher frequencies, but the large number of propagating modes makes individual peak detection difficult. Further, the pressure as function of range for these frequencies was only available for ranges between 1700 and 3700 m on the return leg due to limitations on the recording system. When Safari or Kraken are used to determine where modal peaks are expected, the peaks in the measured data are, however, recognizable and appear at similar wave numbers. Since the large number of propagating modes and short aperture make these plot non-illustrative, they are excluded.

Table 5.3: Measured vs. Calculated modal eigenvalues for 220.5-635 Hz.

Frequency (Hz)	Mode #	k_n model (1/m)	k_n measured (1/m)
220.5	1	.926	.9296
220.5	2	.866	.8772
415	1	1.765	1.763
415	2	1.730	1.734
415	3	1.667	1.663
415	4	1.564	1.562
635	1	2.710	2.711
635	2	2.686	2.691
635	3	2.643	2.642
635	4	2.581	2.576
635	5	2.500	2.506
635	6	2.398	2.379

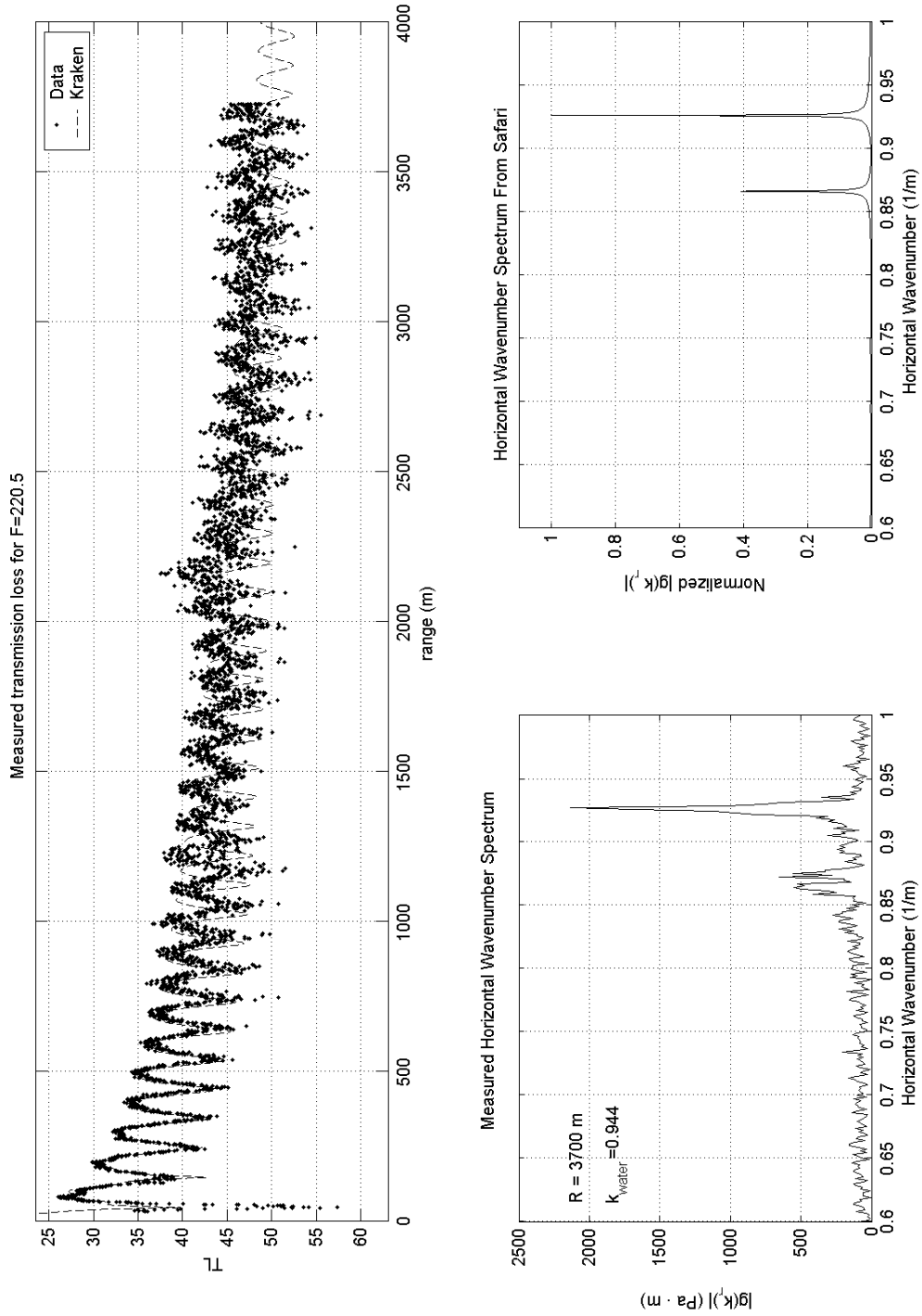


Figure 5.20: Transmission loss and estimated wavenumber spectrum for 220.5 Hz measured on 10 DEC 2005. The calculated values given by Kraken use the derived geo-acoustic profile from Chapter 4 assuming attenuation described by a depth independent Biot time constant.

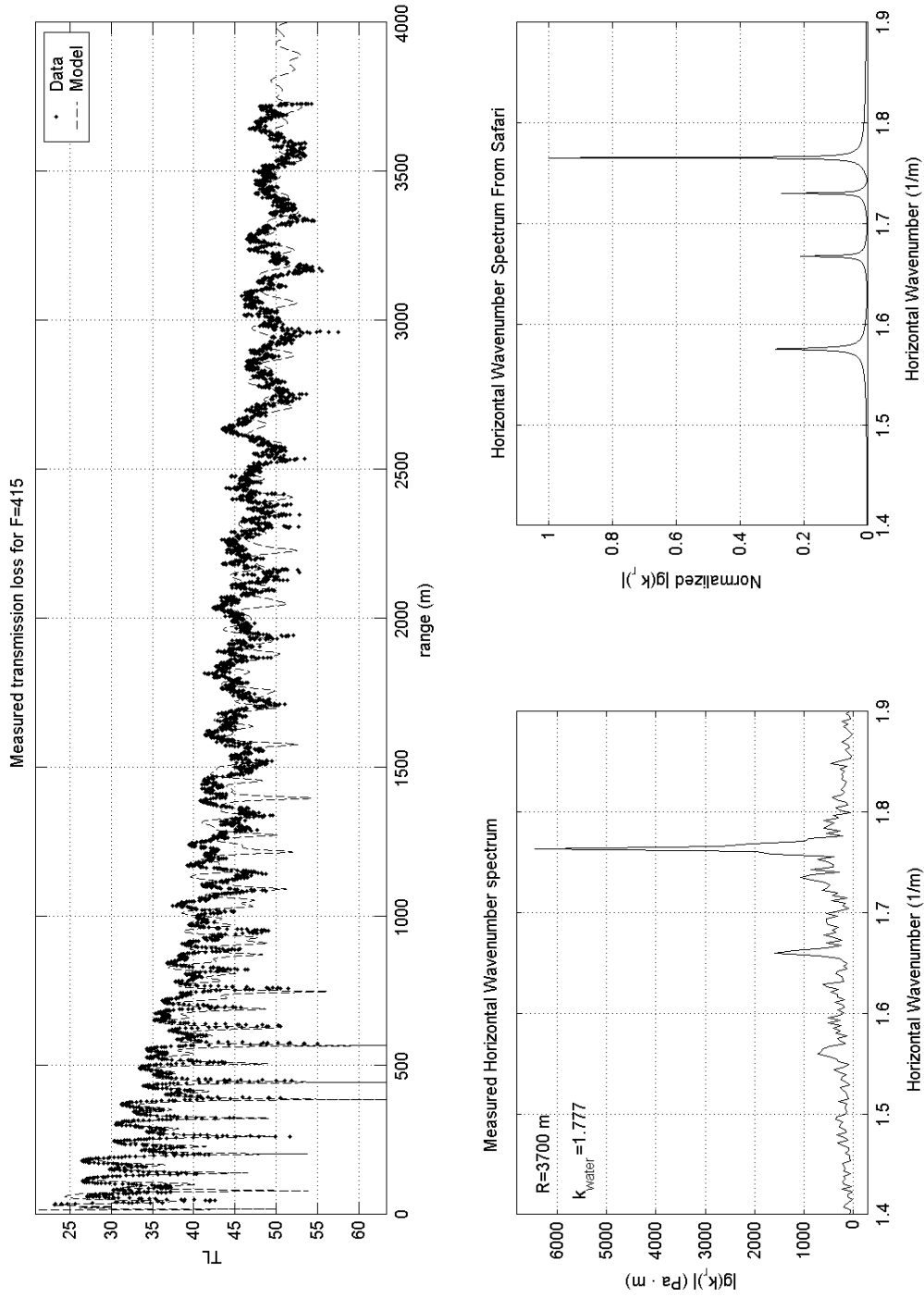


Figure 5.21: Transmission loss and estimated wavenumber spectrum for 415 Hz measured on 10 DEC 2005. The calculated values given by Kraken use the derived geo-acoustic profile from Chapter 4 assuming attenuation described by a depth independent Biot time constant.

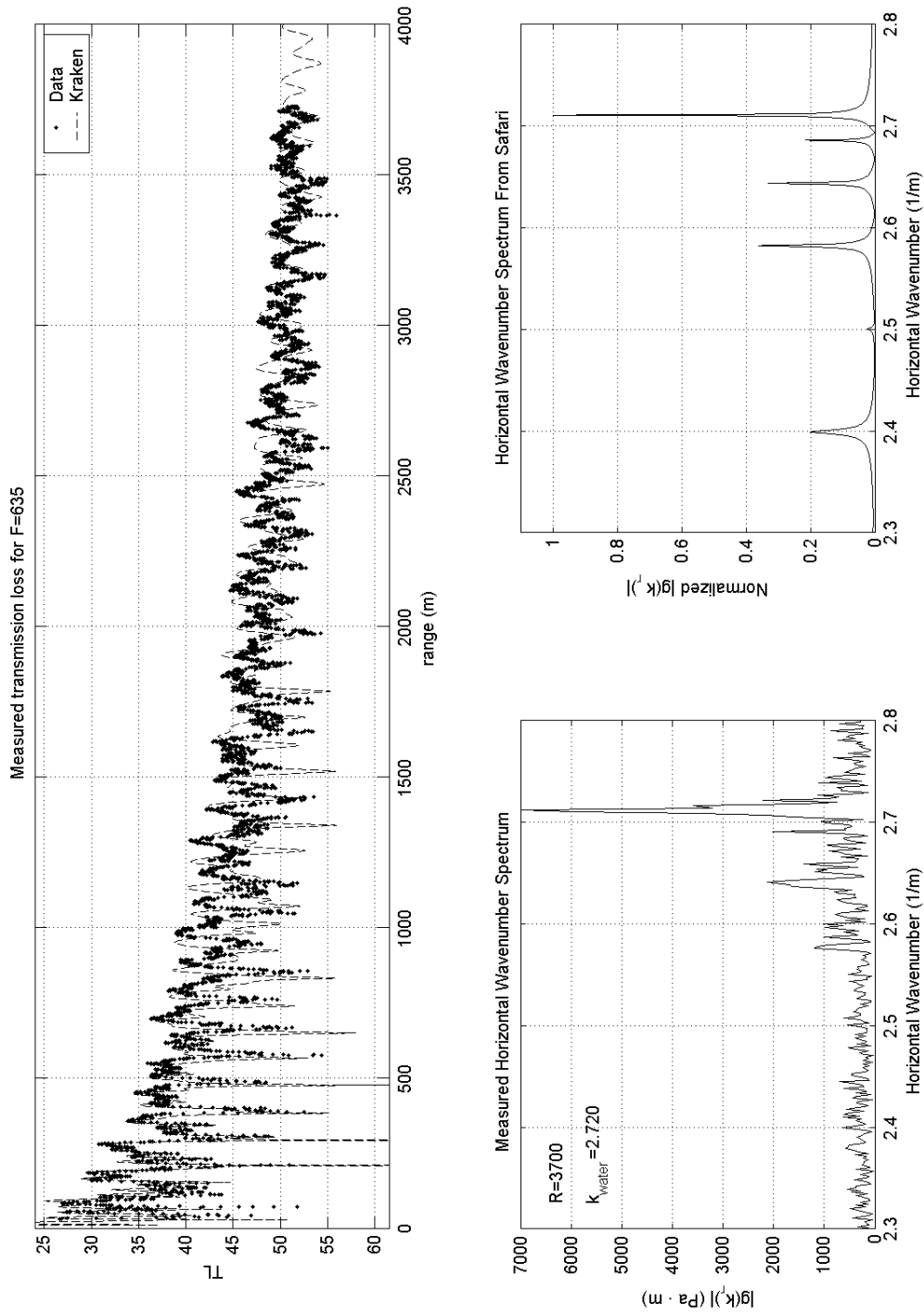


Figure 5.22: Transmission loss and estimated wavenumber spectrum for 635 Hz measured on 10 DEC 2005. The calculated values given by Kraken use the derived geo-acoustic profile from Chapter 4 assuming attenuation described by a depth independent Biot time constant.

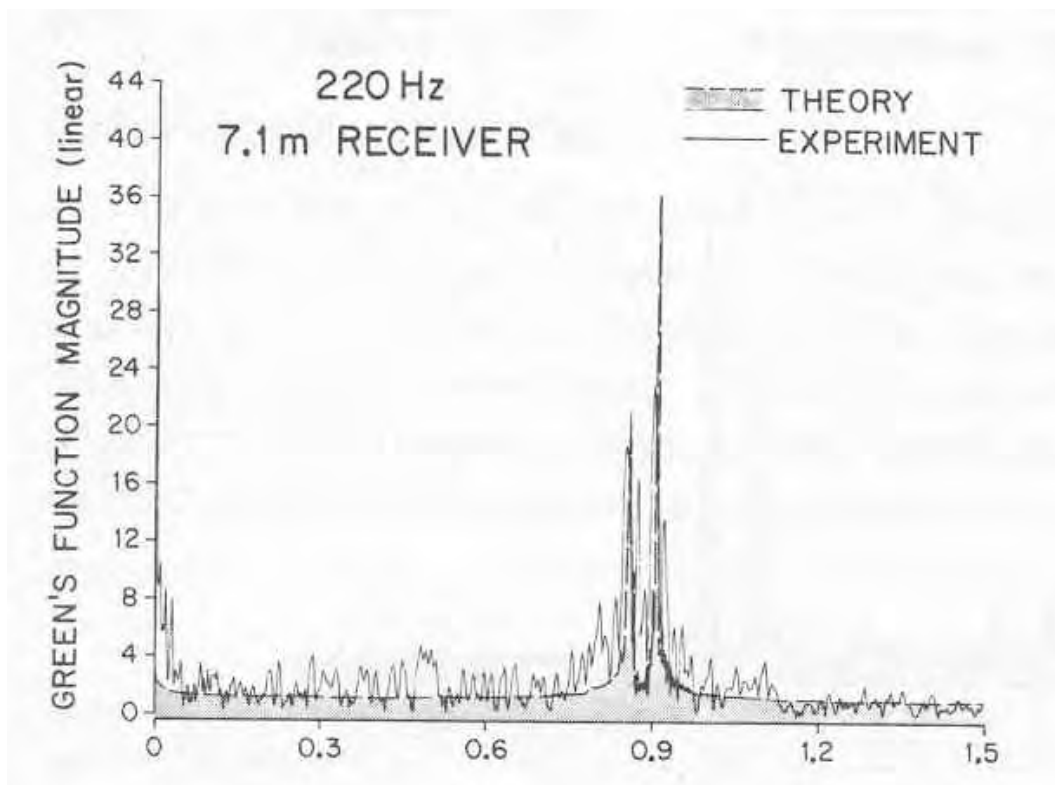


Figure 5.23: Horizontal wavenumber measured and calculated using a profile determined using perturbative inverse techniques as reported by Frisk *et al.* [91].

5.3.3 Attenuation Profiles

The theory presented in section 2.3.1 gives a method to determine the attenuation depth dependence based on the ratio of measured data vs. calculated data. This method requires the measurement of the modal attenuation coefficient which is given by fitting the modal amplitude as a function of range to $e^{-\alpha_n r}$. Thus a standard quadrature Hankel transform was applied to the data using a 2 km sliding window in order to recover the modal amplitude. Figure 5.24 shows a water-fall plot of the estimated wavenumber spectrum as a function of range for 415 Hz as an example of using this method. The ranges indicated are the minimum range of the window and the vertical axis is the linear magnitude of the spectrum. The horizontal axis is limited to 1.5 to 1.8 m^{-1} to enhance viewability.

From figure 5.24 it is clear that the first mode has a very small attenuation coefficient, as expected by theory, since it does not significantly decrease in amplitude. The second mode is not well excited and has a wave number of 1.735 m^{-1} . The third and fourth modes are also apparent at 1.660 and 1.559 m^{-1} respectively. Within the horizontal wavenumber spectrum as a function of range there are several features which are worth discussing. The effect of modal attenuation is very clear in the fourth mode, which visibly decreases in amplitude with range. The third mode shows the same effect but also very clearly shows a modal bifurcation which becomes evident starting with the range window beginning at 200 m. Given that the window aperture is 2km, this places the center for the range window at 1200 m. At this range, the down-slope region seen in figure 5.18 begins to dominate the data contained within the sliding window and the modal wavenumber shifts from wavenumber for 12.9 m depth to the wave number for 13.8 m. This was seen earlier in the data for 220.5 Hz presented in table 5.2. For the range window that begins at 700 m, the down-slope effects are even more apparent as the measured horizontal wavenumber estimate for the third mode degenerates into multiple peaks.

Figures 5.25 and 5.26 show the mode amplitudes as a function of range for modes 3 and 4 shown in figure 5.24 along with the corresponding exponential fits to the data.

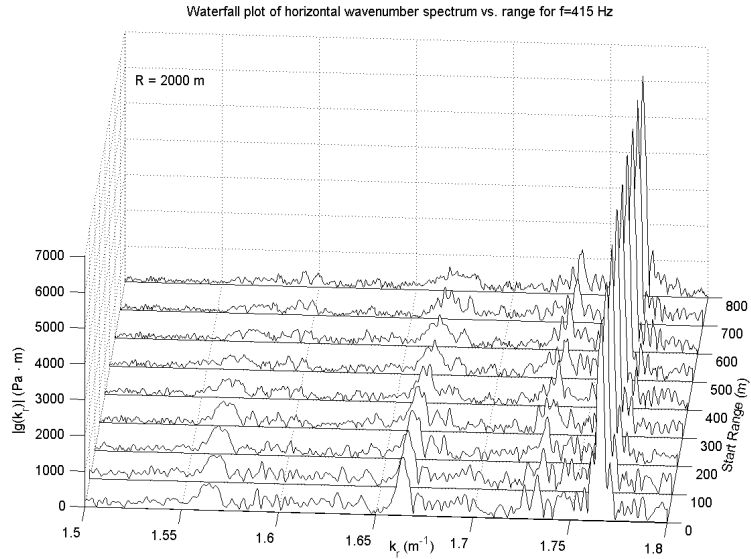


Figure 5.24: Waterfall plot of estimated horizontal wave number spectrum at 415 Hz vs. range using a sliding window and standard quadrature Hankel transform routines.

The modal amplitudes here are given by the local peak in the wavenumber spectrum and the modal attenuation coefficient estimates are given by the coefficient in the exponent of the fit. The results for mode 4 in 5.25 show excellent agreement with an exponential fit, while the results for mode 3 in 5.26 are less consistent with an exponential fit. Some less excited modes, such as mode 2 in figure 5.24, as well as some modes which have very little attenuation actually have modal amplitudes which increase with range. These increases are caused by a combination of low modal attenuation and bathymetry changes. Since the modal amplitude is dependent on the mode function at the source and at the receiver,

$$a_n \propto Z(z_o)Z(z) \quad (5.14)$$

a change in water depth which changes the mode function at the receiver can cause a change in the modal amplitude. Table 5.4 gives the measured modal attenuation coefficients as well as modeled modal attenuation coefficients assuming an attenuation at the interface of 0.3 dB/m at 1 kHz and a quadratic frequency dependence. Since a growing mode amplitude is

equivalent to a negative modal attenuation, such measurements are indicated by a negative value in the table. The observation to be made with this table is that the measured modal attenuations only marginally agreed with theory using the three attenuation profiles discussed in Chapter 4; the Hamilton profile, the Modified Biot profile, and a constant profile. From figure 5.24 and table 5.2 it is clear that the problems are associated with the changing eigenvalues and modal amplitudes due to range dependence. One possible way to solve the varying mode function problem is to use the integral of the horizontal wave number spectrum below each modal peak as a function of range to determine the modal attenuation. Examination of mode 3 in figure 5.24 at 0 m range and 800 m range shows, however, that determination of the correct range of integration is not a clearly definable problem due to peak spreading.

Further, Hankel transforms are phase sensitive measurements and thus are affected by the noise field as discussed with the gain arguments earlier in this chapter. The noise field in the ocean is not homogenous, white, or stationary. Thus, the output of a Hankel transform may contain the effects of the signal and a partially coherent noise field.

Because of these problems, the methods discussed in section 2.3.1 which use modal attenuation coefficients to determine the depth dependence of the sediment attenuation, did not converge to meaningful answers. Information obtained from the analysis such as that shown in figure 5.24 is still useful, however, in characterizing the effects of the range dependence on the transmission loss.

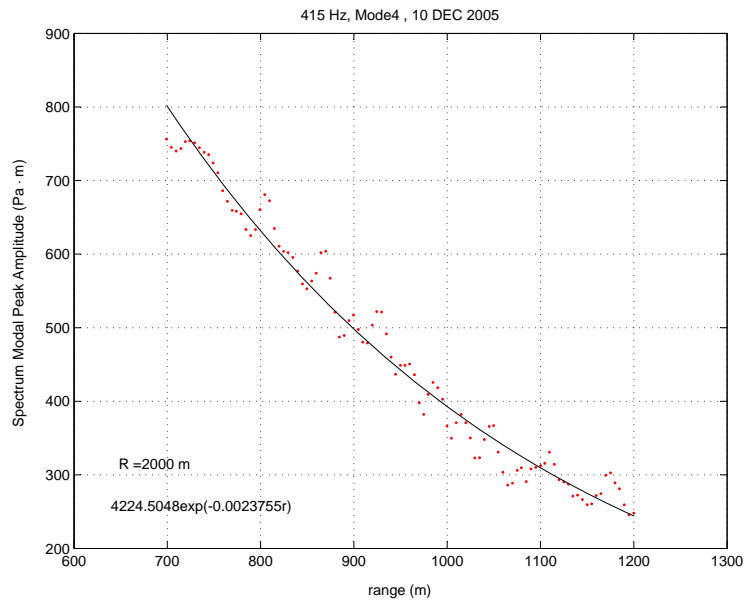


Figure 5.25: Example of estimated mode amplitude vs. showing a clear modal attenuation coefficient by fitting. The case here is mode 4 at 415 Hz.

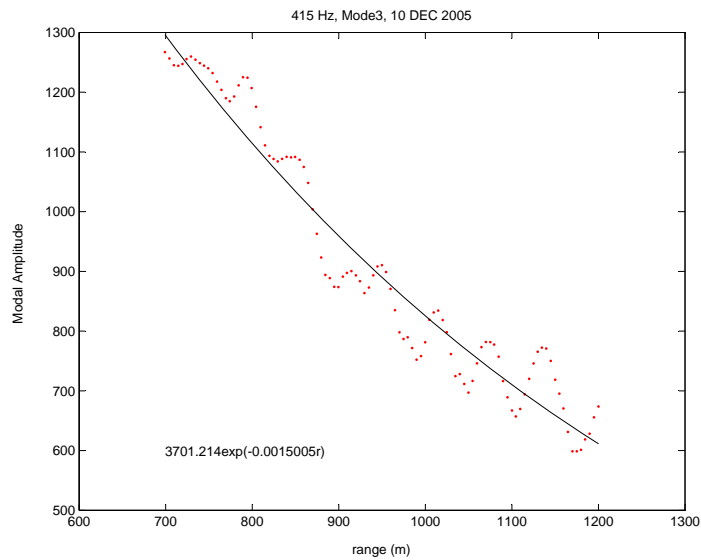


Figure 5.26: Example of estimated mode amplitude vs. range showing a noisy fitting used to determine the modal attenuation coefficient. The case here is mode 3 at 415 Hz.

Table 5.4: Modal attenuation coefficients measured and calculated for the lowest frequencies. The number of modes in the higher frequencies obscures the ability to separate out individual modes easily. Negative values indicate a measured increase in modal amplitude.

Frequency (Hz)	Mode	MAC_{const}	MAC_{Biot}	$MAC_{Hamilton}$	$MAC_{Measured}$
220.5	1	9.448×10^{-5}	9.177×10^{-5}	7.019×10^{-5}	.0001377
220.5	2	.0003407	.000328	.000235	.000456
415	1	7.95×10^{-5}	7.82×10^{-5}	6.61×10^{-5}	.000135
415	2	.000275	.000269	.000225	-.000147
415	3	.000569	.000556	.000447	.00150
415	4	.00136	.00131	.000953	.00238
635	1	6.33×10^{-5}	6.25×10^{-5}	5.59×10^{-5}	-5.549×10^{-5}
635	2	.000232	.000229	.000204	-.000649
635	3	.000467	.000460	.000405	.001858
635	4	.000777	.000764	.000658	.00148
635	5	.00131	.00128	.00106	.000488
635	6	.00320	.00310	.00229	.001614

5.4 Frequency Dependence of Attenuation

Three proposed depth dependent profiles were hypothesized: a constant profile, a profile consistent with a depth independent Biot time constant, and a profile consistent with Hamilton's empirical relations. For the case of a slightly range dependent environment, the appropriate approach to take is then hypothesis testing. By that, it is meant that given calculations based on the hypothesis of the attenuation profile, do the measurements agree with each hypothesis?

From the previous section, it is clear that using modal amplitude arguments to determine the correct depth dependence of the attenuation can not provide a definitive answer. At this point, the three profiles are considered equally as likely statistically and the work will proceed using all three profiles in a hypothesis test to determine the range of applicability of each profile.

Table 5.2 showed that while that the problem at hand is really slightly range dependent, modeling the problem as a range independent problem with average depths and profiles will be a good approximation. Much information, especially regarding the attenuation, can therefore be obtained by considering a range independent approximation to the problem. Consider the asymptotic form of the normal mode solution to the waveguide problem,

$$p(r) \approx \sqrt{2\pi} e^{i\pi/4} \sum_{n=1}^N a_n Z_n(z_0) Z_n(z) \frac{e^{ik_n r - \alpha_n r}}{\sqrt{k_n + i\alpha_n}}. \quad (5.15)$$

Range dependence of depth profiles affects the eigenfunctions Z_n and the eigenvalues k_n according to the modal equation

$$\rho(z) \frac{\partial}{\partial z} \left[\frac{1}{\rho(z)} \frac{\partial Z_n(z)}{\partial z} \right] + \left[\frac{\omega^2}{c^2(z)} - k_n^2 \right] Z_n(z) = 0. \quad (5.16)$$

Figure 5.24 showed that as long as a mode is not weakly excited, the product $Z_n(z_0)Z_n(z)$ does not change significantly. The real and imaginary parts of the eigenvalues do, however, change. From equation (5.15) a small change in the real part of k_n will cause a signifi-

cant change in the phase of the pressure because k_n is multiplied by the range and is in the argument of a sinusoid. The imaginary part is in the argument of a real exponential, and thus affects the amplitude. A small change in the imaginary part is therefore a small change in the attenuation and only contributes to a small change in the pressure amplitude. Therefore, while modeling a range dependent environment by an approximate range independent environment will give an incorrect phase variation, the range averaged mean square pressure, which eliminates phase variations and depends only on amplitude, will be correctly modeled.

It should be noted that there is not a strong range dependence in the bottom properties. The site survey discussed in Chapter 4 showed with precision depth sounders and bottom samples that the bottom composition in the region was essentially uniform in the top several meters. Figure 5.18, however showed a bathymetry with long range scale variations such as up-slope and down-slope regions as well as short range scale variations consistent with a rough bottom. In order to recover the phase variations at range, all of the bathymetry features on the order of a wavelength must be modeled. This is not computationally feasible. Since this work is concerned primarily with the attenuation effects, the proper comparison of theory to measurement is the range averaged transmission loss and not the modal interference pattern.

Because of the problems discussed earlier with the September data set and the fact that only 2 km was reached, the data used to determine the attenuation characteristics comes from the December experiment. Figures 5.27 to 5.33 show the measured transmission loss as a function of range with the transmission loss predicted by each of the three numerical models. Overlap processing was used and the distance between sample points is approximately 0.75 m, the array spacing. The output of the numerical models was set to give a similar range spacing to eliminate averaging bias. The input geo-acoustic data for the numerical codes are as shown in each figure. The sound speed profile and the density profiles are as determined from the pre-experiment site survey and the attenuation profile for the time being is assumed to be given by a depth independent Biot time constant.

These figures show excellent agreement in both average level and phase of the received signal out to approximately 600 meters. Beyond this range, the range dependent effects are seen in the mismatch of the phase of the measured and calculated transmission losses. The character of the transmission loss curves and the range averaged transmission loss values, however appear to agree quite well between model and measurement out to 4 km.

One feature that is not fully recovered in the measured data is the deep nulls evident in the calculated values. This is clearly seen for the nulls from 700 m out in figure 5.29. Deep nulls are caused by strong destructive interference and are very localized. Since the array is moving, there is some range averaging within each measurement. The forward velocity was approximately 1.5 m/s and the Fourier transform time interval used was 0.76 s. This means that each pressure data point is in fact range averaged over approximately 1.15m. Very localized interference effects, therefore, are averaged out. In order to compare the measured range averaged transmission loss results to the calculated results, this effect must be accounted for. Otherwise, the calculated values will have much more loss. To do this, a cutoff level was determined for each signal in each range interval of interest. Calculated data points with transmission losses greater than this cut off level were omitted from the range averaged result. To determine this cutoff level, the difference between the lowest and highest measured transmission loss in the range of interest was found. The cutoff level was then set to be this amount greater than the lowest calculated transmission loss in the range interval.

In figures 5.30 to 5.33 the source is turned off at the beginning and end of the vehicle path shown. This makes it very easy to estimate the signal to noise ratio. The signal to noise ratio, however, can not be used to determine the cutoff level mentioned above because this effect is not a signal to noise effect. The inability of the array system to measure some of the deep nulls present in the models comes from the fact that the array is moving and the data inherently range averaged.

At higher frequencies interface scattering effects can cause a decrease in the coherence of the field. Strong interference patterns are the result of good coherence. Therefore, using

the measured data to define cutoff levels also easily accounts for such artifacts which may be in the data but computationally difficult to model.

The data sets for the inbound leg contain less data than the outbound legs. Once it was determined that the vehicle had in fact turned around, it took some time to switch the frequencies on the signal generator. During this time the vehicle continued on its path back to the ship. The point at which the source is switched to the higher frequencies is clearly evident at a range of 3700 m.⁴ Further, the mini-disc recorders used in the system can record only up to 90 minutes of data. A stop watch was used on board the ship to estimate the time at which the recorders ran out of disk space. Once that time was surpassed, the source was turned off to minimize the environmental impact on marine wildlife. While it was assumed that the recorders had stopped and no additional acoustic data was being recorded, the mini-discs often have capacities larger than their rating, which was the case here. Thus, the source was turned off at about 1700 m range even though the recorders continued to record the received signal level. The only benefit was that the signal to noise ratio of the system and processing is then easily seen to be on the order of 30 dB .

The transmission loss results for the inbound leg also show a sudden decrease in transmission loss for a few hundred meters near 2km. This was caused by a passenger on the ship accidentally brushing up against the source amplifier and increasing the gain. Once this error was noticed, the gain was returned to its original position. This small corrupted section was, however, not used in calculations whenever possible.

Although the geo-acoustic profiles are described in Chapter 4, figure 5.34 gives a graphical representation of the geo-acoustic model used in the numerical modeling. The water column is essentially isovelocity with a sound speed of 1467 m/s. The quadratic sediment layer is a layer with sound speed and density properties determined in the site survey and an attenuation that is at first assumed to be proportional to frequency squared. This power law is later relaxed to be somewhere between linear and quadratic. The computa-

⁴The reader is reminded that for the inbound leg the vehicle progresses in time from greater range to lesser range.

tional bottom is required to mimic the fact that the real ocean floor extends essentially to infinity. Since a computer code can not extend to infinity, the computational bottom is included and has properties identical to the bottom of the sediment layer except that the attenuation is zero for most of the layer and then increases to very large values to prevent false returns from the bottom termination used by the computer.

The next step in finding the frequency dependence of the attenuation was to select a reference frequency and adjust the attenuation at the interface for that frequency to yield calculated range averaged transmission loss results identical to the measured range averaged transmission loss results. The reference frequency chosen was 1228 Hz and range averaging was performed over 1 km long segments of the data to ensure that all interference effects would be averaged out. Since the inbound data set only extended from 1700 m to 3700 m, and the data was corrupted near 2000 m by human error, the range interval chosen for the return leg was 2600 m to 3600 m. This was the 1 km long stretch of reliable data that was furthest from the source, and thus had the greatest accumulation of attenuation effects.

The attenuation in the sediment layer at each other frequency was then obtained by using the equation

$$\alpha(f) = K_{f_0} \left(\frac{f}{f_0} \right)^n \quad (5.17)$$

for some value of n which was allowed to vary. K_{f_0} here is the attenuation at the reference frequency in units of dB/m. Since the computer codes required attenuation in units of dB/wavelength, this was actually implemented as

$$\alpha[\text{db/wavelength}] = K_{f_0} \left(\frac{f}{f_0} \right)^{n-1} \frac{c}{f_0} \quad (5.18)$$

where c is the speed of sound in the sediment. After the analysis is complete, the attenuation must be expressed at 1 kHz because this is the reference frequency chosen in most of the literature.

If the value of K_{f_0} is adjusted such that the calculated transmission loss matches the measured transmission loss at the reference frequency, then changes in the exponent n will most greatly affect the frequencies furthest away from the reference frequency. To improve fitting accuracy, more data points are thus required at the frequencies furthest away from the reference. Thus, the range averaged transmission loss is determined for the calculated data as well as the measured data for the following frequencies at the following range intervals:

1000-2000m 220.5, 415, and 635 Hz (outbound),

2000-3000m 220.5, 415 and 635 Hz (outbound),

2600-3600m 220.5, 415, 635 (both outbound and inbound), 823, 1031, 1228 Hz.

Figures 5.35 through 5.37 show the measured and calculated transmission losses as a function of frequency using all three numerical models at the different range intervals. These plots assume an attenuation at 1228 Hz at the interface of 0.3 dB/m.

The iteration routine used to find the best fit frequency dependence uses the parabolic equation code because it is easy to implement and provides consistent results. Further the large scale range dependent bathymetry from figure 5.18 is easily included. For ease in notation, the range averaged transmission loss (RATL) measured will be referred to as $\langle TL \rangle_R$ and the range averaged transmission loss calculated using the parabolic equation code (PE) will be referred to as $\langle TL_{PE} \rangle_R$. For each assumed attenuation profile, the numerical routine performs the following steps which are summarized in a flow chart in figure 5.38:

1. $\langle TL_{PE} \rangle_R$ is calculated using PE with the geo-acoustic model described above assuming an initial guess for attenuation of $K_{f_0} = 0.34$ db/m at the surface at the reference frequency. This initial guess is based on the attenuation at 1kHz reported in reference [41].

2. The reference attenuation factor, K_{f_0} , is adjusted in an iterative fashion to determine the best fit value of K_{f_0} at f_0 . This is accomplished by comparing $\langle TL_{PE} \rangle_R$ to $\langle TL \rangle_R$ at f_0 .
3. Once the best fit K_{f_0} is determined, an iteration is performed for each frequency over a range of values of n in $\alpha = K_{f_0}(f/f_0)^n$. For each value of n in the iteration, the following steps are performed:
 - The modeled attenuation is set by $\alpha = K_{f_0}(f/f_0)^n$ with the best fit K_{f_0} from step 2 and the current value of n .
 - $\langle TL_{PE} \rangle_R$ is found using PE with this modeled attenuation for each frequency and range interval described above.
 - $\langle TL_{PE} \rangle_R$ is compared to $\langle TL \rangle_R$ which is found by range averaging the measured data. The comparison is done by performing a least squares fit of $\langle TL_{PE} \rangle_R$ to $\langle TL \rangle_R$ using data points from each frequency and range interval.
 - From the least squares fit, a best fit slope is assigned to the current value of n .
4. The best fit frequency dependence is determined by the value of n for which the slope of the fit most nearly equals 1.0.

Figure 5.39 shows the range averaged transmission loss calculated, $\langle TL_{PE} \rangle_R$, vs. the range averaged transmission loss measured, $\langle TL \rangle_R$, for a few different values of n . The line in the figure is a line with a slope of exactly 1.0. Figure 5.40 shows the slope of the best fit line between the calculated and measured values as a function of n for the case where the bottom has a depth dependence given by a depth independent Biot time constant. The best fit value of n is $n = 1.87$. This process was repeated assuming a constant attenuation depth profile and a profile consistent with Hamilton's empirical relations. Table 5.5 summarizes the results which lie just below the limits of Hamilton's attenuation values at 1kHz [30] for the measured porosity of 49%.

The values summarized in table 5.5 agree very well with Zhou and Zhang's reported summary of attenuation in sandy sediments in 16 different regions around the world [41]. For reference, their figure of attenuation as a function of frequency in sandy-sediments is included in figure 5.41. The best fit attenuation determined by Zhou and Zhang was

$$\alpha(f) = 0.34 \left(\frac{f}{1kHz} \right)^{1.84} [dB/m]. \quad (5.19)$$

Here the best fit is

$$\alpha(f) = K \left(\frac{f}{1kHz} \right)^{1.87} [dB/m] \quad (5.20)$$

where K ranges from 0.261 to 0.273 depending on the profile assumed in table 5.5. The resulting attenuation for a constant profile at 220.5 Hz would be .015 dB/m, consistent with the value found at the Frisk-Lynch-Rajan site in Nantucket Sound for 220.5 Hz, .011 dB/m [93].

Table 5.5: Summary of results for best fit n for each attenuation profile.

Profile	Best fit K_{1kHz} [db/m]	Best fit n
Constant	0.261	1.89
Biot	0.263	1.87
Hamilton	0.273	1.70

In section 2.2.2 it was shown that the modal attenuation coefficient is related to the depth integrated product of the attenuation profile and the modal functions. If the simplified low frequency approximation to the Biot theory is used, the attenuation depends on

$$\alpha_n = \alpha_n \left(\omega^2 \int \frac{\tau_B}{\rho c^2} Z_n^2 dz \right). \quad (5.21)$$

More generally it depends on

$$\alpha_n = \alpha_n \left(\int \frac{\alpha(\omega, z)}{\rho c} Z_n^2 dz \right) \quad (5.22)$$

Since the frequency dependent attenuation appears in the integrand, the overall (or appar-

ent) attenuation has a frequency dependence that depends on the frequency dependence of every layer in the bottom. Consider the case where the bottom is composed of a sediment which has a constant attenuation profile that is exactly dependent on ω^2 to infinite depth. In that case, the attenuation would come out of the integral and the overall attenuation would exactly depend on an attenuation which is proportional to ω^2 . Similarly, if the sediment was completely uniform with a linear frequency dependence, ω^1 , then the frequency dependence of the overall attenuation would depend on attenuation with a linear dependence. If it were assumed that the frequency dependence in the sediment was uniform when in fact there was a quadratic layer overlying a linear layer, the modal attenuation would then appear to depend on an attenuation described by $1.0 < n < 2.0$. This is the case here as the best fit value of n is $n = 1.87$ for a Biot depth profile. It was thus hypothesized that these results are readily explained by the theory if the bottom is modeled as a quadratic layer of thickness⁵ z_c . Figure 5.42 shows this model schematically.

To test this hypothesis, an iterative routine was again performed that compared the measured range averaged transmission loss to the range averaged transmission loss output from RAM. In this case, the attenuation profile was assumed to be exactly quadratic in the first layer and exactly linear in the second layer. 1228 Hz was assumed as the reference frequency in both layers, so there is no difference in attenuation in the layers at 1228 Hz. The iterative fitting process used before to find the best fit n was then repeated, this time adjusting z_c to find the best layer thickness. Figure 5.43 shows the range averaged transmission loss calculated compared to measured for several values of z_c . The line shown has a slope of 1. Figure 5.44 shows the slope of the best fit line between calculated and measured values as a function of z_c . The result is that a quadratic sediment layer with a thickness of 5.5 meters overlying a linear layer is the best fit. This is consistent with the result presented by Stern, Bedford, and Millwater [117] in which they allowed the frame

⁵Here the layer thickness is denoted as z_c , termed the characteristic depth. This nomenclature was adopted because it is most probable that any variation in frequency dependence would be a smooth variation, with a characteristic depth marking a $1/e$ depth, half way between the regions where the dependence is exactly 1.0 and 2.0, or some other metric.

moduli in the sediment have a depth dependence. The frequency dependent attenuation profile that they calculated, as seen in their figure 4, is nearly quadratic in frequency near the surface and converges to a linear dependence near 10 m deep. They, however, allowed for a smoothly varying profile while the profile here is a step function.

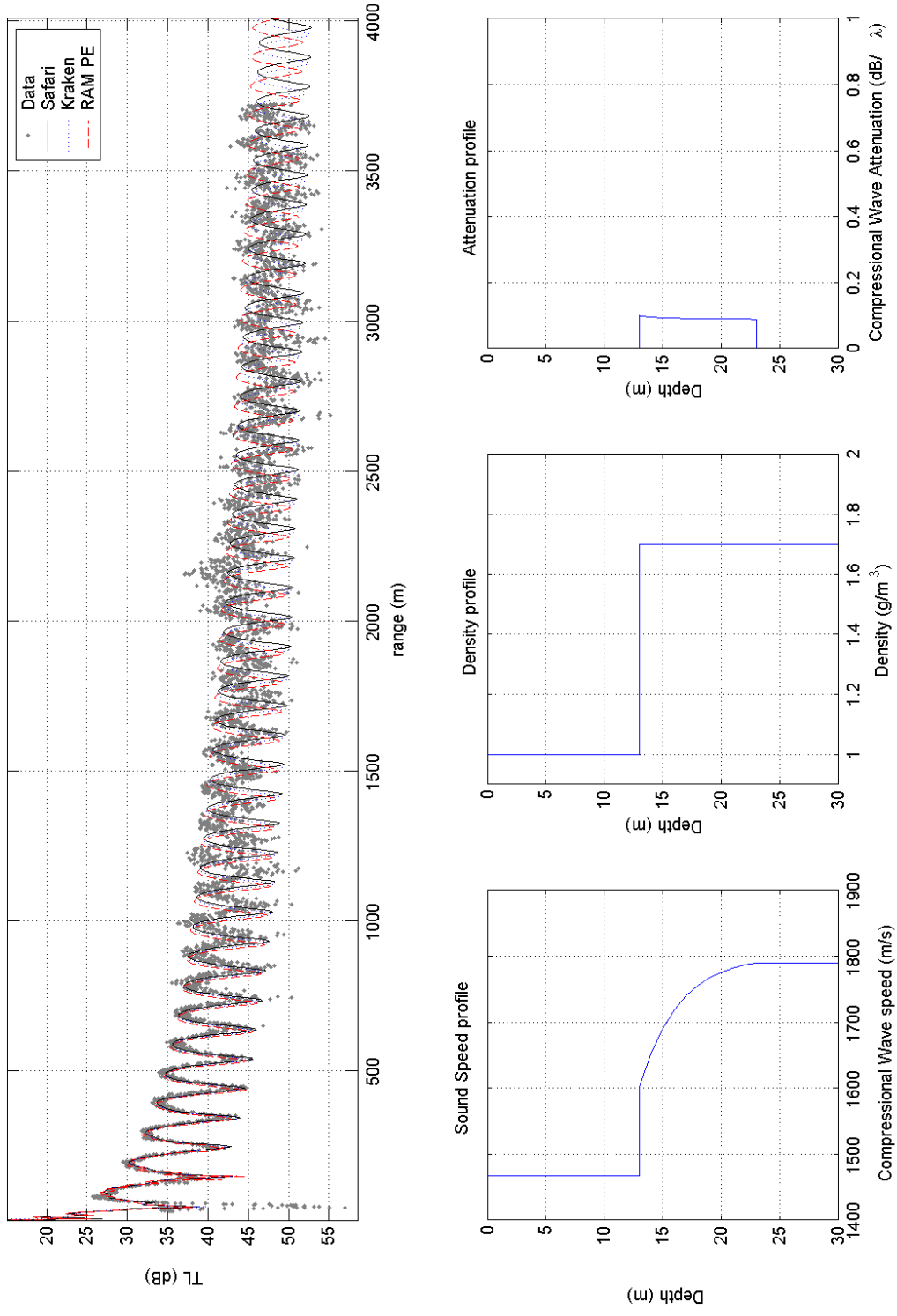


Figure 5.27: Comparison of measured transmission loss to calculated transmission loss using three different models for 220.5 Hz.

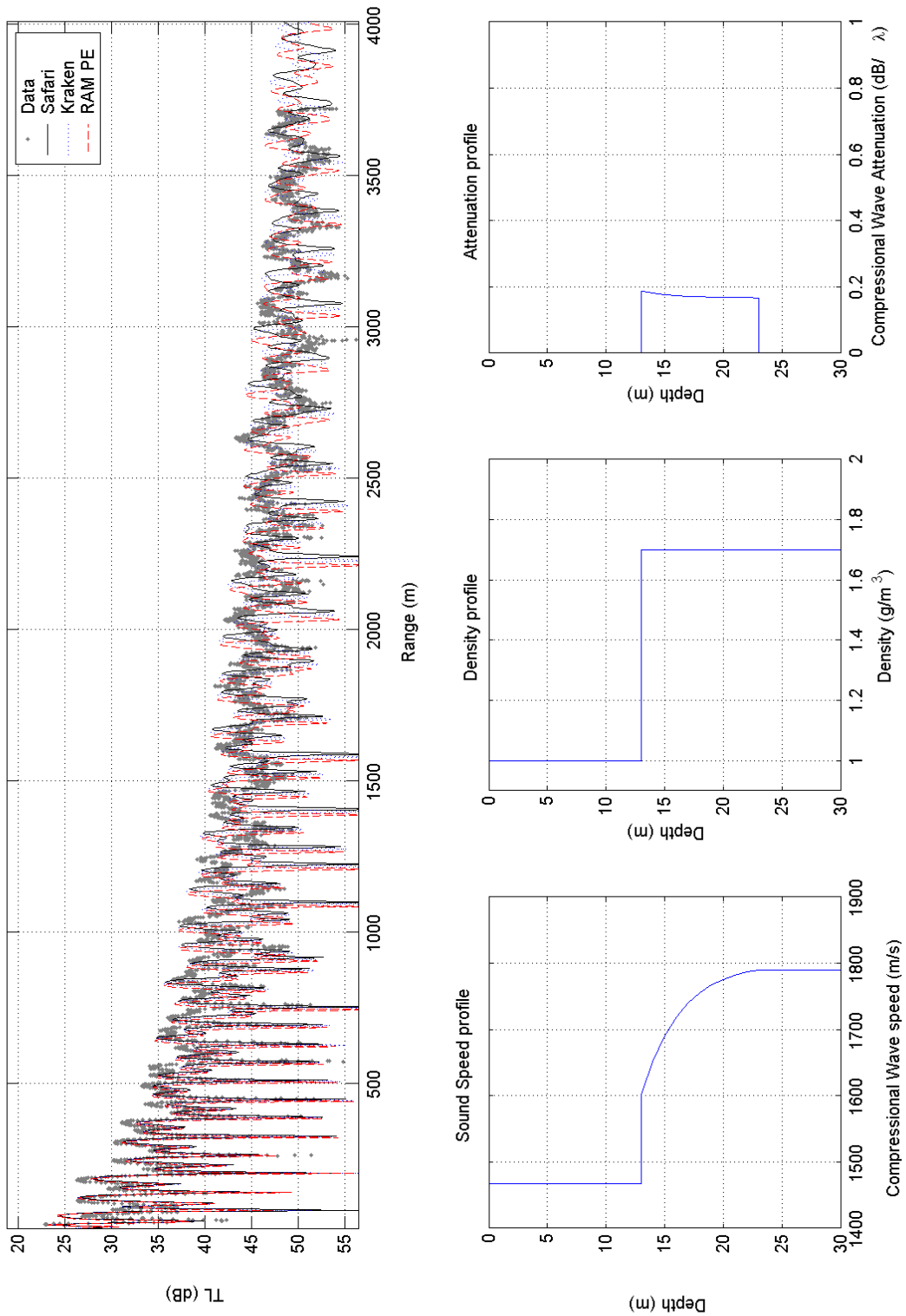


Figure 5.28: Comparison of measured transmission loss to calculated transmission loss using three different models for 415 Hz.

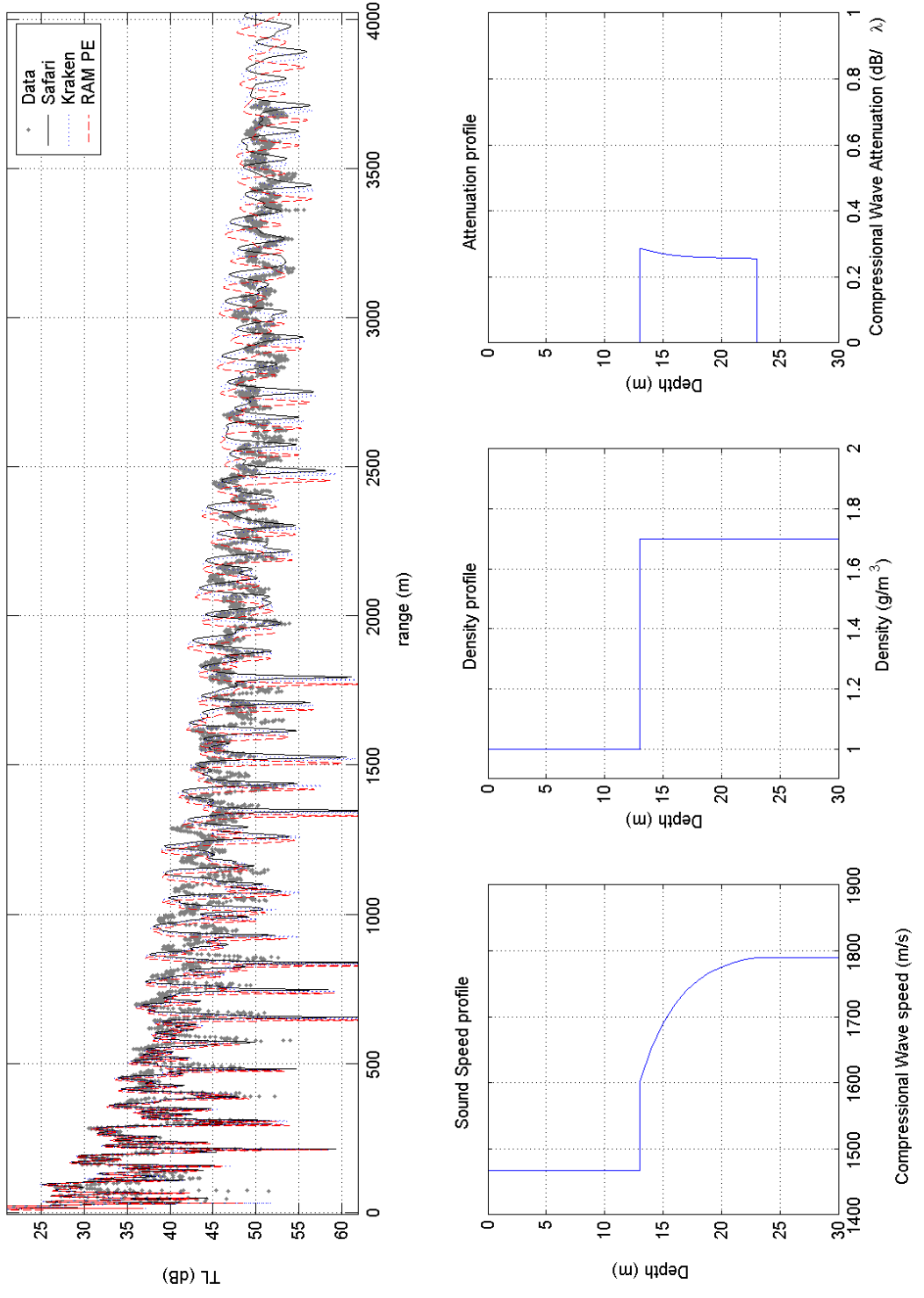


Figure 5.29: Comparison of measured transmission loss to calculated transmission loss using three different models for 635 Hz on the outbound leg.

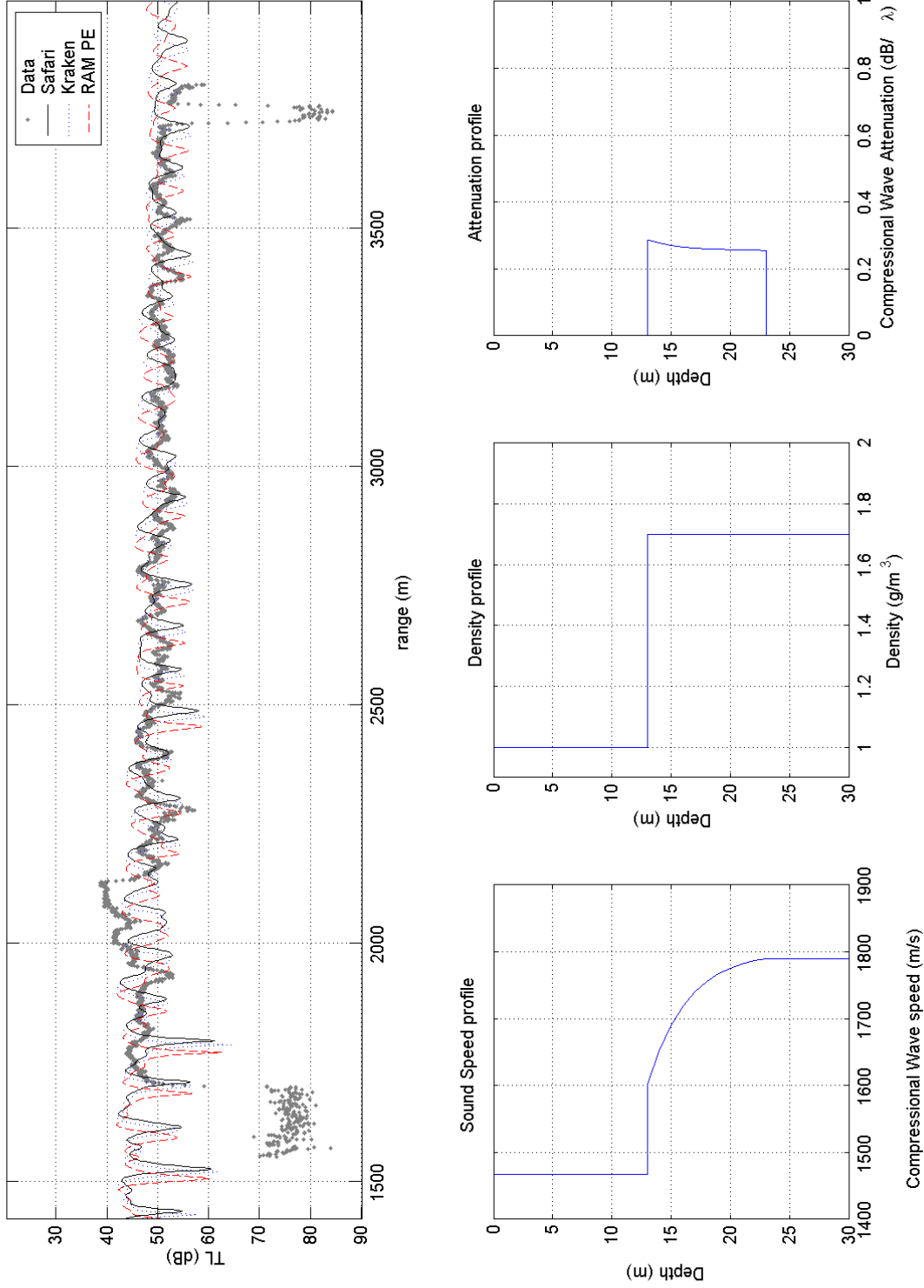


Figure 5.30: Comparison of measured transmission loss to calculated transmission loss using three different models for 635 Hz on the inbound leg.

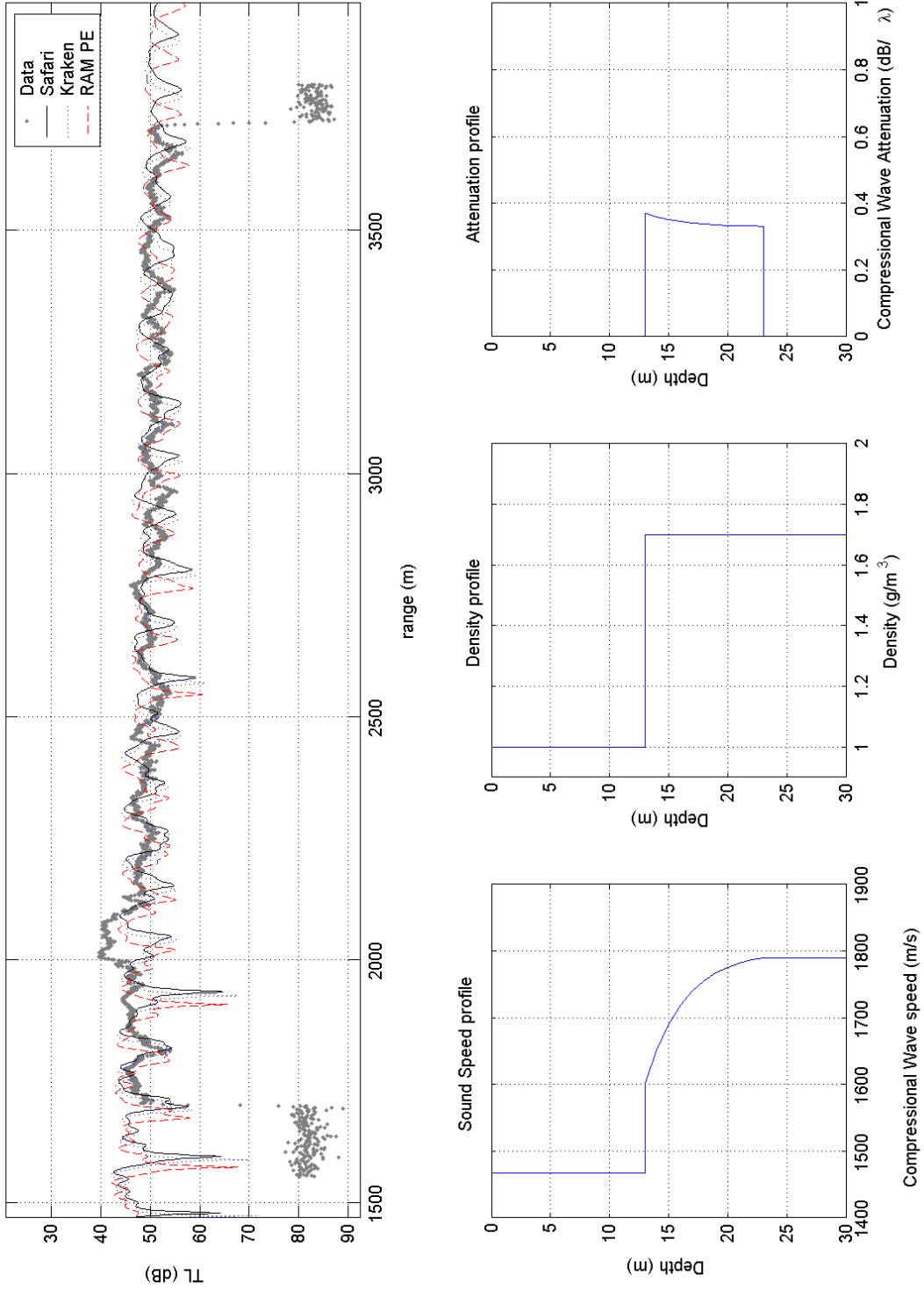


Figure 5.31: Comparison of measured transmission loss to calculated transmission loss using three different models for 823 Hz.

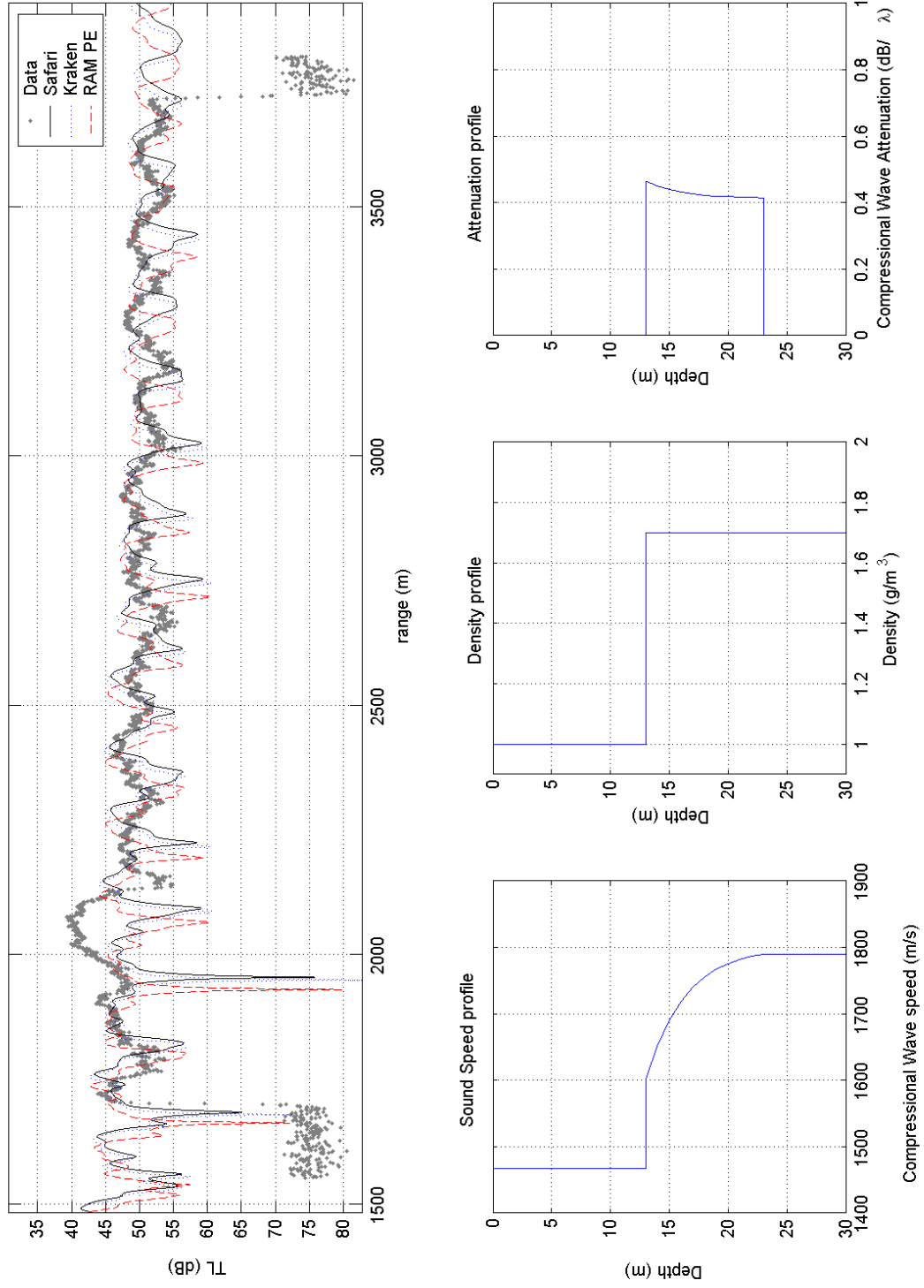


Figure 5.32: Comparison of measured transmission loss to calculated transmission loss using three different models for 1031 Hz.

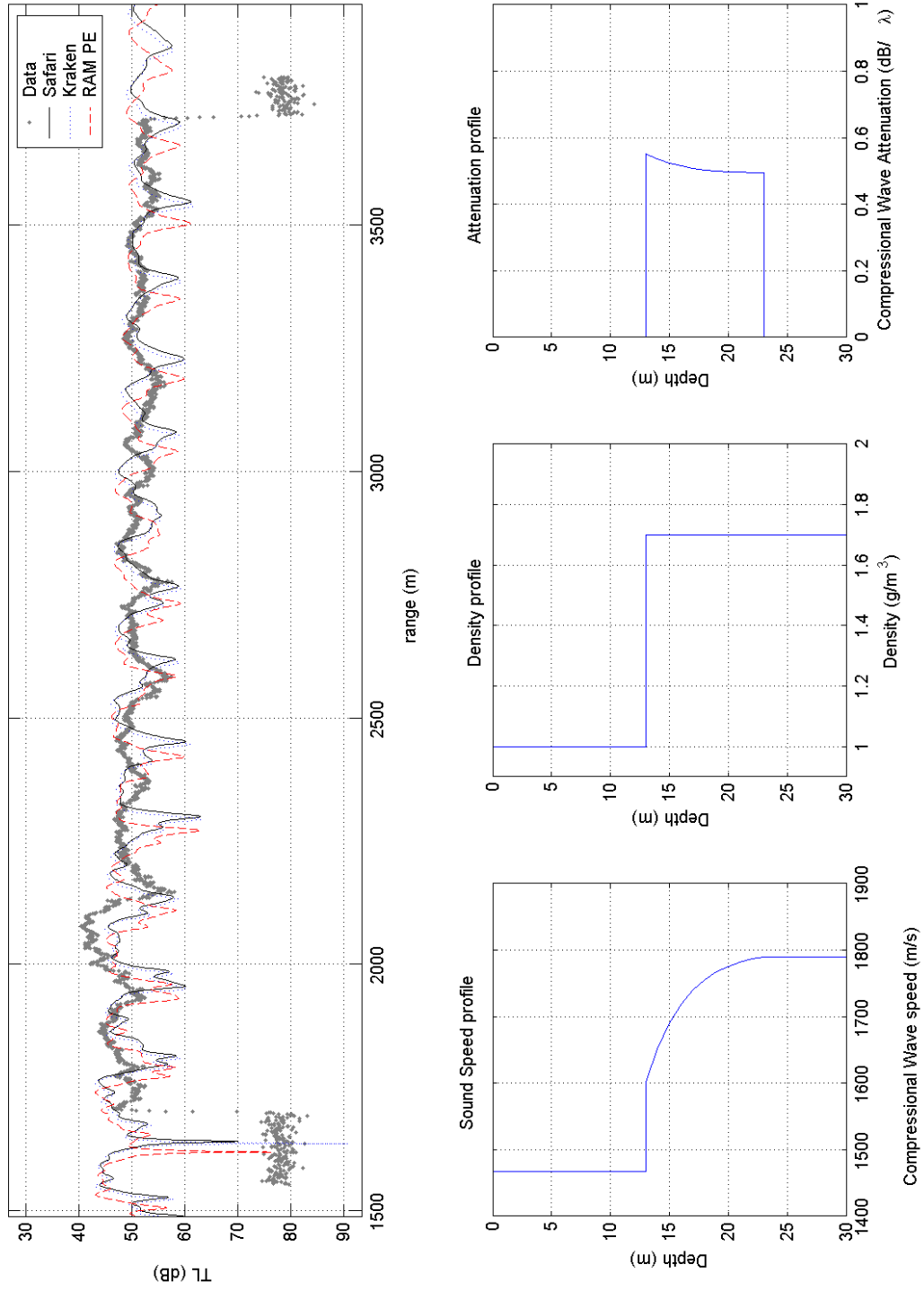


Figure 5.33: Comparison of measured transmission loss to calculated transmission loss using three different models for 1228 Hz.

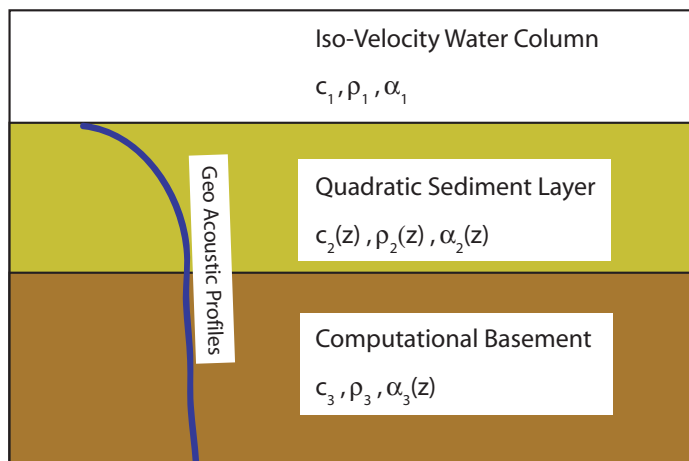


Figure 5.34: Schematic of the 3 layer geo-acoustic model used for a Biot bottom. The sediment layer has attenuation with a quadratic frequency dependence. The computational basement has uniform properties equal to the bottom of the sediment layer except that the attenuation increases at depth to prevent false returns.

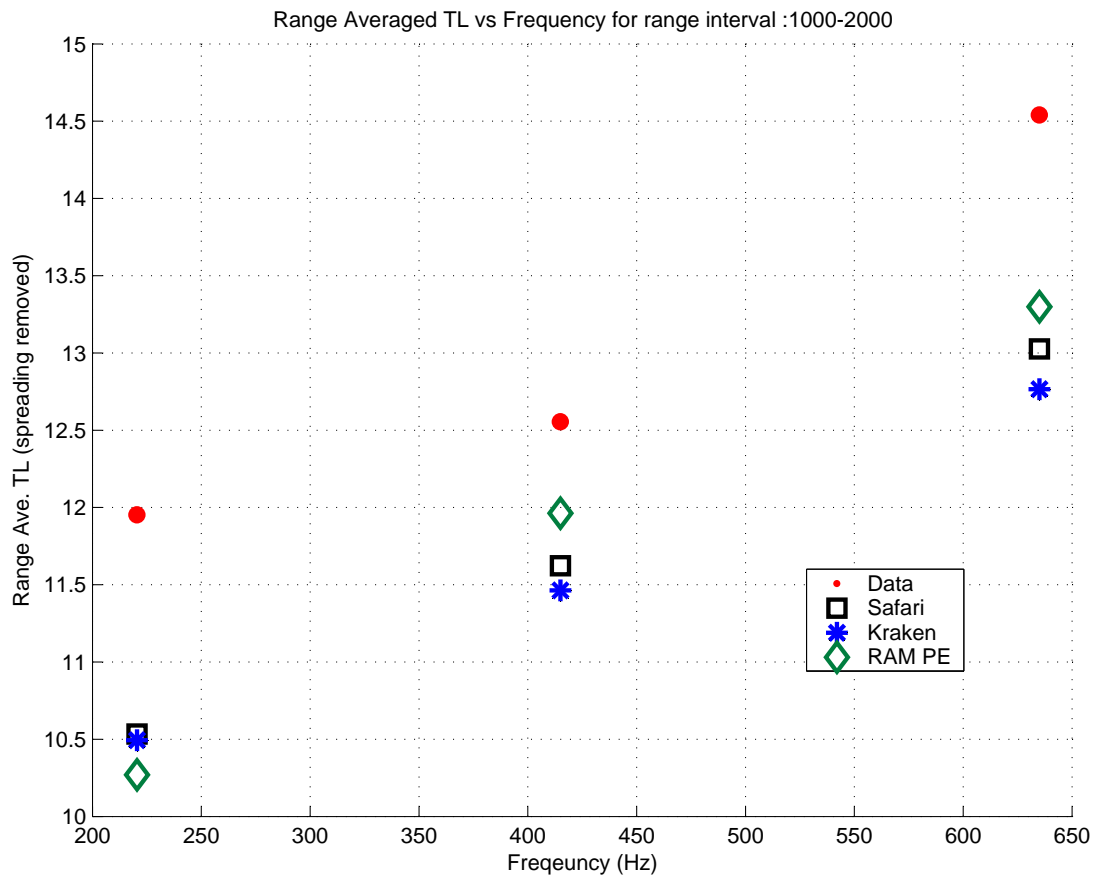


Figure 5.35: Comparison of measured and calculated transmission loss for 1000-2000m range, 10 DEC 2005.

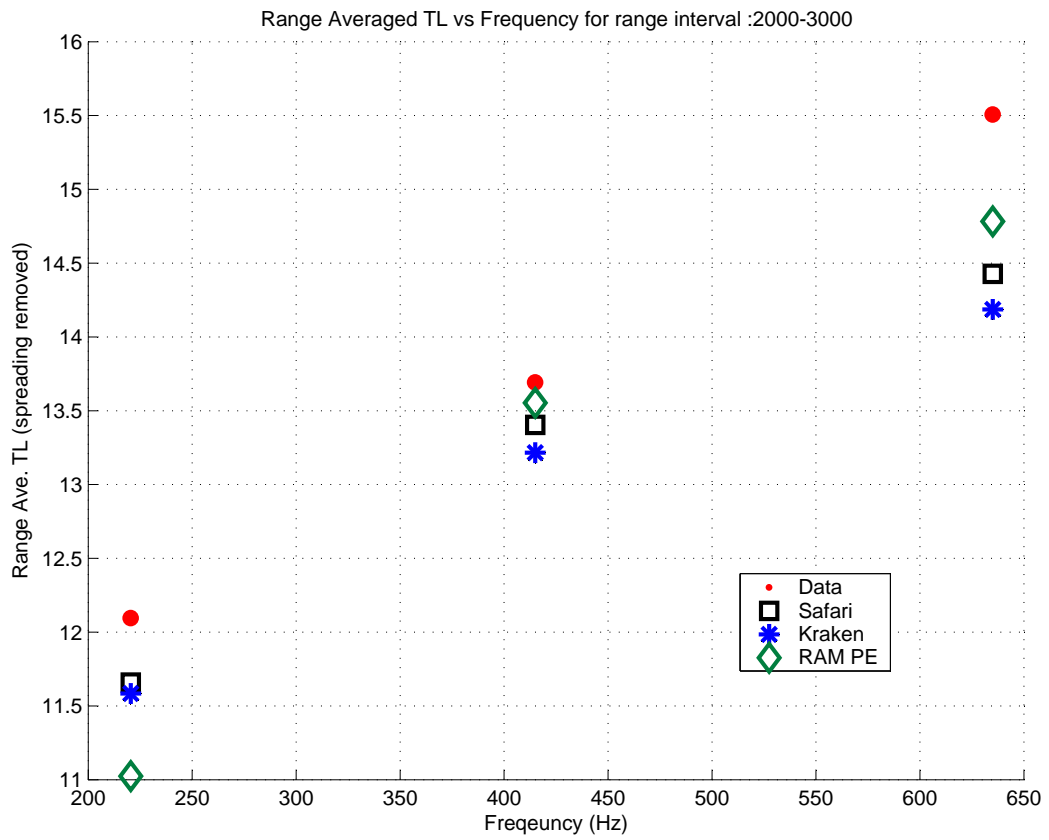


Figure 5.36: Comparison of measured and calculated transmission loss for 2000-3000m range, 10 DEC 2005.

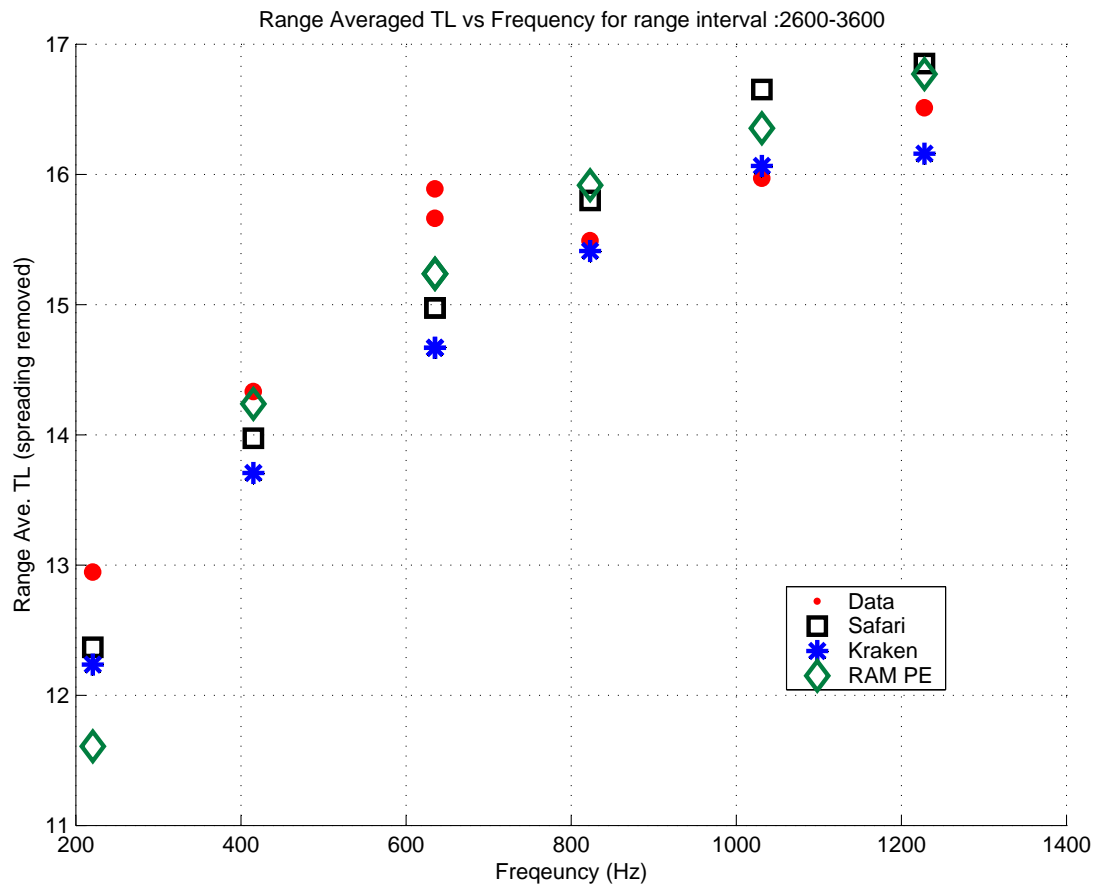


Figure 5.37: Comparison of measured and calculated transmission loss for 2600-3600m range, 10 DEC 2005.

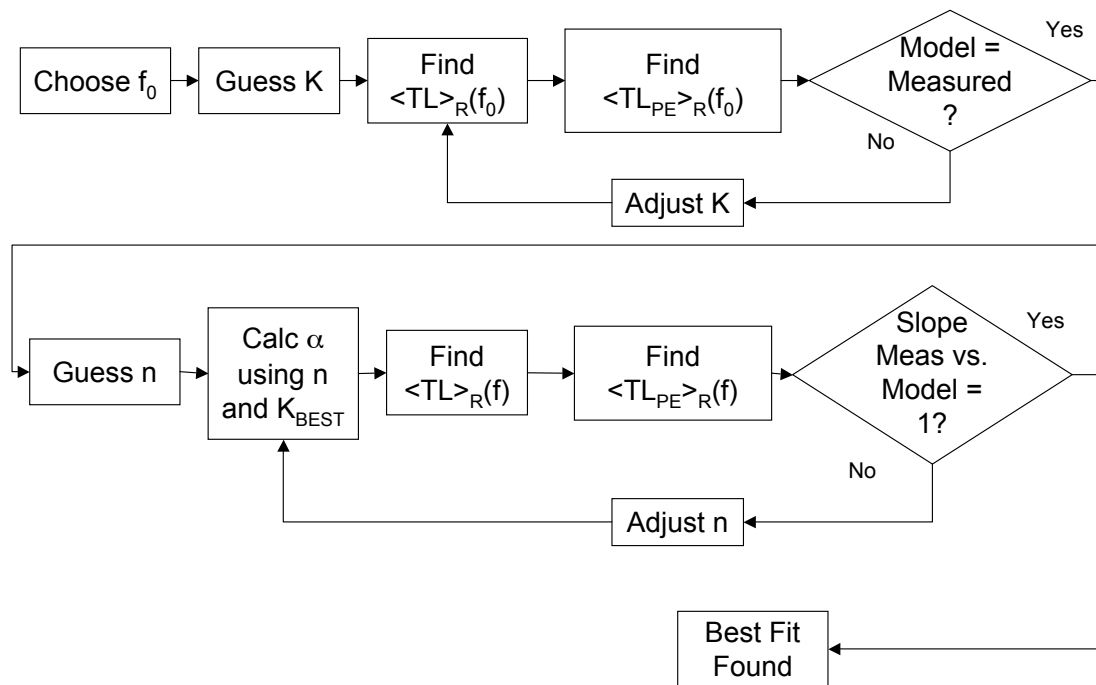


Figure 5.38: Flow chart depicting the iterative determination of the frequency dependent attenuation.

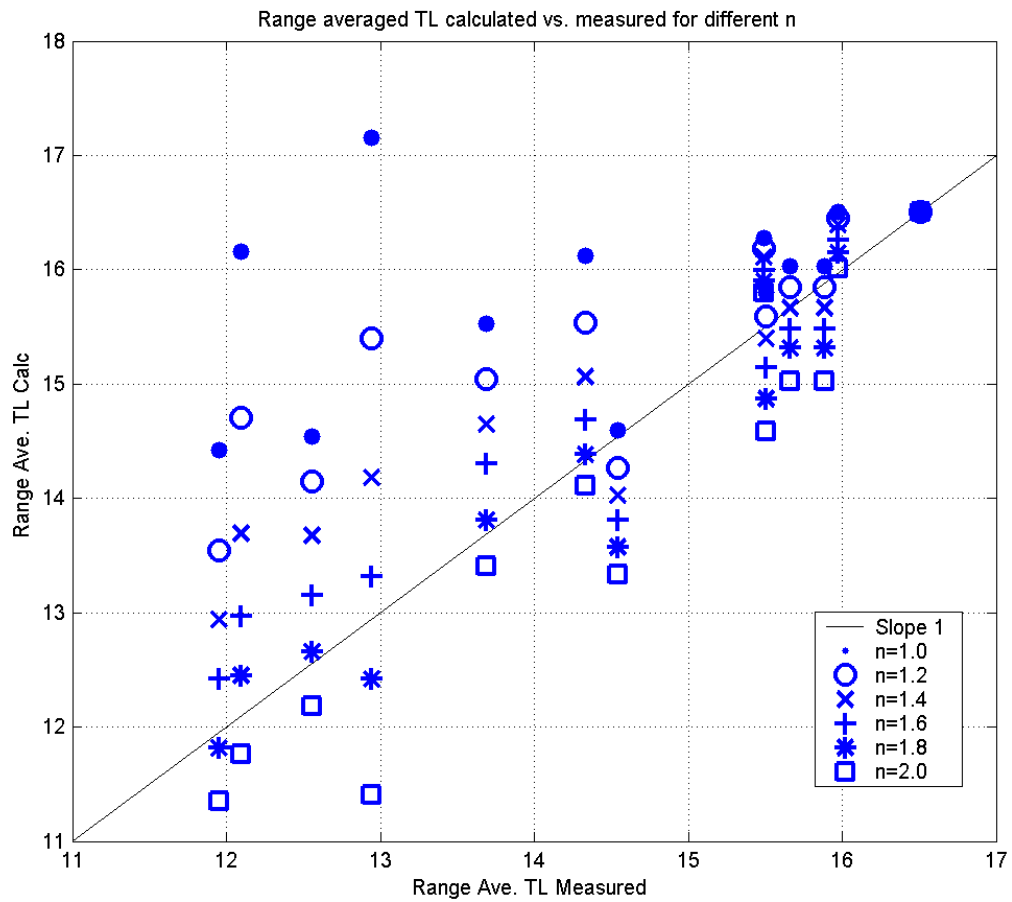


Figure 5.39: Comparison of measured and calculated transmission loss assuming an modified Biot profile with varying frequency dependence, 10 DEC 2005.

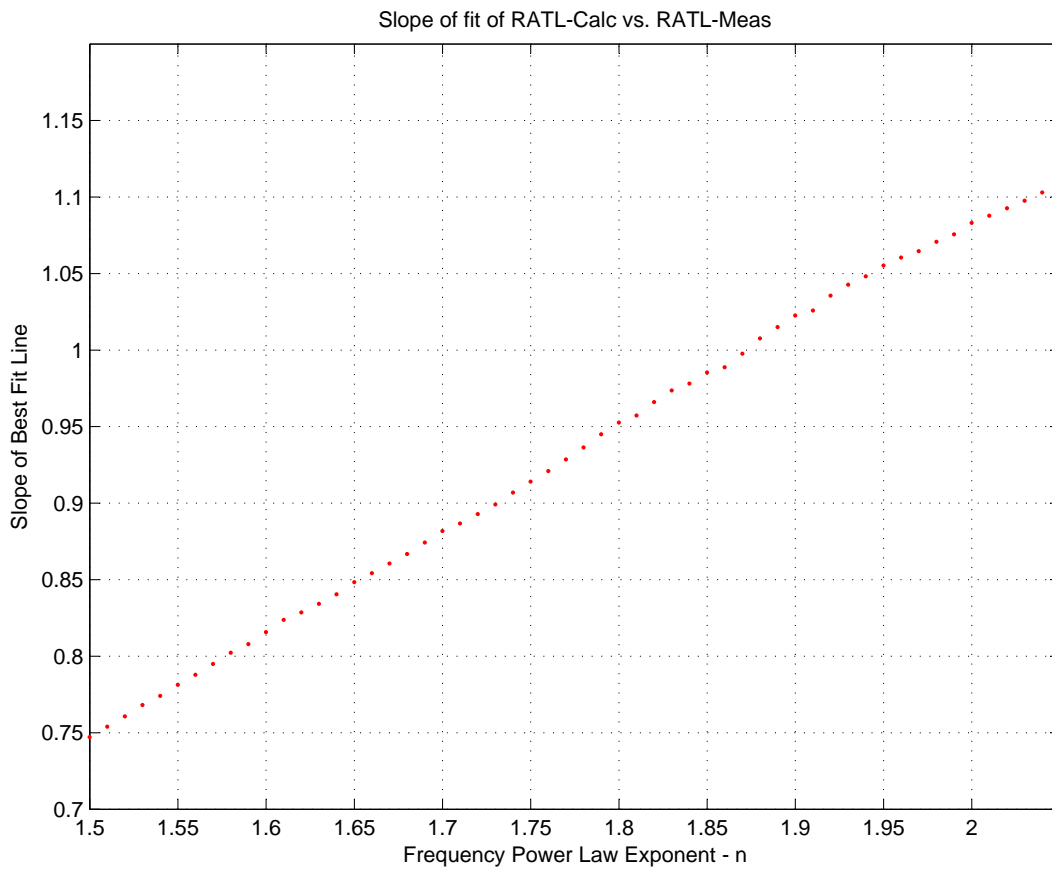


Figure 5.40: Slope of best fit between measured and calculated range averaged transmission loss assuming a modified Biot profile as a function of power law exponent, 10 DEC 2005.

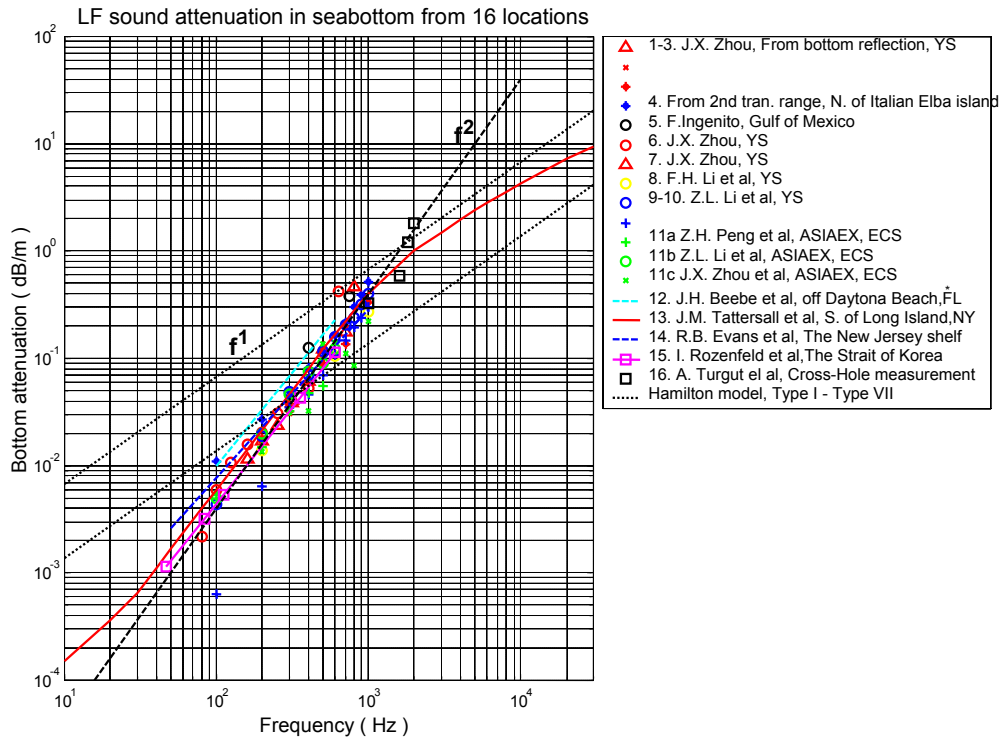


Figure 5.41: Attenuation in silty-sand sediments from 16 locations around the world, reported by Zhou and Zhang [41]

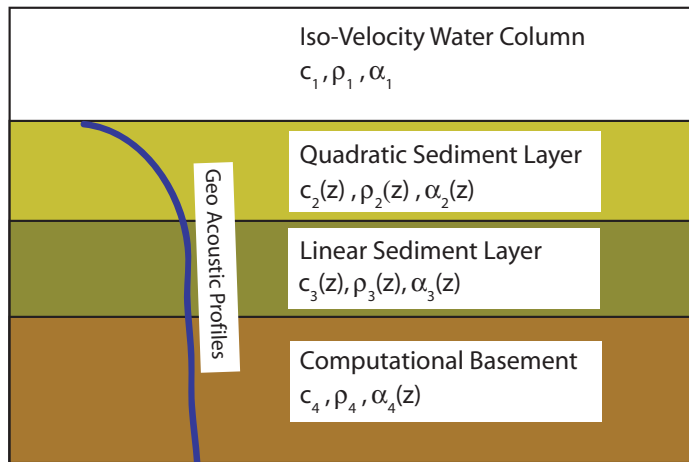


Figure 5.42: Schematic of the 3 layer geo-acoustic model used for a Biot bottom with an underlying constant Q layer. The sediment has a layer where attenuation is dependent on f^2 over a layer where attenuation is dependent on f^1 . The computational basement has uniform properties equal to the bottom of the sediment layer except that the attenuation increases at depth to prevent false returns.

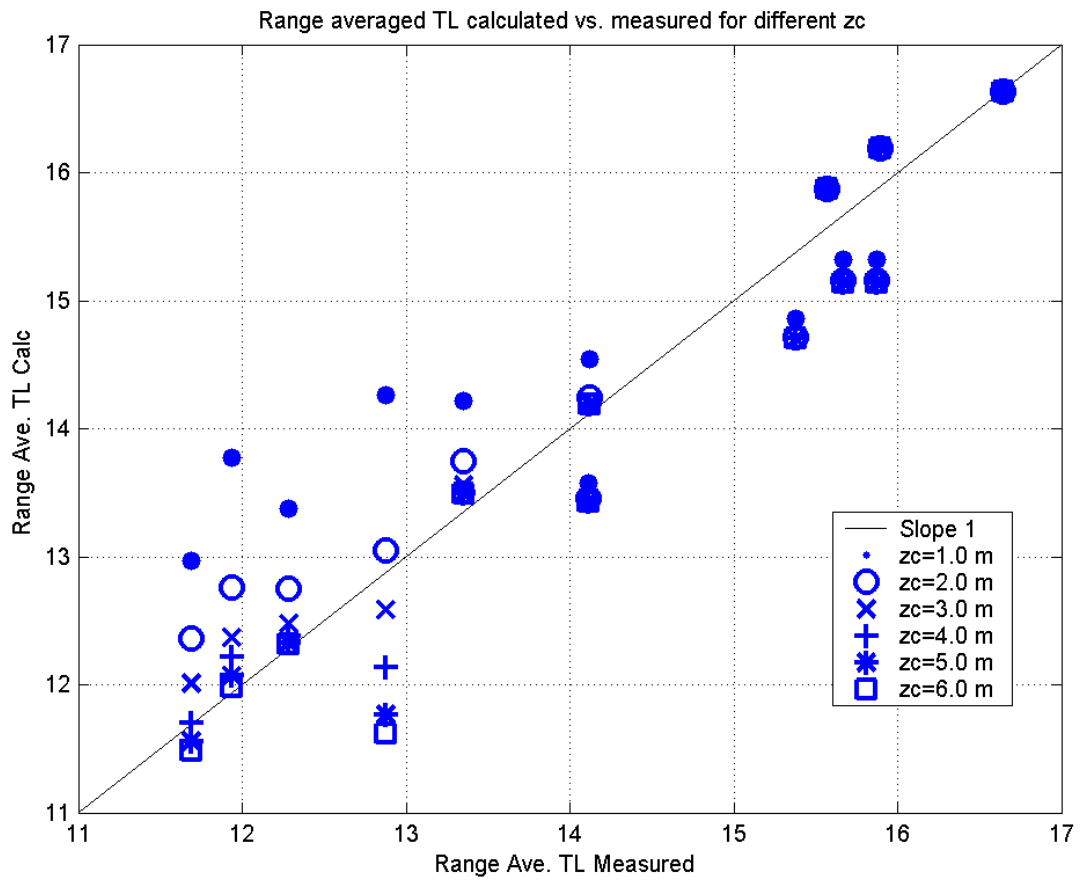


Figure 5.43: Comparison of measured and calculated transmission loss assuming a quadratic bottom over a linear bottom with varying layer thickness, 10 DEC 2005.

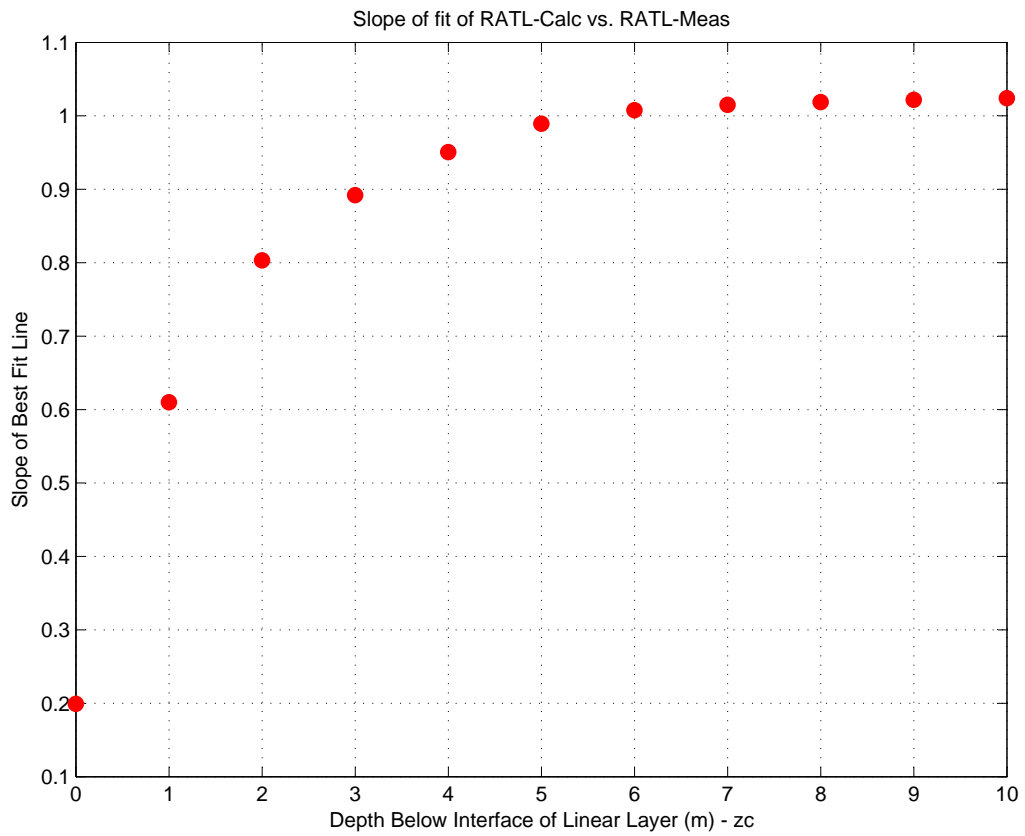


Figure 5.44: Slope of best fit between measured and calculated range averaged transmission loss assuming a quadratic bottom over a linear bottom as a function of layer thickness, 10 DEC 2005.

5.5 Error Analysis

In ocean acoustic measurements, the systems are often too complicated to propagate measurement errors through to a final result. In this case, the overlap processing provides a means to characterize the measurement error because the received signal level is measured at each range 6 times (see section 2.3.2). Figure 5.45 shows the standard deviation of the received signal level as a function of range for the measurements made in December. The standard deviation is determined at each range interval by

$$s = \sqrt{\frac{1}{N-1} \sum_{i=1}^N (RSL_i - \overline{RSL})^2}; \quad (5.23)$$

$$\overline{RSL} = \frac{1}{N} \sum_{i=1}^N RSL_i \quad (5.24)$$

where RSL_i is the received signal level on the i^{th} overlapped hydrophone at the given range, \overline{RSL} is the mean received signal level at that range, and N is the number of hydrophones in the array, in this case 6. Normalization by $N - 1$ is used in the sample standard deviation to produce an un-biased result. A standard deviation in the received signal level is not meaningful for the case where the received signal level is noise dominated because the reported standard deviation is then really that of the noise, not the signal. The signal is quasi-deterministic and the noise is random, so by definition the standard deviation is much higher for the case of noise. This is evident in figure 5.45 at the end of each run when the source is turned off. For example, at 1228 Hz the standard deviation when the source is on is on the order of 1 dB. When the source is off the standard deviation is on the order of 5 dB, in agreement with the 5.6 dB standard deviation of noise caused by distance sources predicted by Dyer [118]. Further, the peaks in the standard deviation seen for 220.5, 415, and 635 Hz correspond to the destructive interference nulls in the received signal levels where the received signal is noise dominated. In this case, one can consider the noise to be the contribution of the other tones, as well as distant noise, which would give an expected

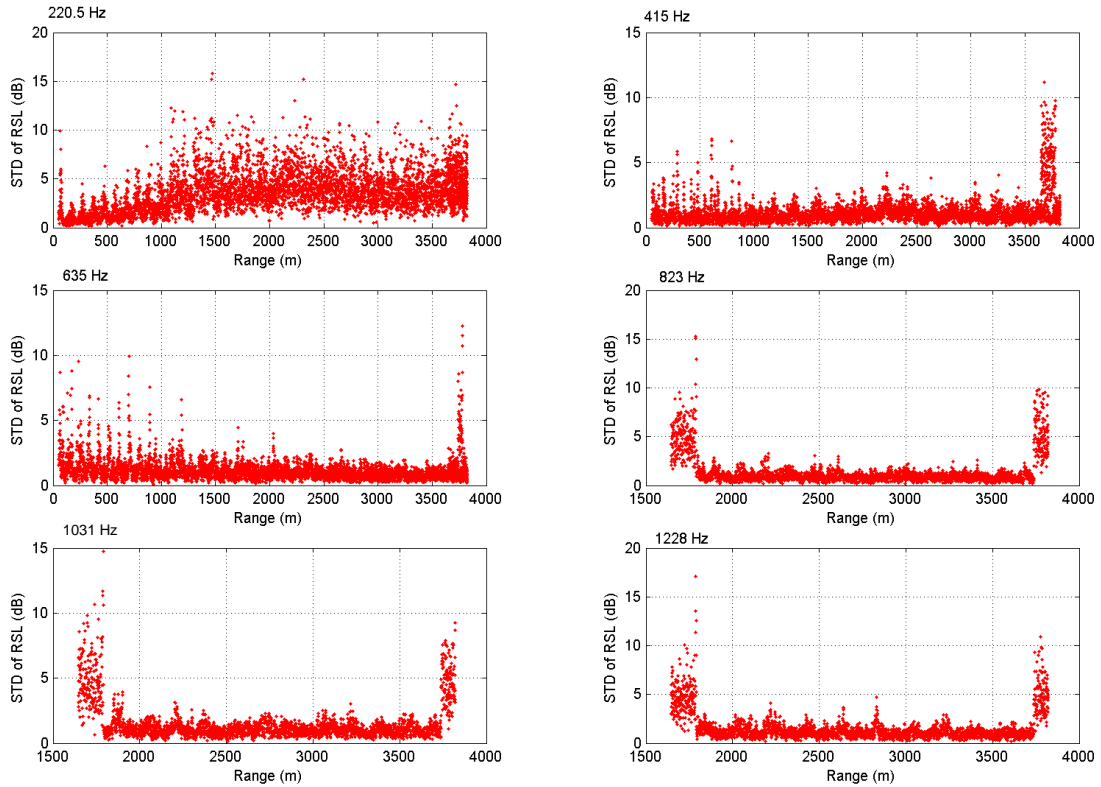


Figure 5.45: Estimated standard deviation of the received signal levels as a function of range and frequency.

standard deviation between 2.3 dB and 5.6 dB [118]. Therefore, in determining the error caused by the variation in the received signal level, one must exclude the artificially large standard deviations caused by interference effects. As an example, the standard deviation at 220.5 Hz for ranges less than 1 kHz is on the order of 1 dB even though the peaks approach 5 dB.

An average standard deviation was found for each frequency by fitting a line through the data shown in figure 5.45 such that the line followed the trend of data excluding the data points which were noise dominated. This gives the average standard deviation at 220.5 Hz as 4 dB and the standard deviation for all other frequencies as approximately 1 dB. It is then assumed that the error in the received signal level due to random variations is given by the standard deviation of the signal level so that the error can be propagated

to the reported range averaged values.

Transmission loss is given by

$$TL = SL - RSL \quad (5.25)$$

where SL is the source level. While this is truly a logarithmic equation, the process described in the previous section fits the levels, not the intensities. Thus using the measured standard deviations of levels is justified. In the experiment an accurate rubidium clock and a stable amplifier were used. Therefore, once set, the source level had negligible random errors. As discussed earlier, even though the source levels were monitored, they exhibited some absolute level bias uncertainties. These will be considered shortly.

From chapter 3, it is known that the calibration error for the array was $\pm 1.5dB$. Assuming the calibration errors and measurement errors of the received signal level to be independent and gaussian⁶ gives

$$E_{TL} = \sqrt{E_{Meas}^2 + E_{Calib}^2} \quad (5.26)$$

which then gives an average error in each transmission loss point of about 2 dB. From transmission loss, the range averaged transmission loss is calculated. If each point in range is viewed as an independent measurement of the range averaged transmission loss, then the error in the range averaged transmission loss measured is

$$E_{RATL} = \frac{E_{TL}}{\sqrt{N}} \quad (5.27)$$

where N is the number of range points in the interval. Using a range interval of 1km with

⁶It is recognized here that the probability density in the logarithmic domain is in fact given by $P(y) = (1/2\sigma^2)\exp(y - \exp(y)/2\sigma^2)$, the log density [118]. However, about the most probable point, the log density can be approximated by a gaussian density, which simplifies the analysis. It is shown that the source bias error dominates the uncertainty and this approximation thus does not affect the results.

a measurement spacing of 0.75m, $N \approx 1333$. Therefore,

$$E_{RATL} = \frac{E_{TL}}{36.5} \quad (5.28)$$

which gives the average error in range averaged transmission loss due to random effects as 0.055 dB.

The total error in the range averaged transmission loss also contains a bias due to the source level uncertainty. It is estimated that this uncertainty is on the order of 1dB. Since the random measurement errors are negligible compared to the bias error, the error involved with the fitting process is given by standard regression analysis with uniform weighting.

$$E_y = \sqrt{\frac{1}{M-2} \sum_{i=1}^M (y_i - A - Bx_i)^2}. \quad (5.29)$$

$$E_A = E_y \sqrt{\frac{\sum_{i=1}^M x_i^2}{\Delta}}. \quad (5.30)$$

$$E_B = E_y \sqrt{\frac{M}{\Delta}}. \quad (5.31)$$

$$\Delta = M \sum_{i=1}^M x_i^2 - \left(\sum_{i=1}^M x_i \right)^2. \quad (5.32)$$

Here y is the calculated range averaged transmission loss, x is the measured range averaged transmission loss, E' s are the associated errors for the variable denoted in their subscripts, M is the number of measurements, A is the intercept of the fit, and B is the slope of the fit. M here is the number of frequency and range interval $\langle TL \rangle_R$ measurements ($M = 13$) and is distinguished from N , the number of measurements of pressure made at each range ($N = 6$). Applying the regression analysis gives an error in the slope of ± 0.10 for all three models at the n which gave B closest to 1.0. This was also approximately the error in the slope for the other attempted values of n . This implies that the hypothesis of n with any value for which the best fit slope was between 0.90 and 1.10 was a true hypothesis with level of confidence 95%. The plot in figure 5.40 shows that this gives $1.74 < n < 2.04$

corresponding to an error

$$n = 1.87 \begin{matrix} +.17 \\ -.13 \end{matrix}. \quad (5.33)$$

The variation of n corresponding to assuming a Hamilton, Biot, or constant different depth profile was

$$n = 1.87 \begin{matrix} +.02 \\ -.17 \end{matrix}. \quad (5.34)$$

as given in table 5.5. Assuming the errors to be independent gives the final value of n including errors to be

$$n = 1.87 \begin{matrix} +.17 \\ -.21 \end{matrix}. \quad (5.35)$$

Since the error bounds on the value of n are larger than the differences between the values of n for the different bottom profiles, all three bottom profiles pass the hypothesis test. The hypothesis that the frequency dependence of the attenuation in the sediment was anything outside of 1.66 to 2.04, is rejected. The hypothesis presented by the simplified Biot theory that the frequency dependence is quadratic is accepted by this hypothesis test.

Chapter 6

Summary and Conclusions

6.1 The System and Experiment

In this work, the acoustics of ocean sediments near the water-sediment interface has been investigated using autonomous technology. The motivation was the need for site specific sediment data and the monetary and time costs associated with doing so with a traditional experiment involving ships, long towed array and moored assets. It was hypothesized that an autonomous underwater vehicle towed hydrophone array could provide accurate, cost efficient, and timely results if the problems of drag, power, and vehicle noise could be overcome.

A six channel prototype array was carefully constructed to be low-noise and exhibit low drag. This prototype was attached to a recording system composed of off-the-shelf components and strapped to the underside of a REMUS AUV as a proof of concept system. The vehicle and array system was characterized, calibrated, and optimized with controlled tests at a Navy facility and at-sea engineering tests in Buzzards Bay, MA. Vehicle radiated noise measurements indicated that separation of the acoustic sensors from the hull was indeed needed which supported the use of a towed array. It was also shown that, while the system was unstable when the array was attached in an unfavorable location, careful consideration of the array attachment point allowed for the built in AUV feedback control

system to stably tow the array. The drag was estimated to be 14.3 N while the drag expected by comparison to U.S. Navy tow tests was 11.2 N. The difference between the measured drag and estimated drag was attributed primarily to the high drag drogue used in the prototype array. This drogue was included to straighten the array and minimize array motion, both of which were determined to be small enough to be negligible at the lowest frequencies. At higher frequencies, the effect of vehicle controller oscillations and array motion were characterized.

While an angle dependent reflection coefficient experiment was also theoretically proposed, the synthetic aperture Hankel Transform characterization of the sediment was chosen to prove the effectiveness of the system to perform at-sea measurements. In an experiment performed in Nantucket Sound in September of 2005, the AUV towed array system successfully maintained a steady depth and course radially out from a source to 2 km while recording the received complex pressure at 635, 823, 1031, and 1228 Hz. In December of the same year, the course was extended out to 4 km and back using frequencies down to 220.5 Hz in an iso-velocity water column.

Comparison of the relative array signal gain to theoretical limits as a function of the length of the synthetic aperture was used to determine the processing limits of the system. Assuming that the array was straight, stable, and followed the path of the vehicle allowed for the formation of a synthetic aperture that was on the order of the longitudinal coherence length of the waveguide. This indicated that more advanced shape estimation, motion compensation, and overlap correlation were not required at low frequency to form a synthetic aperture in the end-fire direction, a requirement of the Hankel transform technique.

A pre-experiment site survey was performed to characterize the test site before conducting the Nantucket Sound experiment. The goal was to characterize the bottom in the area with non-acoustic means so that a multi-parameter inversion for bottom properties was not required. The survey included a precision depth sounder as well as bottom samples. Using this data, a model of the depth dependent geo-acoustic profiles was determined that was consistent with the literature and with the derived theory.

While the experiment was carefully setup and performed, in the first attempt at using the AUV towed array to characterize the bottom, unanticipated problems caused differences in the measured and modeled wavenumber spectra. During post-calibration, it was found that the acoustic source had broken and was exhibiting directional properties. This explained the differences between the measured and modeled spectra. In the December 2005 experiment, a different source was used and after accounting for source uncertainties and navigational errors, the horizontal wavenumber spectra were recovered. A comparison of the spectra of the measurements with those produced by propagation codes verified the assumed sound speed and density profiles in the sediment. The high quality of the measured spectra also demonstrated the ability of the AUV towed array system to take advantage of the physical aperture of the array to improve the signal to noise ratio.

The measured values of the received signal as a function of range also exhibited attenuation related phenomena that agreed well with theory. Taking advantage of the finite aperture, and using a sliding range window over the data, modal amplitudes were recovered as a function of range that indicated the modal attenuation coefficients. The recovered modal attenuation coefficients were consistent with the modeled attenuation profiles, but inversions using the modal attenuation coefficients to find the depth dependent profiles had large error bounds. A hypothesis testing approach was then adopted but required accurate modeling of the transmission loss which, in turn, required knowledge of the range dependence of the geo-acoustic properties.

Variations of modal eigenvalues with range measured using the sliding window synthetic Hankel transform were almost completely described by the bathymetry change with range, revealing that the bottom was nearly range independent. This supported the assumption that, while slightly range dependent, the bottom could be approximated by a range independent model assuming an average profile for sound speed, density, and attenuation.

Range dependence in the sediment sound speed profile affects the phase of the interference patterns in the received field but does not significantly affect the range averaged transmission loss. This supported the use of a range independent model with range aver-

aged transmission loss as the basis for comparison to recover attenuation properties. The effect of assuming the wrong depth dependence of attenuation was shown by comparing the results using a profile consistent with Biot theory, a constant profile, and power profile consistent with Hamilton. The frequency dependence of the attenuation in the sediment was determined by finding the frequency dependent exponent which provided the best least squares fit of the data with the forward model. Hypothesis testing showed that the three suggested depth dependent profiles were supported by the data, but a true hypothesis was only found for a non-linear frequency dependent exponent of $n = 1.87$, ($s = -0.21, +0.17$). Considering the sediment as a composite, the depth variation predicted by the simplified Biot theory is physically sound and proportional to $c^{-1}(z)$. This derived simplified Biot theory gave a frequency dependence of f^2 , but the lower exponents given by the measurements were explained by a depth variation of the attenuation power law due to compaction. The usefulness of the simplified Biot theory was thus demonstrated because models using only the three parameters in the simplified theory (c , ρ , and τ_B) were able to accurately model long range transmission loss while the full Biot theory would require significantly more parameters. Further, the inferred attenuation agreed in both magnitude and frequency dependence with a summary of recent measurements for silty-sand bottoms.

The quality of the measurements provided by the REMUS towed array system demonstrated that this system was capable of making accurate measurements of site specific boundary conditions at the water-sediment interface. While this type of experiment motivated the design and construction of an AUV towed array system, it is only one of many potential applications of this new measurement system. For example, it can also be used as a cheap surveillance system capable of monitoring ports and providing acoustic intelligence in enemy waters. Range corrections provided by acoustic measurements on the array can also reduce the navigational error of navigating an AUV by dead reckoning.

6.2 Future Directions

As with any work that presents new measurements using a new measurement system, this dissertation has both answered questions and brought new questions about. It was shown that the developed system was effective as an accurate and economical ocean measurement system and that the derived theory explained the frequency dependence of the observed measurements. At the same time, alternate experiments, new navigational correction schemes, different uses for the new system, and new hardware were suggested.

Focusing first on a second experiment that can be performed with this system, one need only look back to Chapter 2 to see that a bottom loss as a function of grazing angle experiment was suggested. The idea was that the bottom loss curve contains information about the mechanics of the sediment and can thus be used to infer sediment properties. The vehicle and array system would simply be required to navigate through several constant altitude-from-bottom paths to determine an experimental bottom loss curve by exploiting the directional characteristics of the towed array. The reason this was not performed here is because this measurement would be very sensitive to noise corruption and would require the development of a low power, on-board, low frequency sound source for the AUV.

This brings about the second area of future directions, new hardware for the new system. If a low power, on-board, low frequency sound source were developed, the angle dependent reflection loss experiment could be performed. If the AUV towed array system were navigated very close to the bottom interface, this new source and receiver system could also be used to detect and measure the evanescent surface waves predicted for a water sediment interface.

Other new hardware components can also be envisioned. A pivoting harness for the tow point of the towed array would allow the vehicle to maintain a tighter radius of curvature if maneuverability became an issue. An internal recording system, which would eliminate the added drag of an external canister, should be considered a must for future systems and would enable the extension of mission times by the use of larger hard drives and lower

sampling rates. A longer array with more channels would improve the resolution of the system and digitizing the data within the array would limit the tow cable size to a few conductors, preventing an extreme increase in system weight with system length. Further, a dynamic, automatic ballasting system would enable the vehicle to dive with ease while towing an array and could include a fail safe to ensure the vehicle could surface under the largest water density variations expected in the ocean.

Making use of one of problems solved in this work, one could develop more robust navigational correction schemes for AUV's. In this work, acoustic correction schemes were described and used including doppler correction and shallow water modal correction. A vehicle which has the ability to take advantage of low frequency acoustic sensor output to use this navigational correction schemes to improve positional accuracy.

One could also extend the use of the AUV towed array system to applications not fully discussed in this dissertation. For example, passive synthetic aperture techniques could be applied to this system which would allow for the passive surveillance of ports. Coupled with the addition of an on-board low frequency source, this system could also be used to actively detect objects buried beneath the sediment.

With the addition of an internal recording system capable of longer recording times, since the vehicle samples the local environment at the position of the array, this system would be a perfect platform for studying the effect of oceanographic variability (internal waves and solitons) on acoustic transmission over long ranges. Additionally, this system allows for making multiple measurements at various frequencies, over the same section of ocean under various conditions. One could imagine studying transmission over a path with an iso-velocity water column and returning in a later season with a small boat of opportunity to perform the same measurement over the exact same path with a surface duct or similarly changed water profile.

Finally, the improvements that could be made to the measurements made in this dissertation would focus on minimizing the errors associated with the measurements. A future experiment could use the same geographic path in Nantucket Sound while including

frequencies not used in this experiment. More data points taken over the same patch of sediment will yield results with narrower error bands. Further, the use of alternate means to determine the modal attenuation coefficients could allow the use of the modal attenuation coefficient method developed in this work to more accurately determine the attenuation as a function of depth in the sediment with no assumed frequency dependence.

Appendices

Appendix A - Matlab Codes

Any programs which simply opened data files and plotted them were omitted to conserve space. Such codes are not illustrative. There are also several codes which are identical for the September and December experiments other than parameters. Codes that fall into this category are included only once and the changes required to use it for the other experiment are included in the comments. Some of the codes are shortened for brevity by omitting repetitive portions. Again, this is included in the comments.

Figure A.1 shows the flow of information between the program sub groups in order to complete the analysis in this thesis. Below the flow chart is a list of programs which were used in the calculations for each sub-group. A description of what each code does is included in the commenting for the code.

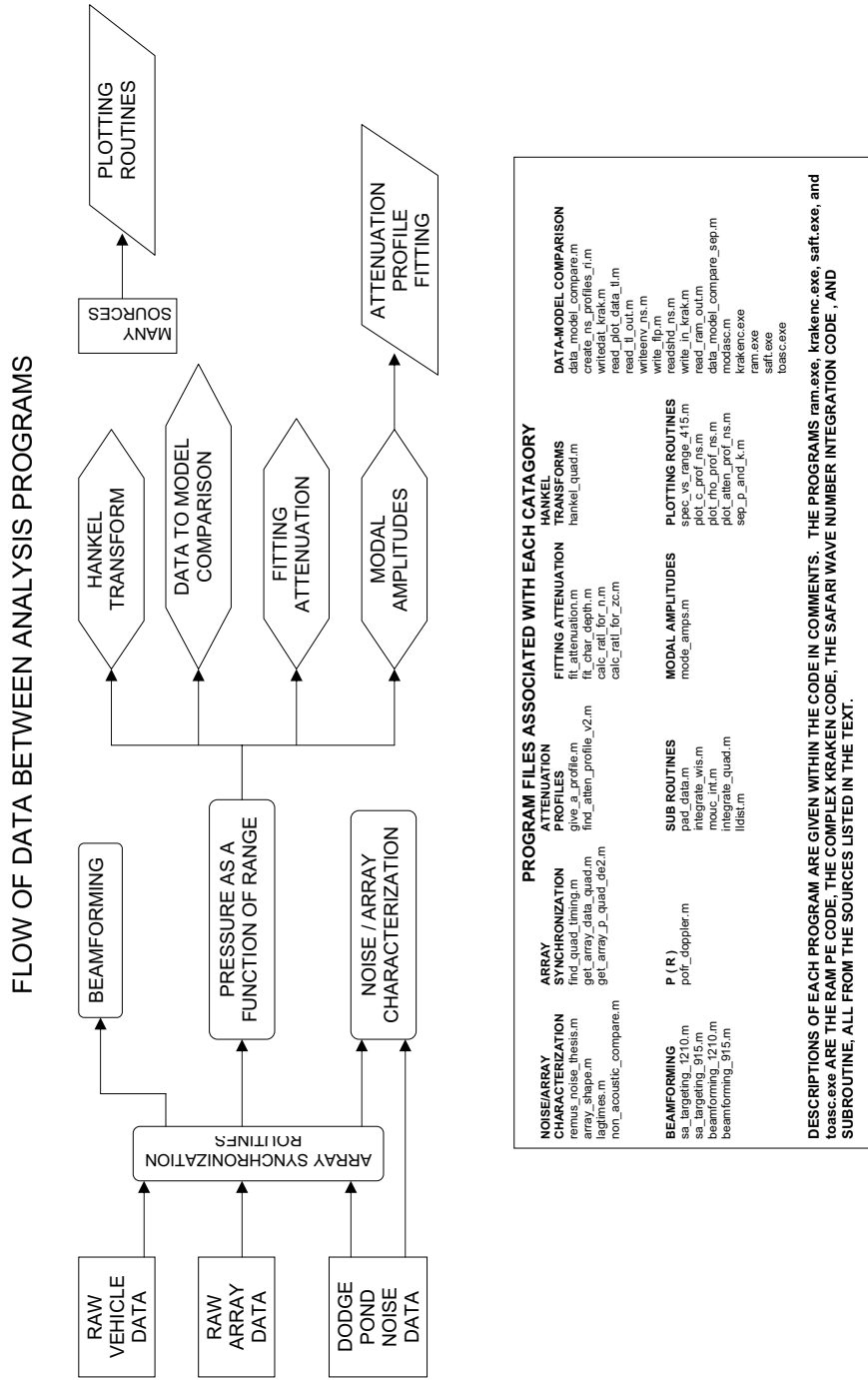


Figure A.1: Diagram showing flow of data in the computations. Each block represents a set of data or a computer program group. The arrows and lines indicate the input and output of each group and where they are used.

Codes Used in Main Analysis

arrayshape.m

```
%this m-file will take the previously calculated time delay data and
%compute a slope for each time sample, approximate a linear deviation in
%meters from a straight line for each channel at each time, and calculate a
%bearing to the 2500 Hz source. From this an estimate of the array shape
%can be made

load time_delay_data1
%load state1
c=1430;           % Approximate sound speed m/s
dh=.75;          % Separation between Hydrophones (m)
f=2500;          % Frequeuncy to Consider

%Create blank Data structures
slopes=[];
lin_dev=[];
phase_dev=[];

x=linspace(0,3.75,6); %position of the hydrophones relative to channel 1

%start a figure on which the time lags and slopes will be plotted.
figure;
hold on
for ii=1:size(test,1)

    t_meas=[0 test(ii,2:end)]; %the measured time lag to each channel for interval ii

    [P S]=polyfit(x,t_meas,1); %fit the time lags to a line
    slopes=[slopes P(1)]; %add to the slope output vector
    t_fit=x*P(1); %determine the fit times from the fit data
    t_dev=t_meas-t_fit; %determine the difference between the fit and measured
    if sum(abs(t_dev)>.1E-3)==0 %eliminate outliers due to bad processing.
        plot(x,t_meas,'bo-') %plot the measured time lags
        %construct the phase deviation and the spatial deviation output
        %vectors from the time lag differnce.
        phase_dev=[phase_dev; 360*t_dev*f];
        lin_dev=[lin_dev; [test(ii,1) t_dev*c]];
    end
end
%Plot the output:
grid
xlabel('Distance along array starting at first hydrophone (m)');
ylabel('Time Lag from Ch1');
title('Time Lag From Channel 1 vs. Array Location for Several Time Samples');

figure;
hold on

for ii=1:size(lin_dev,1)
    plot(x,lin_dev(ii,2:end),'ro');
    plot(x,lin_dev(ii,2:end),'r-');
end
plot(x,mean(lin_dev(:,2:end),1),'k*-');
xlabel('Distance along array starting at first hydrophone (m)');
ylabel('Distance deviation (m)');
title('Max Array Vertical Displacements from deviation from least squares fit of time delays');
grid
axis([0 3.75 -.15 .15])
```

beamforming_1210.m

```
%beamforming of data on Dec 10, 2005.

%this m-file will analyze the conventional as well as synthetic aperature beamforming for the Remus
%towed array run on Dec 10, 2005 aboard R/V Tioga

%This file is identical to beamforming_915.m except that it references the
%data for 10 DEC 2005 instead of 15 SEP 2005.

%The following is done in this program.

%1. get bf times by using the vehicle data
    %a. find x vs. t from remus log file
    %b. use spline interpolation to find t for x=N*array_length

%2. Use the get_array_p_quad function to find the complex pressures
%   at each one of these times t(N) thus forming P(x) for each freq

%3. In the same loop as step 2, find the beam formed output for each time
%t(N) for each frequency using
%   a conventional beamformer

%4. With P(r), loop over sub aperatures correcting each succuesive sub aperatures phase using the
%   recorder clock by subtracting 2*pi*f*t from the phase

%5. Compare average of step 3 with the SA case

%6. Compare the gain vs. #sub aperatures

%%%%%%%%%%%%%%%%%%%%%%%%%%%%%%%%%%%%%%%%%%%%%%%%%%%%%%%%%%%%%%%%%%%%%%%%
%Parameters: (Change these to adjust date, frequency, start point,etc.)
%%%%%%%%%%%%%%%%%%%%%%%%%%%%%%%%%%%%%%%%%%%%%%%%%%%%%%%%%%%%%%%%%%%%%%%%
%load ctd data to get sound speed
load 1210ctd      %CTD data from REMUs
c=sound_speed(end); %sound speed in m/s
%load remus data
load 1210state
remus_time=mission_time-44137.578+10*60+.5; %time shift found emprically
%set up array file structure for the 05121001 data set
struct=find_quad_timing(1210);

n_doppler=21; %number of points to use in doppler estimation

start_index=3800; %Sample number from REMUS nav data to begin at -use 3500 for return trip
vel_error=1-.021; %Estimated Navigational error mutliplier
is_noise=0; %Set to 1 if the measurment is noise
fs=1228; %Frequency (Hz) of desired Beamformer
f_interest2=1228; %Frequency (HZ) to stear to (demonstrates steering error if not == fs)
N_max=100; %Number of subaperatures to consider
d_sep_vec=[4.5]; %use 4.5 for sampling of 0.75m with no overlap
                %dictates the distance the array moves in between sub
                %aperatures
L=12; %meters behind REMUS of channel 1

%Tioga Coordinants:
T_lat=41.36679596; %Degrees Latitude
T_lon=-70.19930771; %Degrees Longitude

%Beamformer Constants
dt=.76; %seconds over which to perform fft
nfft=2^15; %NFFT
%setup angle vector to look over. We will use a coarse vector for conventional and a fine vector
```



```

%for the synthetic case
theta_fine=linspace(-pi/2,pi/2,301);
theta_coarse=linspace(-pi/2,pi/2,46);
%%%%%%%%%%%%%%%%%%%%%%%%%%%%%%%%%%%%%%%%%%%%%%%%%%%%%%%%%%%%%%%%%%%%%%%%

%set up cartesian coordinates with the source at the origin.
[x y d]=lldist(T_lat,T_lon,latitude,longitude);

%%%%%%%%%%%%%%%%%%%%%%%%%%%%%%%%%%%%%%%%%%%%%%%%%%%%%%%%%%%%%%%%%%%%%%%%
%part 1:  a: find x vs. t from remus log file.

ndsep=length(d_sep_vec);    %number of seperations in d_sep_vec.  The
                            %program will cycle through these, so one
                            %could define a sequence of separations
                            %to try different sampling routines.

%start at x(start_index),y(start_index)
X=x(start_index);
Y=y(start_index);
T=remus_time(start_index);
x_last=X;                  %remember the coorindates from the previous loop
y_last=Y;
t_last=T;
fprintf('\n\nAssemble T and r vectors:\n\n');    %keep the user informed
nav_error=[];    %included to adjust nav error... not needed
for N=1:N_max
    %find distance from last point to each point in remus_time_short where remus_time_short is
    %remus time (current_index:end) where current index is given by the index of the first value of
    %remus_time such that remus_time>t_last
    fprintf('%i ',N);
    if mod(N,20)==0
        fprintf('\n');
    end
    ii=N-1;
    d_sep=d_sep_vec(mod(ii,ndsep)+1);
    current_index=min(find(remus_time>t_last));
    remus_time_short=[t_last remus_time(current_index:end)];
    x_short=x(current_index:end);
    y_short=y(current_index:end);
    dd=[0 sqrt((x_short-x_last).^2+(y_short-y_last).^2)];

    %now interpolate for the time where dd=4.5
    t_current=interp1(dd(1:20),remus_time_short(1:20),d_sep,'linear');
    %included indexing to avoid come back error
    T=[T t_current];

    %now use t_current to interpolate x_current and y_current
    x_current=interp1(remus_time,x,t_current,'linear');
    y_current=interp1(remus_time,y,t_current,'linear');

    %now form X and Y
    X=[X x_current]; Y=[Y y_current];
    x_last=x_current; y_last=y_current;
    t_last=t_current;
end

%Generate blank data structures to loop over
X_hphone=[]; Y_hphone=[];
Y_keep=Y;    %we'll need this later

x_h=(3.75:-.75:0)+L;    %hydrophone positions
x_h=-x_h;    %meters behind remus

```

```

dZ=sqrt(diff(X).^2+diff(Y).^2);
Z=[0 cumsum(dZ)]; %distance from origin

%loop over positions of REMUS found above to find the positions of the
%hydrophones, which should be on the same path and and x_h meters behind
ii_min=1;
for ii=1:length(Z)
    zeta=Z-Z(ii); %position behind remus
    if zeta(1)>min(x_h)
        ii_min=ii_min+1;
    else
        x_hphone_current=interp1(zeta,X,x_h,'linear');
        y_hphone_current=interp1(zeta,Y,x_h,'linear');
        X_hphone=[X_hphone x_hphone_current];
        Y_hphone=[Y_hphone y_hphone_current];
    end
end

T=T(ii_min:end); %times for signal evaluation
rr=sqrt(X_hphone.^2+Y_hphone.^2); %Source to hydrophone ranges.

for f_interest=fs %loop over all frequencies of interest
%intialize empty variables
beam_conv=[]; %conventional beam former output vs time and bearing
beam_SA=[]; %Synthetic aperture beam former output vs N_subaperture and bearing
P=[]; %complex pressure at each hydrophone position given in x
SA_gain=[]; %synthetic aperture gain vs. N_subaperutre
nSA=[]; %number of synthetic apertures
xx=[]; %x-positions
yy=[]; %y-positions
fprintf('\n\n Beamforming \n\n'); %keep the user informed

%loop over the vector of times for which we know the hydrophones are
%properly spaced and get the acoustic data at those points.
for ii=1:length(T);
    fprintf('%i ',ii);
    if mod(ii,20)==0
        fprintf('\n');
    end

    x_current=X_hphone(6*ii-5:6*ii);
    y_current=Y_hphone(6*ii-5:6*ii);
    xx=[xx x_current];
    yy=[yy y_current];
    %read in the array data starting at t_current
    [Y FS NBITS]=get_array_data_quad(T(ii)-dt/2,dt,struct);
    %get the complex P values for each f_interest including the effects of
    %doppler
    if exist('doppler_guess');
        [P_current v_est_dop]=get_array_p_quad_de2(Y,FS,f_interest,n_doppler,doppler_guess);
    else
        [P_current v_est_dop]=get_array_p_quad_de2(Y,FS,f_interest,n_doppler);
    end
    %%%%%%%%%
    clear Y
    P_current=P_current(6:-1:1); %Ranges and channels are in opposite order
    %now correct each complex pressure for the correct phase given by the time
    P_current=P_current*exp(-i*2*pi*f_interest*T(ii));

%now assemble the total pressure vector

```

```

P=[P P_current];

%now beamform the data:
Z=[];
x_rel=sqrt((x_current-min(x_current)).^2+(y_current-min(y_current)).^2);
x_rel=x_rel-mean(x_rel);
if x_rel(end)<x_rel(1) %incoming
    x_rel=-x_rel;
end
for a=theta_coarse
    S=exp(i*2*pi*f_interest2/c*x_rel*vel_error*sin(a));
    Z=[Z abs(S*P_current')];
end
beam_conv=[beam_conv Z'];

%now try the SA case

Z=[];

x_rel=sqrt((xx-min(xx)).^2+(yy-min(yy)).^2);
x_rel=x_rel-mean(x_rel);
if x_rel(end)<x_rel(1) %incoming
    x_rel=-x_rel;
end

for a=theta_fine
    W=eye(size(W)); %uniform shading
    S=exp(i*2*pi*f_interest2/c*x_rel*vel_error*sin(a)); %steering vector
    Z=[Z abs(S*W*P')];
end
beam_SA=[beam_SA Z'];
if is_noise==1
    SA_gain=[SA_gain 20*log10(mean(Z))-20*log10(mean(mean(beam_conv')))];
else
    SA_gain=[SA_gain 20*log10(max(Z))-20*log10(max(mean(beam_conv')))];
end

nSA=[nSA ii];

end

%Plot showing the locations of the hydrophones
figure
plot(X_hphone,Y_hphone,'ro');
xlabel('East-West (m)');
ylabel('North - South (m)');
title('Location of hydrophones for beamforming');
grid
axis equal

%surface plot of bf output for conventional array vs bearing, time
h1=figure;
set(h1,'renderer','zbuffer');
surf(theta_coarse*180/pi,T,20*log10(beam_conv'/1e-6))
axis([-90 90 min(T) max(T)])
view(2);
shading flat
xlabel('Bearing (degrees)');
ylabel('Time(s)');
colorbar
title({strcat('Conventional Beamformer output vs. time for f=',num2str(f_interest))...
;strcat('Mission on 10 DEC 05 - R/V Tioga - dB re \mu Pa^2 Range ~',num2str(mean(rr)))});

```

```

%surface plot of bf output for sa case vs. bearing, N
h1=figure;
set(h1,'renderer','zbuffer');
surf(theta_fine*180/pi,nSA,20*log10(beam_SA'/1e-6))
axis([-90 90 min(nSA) max(nSA)])
view(2);
shading flat
title({strcat('Synthetic Aperture Beamformer output vs. N_{sub-ap} for f=',num2str(f_interest))...
; 'Mission on 10 DEC 05 - R/V Tioga - dB re \mu Pa^2'});

```

```

%produce a plot of SA signal gain vs. N
figure
plot(nSA(2:end),SA_gain(2:end),'k');
hold on
plot(nSA,20*log10(nSA),'k--');
plot(nSA,10*log10(nSA),'k-.');
legend('S.A. gain','20 Log N','10 Log N');
title({strcat('Synthetic Aperture Relative Signal Gain Vs. N for f=',num2str(f_interest))});
grid
xlabel('N_{sub-aperture}');
ylabel('dB');

```

```

figure
plot(theta_fine*180/pi,20*log10(beam_SA(:,end)/1e-6),'b-');
hold on
plot(theta_coarse*180/pi,20*log10(mean(beam_conv'/1e-6)),'r--');
xlabel('Bearing (degrees)');
ylabel('dB re \mu Pa^2');
title({strcat('Conventional vs. Synthetic Aperture Beamforming for f=',num2str(f_interest))});
legend('Synthetic Aperture','Average Conventional');
text(-90,75,{strcat('N_{sub ap}=',num2str(N_max));'N_{array}=6'});

```

calc_ratl_for_n.m

```

function [ratl]=calc_ratl_for_n(freq_in,k_atten,f0,n,range,snr,date_num);

%this function will use RAM PE to calculate the range averaged transmission
%loss at the frequency contained in freq_in
%using an attenuation in the bottom given by a=k_atten(f/f0)^n. The
%range averaging will occur over the range given by the input range=[rmin
%rmax];

%snr is used to incorporate the effects of the noise floor. deep nulls
%that are more then snr below the peaks are not considered.
switch date_num
case 1210
%Bathymetry for RAM
rb=[0 600 1500 2300 3000 3600 5250]; %ranges in m
zb=[12.8 12.8 13.8 13.8 14 13.4 13.4]; %depths in m
c=1600; %approximate sound speed in the bottom

%file information for RAM
inpfil='nantucket1.dat';
root = inpfil( 1:length( inpfil ) - 4 );
write_root=inpfil( 1:length( inpfil ) - 5 );

%first, generate the standard data structure.
clear profiles

```

```

create_NS_profiles_RI;
alpha=profiles.alpha;
%update the frequency of the profile data
profiles.freq=freq_in;
%adjust the attenuation in the sediment for the correct frequency dependence
alpha_s=k_atten*(profiles.freq/f0)^(n-1)/f0*c;
profiles.cofz_s1(:,5)=alpha*alpha_s;

%run RAM
write_in_krak(profiles,write_root,rb,zb);
eval(['!ram.bat ',write_root]);
ram_data=read_ram_out(write_root);

ratl_min=range(1); %define the min and max range from the input
ratl_max=range(2);

%%%%%%%%%%%%%%%%%%%%%%%%%%%%%%%%%%%%%%%%%%%%%%%%%%%%%%%%%%%%%%%%%%%%%%%%
%Calculate the Range ave TL
%find the indices in the ram data corresponding to the range interval
I=find(((ram_data.R*1000)>ratl_min).*((ram_data.R*1000)<ratl_max));

rsl_max=min(ram_data.TL(I)); %find the max received signal level (min TL)
TL_data=ram_data.TL(I); %window the TL data for range
TL_range=ram_data.R(I)*1000; %convert to meters
J=find(TL_data<(rsl_max+snr)); %find the index in the range within snr of rsl_max
%compute the average of the remaining points.
ratl=mean(TL_data(J)-10*log10(mean(TL_range(J))));

case 915
%Bathymetry for RAM
rb=[0 200 1000 1600 3000 3600 5250];
zb=[10.6 13.5 13.5 14.0 14 14 14];
c=1660;

%first, generate the standard data structure.
clear profiles
create_NS_profiles_sep;
alpha=profiles.alpha;

%now do the same as above in the 1210 case. This is omitted in the
%copy provided in the dissertation to conserve space.
end

```

calc_ratl_for_zc.m

```

function [ratl]=calc_ratl_for_n(freq_in,k_atten,f0,zc,range,snr,date_num);

%this function will use RAM PE to calculate the range averaged transmission
%loss at the frequency contained in freq_in using an attenuation law in
%the bottom given by given by  $a=k\_atten(f/f0)^n$ . n is exactly 2 for depths
%less than zc below the sediment interface and exactly 1.0 for depths
%greater than zc from the interface. The range averaging will occur over
%the range given by the input range=[rmin rmax];

%snr is used to incorporate the effects of the noise floor. deep nulls
%that are more than snr below the peaks are not considered.

switch date_num
case 1210
%Bathymetry for RAM

```

```

rb=[0 600 1500 2300 3000 3600 5250]; %ranges in m
zb=[12.8 12.8 13.8 13.8 14 13.4 13.4]; %depths in m
c=1600; %approximate sound speed in the bottom

%file information for RAM
inpfil='nantucket1.dat';
root = inpfil( 1:length( inpfil ) - 4 );
write_root=inpfil( 1:length( inpfil ) - 5 );

%first, generate the standard data structure.
clear profiles
create_NS_profiles_RI;
alpha=profiles.alpha;
%update the frequency of the profile data
profiles.freq=freq_in;
%adjust the attenuation in the sediment for the correct depth
%dependence
c_prof=profiles.cofz_s1(:,2); %compressional wave speed
tau_b_s=k_atten/(f0^2)*2*c_prof(1); %biot time constant
%define the attenuation:
profiles.cofz_s1(:,5)=tau_b_s*(f0/freq_in+(1-f0/freq_in)*((z-min(z))<z_c))/2./c_prof*freq_in^2;
profiles.cofz_s1(:,5)=profiles.cofz_s1(:,5)/freq_in*c; %to put in correct units for code
%update the computational basement
profiles.cofz_comp(1,5)=profiles.cofz_s1(end,5);
profiles.cofz_comp(2,5)=profiles.cofz_s1(end,5);

%run RAM
write_in_krak(profiles,write_root,rb,zb);
eval(['!ram.bat ',write_root]);
ram_data=read_ram_out(write_root);

ratl_min=range(1); %define the min and max range from the input
ratl_max=range(2);

%%%%%%%%%%%%%%%%%%%%%%%%%%%%%%%%%%%%%%%%%%%%%%%%%%%%%%%%%%%%%%%%%%%%%%%%
%Calculate the Range ave TL
%find the indecies in the ram data corresponding to the range interval
I=find((ram_data.R*1000)>ratl_min).*((ram_data.R*1000)<ratl_max));

rsl_max=min(ram_data.TL(I)); %find the max recieved signal level(min TL)
TL_data=ram_data.TL(I); %window the TL data for range
TL_range=ram_data.R(I)*1000; %convert to meters
J=find(TL_data<(rsl_max+snr)); %find the index in the range within snr of rsl_max
%compute the average of the remaining points.
ratl=mean(TL_data(J)-10*log10(mean(TL_range(J))));

case 915
%Bathymetry for RAM
rb=[0 200 1000 1600 3000 3600 5250];
zb=[10.6 13.5 13.5 14.0 14 14 14];
c=1660;

%first, generate the standard data structure.
clear profiles
create_NS_profiles_sep;
alpha=profiles.alpha;

%now do the same as above in the 1210 case. This is omitted in the
%copy provided in the disertation to conserve space.
end

```

create_ns_profiles_ri.m

```
%create_NS_profiles_RI
%this m-file will be used to generate the base Nantucket Sound geo-acoustic
%profiles for use with KRAKEN-c, RAM PE, and Safari. The profiles are
%range independent even though the code is written in a general form to
%allow for inclusion of range dependence.

%the main output is a structure "profiles" which contains all of the
%necessary data.

%if the attenuation exponent is not defined, assume quadratic
if (exist('atten_exp')==0
    atten_exp=2;
end

%range independent
profiles.envfil = 'Nantucket_RD.env'; %file name
profiles.title= '''Nantucket Sound Range Independent'''; %plot title
profiles.freq = 1000; %Hz Source freq.
profiles.sd = 6.4; %meters Source Depth
profiles.rd =6.0; %meters Receiver Depth
profiles.rr = 0; %no reciever variations
profiles.rmax = 5.25; %km max range to consider
profiles.rmin = 0; %km min range to consider
profiles.nr = 7000; % number of reciever ranges

profiles.ranges(1)=0; %= profile ranges (0 for range independ)
profiles.n = 1; %number for profiles

%Info for SAFARI
profiles.options='N I J T'; %see safari manual
profiles.k=[2^14 1 2^14]; %safari k sampling
%%%%%%%%%%%%%%%%%%%%%%%%%%%%%%%%%%%%%%%%%%%%%%%%%%%%%%%%%%%%%%%%%%%%%%%%
%first range:
%if a parameter has 2 indecies, the first is the profile number
%corresponding to the ranges in profiles.ranges. Range dependence is built
%in by updating the profile information at the ranges in profiles.ranges.
%The second index is the layer number. If there is only one index it is the
%profile number

profiles.Nmedia(1) = 3; %number of media layers
profiles.topopt(1) = {''CVW''}; %top options see Kraken manual
profiles.Npts(1,1) = 300; %number of points to use in the mth media
profiles.Npts(1,2)= 300; %number of points to use in the mth media
profiles.Npts(1,3)= 300; %number of points to use in the mth media

profiles.sigma(1,1) = 0.0; % surface roughness
profiles.sigma(1,2) = 0.0; % surface roughness
profiles.sigma(1,3) = 0.0; % surface roughness

profiles.CL(1,1) = 0.0; %correlation length
profiles.CL(1,2) = 0.0; %correlation length
profiles.CL(1,3) = 0.0; %correlation length

profiles.Depth(1,1) = 13.0; %depth of water column
profiles.Depth(1,2) = 23; %depth of sediment
profiles.Depth(1,3) = 30; %depth of computational bottom

%the item profiles.cofz contains the names of the profile entries. For
%example here,the first layer in the first profile is called
%profiles.cofz_wc so profiles.cofz(1,1)={'cofz_wc1'}
%%%%%%%%%%%%%%%%%%%%%%%%%%%%%%%%%%%%%%%%%%%%%%%%%%%%%%%%%%%%%%%%%%%%%%%%
profiles.cofz(1,1) = {'cofz_wc1'};
```

```

profiles.cofz_wc1=[ 0 1467.45 0.0 1.0 0 0;           %sound speed profile in water
                  13.0 1467.75 0.0 1.0 0 0 ];      %z cp cs rho ap as
%%%%%%%%%%%%%%%%%%%%%%%%%%%%%%%%%%%%%%%%%%%%%%%%%%%%%%%%%%%%%%%%%%%%%%%%
profiles.cofz(1,2)= {'cofz_s1'};
%attenuation at surface of sed
alpha_s=0.3*(profiles.freq/1000)^(atten_exp-1)/1000*1500; % db/lambda
rho_s=1.7; %g/cm^3 Density
%sediment depths:
z_vec=13.0:0.5:23.0;
z_vec=z_vec';
%construct profile structure
profiles.cofz_s1=[z_vec zeros(size(z_vec)) zeros(size(z_vec))...
rho_s*ones(size(z_vec)) zeros(size(z_vec)) zeros(size(z_vec))];
profiles.cofz_s1(:,2)=1600+200*(1-exp(-.3*(profiles.cofz_s1(:,1)-profiles.cofz_s1(1,1))));

%depths for use later
z=profiles.cofz_s1(:,1);

%Attenuation
%%%%%%%%%%%%%%%%%%%%%%%%%%%%%%%%%%%%%%%%%%%%%%%%%%%%%%%%%%%%%%%%%%%%%%%%
%Hamilton Attenuation (Uncomment for use)
% alpha=((z.*(z>13))-13).^d_exp.*(z>13);
% I=find(z==13);
% alpha(I)=alpha(I+1);

%%%%%%%%%%%%%%%%%%%%%%%%%%%%%%%%%%%%%%%%%%%%%%%%%%%%%%%%%%%%%%%%%%%%%%%%
%Modified Biot Attenuation (Uncomment for use)
alpha=1./profiles.cofz_s1(:,2);

%%%%%%%%%%%%%%%%%%%%%%%%%%%%%%%%%%%%%%%%%%%%%%%%%%%%%%%%%%%%%%%%%%%%%%%%
%Uniform (Uncomment for use)
%alpha=ones(size(z));

%%%%%%%%%%%%%%%%%%%%%%%%%%%%%%%%%%%%%%%%%%%%%%%%%%%%%%%%%%%%%%%%%%%%%%%%
%Insert the Attenuation into the structure
alpha=alpha/alpha(1); %normalize to surface
profiles.cofz_s1(:,5)=alpha*alpha_s; %assumes serperable freq and depth.

%%%%%%%%%%%%%%%%%%%%%%%%%%%%%%%%%%%%%%%%%%%%%%%%%%%%%%%%%%%%%%%%%%%%%%%%
%%% Computational Bottom %%%
ac=profiles.cofz_s1(end,5);
profiles.cofz(1,3)= {'cofz_comp'};

profiles.cofz_comp=[23 profiles.cofz_s1(end,2) 0.0 1.7 0 0;
                  30 profiles.cofz_s1(end,2) 0.0 1.7 0 0];

profiles.botopt(1,:) = {'''A'''}; %see Kraken manual
profiles.bot_sig(1)=0.0; %bottom roughness
profiles.cpb(1)= profiles.cofz_s1(end,2); % pressure wave speed in the bottom
profiles.csb(1)=0; % shear wave speed in the bottom
profiles.rhob(1)=1.8; % density in the bottom
profiles.apb(1)=10; %comp. attenuation in the bottom at depth
profiles.asb(1)=20; %shear attenuation in the bottom at depth
profiles.cmin(1)=100; % mininum sound speed.
profiles.cmax(1)=2400; % maximum sound speed.
profiles.cmax_s(1)=1e6; %max sound speed for safari
profiles.cmin_s(1)=900; %min sound speed for safari
profiles.alpha=alpha; %for use outside profiles

```

data_model_compare.m

```

%data_model_compare_both
%this m-file will be used to compare the measured TL vs. the modeled TL for
%the dec 10 2005 experiment in Nantucket sound
%This version will use Safari, Kraken, and RAM
%All of the range average transmission losses have cylindrical spread
%removed

```



```

%change this data up front to use this code for the september data set as data_model_compare_sep

SL = [139.4 149.8 156.7 159.4 159 155.2 156]; %Source Levels
Freq=[220.5 415 635.0001 635 823 1031 1228];% Source frequenices
snr=[8 10 10 10 10 10 10]; %Used to get rid of deep nulls
atten_exp=2; %attenuation frequency exponent.
k_att=0.3; %attenuation constant @ 1k
SL=SL+3; %account for the fact that measurments are amplitude and SL is rms

%min and max range for range averaged TL measurement
ratl_min=1000;
ratl_max=2000;

direction=[1 1 1 -1 -1 -1 -1]; %indicates the direction the vehicle
is traveling for each data set %1 indicates outgoing -1 indicates
%incoming

%DATA files. These are output from the pofr_doppler command for each freq.
files={'pofr_220_dop.mat','pofr_415_dop.mat','pofr_635_dop_out.mat',...
'pofr_635_dop.mat','pofr_823_dop.mat'...
,'pofr_1031_dop.mat','pofr_1228_dop.mat'};

%Bathymetry for RAM
rb=[0 600 1500 2300 3000 3600 5250];
zb=[12.8 12.8 13.8 13.8 14 13.4 13.4];

%Open a figure on which to plot the RATL
fratl=figure;

%Loop over all of the frequencies
for sig_freq=[220.5 415 635.0001 635 823 1031 1228];%[220.5 415 635.0001 635 823 1031 1228];
%the 635.0001 frequeny allows for differentiation between inbound and
%outbound
iff=find(Freq==sig_freq); %frequency index

%saferi input file
inpfil='nantucket1.dat';
root = inpfil( 1:length( inpfil ) - 4 );
write_root=inpfil( 1:length( inpfil ) - 5 );

%plot the measured data vs. range
load(char(files(iff))); %load the correct input file

%Use emperical range corrections found from the bahtymetry, k-spectrum, doppler, and GPS
total_travel=cumsum(diff(abs(R_ave))); %total travel
ddr=[0 diff(R_ave)]; %range differences
total_travel=[0 total_travel]; %REMUS starts at 0
%percent error change as a function of range:
percent_error=2.1/100.*(ddr>0)-3.3/100*(ddr<0);

drift_error=cumsum(ddr.*percent_error); %find range error
R_out=R_ave-20-drift_error; %correct range including offset

%determine which data points are inbound and which are outbound
outgoing=zeros(size(R_ave));
for jj=2:length(R_ave);
if R_ave(jj)>R_ave(jj-1);
outgoing(jj)=1;
else
outgoing(jj)=-1;
end
end

```

```

end
outgoing(1)=outgoing(2);
I=(outgoing==direction(iff)); %changes index to only include the correct direction
I=find(I);

%determine and plot the TL
TL=-(20*log10(abs(P_ave)/1e-6)-SL(iff));
fn=figure;
subplot(2,1,1);
plot(R_out(I),TL(I),'r.','Color',[.5 .5 .5]);

%range averaged tl
rr=R_out(I);
tl=TL(I);
I=find((rr>ratl_min).*(rr<ratl_max));
ra_tl=mean(tl(I))-10*log10(mean(rr(I)));
figure(frat1);
hold on
plot(Freq(iff),ra_tl,'r.');
```

```

%%%%%%%%%%%%%%%%%%%%%%%%%%%%%%%%%%%%%%%%%%%%%%%%%%%%%%%%%%%%%%%%%%%%%%%%
%%%%%%%%%%%%%%%%%%%%%%%%%%%%%%%%%%%%%%%%%%%%%%%%%%%%%%%%%%%%%%%%%%%%%%%% Numerical Modeling %%%%%%%%%
%First, generate the standard data structure.
clear profiles
create_NS_profiles_RI;
%generate the extra data stucture needed by the field program
opt1='R'; %cylindrical coords
opt2='A'; %adiabatic model
field.opt=strcat('','opt1,opt2,');
field.nmodes=9999;
```

```

%adjust the profile frequency to the correct frequency
profiles.freq=sig_freq
%adjust the attenuation in the sediment for quadratic attenuation
alpha_s=k_att*(profiles.freq/1000)^(atten_exp-1)/1000*1500;
profiles.cofz_sl(:,5)=alpha*alpha_s;
%%%%%%%%%%%%%%%%%%%%%%%%%%%%%%%%%%%%%%%%%%%%%%%%%%%%%%%%%%%%%%%%%%%%%%%%
%safrari

writedat_krak(profiles,write_root);

%run safari
eval(['!saft ', root]);

%read in the TL data
read_plot_data_tl
read_tl_out;
id = 1; %default to the first depth

%%%%%%%%%%%%%%%%%%%%%%%%%%%%%%%%%%%%%%%%%%%%%%%%%%%%%%%%%%%%%%%%%%%%%%%% Find the calc and plot it.
rs=TL_data(:,1,id)*1000;
tls=TL_data(:,2,id);
I=find((rs>ratl_min).*(rs<ratl_max));
rsl_max=min(tls(I));
TL_data2=tls(I);
TL_range=rs(I);
J=find(TL_data2<(rsl_max+snr(iff))); %this removes the deep nulls
ratl=mean(TL_data2(J)-10*log10(mean(TL_range)));
figure(frat1);
hold on
plot(profiles.freq,ratl,'ks');
```

```

%plot the TL data
figure(fn)
subplot(2,1,1);
hold on
plot(TL_data(:,1,id)*1000,TL_data(:,2,id),'k-'); %tl data in safari is in km not m

%%%%%%%%%%%%%%%%%%%%%%%%%%%%%%%%%%%%%%%%%%%%%%%%%%%%%%%%%%%%%%%%%%%%%%%%
%kraken
%write the env file
writeenv_NS;
%write the field file
write_flp;
%run krakenc
eval(strcat('!krakenc < ',profiles.envfil));
%run field
eval(strcat('!field < ',field.flpfil));
%run toasc.exe
!toasc.exe

%read in the ascii data file and plot it
filename='ascfil'; isd=1;
readshd_NS;

%plot the TL data
figure(fn)
subplot(2,1,1);
hold on
plot(rr,-20*log10(abs(pressure_c)),'b:')

%Calc and plot range averaged tl

I=find((rr>ratl_min).*(rr<ratl_max));
rsl_max=min(-20*log10(abs(pressure_c(I))));
TL_data=-20*log10(abs(pressure_c(I)));
TL_range=rr(I);
J=find(TL_data<(rsl_max+snr(iff))); %this removes the deep nulls
ratl=mean(TL_data(J)-10*log10(mean(TL_range)));
figure(fratl);
hold on
plot(profiles.freq,ratl,'b*')

%%%%%%%%%%%%%%%%%%%%%%%%%%%%%%%%%%%%%%%%%%%%%%%%%%%%%%%%%%%%%%%%%%%%%%%%

%RAM
% %write the in file
write_in_krak(profiles,write_root,rb,zb);
eval(['!ram.bat ',write_root]);
ram_data=read_ram_out(write_root);

%plot the TL data
figure(fn)
subplot(2,1,1);
hold on
plot(ram_data.R*1000,ram_data.TL,'r--');

%Calc and plot the range ave TL
I=find(((ram_data.R*1000)>ratl_min).*((ram_data.R*1000)<ratl_max));
rsl_max=min(ram_data.TL(I));
TL_data=ram_data.TL(I);

```

```

    TL_range=ram_data.R(I)*1000;
    J=find(TL_data<(rsl_max+snr(iff)));
    %ra_tl=mean(TL_data(J)-10*log10(mean(TL_range(J))));
    ra_tl=mean(TL_data(J)-10*log10(mean(TL_range)));
    figure(fratl);
    hold on
    plot(profiles.freq,ra_tl,'gd')

%%%%%%%%%%%%%%%%%%%%%%%%%%%%%%%%%%%%%%%%%%%%%%%%%%%%%%%%%%%%%%%%%%%%%%%%
%Format the figures:
figure(fn)
subplot(2,1,1);
xlabel('range (m)')
ylabel('TL');
set(gca,'ydir','reverse')
grid
legend('Data','Safari','Kraken','RAM PE');
title(strcat('Comparison of measured vs. result from Safari for F=',num2str(sig_freq),...
' RD= ',num2str(profiles.rd(1))));
%plot the computational c profile
subplot(2,3,4);
plot_c_prof_NS;
axis([1400 1900 0 30]);
%plot the computational rho profile
subplot(2,3,5);
plot_rho_prof_NS;
axis([.9 2 0 30]);
%plot the computational atten profile
subplot(2,3,6);
plot_atten_prof_NS;
axis([0 1 0 30]);
end

%Format the RATL vs. FREQ figure
figure(fratl);
grid
legend('Data','Safari','Kraken','RAM PE');
xlabel('Frequency (Hz)');
ylabel('Range Ave. TL (spreading removed)');
title(strcat('Range Averaged TL vs Frequency for range interval :',num2str(ratl_min),...
'-' ,num2str(ratl_max)));

```

find_atten_profile_v2.m

```

%find_atten_prof_v2

%this is a revised version of the program to find the attenuation profile
%in the sediment. It uses a golden section search method to optimize the
%error between measured and modeled values to determine the best fit
%attenuation profile over all normalized modal attenuation coefficients.

%first, generate the standard data structure.
create_NS_profiles_RI;

%%%%%%%%%%%%%%%%%%%%%%%%%%%%%%%%%%%%%%%%%%%%%%%%%%%%%%%%%%%%%%%%%%%%%%%%
% %%%%%%%%%%
%for 415 Hz data set
%MACS:
mode_alpha=[.00013489 -.00014661 .0015005 .0018467];
%set the frequency
freq=415;
modes_used=[3 4];

```

```

%%%%%%%%%%%%%%%%%%%%%%%%%%%%%%%%%%%%%%%%%%%%%%%%%%%%%%%%%%%%%%%%%%%%%%%%
%update the profiles for many depths and the new frequency
dz=0.1; %separation between depths in the vector z
profiles.freq=freq;
%find the depth of the last layer
max_depth=profiles.Depth(end);
%setup the new receiver depth vector
rd_new=0:dz:(max_depth);

profiles.rd=rd_new;
profiles.rr=zeros(size(rd_new));
%%%%%%%%%%%%%%%%%%%%%%%%%%%%%%%%%%%%%%%%%%%%%%%%%%%%%%%%%%%%%%%%%%%%%%%%

%generate the extra data structure needed by the field program
opt1='R'; %cylindrical coords
opt2='A'; %adiabatic model
field.opt=strcat(' ',opt1,opt2,' ');
field.nmodes=9999;
%%%%%%%%%%%%%%%%%%%%%%%%%%%%%%%%%%%%%%%%%%%%%%%%%%%%%%%%%%%%%%%%%%%%%%%%
%% KRAKEN %%%%%%%%%
%write the env file
writeenv_NS;
%write the field file
write_flp;

%run krakenc
eval(strcat('!krakenc < ',profiles.envfil));

%run field
eval(strcat('!field < ',field.flpfil));

%run toasc.exe
!toasc.exe

%read in the ascii data file and plot it
filename='ascfil'; isd=1;
readshd_NS;

%convert the mod file to asc
modasc;

%get the mode info
[M z ck]=get_modes; %modification of the code with Kraken. Returns Mode functions, depths and k's
[num_depths num_modes]=size(M);
%%%%%%%%%%%%%%%%%%%%%%%%%%%%%%%%%%%%%%%%%%%%%%%%%%%%%%%%%%%%%%%%%%%%%%%%
%determine the depth dependent sound speed, and density as well as the phase
zc=[0 profiles.cofz_s1(1,1)-.001 profiles.cofz_s1(:,1) profiles.cofz_s1(end,1)+.001 max_depth];
c=[profiles.cofz_wc1(:,2) profiles.cofz_s1(:,2) profiles.cofz_comp(1,2) profiles.cofz_comp(end,2)];
cc=interp1(zc,c,z,'linear');
%this gets the sound speed profile on the find z grid using the data from the input file

rho=ones(size(cc))+0.7*(z>=13); %1.0 before 13m and 1.7 after
rho=rho*100^3/1000; %convert g/cm^3 to kg/m^3

%%%%%%%%%%%%%%%%%%%%%%%%%%%%%%%%%%%%%%%%%%%%%%%%%%%%%%%%%%%%%%%%%%%%%%%%
%now we perform golden section minimization
L=(3-sqrt(5))/2; K=1-L; %the golden section fractions

%define the starting guesses for gamma based on the golden sections
gamma_guess=[-2 -2*L-(L*K) -2*L 0];

%set up the depth dependent attenuation profiles
atten_hat=[];

```

```

for ii=1:4
    a_temp=give_a_prof(z,gamma_guess(ii));
    atten_hat=[atten_hat a_temp'];
end

%now set up the initial error vector
E=[];
for ii=1:4
    [G D]=find_gd(atten_hat(:,ii),M(:,modes_used),freq,z,ck(modes_used),rho,...
    cc,-mode_alpha(modes_used));
    fprintf('\n gamma %g \t\t G %g\t\t D %g\n',gamma_guess(ii), G(end),D(end));
    E=[E abs((G-D)*(G-D)')];
end

tol=1e-5;
while abs(gamma_guess(1)-gamma_guess(4))>tol
    if E(2)<E(3) %keep gamma_guess( 1 2 3) define new point in the larger of the intervals
        %find next guess point
        if abs(gamma_guess(1)-gamma_guess(2))>abs(gamma_guess(2)-gamma_guess(3))
            gamma_new=gamma_guess(2)-L*abs(gamma_guess(1)-gamma_guess(2));
            gamma_guess=[gamma_guess(1) gamma_new gamma_guess(2) gamma_guess(3)];
        else
            gamma_new=gamma_guess(2)+L*abs(gamma_guess(3)-gamma_guess(2));
            gamma_guess=[gamma_guess(1) gamma_guess(2) gamma_new gamma_guess(3)];
        end
        %find new attenuation profile matrix
        atten_hat=[];
        for ii=1:4
            a_temp=give_a_prof(z,gamma_guess(ii));
            atten_hat=[atten_hat a_temp'];
        end
        %find new error vector
        E=[];
        for ii=1:4
            [G D]=find_gd(atten_hat(:,ii),M(:,modes_used),freq,z,ck(modes_used),...
            rho,cc,mode_alpha(modes_used));
            E=[E abs((G-D)*(G-D)')];
        end
    else %keep gamma_guess(2 3 4) define new point in the larger of the intervals
        %find next guess point
        if abs(gamma_guess(2)-gamma_guess(3))>abs(gamma_guess(3)-gamma_guess(4))
            gamma_new=gamma_guess(3)-L*abs(gamma_guess(2)-gamma_guess(3));
            gamma_guess=[gamma_guess(2) gamma_new gamma_guess(3) gamma_guess(4)];
        else
            gamma_new=gamma_guess(3)+L*abs(gamma_guess(4)-gamma_guess(3));
            gamma_guess=[gamma_guess(2) gamma_guess(3) gamma_new gamma_guess(4)];
        end
        %find new attenuation profile matrix
        atten_hat=[];
        for ii=1:4
            a_temp=give_a_prof(z,gamma_guess(ii));
            atten_hat=[atten_hat a_temp'];
        end
        %find new error vector
        E=[];
        for ii=1:4
            [G D]=find_gd(atten_hat(:,ii),M(:,modes_used),freq,z,ck(modes_used),rho,...
            cc,mode_alpha(modes_used));
            E=[E abs((G-D)*(G-D)')];
        end
    end
end
end

```

```

[minE I]=min(E)
fprintf('Gamma is %g with mse %g',gamma_guess(I),E(I));

```

find_quad_timing.m

```

function struct=find_quad_timing(run)
%this m-file will determine the correct weights A2,B2,C2,A3,B3,C3 such that
%rounding of

%t2=A2+B2*t1+C2*t1^2
%t3=A3+B3*t1+C3*t1^2

%will give the least squares error for a quadratic fit to line up the
%timing pulses for REMUS towed array system.

%generates a structure struct with all of the necessary info!
switch run
    case 1210
        load 1210timing.mat; %contains T1,T2,T3 which have all of the timing pulse sample numbers
        struct.filenamees={'05121001Disk1.wav','05121001Disk2.wav','05121001Disk3.wav'};
    case 915
        load 915_timing.mat
        struct.filenamees={'05091501Disk1.wav','05091501Disk2.wav','05091501Disk3.wav'};
    otherwise
        error('bad run');
end

[P S mu]=polyfit(T1,T2,2);

A2=(P(3)-P(2)*mu(1)/mu(2)+P(1)*mu(1)^2/(mu(2)^2));
B2=(P(2)/mu(2)-2*P(1)*mu(1)/(mu(2)^2));
C2=(P(1)/(mu(2)^2));

[P S mu]=polyfit(T1,T3,2);

A3=(P(3)-P(2)*mu(1)/mu(2)+P(1)*mu(1)^2/(mu(2)^2));
B3=(P(2)/mu(2)-2*P(1)*mu(1)/(mu(2)^2));
C3=(P(1)/(mu(2)^2));

struct.disk2=[A2 B2 C2];
struct.disk3=[A3 B3 C3];

```

fit_attenuation.m

```

%this m-file will try to determine the best fit of  $\alpha = k(f/f_0)^n$  for the
%measurments and data using RAM PE as the model. It will do so by doing
%the following:
%1. find the measured range averaged transmission loss over some range
%interval ratl_min - ratl_max

%2. Set a reference frequency fo

%3. Adjust the parameter k_atten in the emperical relationship  $\alpha = k(f/f_0)^n$  to fit the data at fo

%4. Compare the fitting parameters for tl_measured vs tl_calc for the
%frequencies below fo using a range of exponents  $n = n_{min} \rightarrow n_{max}$ 

%The function calc_ratl_for_n can be used to calculate the range averaged
%transmission loss over a certain range given an attenuation law.

%THIS CODE IS IDENTICAL TO fit_char_depth EXCEPT IN THAT CODE YOU LOOP
%zc_try AND USE THE FUNCTION calc_ratl_for_zc
%%%%%%%%%%%%%%%%%%%%%%%%%%%%%%%%%%%%%%%%%%%%%%%%%%%%%%%%%%%%%%%%%%%%%%%%

```

```

%PARAMETERS

range_type=0; %use zero for same r_min, rmax over all frequencies,
% use 1 for specifying a number of wavelengths
range_data=[1000 2000;
            2000 3000;
            2600 3600]; %if range_type =0 [r_min r_max] if range_type=1 [r_center, n_lambda];

f0=1228; %reference freq
snr_f0=10; %used to get rid of nulls
SL = [139.4 139.4 139.4 149.8 149.8 149.8 156.7 156.7 156.7 159.4 159 155.2 156]; %SL
Freq= [ 220.5 220.5 220.5 415 415 415 635 635 635 635 823 1031 1228];

snr_spread= [ 11 10 8 11 10 10 11 10 10 10 10 10 10];
%this is used to incorporate the effect
%of noise in the RATL calc. Do not
% consider deep nulls below the noise floor
%this vector is the emperical estimate
%of the difference between the max RSL
%and the noise floor.

range_int= [ 1 2 3 1 2 3 1 2 3 3 3 3 3]; %allows for the use of multiple range
%intervals defined by range_data(range_int,:);
SL=SL+3; %account for the fact that measurments are amplitude and SL is rms
direction= [1 1 1 1 1 1 1 1 -1 -1 -1 -1]; %indicates the direction the
%vehicle is traveling for each data set
%1 indicates outgoing -1 indicates incoming

%input files:
files={'pofr_220_dop.mat','pofr_220_dop.mat','pofr_220_dop.mat','pofr_415_dop.mat',...
      'pofr_415_dop.mat','pofr_415_dop.mat','pofr_635_dop_out.mat','pofr_635_dop_out.mat',...
      'pofr_635_dop_out.mat','pofr_635_dop.mat','pofr_823_dop.mat','pofr_1031_dop.mat','pofr_1228_dop.mat'};

%Bathymetry for RAM
rb=[0 600 1500 2300 3000 3600 5250];
zb=[12.8 12.8 13.8 13.8 14 13.4 13.4];

%starting attenuation constant:
k_atten_start=0.34;
%Values of n to try:
n_try=[1.0 1.2 1.4 1.6 1.8 2.0];

plot_colors=['m','b','g','r','k','c'];
plot_symb=['^','.',',','o','x','+', '*','s','d','v'];

%open a log file:
file_string=strcat('fit_atten',datestr(now,30),'.log');
fod=fopen(file_string,'w');
fprintf(fod,'Log file for fitting of attenuation profiles\n');
fprintf(fod,datestr(now));
fprintf(fod,'\nReference Frequency = %g\n\n',f0);

%%%%%%%%%%%%%%%%%%%%%%%%%%%%%%%%%%%%%%%%%%%%%%%%%%%%%%%%%%%%%%%%%%%%%%%%
%first, we loop over the frequencies less than and including the reference
%frequency to find the measured RATL for these frequencies
f_use=find(Freq<=f0); %index of frequenies to use
ratl_meas=[]; %measured RATLS

fprintf(fod,'\nMEASURED DATA: \n ');
for f_index=f_use
    fprintf(fod,'\n%g',Freq(f_index));

```



```

%plot the measured data vs. range
load(char(files(f_index))); %load the correct input file

%Use emperical range corrections found from the bahtymetry, k-spectrum, doppler, and GPS
total_travel=cumsum(diff(abs(R_ave))); %total travel
ddr=[0 diff(R_ave)]; %range differences
total_travel=[0 total_travel]; %REMUS starts at 0
%percent error change as a function of range:
percent_error=2.1/100.*(ddr>0)-3.3/100*(ddr<0);

drift_error=cumsum(ddr.*percent_error); %find range error
R_out=R_ave-20-drift_error; %correct range including offset

%seperate the outgoing track from the incoming
outgoing=zeros(size(R_ave));

for jj=2:length(R_ave);
    if R_ave(jj)>R_ave(jj-1);
        outgoing(jj)=1;
    else
        outgoing(jj)=-1;
    end
end
outgoing(1)=outgoing(2);
I=(outgoing==direction(f_index)); %changes index to only include the correct direction
I=find(I);

%find the transmission loss
TL=-(20*log10(abs(P_ave)/1e-6)-SL(f_index));

%Calculate the range averaged tl
rr=R_out(I); %only use correct direction
tl=TL(I);
if range_type==1 %find the range over which to average in terms of number of wavelengths
    range_center=range_data(range_int(f_index),1);
    n_lambda=range_data(range_int(f_index),2);
    lambda=1500/Freq(f_index);
    ratl_min=range_center-n_lambda/2*lambda;
    ratl_max=range_center+n_lambda/2*lambda;
else
    ratl_min=range_data(range_int(f_index),1);
    ratl_max=range_data(range_int(f_index),2);
end
fprintf(fod,'\t Range - %g -> %g',ratl_min,ratl_max);
if direction(f_index) == -1
    fprintf(fod,'\t inbound');
else
    fprintf(fod,'\t outbound');
end

I=find((rr>ratl_min).*(rr<ratl_max));
ra_tl=mean(tl(I))-10*log10(mean(rr(I)));
fprintf(fod,'\tRange ave TL = %g (spreading removed) SL = %g\n',ra_tl,SL(f_index)-3);
ratl_meas=[ratl_meas ra_tl];
end

%%%%%%%%%%%%%%%%%%%%%%%%%%%%%%%%%%%%%%%%%%%%%%%%%%%%%%%%%%%%%%%%%%%%%%%%
%Adjust the parameter k_atten in the emperical relationship
%alpha=k(f/f0)^n to fit the data at f0 for the longest range
k_atten=k_atten_start;
n=1; %frequency dependence does not matter at this point.
if range_type==1 %find the range over which to average in terms of number of wavelengths

```

```

        range_center=range_data(end,1);
        n_lambda=range_data(end,2);
        lambda=1600/f0;
        ratl_min=range_center-n_lambda/2*lambda;
        ratl_max=range_center+n_lambda/2*lambda;
    else
        ratl_min=range_data(end,1);
        ratl_max=range_data(end,2);
    end

%find the ratl at f0 using the above starting point and iterating 12 times

iteration_data=[];
for ii=1:12
    ratl=calc_ratl_for_n(f0,k_atten,f0,n,[ratl_min ratl_max],snr_f0,1210);
    k_atten_new=k_atten*ratl_meas(end).^5/ratl.^5;
    iteration_data=[iteration_data;ii,k_atten,k_atten_new,ratl_meas(end),ratl];
    k_atten=k_atten_new;
end
fprintf(fod,'\n\n%%%%%%%%%%%%%%%%%%%%%%%%%%%%%%%%%%%%%%%%%%%%%%%%%%%%%%%%%%%%%%%%%%%%%%%%\n\n');
fprintf(fod,'Find the correct attenuation at the reference freq\n');
fprintf(fod,'Iteration k_old k_new ratl_meas ratl_calc(k_old)\n');
fprintf(fod,'%g \t %g \t %g \t %g \t %g\n',iteration_data);

%%%%%%%%%%%%%%%%%%%%%%%%%%%%%%%%%%%%%%%%%%%%%%%%%%%%%%%%%%%%%%%%%%%%%%%%
%Compare the fitting parameters for tl_measured vs tl_calc for the
%frequencies below f0 using a range of exponents n given by n_try
fprintf(fod,'\n\n\n');
fprintf(fod,'Find the correct frequency dependent exponent n:\n');

fit_slope=[];
slope_fig=figure;
grid
plot([11 17],[11 17],'k');
index_data=[];
jj=0;
for nn=n_try
    jj=jj+1;
    %loop over the frequencies in f_use to find the calculated ratl for
    %each frequency
    ratl_calc=[];
    for ff=f_use
        if range_type==1 %find the range over which to average in terms of number of wavelengths
            range_center=range_data(range_int(ff),1);
            n_lambda=range_data(range_int(ff),2);
            lambda=1500/Freq(ff);
            ratl_min=range_center-n_lambda/2*lambda;
            ratl_max=range_center+n_lambda/2*lambda;
        else
            ratl_min=range_data(range_int(ff),1);
            ratl_max=range_data(range_int(ff),2);
        end

        ratl=calc_ratl_for_n(Freq(ff),k_atten,f0,nn,[ratl_min ratl_max],snr_spread(ff),1210);
        ratl_calc=[ratl_calc ratl];
    end
    fprintf(fod,'n=%g\n',nn);
    fprintf(fod,'\nRATL_meas=');
    fprintf(fod,'\t%g',ratl_meas);
    fprintf(fod,'\nRATL_calc=');
    fprintf(fod,'\t%g',ratl_calc);
end

```

```

    %find the fit of ratl_meas vs ratl_calc
    [a b]=polyfit(ratl_meas,ratl_calc,1);
    fit_slope=[fit_slope a(1)];
    plot_str=strcat(char(plot_colors(mod(ceil(jj/9),6)+1)),char(plot_symb(mod(jj,9)+1)));
    figure(slope_fig);
    hold on
    plot(ratl_meas,ratl_calc,plot_str);
    index_data=[index_data num2str(nn,'%1.2f')];

    fprintf(fod,'\nFit slope =%g\nFit Intercept=%g\n\n',a(1),a(2));
end
xlabel('Range Ave. TL Measured');
ylabel('Range Ave. TL Calc');
title('Range averaged TL calculated vs. measured for different n');
legend('Lin',index_data);

%plot the best fit slope vs. n
figure
plot(n_try,fit_slope,'r.');
```

get_array_data_quad.m

```

function [Y,FS,NBITS]=get_array_data_quad(start1,duration,struct);
%this function will import the array data for all 6 channels for the BU
%prototype array. It uses quadratic fitting to determine the timing

%It will output a matrix Y where each column of Y is a channel and each row
%a time sample. For example, to see all of channel 1, use Y(:,1). It
%also outputs the sampling frequency and the number of bits.

%The required inputs are the channel 1 starting time in seconds and the
%duration of the signal to export in seconds.
%If the starting time for channel 1 is above 6000, it will default to
%sample number instead of seconds.

%Also, an array structure is
%required. This includes the precomputed vaules of A2,B2,C2,A3,B3,C3 such
%that rounding of

%t2=A2+B2*t1+C2*t1^2
%t3=A3+B3*t1+C3*t1^2

%will give the least squares error for a quadratic fit to line up the
%timing pulses. To get this structure, run find_quad_timing.m

%the sampling frequency for the recorders is 44100;
fs=44100;

%array calibration
array_const=530.8; %Pa/V
rec_const=array_const/4; %Pa/wav

A2=struct.disk2(1);
B2=struct.disk2(2);
C2=struct.disk2(3);
```

```

A3=struct.disk3(1);
B3=struct.disk3(2);
C3=struct.disk3(3);

%convert the channel 1 start and stop time into sample time
if start1<6000
    start1=round(fs*start1);
end
stop1=round(start1+fs*duration);

%each channel requires a shift and a stretch

start2=A2+B2*start1+C2*start1^2;
start2=round(start2);
stop2=round(start2+stop1-start1);

start3=A3+B3*start1+C3*start1^2;
start3=round(start3);
stop3=round(start3+stop1-start1);

%now read in the wav files:
[Y1 FS NBITS]=wavread(char(struct filenames(1)),[start1,stop1]);
[Y2 FS NBITS]=wavread(char(struct filenames(2)),[start2,stop2]);
[Y3 FS NBITS]=wavread(char(struct filenames(3)),[start3,stop3]);

%construct the matrix from the sub sets
Y=[Y1 Y2 Y3];

%convert the matrix to Pa:
Y=Y*rec_const;

```

get_array_p_quad_de2.m

```

function [Y,v_est_dop]=get_array_p_quad(y,FS,f_interest,n_dop,v_guess)
%%this function will take as it's input a matrix of output from the BU towed
%hydrophone array. It will output the complex pressure at each channel for a given frequency
%It uses a numerical quadrature technique that normalizes by the unit solution at a given frequency

%Edit 3/4/05 JDH to include the doppler correction. At the higher
%frequencies the doppler will force the signal outside of the bin for this
%quasi-fft;
%this version is designed to be used when the doppler is not necessarily known,
%but it is known to be within the range of speeds of the AUV.

%if n_dop is included, use n_dop points between doppler min and doppler max
% if v_guess is included, doppler min and doppler max are based on v_guess
% +/- 10%

c=1500; %approximate speed of sound
if nargin<5
    v_guess=0;
    if nargin<4
        n_dop=101;
    end
    max_vehicle_speed=2.5; %m/s

    D=linspace(-max_vehicle_speed/c,max_vehicle_speed/c,n_dop);
else
    if v_guess==0;

```

```

        v_guess=1;
    end
    if n_dop==[];
        n_dop=101;
    end
    D=linspace(0.9*v_guess/c,1.1*v_guess/c,n_dop);
end
[n q]=size(y);
n_freq=length(f_interest);
%%%%%%%%%%%%%%%%%%%%%%%%%%%%%%%%%%%%%%%%%%%%%%%%%%%%%%%%%%%%%%%%%%%%%%%%
t=[0:n-1];
t=t/FS;
t=t(:); %t is a column vector
D=D(:)'; %D is a row vector

Y=zeros(length(f_interest),q);

for jj=1:length(f_interest)
    f=f_interest(jj)*(1-D);
    %Fourier transform at frequencies f done by quadrature
    basec=cos(2*pi*t*f);
    bases=sin(2*pi*t*f);

    num1=y'*basec;
    num2=y'*bases;
    %the output will be greatest at the doppler frequency
    [a b]=max(abs(sqrt(num1.^2+num2.^2)))';

    den=diag(basec(:,b)'*basec(:,b));
    C=diag(num1(:,b))./den;
    den=diag(bases(:,b)'*bases(:,b));
    S=diag(num2(:,b))./den;
    Y(jj,:)=(C+i*S)';
end
v_est_dop=D(round(mean(b)))*c;

```

give_a_prof.m

```

function [alpha]=give_a_prof(z,gamma);

%this function will return the attenuation profile as a function of depth
%for a given parameter gamma.

%this is done in a function to ease changing the model for a(z) used.

%Using the modified biot theory:
I=find(z>=13);
c=1600+200*(1-exp(-.3*(z-z(min(I))))).*(z>=13);
alpha=1./c.*(z>=13);
alpha=alpha/max(alpha);
tau_of_z=1-gamma*(z/z(min(I))-1);
alpha=tau_of_z.*alpha;

```

hankel_quad.m

```

function [g,k]=hankel_quad(P,R,k_in);

%this function will evaluate the hankel transform over the vector k_in by
%the trapezoid rule

%make P and R column vecs and k_in a row vec

```

```

P=P(:);
R=R(:);
k_in=k_in(:)';

%Find Quadrature Weights from the R vector
W=integrate_wis(R,2);
%Find the Bessel Function Kernel
J=besselj(0,R*k_in);
%Integrate by quadrature
I=W.*P.*R;
g=I'*J;

%give the output k vector mimicing the input
k=k_in;

```

integrate_quad.m

```

function I=integrate_quad(x,y,n);

%this function will numerically integrate the function y=f(x) over the
%interval of x using an interpolary quadrature rule of order n determined
%by the mehtod of undetermined coefficients.
%if n=2 this is the trapezoidal rule
%if n=3, this is simpson's rule
%etc.

%if size(x)=size(y) is not evenly divisible by n, then the last section
%will be evaluated with n+1 have more points
num_intervals=floor((length(x)-1)/(n-1));
n_last=mod((length(x)-1),(n-1));
if n_last~=0;
    n_last=n+mod((length(x)-1),(n-1));
    num_intervals=num_intervals-1;
end

I=0; %initialize the output

for ii=1:num_intervals
    ns=(ii-1)*(n-1)+1;
    xi=x(ns:ns+n-1); %xi is the ii'th subset of xi
    yi=y(ns:ns+n-1); %yi is the ii'th subset of yi
    wi=mouc_int(xi,xi(1),xi(end)); %determine quadrature weights using mouc
    I=I+yi*wi; %multiply and add
end

%now do last interval as long as it must be done
if n_last~=0
    xi=x(end-n_last+1:end);
    yi=y(end-n_last+1:end);
    wi=mouc_int(xi,xi(1),xi(end));
    I=I+yi*wi;
end

```

integrate_wis.m

```

function W=integrate_quad(x,n);

%this function will produce the weights for numerically integrating
%a function defined as y=f(x) over the
%interval of x using an interpolary quadrature rule of order n determined

```

```

%by the mehtod of undetermined coefficients.
%if n=2 this is the trapezoidal rule
%if n=3, this is simpson's rule
%etc.

%if size(x) is not evenly divisible by n, then the last section
%will be evaluated with n+1 have more points
num_intervals=floor((length(x)-1)/(n-1));
n_last=mod((length(x)-1),(n-1));
if n_last~=0;
    n_last=n+mod((length(x)-1),(n-1));
    num_intervals=num_intervals-1;
end

W=[];
ns=1;
xi=x(ns:ns+n-1); %xi is the ii'th subset of xi
W=mouc_int(xi,xi(1),xi(end)); %determine quadrature weights using mouc

for ii=2:num_intervals
    ns=(ii-1)*(n-1)+1;
    xi=x(ns:ns+n-1); %xi is the ii'th subset of xi
    wi=mouc_int(xi,xi(1),xi(end)); %determine quadrature weights using mouc
    lastW=W(end);
    W(end)=W(end)+wi(1);
    W=[W; wi(2:end)];
end

%now do last interval as long as it must be done
if n_last~=0
    xi=x(end-n_last+1:end);
    wi=mouc_int(xi,xi(1),xi(end));
    lastW=W(end);
    W(end)=W(end)+wi(1);
    W=[W; wi(2:end)];
end
end

```

lagtimes.m

```

function tlags=lagtimes(t_start,n_windows,t_window,f_des)

%this function will return a list of lag times in the form
%[approx_recording time tlag2 tlag3 tlag4 tlag5 tlag6]. It takes as its
%input the starting time for the evaluation, the number of lag time
%calculations to make (n_windows) and the duration of the sample for each
%calculation. It filters the array signals around the frequency given by
%f_des. For the dodge pond dec 04 experiment, f should be 2500 , 9000, 11000,
%or 12000;
Flower=f_des-50; %Lower filter Frequency
Fupper=f_des+50; %Upper filter Frequency
NFFT=2^10; %Bits in FFT
FS=44100; %Sampling frequency (44100 is standard)

for ii=1:n_windows
    %determine start and stop samples for channel 1 and 2
    start1=round(t_start*FS+(ii-1)*t_window*FS);
    stop1=round(start1+t_window*FS);

    %determine start and stop samples for the other channels
    [start2 stop2 start3 stop3]=startshort2(start1,stop1);

```

```

%read in the data
[Y1 FS NBITS]=wavread('disc1.wav',[start1 stop1]);
[Y2 FS NBITS]=wavread('disc2.wav',[start2 stop2]);
[Y3 FS NBITS]=wavread('disc3.wav',[start3 stop3]);

%filter the data with a bandpass filter
[B,A]=butter(2,[2*Flower/FS 2*Fupper/FS]);
Y1(:,1)=filter(B,A,Y1(:,1));
Y1(:,2)=filter(B,A,Y1(:,2));
Y2(:,1)=filter(B,A,Y2(:,1));
Y2(:,2)=filter(B,A,Y2(:,2));
Y3(:,1)=filter(B,A,Y3(:,1));
Y3(:,2)=filter(B,A,Y3(:,2));

%form time vectors and plot waveforms once only
if ii==1
    t1=(1:size(Y1,1))/FS;t=t1;
    t2=(1:size(Y2,1))/FS;
    t3=(1:size(Y3,1))/FS;
    Plotwf2;
end

%find the Cross spectral Densities between channel 1 and every other channel.

[P12,F12]=csd(Y1(:,1),Y1(:,2),NFFT,FS,hann(NFFT),NFFT/2);
[P13,F13]=csd(Y1(:,1),Y2(:,1),NFFT,FS,hann(NFFT),NFFT/2);
[P14,F14]=csd(Y1(:,1),Y2(:,2),NFFT,FS,hann(NFFT),NFFT/2);
[P15,F15]=csd(Y1(:,1),Y3(:,1),NFFT,FS,hann(NFFT),NFFT/2);
[P16,F16]=csd(Y1(:,1),Y3(:,2),NFFT,FS,hann(NFFT),NFFT/2);

%find the maximum in the CSD's
[max2 peakindex2]=max(abs(P12));
[max3 peakindex3]=max(abs(P13));
[max4 peakindex4]=max(abs(P14));
[max5 peakindex5]=max(abs(P15));
[max6 peakindex6]=max(abs(P16));

%find the time lags
tlag2=angle(P12(peakindex2))./(2*pi)./F12(peakindex2);
tlag3=angle(P13(peakindex2))./(2*pi)./F13(peakindex3);
tlag4=angle(P14(peakindex2))./(2*pi)./F14(peakindex4);
tlag5=angle(P15(peakindex2))./(2*pi)./F15(peakindex5);
tlag6=angle(P16(peakindex2))./(2*pi)./F16(peakindex6);

%Plot the aligned data (only once)
if ii==1
    figure
    plot(t1,Y1(:,1));
    hold on
    plot(t1,Y1(:,2),'r');
    plot(t2,Y2(:,1),'g');
    plot(t2,Y2(:,2),'m');
    plot(t3,Y3(:,1),'y');
    plot(t3,Y3(:,2),'c');
    xlabel('Time (s)');
    ylabel('Output');
    title('Aligned output');
    legend('Ch1','Ch2','Ch3','Ch4','Ch5','Ch6');
    grid
end

%output the time lags
if ii==1;

```



```

        tlags=[start1/FS tlag2 tlag3 tlag4 tlag5 tlag6];
    else
        tlags=[tlags; [start1/FS tlag2 tlag3 tlag4 tlag5 tlag6]];
    end
end
end

```

lldist.m

```

function [x,y,d]=lldist(lat1, lon1,lat2,lon2);

%this function uses an approximation to degrees per meter
%to give a relative x, y between two lat/lon positions.
%It also gives d, the linear distance between
%the two points;

%At 41 degrees north, - Nantucket Sound
meters_per_1deglat=111061;
meters_per_1deglon=83668;

x=(lon2-lon1)*meters_per_1deglon;
y=(lat2-lat1)*meters_per_1deglat;
d=sqrt(x.^2+y.^2);

```

modasc.m

```

%this program will create an ascii mod file
%the existing ascii mod file generator puts out to the screen, not a file, as is needed

if exist('modfil1')
    !copy modfil1 modfil
else
    errordlg('Modfil1 Does Not exist - run kraken!!!');
    return
end

if exist('ascmod') == 2
    !del ascmod
end

diary('ascmod');
eval('!modasc');
diary off;

```

mode_amps.m

```

%this m-file will try to determine the modal amplitude vs. range for 415
%Hz. It can be modified to be used with any frequency.

%%%%%%%%%%%%%%%%%%%%%%%%%%%%%%%%%%%%%%%%%%%%%%%%%%%%%%%%%%%%%%%%%%%%%%%%
load pofr_415_dop %load in the data from pofr_doppler output
%approximate wavenumbers:
k1=1.763;
k2=1.735;
k3=1.660;
k4=1.559;
ks=[k1 k2 k3 k4];
k_use=[1:4]; %which ones to find
r=linspace(200,700,101); %ranges to start windows at
dk=.02; %+/- interval to look at in k space
nk=201; %number of points in k-space

```

```

range_int=1000; %range window
hank_range=6000; %zero-pad out to this range.

%Use emperical range corrections found from the bahtymetry, k-spectrum, doppler, and GPS
total_travel=cumsum(diff(abs(R_ave))); %total travel
ddr=[0 diff(R_ave)]; %range differences
total_travel=[0 total_travel]; %REMUS starts at 0
%percent error change as a function of range:
percent_error=2.1/100.*(ddr>0)-3.3/100*(ddr<0);

drift_error=cumsum(ddr.*percent_error); %find range error
R_ave=R_ave-20-drift_error; %correct range including offset

%This selects only the outgoing portion
PP=P_ave(1:5060);
RR=R_ave(1:5060);

%loop over the k values to look at and find the MACS:
for k_ind=k_use;%[k3];
k=ks(k_ind); %the k value for this loop
k_in=linspace(k-dk,k+dk,nk); %range in k is possible due to range dep.

R=[]; %range data ouput
g_max=[]; %Horizontal wavenumber spectra output

fprintf('\n');
for rr=r
fprintf('%g ',rr); %to keep the user informed

I=find((RR>rr).*(RR<rr+range_int)); %apply the range window
R=[R mean(RR(I))]; %build the R output vector of ave ranges
[P_pad R_pad]=pad_data(PP(I),RR(I),hank_range); %pad the windowed data out to 6k
[g_k_out]=hankel_quad(P_pad,R_pad,k_in); %compute the HT
[a imax]=max(abs(g)); %find the peak in the k-spectrum
g_max=[g_max a]; %construct the output k value vector
end

figure %plot the Mode amplitude as a function of range
plot(R,g_max,'r');
title(strcat('Mode ',num2str(k_ind)));
xlabel('range (m)');
ylabel('Amplitude');

%%fit the Decay and display it on the plot
[a b]=polyfit(R,log(abs(g_max)),1);
hold on
text(min(R),min(g_max),strcat(num2str(exp(a(2))), 'exp(', num2str(a(1)), 'r'));
hold on
plot(R,exp(a(2))*exp(a(1)*R), 'k')
end

```

mouc_int.m

```

function w=mouc_int(x,lower_bound,upper_bound)

%this function will take as its input a vector x=x_i i=1:n and return the
%coefficients w_i for use in a quadrature rule. These coefficients are
%determined by the method of un-determined coefficients and inverting the
%Vandermonde matrix to make sure that the first n polynomial basis
%functions would be integrated exactly.

```

```

a=lower_bound;
b=upper_bound;

n=length(x);
x=x(:); %make sure x is a column vec
x=x'; %make x a row vec

%subtract x(1) from each entry in x to help avoid poorly scaled matrices
%later. This will not affect the weighting if we so adjust a and b as
%well
xx=x(1);
x=x-xx;
a=a-xx;
b=b-xx;

c=[];
%create vector of solutions to int x^(n-1) dx
for ii=1:n
    c(ii)=(b^ii-a^ii)/ii;
end
c=c(:); %make sure c is a column vec

%create vandermonde matrix
V=[];
for ii=1:n
    V(ii,:)=x.^(ii-1);
end

w=inv(V)*c;

```

non_acoustic_compare.m

```

%this m-file will compute the speed vs. rpm, power vs. speed, rpm
%vs. power curves for a vehicle with nothing on it, with only
%the canister, and with the canister and the array. The data file fo the
%vehicle with noting on it comes from a completely different vehicle, so
%it probably should not be used for comparisons.

```

```

%%%%%%%%%%%%%%%%%%%%%%%%%%%%%%%%%%%%%%%%%%%%%%%%%%%%%%%%%%%%%%%%%%%%%%%%
%nothing on it.

```

```

load none.mat
figure

```

```

power=current_amps.*volts;

```

```

%speed vs. rpm
subplot(221)
plot(thruster_rpm,estimated_velocity,'k.');
```

```

xlabel('RPM');
ylabel('Est. Vel. m/s');
title('Speed vs. RPM');

%speed vs. power
subplot(222)
plot(estimated_velocity,power,'k.');
```

```

xlabel('Est. Vel. m/s');
ylabel('Est. Power (w)');
title('Power vs. Speed');

%rpm vs. power
subplot(223)
plot(thruster_rpm,power,'k.');
```

```

xlabel('RPM');
ylabel('Est. Power (w)');
title('Power vs. RPM');
%%%%%%%%%%%%%%%%%%%%%%%%%%%%%%%%%%%%%%%%%%%%%%%%%%%%%%%%%%%%%%%%%%%%%%%%
%now do the case for the canister

load can.mat

%Code here is the same as above, just for the new data set... omitted in text for brevity

%%%%%%%%%%%%%%%%%%%%%%%%%%%%%%%%%%%%%%%%%%%%%%%%%%%%%%%%%%%%%%%%%%%%%%%%
%now do the case for the array

load 1210stat.mat

%Code here is the same as above, just for the new data set... omitted in text for brevity

```

pad_data.m

```

function [P_pad,R_pad]=pad_data(P,R,R_max);

%this function will take in a vector P of Complex Pressure data, a vector R of range data
%and a value R_max. It will then output a vector P_pad and R_pad where R_pad is the padded
%range vector with ranges from 0 to R_max. The sample spacing in R_pad is the mean sample
%spacing in R to avoid sampling problems. P_pad then is the zero padded complex pressure
%vector and has the values P and the range R, and zeros for all other ranges in R_pad

%first, make sure P and R are row vectors
P=P(:)';
R=R(:)';

%make sure R is ascending
if R(end)<R(1)
    %decending
    R=R(end:-1:1); %reverse order
    P=P(end:-1:1);
end

%this function is used to zero pad the acoustic data from zero to some
%range R_max.

dr2=round(mean(diff(R))); %determine the mean range spacing of R

if max(R)<R_max %then we need to zero pad the end
    if min(R)>0 %then we need to zero pad the beginning
        %the number of new points to from 0 to min(R) to keep the same mean spacing
        NR1=round((min(R))./dr2-1);

        % the number of new points to add from max(R) to R_max to keep the same mean spacing
        NR2=round((R_max-max(R))./dr2-1);

        %create the padded R vector by adding on range points before and after the
        %vector R such that the vector goes from 0 to R_max with out changing the
        %mean spacing

        R_pad=[linspace(0,min(R)-dr2,NR1),R,linspace(max(R)+dr2,R_max,NR2)];

        %create the padded P vector by adding zeros to the beginning in end of P in
        %the exact same numbers as were added to R
        P_pad=[zeros(1,NR1),P,zeros(1,NR2)];
    end
end

```

```

else %we do not need to zero pad the beginning

    % the number of new points to add from max(R) to R_max to keep the same mean spacing
    NR2=round((R_max-max(R))./dr2-1);

    %create the padded R vector by adding on range points before and after the
    %vector R such that the vector goes from 0 to R_max with out changing the
    %mean spacing

    R_pad=[R,linspace(max(R)+dr2,R_max,NR2)];

    %create the padded P vector by adding zeros to the beginning in end of P in
    %the exact same numbers as were added to R
    P_pad=[P,zeros(1,NR2)];
end
else %we do not have to zero pad the end
    if min(R)>0 %then we need to zero pad the beginning
        %the number of new points to from 0 to min(R) to keep the same mean spacing
        NR1=round((min(R))./dr2-1);

        %create the padded R vector by adding on range points before and after the
        %vector R such that the vector goes from 0 to R_max with out changing the
        %mean spacing

        R_pad=[linspace(0,min(R)-dr2,NR1),R];

        %create the padded P vector by adding zeros to the beginning in end of P in
        %the exact same numbers as were added to R
        P_pad=[zeros(1,NR1),P];
    end
end
end

```

plot_c_profile_NS.m

```

%this-mfile will read in the sound velocity profile used for modeling and plot it.
%the data comes from the structure profiles

%The functions plot_atten_profile_NS and plot_rho_profile_NS do exactly the same thing
%with the same commands, but load in the attenuation data and density data instead.
c_prof=[];
depth_prof=[];

ii=1; %plot the first profile in the range dependent case

for jj=1:profiles.Nmedia(ii);
    ssp_temp=eval(strcat('profiles.',char(profiles.cofz(ii,jj))));
    c_prof=[c_prof;ssp_temp(:,2)];
    depth_prof=[depth_prof;ssp_temp(:,1)];
end
depth_prof=[depth_prof; depth_prof(end);depth_prof(end)+20]; %tack on the basement
c_prof=[c_prof;profiles.cpb(ii);profiles.cpb(ii)];

plot(c_prof,depth_prof)
set(gca,'ydir','reverse');
xlabel('Compressional Wave speed (m/s)');
ylabel('Depth');
axis([0.9*min(c_prof) 1.1*max(c_prof) min(depth_prof) max(depth_prof)]);
grid
title('Sound Speed profile');

```

pofr_doppler.m

```

%This m-file will be used to find the complex P(r) for a given frequency of interest during the

```

%10 DEC 2005 Experiment. Other than the parameters used in the input, it is identical to the %routine used for September to do the same thing.

```
%%%%%%%%%%%%%%%%%%%%%%%%%%%%%%%%%%%%%%%%%%%%%%%%%%%%%%%%%%%%%%%%%%%%%%%%
%Parameters
%%%%%%%%%%%%%%%%%%%%%%%%%%%%%%%%%%%%%%%%%%%%%%%%%%%%%%%%%%%%%%%%%%%%%%%%
%load ctd data to get sound speed
load 1210ctd          %CTD data from REMUs
c=sound_speed(end); %sound speed in m/s
%load remus data
load 1210state
remus_time=mission_time-44137.578+10*60+.5; %time shift found empirically
%set up array file structure for the 05121001 data set
struct=find_quad_timing(1210);

n_doppler=21; %number of points to use in doppler estimation

start_index=3800; %Sample number from REMUS nav data to begin at -use 3500 for return trip
f_interest=1228; %Frequency (HZ) to consider
N_max=100;      %Number of subapertures to consider
L=12;          %meters behind REMUS of channel 1

%Tioga Coordinants:
T_lat=41.36679596; %Degrees Latitude
T_lon=-70.19930771; %Degrees Longitude

%Beamformer Constants
dt=.76;          %seconds over which to perform fft
nfft=2^15;      %NFFTd_sep=1.5;

%Overlap processing Parameters:
overlaps_per_hphone=1;
use_overlap_ave=1; %set to 1 to use overlap averaging, 0 not to

%if we want to get an average pressure at each position, we can overlap
%with windows of the array so that there are 1,3, or 6 measurements at
%each location.
if use_overlap_ave
switch overlaps_per_hphone
    case 1 %sample each point in space once
        d_sep=4.5;
    case 6 %sample each point in space 6 times - overlap every channel
        d_sep=0.75;
    otherwise
        error('d_sep inconsistent');
end
end

%%%%%%%%%%%%%%%%%%%%%%%%%%%%%%%%%%%%%%%%%%%%%%%%%%%%%%%%%%%%%%%%%%%%%%%%

%set up cartesian coordinates with the source at the origin.
[x y d]=lldist(T_lat,T_lon,latitude,longitude);

%%%%%%%%%%%%%%%%%%%%%%%%%%%%%%%%%%%%%%%%%%%%%%%%%%%%%%%%%%%%%%%%%%%%%%%%

%start at x(start_index),y(start_index)
X=x(start_index);
Y=y(start_index);
T=remus_time(start_index);
x_last=X;
y_last=Y;
t_last=T;
disp('Stage 1');
```

```

for N=1:N_max
    %find distance from last point to each point in remus_time_short where remus_time_short is
    %remus time (current_index:end) where current index is given by the index of the first value of
    %remus_time such that remus_time>t_last
    fprintf('%i ',N);
    if mod(N,20)==0
        fprintf('\n');
    end
    ii=N-1;
    current_index=min(find(remus_time>t_last));
    remus_time_short=[t_last remus_time(current_index:end)];
    x_short=x(current_index:end);
    y_short=y(current_index:end);
    dd=[0 sqrt((x_short-x_last).^2+(y_short-y_last).^2)];

    %now interpolate for the time where dd=d_sep
    t_current=interp1(dd(1:20),remus_time_short(1:20),d_sep,'linear');
%included indexing to avoid come back error
    T=[T t_current];

    %now use t_current to interpolate x_current and y_current
    x_current=interp1(remus_time,x,t_current,'linear');
    y_current=interp1(remus_time,y,t_current,'linear');

    %now form X and Y
    X=[X x_current]; Y=[Y y_current];
    x_last=x_current; y_last=y_current;
    t_last=t_current;
end

X_hphone=[]; %create blank vector which will be the vector of hydrophone x positions
Y_hphone=[]; %create blank vector which will be the vector of hydrophone y positions

x_h=(3.75:-.75:0)+L; %hydrophone positions
x_h=-x_h; %meters behind remus

dZ=sqrt(diff(X).^2+diff(Y).^2);
Z=[0 cumsum(dZ)]; %distance from origin

%loop over positions of REMUS found above to find the positions of the
%hydrophones, which should be on the same path and and x_h meters behind
ii_min=1;
for ii=1:length(Z)
    zeta=Z-Z(ii); %position behind remus
    if zeta(1)>min(x_h)
        ii_min=ii_min+1;
    else
        x_hphone_current=interp1(zeta,X,x_h,'linear');
        y_hphone_current=interp1(zeta,Y,x_h,'linear');
        X_hphone=[X_hphone x_hphone_current];
        Y_hphone=[Y_hphone y_hphone_current];
    end
end

%now we find the complex pressure at each channel at each time,
%but we must be careful when assembling P
% because it must go (in terms of channels) [6 5 4 3 2 1 6 5 4 3 2 1....];
P=[];
fprintf('\n\nStage 2\n');
%%%%%%%%%%%%%%%%%%%%%%%%%%%%%%%%%%%%%%%%%%%%%%%%%%%%%%%%%%%%%%%%%%%%%%%%%%
for ti=1:length(T) %loop over the determined evaluation times
    fprintf('%i ',ti); %keep the user informed of the progress
    if mod(ti,20)==0

```

```

        fprintf('\n');
    end
    [Y FS NBITS]=get_array_data_quad(T(ti),dt,struct); %get the data
    %get the complex P values for f_interest and report back an est. doppler speed
    if exist('doppler_guess');
        P_current=get_array_p_quad_de(Y,FS,f_interest,n_doppler,doppler_guess); %include doppler
    else
        P_current=get_array_p_quad_de(Y,FS,f_interest,n_doppler); %include doppler
    end

    P_current=P_current(6:-1:1); %reverse the order of P_current for assembly into P
    %%%%%%%%%%%%%%%%%%%%%%%%%%%%%%%%%%%%%%%%%%%%%%%%%%%%%%%%%%%%%%%%%%%%%%%%%
    %phase correct the P by the time T - This is the critical synthetic aperture step
    P_current=P_current*exp(-i*2*pi*f_interest*T(ti));
    %%%%%%%%%%%%%%%%%%%%%%%%%%%%%%%%%%%%%%%%%%%%%%%%%%%%%%%%%%%%%%%%%%%%%%%%%
    P=[P P_current]; %assemble the pressure vector

end

R=sqrt(X_hphone.^2+Y_hphone.^2); %ranges from x-y

disp('Done!'); %keep the user informed

%now perform averaging over values that should be about at the same range
%for the case where overlapping is used to get
if use_overlap_ave
    switch overlaps_per_hphone
        case 1
            %do nothing - no averaging is necessary
        case 6
            R_ave=[]; %output averaged R vector for 6 measurements
            P_ave=[]; %output averaged P vector for 6 measurements
    %create empty matrices where each column will be a range and each row a measurement
            P_amp=zeros(6,length(X)-(6+3));
            P_phase=zeros(size(P_amp)); %average amp and phase seperately for better performance
            RR=zeros(size(P_amp));

            for ii=1:(length(X)-(6+3))
                Ra=0;
                Paa=0; %average
                Ppa=0;
                for jj=0:5
                    fprintf('%g ',6*ii+jj*(6-1)); %keep the user informed
                    RR(jj+1,ii)=R(6*ii+jj*(6-1));
                    P_amp(jj+1,ii)=abs(P(6*ii+jj*(6-1)));
                    P_phase(jj+1,ii)=angle(P(6*ii+jj*(6-1)));
                end
                fprintf('\n');
            end

            %find the means and variances for each range
            R_ave=mean(RR);
            Ppa=mean(P_phase);
            Paa=mean(P_amp);
            Vaa=var(P_amp);
            Vpa=var(P_phase);
            alpha=Ppa;
            P_ave=Paa.*exp(i*alpha);
        otherwise
            error('d_sep inconsistent');
    end
end
end

```


read_plot_data_tl.m

```
%read_plot_data_tl.m

%this function reads in the plot data from the input file for safari

fid=fopen(inpfil,'r');

titleinp=fgetl(fid);      %read in title
input_opts=fgetl(fid);   %read in the options line
input_opts=strrep(input_opts,' ',''); %remove blanks from options

freq=fscanf(fid,'%f',1); %read in the frequency
if strfind(input_opts,'J')>0 | strfind(input_opts,'j')>0
%then there is coeff after freq
coef=fscanf(fid,'%f',1);
end
num_layers=fscanf(fid,'%i',1); %read in the number of layers

layer_data=zeros(num_layers,8); %read in num_layers lines of layer data

for ii=1:num_layers
    A=fscanf(fid,'%f',8);
    layer_data(ii,:)=A';
end

ds=fscanf(fid,'%f',1); %read in source depth
reciever=fscanf(fid,'%f',4); %read in reciever info
dr=linspace(reciever(1),reciever(2),reciever(3)); %set up dr vector

cmin=fscanf(fid,'%f',1); %read in sound speed info
cmax=fscanf(fid,'%f',1);

ksamp=fscanf(fid,'%f',3); %read in wave number sampling info

rmin=fscanf(fid,'%f',1);
rmax=fscanf(fid,'%f',1); %read in the range info
rlen=fscanf(fid,'%f',1);
rinc=fscanf(fid,'%f',1);
%rmin=rmin*1000; %convert range to meters
%rmax=rmax*1000; %convert range to meters

fclose(fid); %close the input file.
```

read_ram_out.m

```
function [ram_data]=read_RAM_out(filename);

%this function will read in the RAM data contained in filename.tl
%it will return a structure ram_dat as follows
% ram_data.title    plot title
% .date            string with date
% .freq            frequency
% .sd              source depth
% .rd              reciever depth
% .R               range vector
% .TL              transmission loss vector

fid=fopen([filename '.tl']);

ram_data.title=fgetl(fid);
ram_data.date=fscanf(fid,'%c',8);
ram_data.freq=fscanf(fid,'%f',1);
ram_data.sd=fscanf(fid,'%f',1);
```

```

junk=fgetl(fid);

ram_data.rd=fscanf(fid,'%f',1);
data=fscanf(fid,'%g');

ram_data.R=data(1:2:end);
ram_data.TL=data(2:2:end);
fclose(fid);

```

read_tl_out.m

```

%read_tl_out
%this subroutine is used to read in the TL output of the TL module of safari.

%first, read in the input data
read_plot_data_tl;

%now open the output file for reading:
out_file_name=[root '.tl'];

fid=fopen(out_file_name,'r');

%read in the stuff at the top of the file that is not needed:

trash=fgetl(fid);
trash=fgetl(fid);
trash=fgetl(fid);

%now, read in the TL data for each range
num_depths=reciever(3);
TL_data=[];
for ii=1:num_depths
    TL_current=[];
    [data test]=fscanf(fid,'%f',4);
    while test==4
        TL_current=[TL_current;data'];
        [data test]=fscanf(fid,'%f',4);
    end
    TL_data(:,:,ii)=TL_current;
    trash=fgetl(fid);
trash=fgetl(fid);
trash=fgetl(fid);
end
fclose(fid); %close the output file

```

readshd_ns.m

```

% reads the shade file data from KRAKEN
% you must set
% filename name of shade file
% isd index of source depth

% open the file
fid = fopen( filename, 'r' );

% read

pltitl = fgetl( fid );
junk   = fgetl( fid );
junk   = fscanf( fid, '%f', 1 );
nsd    = fscanf( fid, '%i', 1 );
nrd    = fscanf( fid, '%i', 1 );
nrr    = fscanf( fid, '%i', 1 );

```

```

sd    = fscanf( fid, '%f', nsd );
rd    = fscanf( fid, '%f', nrd );
rr    = fscanf( fid, '%f', nrr );

for ii = 1:isd
    pressure = fscanf( fid, '%f', [ 2 * nrr, nrd ] );
    %ii, size( pressure )
end

pressure_c=pressure(1:2:2*nrr)+i*pressure(2:2:2*nrr);

rkm = rr / 1000.0;

```

remus_noise_thesis.m

```

%This m-file will analyze the directional data generated by
%remus_noise_dir_gen.m The output of that m-file is saved in a workspace
%labeled remus_noise_dir.mat. that m-file can be re-run if need be.

```

```

%load the remus noise data:
load remus_noise_dir.mat

```

```

%because NFFT=FS, Fxx(n) = n Thus, given a frequency of
%interest, it's index is Fxx is given by (f);

```

```

%first, plot the noise data for 180 degrees with the ambient data
figure;
semilogx(Fxx,spec(19,:),'k-');
xlabel('Frequency (Hz)');
ylabel('Power Spectral Density (dB re 1 \mu Pa / Hz)');
%legend('Aft of vehicle @ 1m','Ambient Noise');
title('Radiated Noise Directly Aft @ 1m, 1411 RPM, 06 DEC 04');
axis([100 10000 60 130]);
grid

```

```

figure;
semilogx(Fxx,amb_level,'k-');
xlabel('Frequency (Hz)');
ylabel('Power Spectral Density (dB re 1 \mu Pa / Hz)');
%legend('Aft of vehicle @ 1m','Ambient Noise');
title('Ambient Noise for 06 DEC 04 Dodge Pond Measurements');
axis([100 10000 40 90]);
grid

```

```

%now plot a small portion of the directionality data in the
%frequency range 500Hz - 1500Hz

```

```

% figure
% surf(theta,Fxx(500:1500),spec(:,500:1500));
% view(2);
% shading interp
% xlabel('Bearing (degrees)');
% ylabel('Frequency (Hz)');
% colorbar

```

```

%average the levels in bands and plot this as a function of
%direction
theta_rad=theta*pi/180;

```

```

cax=figure;

%now between 500 and 600
subplot(2,3,1);
level_ave=mean(spec(:,500:600),2)';
polarlim(theta_rad,level_ave,'k-',110);
title('Average level in the 500-600 Hz band');
xlabel('Bearing (degrees) - 180=aft');
set(gca,'ylim',[0 130]);

%do the same fore the other frequency bands.... omitted in printed version for brevity

suptitle('Measured Directionality of Radiated Noise 06 DEC 04')

%Now use only the peaks in a directionality plot
cax2=figure;

% between 500 and 600
subplot(2,3,1);
level_ave=mean(spec(:,585:592),2)';
polarlim(theta_rad,level_ave,'k-',130);
title('Average level in the 585-592 Hz band');
xlabel('Bearing (degrees) - 180=aft');
set(gca,'ylim',[0 130]);

%do the same fore the other frequency bands.... omitted in printed version for brevity

suptitle('Measured Directionality of Radiated Noise at Peaks 06 DEC 04')

%now determine the difference between 180 degrees with and without a prop
%%%%%%%%%%%%%%%%%%%%%%%%%%%%%%%%%%%%%%%%%%%%%%%%%%%%%%%%%%%%%%%%%%%%%%%%
%experimental constants
%hydrophone used: h56
%Sensitivity= -165 dB re v/upa
hs=-165; %db re v/upa

%distance between remus and hydrophone = 13m
d2t=13; %m

wav2volt=.316; %found using output of wavread.m and the txt files accompanying the pcm data files
% used to convert the output of wavread into volts.

NFFT=2^15; %16 bit fft - with sample rate of 2^15, this gives 0.5 Hz resolution

spec=[]; %spec will be 19 x NFFT/2 where each row is a direction and each column is a
%frequency. The data in it will be db re 1 upa/hz

[YS]=wavread('180no_prop.wav'); %read in the wav data
Y=Y*wav2volt; %convert wav file to units of volts
[Pxx Fxx_np]=psd(Y,NFFT,FS,hann(NFFT),NFFT/2); %find psd
Pxx=Pxx'*2/FS; %normalize psd and make it a row vector
spec_np=10*log10(Pxx)-hs+20*log10(d2t); %convert to level re 1upa/hz @ 1m

[YS]=wavread('180.wav'); %read in the wav data
Y=Y*wav2volt; %convert wav file to units of volts
[Pxx Fxx]=psd(Y,NFFT,FS,hann(NFFT),NFFT/2); %find psd
Pxx=Pxx'*2/FS; %normalize psd and make it a row vector

```

```

spec_prop=10*log10(Pxx)-hs+20*log10(d2t);    %convert to level re 1upa/hz @ 1m

%Now plot that data
figure
subplot(2,1,1);
plot(Fxx,spec_prop,'k-');
xlabel('Frequency (Hz)');
ylabel('PSD dB re 1uPa^2/Hz @ 1m');
axis([100 10000 60 135]);
grid
title('PSD with prop at 1380 RPM');

subplot(2,1,2);
plot(Fxx_np,spec_np,'k-');
xlabel('Frequency (Hz)');
ylabel('PSD dB re 1uPa^2/Hz @ 1m');
axis([100 10000 60 135]);
grid
title('PSD with no prop at 1380 RPM');

suptitle('Measured Power Spectral Density With and Without a Propellor 06 DEC 04')

```

spec_vs_range_415.m

```

%this m-file will show the progression of the wavenumber spectrum in range
%for the 415Hz data set taken with the REMUS towed array system on 10 DEC 2005

%load the pressure vs. range data set
load pofr_415_dop

%Use empirical range corrections found from the bahtymetry, k-spectrum, doppler, and GPS
total_travel=cumsum(diff(abs(R_ave)));    %total travel
ddr=[0 diff(R_ave)];    %range differences
total_travel=[0 total_travel];    %REMUS starts at 0
%percent error change as a function of range:
percent_error=2.1/100.*(ddr>0)-3.3/100.*(ddr<0);

drift_error=cumsum(ddr.*percent_error); %find range error
R_out=R_ave-20-drift_error;    %correct range including offset

R_ave=R_out;

%adjusting the range to pad out to changes the resolution
pad_range=6000;
k_in=linspace(1.5,1.8,1001); %wavenumber space vector

%only consider the outgoing portion of the towed array data. Also, get rid
%of the first part of the data during the dive.
P_ave=P_ave(50:5060);
R_ave=R_ave(50:5060);

%Window the data:
%create matrix where each row contains a 1 for each range that is in the
%correct interval and 0 for each range that is not. Each column is a
%range corresponding to R_ave. Each row is a different range interval
%corresponding to 0-1km, 1-2 km, 2-3 km , >3 km
I=[(R_ave<2000); ((R_ave>100).*(R_ave<2100));((R_ave>200).*(R_ave<2200)) ;...
((R_ave>300).*(R_ave<2300)); ((R_ave>400).*(R_ave<2400));((R_ave>500).*(R_ave<2500)); ...
((R_ave>600).*(R_ave<2600))];

%find the spectra:

```

```

spec=[];
colors={'r','g','b','k','m','y','c'}; %colors for screen plotting
h1=figure;
hold on

for range_int=1%:7
    fprintf('%g ',range_int);
    %create range and pressure sub-sets that correspond to the current range interval
    PP=P_ave(find(I(range_int,:)));
    RR=R_ave(find(I(range_int,:)));

    %zero-pad
    [P_pad,R_pad]=pad_data(PP,RR,pad_range);

    %now compute the hankel transform
    [g k]=hankel_quad(P_pad,R_pad,k_in);
    %plot(k,abs(g),char(colors(range_int)));
    plot(k,g.*conj(g),char(colors(range_int)));
    spec=[spec;g];
end

[g_max I_max]=max(spec,[],2);
center_range=[500 1000 1500 2000 2500 3000 3500];
xlabel('k');
ylabel('k-spectrum (linear)');
title('Horizontal wavenumber spectrum vs. range interval for f=415 Hz');
legend('0-1 km','0.5-1.5km','1-2 km','1.5-2.5km','2-3km','2.5-3.5km','3-4km');

figure
waterfall(k,center_range,abs(spec));
xlabel('k (1/m)');
ylabel('Range interval');
zlabel('k-spectrum (linear)');
title('Waterfall plot of Horizontal wavenumber spectrum vs. range interval for f=415 Hz');
view([4 50]);

```

startshort2.m

```

function [start2, stop2, start3, stop3]=startshort2(start1,stop1,run);

%this m-file will give the correct starting and stopping sample numbers for
%disks 2 and 3 given the sample range on disk 1 for run various missions
%run in Dodge Pond

switch run
%all of these timing numbers are determined emperically by looking at the
%raw data and lining up the timing pulses at the begining and end. The
%numbers here are sample numbers.
%t1-t6 define time stretches. t11,t22,t33 are alignment times give time shifts.
%at these samples the waveforms will be perfectly aligned.

    case 2          %Dodge pond Run 2
        t1=235247;
        t2=682308;
        t3=188182;
        t4=635249;
        t5=141354;
        t6=588420;
        t11=682308;
        t22=635243;
        t33=588423;
    case 3          %dodge pond run 3
        t1=235247;

```

```

        t2=682308;
        t3=188182;
        t4=635255;
        t5=141354;
        t6=588420;
        t11=14319249;
        t22=12328355;
        t33=14251611;
    case 4

        t1=76843;
        t2=115978092;
        t3=48922;
        t4=115951709;
        t5=5223;
        t6=115907768;

        t11=357345;
        t22=329412;
        t33=285716;
    otherwise
        fprintf('No data!!');
end

%each channel requires a shift and a stretch
%determine stretches between disk 1 and disk 2,3
a=(t2-t1)/(t4-t3);
a2=(t2-t1)/(t6-t5);
%determine time shifts between disk 1 and disk 2,3
t0=t11-t22;
t00=t11-t33;

%give disk 2 start and stop times.
start2=(start1-(1-a)*t11)/a-t0;
start2=round(start2);
stop2=round(start2+stop1-start1);

%give disk 3 start and stop times.
start3=(start1-(1-a2)*t11)/a2-t00;
start3=round(start3);
stop3=round(start3+stop1-start1);

```

write_flp.m

```

%write_flp

%this file will be used to read in data from the profiles structure to
%write a field file.
field.flpfil=strcat(profiles.envfil(1:end-3),'flp');
fod = fopen(field.flpfil, 'w' );

%take the title from the mod file
fprintf(fod, '/',           ! Title\n');

%options
fprintf(fod, '%s \n', field.opt);

%number of modes
fprintf(fod, '%g \n', field.nmodes);

%number of profiles
fprintf(fod, '%g \n', profiles.n);

```

```

%profiles ranges
fprintf(fod,'%f ',profiles.ranges);
fprintf(fod,'\n');

%reciever ranges
fprintf(fod,'%g \n',profiles.nr);
fprintf(fod,'%f %f / \n',profiles.rmin,profiles.rmax);

%sources
fprintf(fod,'%g \n',length(profiles.sd));
fprintf(fod,'%f ',profiles.sd);
fprintf(fod,'/ \n');

%reciver depths
fprintf(fod,'%g \n',length(profiles.rd));
fprintf(fod,'%f ',profiles.rd);
fprintf(fod,'/ \n');

%reciever displacements
fprintf(fod,'%g \n',length(profiles.rr));
fprintf(fod,'%f ',profiles.rr);
fprintf(fod,'/ \n');

fclose(fod);

```

write_in_krak.m

```

function write_in_krak(profiles,filename,rb,zb);
%this function will write a RAM input file using the bottom profile from a
%kraken input structure. The input variables are the profiles structure,
%the filename to write the .in file, rb and zb.

%rb is a vector of bathymetry ranges. zb is a vector of bathymetry
%depths. Using this, RAM can do the randge dependent calculation very
%efficiently. If no range dependence is desired, set rb=[0 max(R)] and
%zb = [bottom_depth bottom_depth];

%modified the kraken input profile structure to include the vector r_update
%(size n)
%the matrix c_update contains n column vectors that are the sound speed profile updates.

%make sure rb and zb are columns
rb=rb(:);
zb=zb(:);

%open the output file:
fod=fopen(strcat(filename, '.in'),'w');

%write the title
fprintf(fod,[profiles.title '\r\n']);

line1=[profiles.freq profiles.sd length(profiles.rd)];
fprintf(fod,'%g %g %g \t\t ! FREQ Zs NRdep\r\n',line1);
fprintf(fod,'%f \t\t\t\t !ZR''s\r\n',profiles.rd);

next_line=[profiles.rmin*1000 profiles.rmax*1000 (profiles.rmax-profiles.rmin)*1000/profiles.nr 1];
fprintf(fod,'%g %g %g %g \t\t ! RMIN RMAX DR NDR\r\n',next_line);
fprintf(fod,'100.0 .1 \t\t\t\t !ZMAX DZ\r\n');

next_line=[1467 8 1 0.0];
fprintf(fod,'%f %g %g %g \t\t\t\t ! CO NP NS RS\r\n',next_line);

```



```

%now print the bathymetry
fprintf(fod, '\t %f %f \r\n', [rb zb]);
fprintf(fod, '-1 -1\r\n');

for ii=1:profiles.n
    if ii~=1
        fprintf(fod, '%f \r\n', profiles.ranges(ii));
    end

    %write the water column data
    water_data=eval(strcat('profiles.', char(profiles.cofz(ii,1))));
    %z_cw=[water_data(:,1) water_data(:,2)];
    z_cw=[0 1467];
    fprintf(fod, '\t %f %f\r\n', z_cw);
    fprintf(fod, '-1 -1\r\n');

    %now the bottom data
    z_cb=[];
    z_rhob=[];
    z_atten=[];
    zzb=profiles.Depth(1);
    for jj=2:profiles.Nmedia(ii);
        krak_prof=(eval(strcat('profiles.', char(profiles.cofz(ii,jj)))))
    %kraken layer info is z cp cs rho ap as
        z_cb=[z_cb; krak_prof(:,1)-zzb krak_prof(:,2)];
        z_rhob=[z_rhob; krak_prof(:,1)-zzb krak_prof(:,4)];
        z_atten=[z_atten; krak_prof(:,1)-zzb krak_prof(:,5)];
    end
    %tack on the high reflection at large depth to get rid of fake
    %reflections
    z_atten=[z_atten; 90 1.0; 100 10.0];
    %write the profile data
    fprintf(fod, '\t %f %f \r\n', z_cb);
    fprintf(fod, '-1 -1\r\n');
    fprintf(fod, '\t %f %f \r\n', z_rhob);
    fprintf(fod, '-1 -1\r\n');
    fprintf(fod, '\t %f %f \r\n', z_atten);
    fprintf(fod, '-1 -1\r\n');

end
fclose(fod);

```

writedat_krak.m

```

function writedat_krak(profiles,filename);

%this function will take the information in structure struct and write it
%to 'filename.dat' as a safari data file.
%This uses a modified Kraken input structure.

%the safari struct has the structure:

%struct.title='title of data set'           string
%struct.options = 'output options'         string
%struct.freq= source frequency              float
%struct.layers= layer data                  n by 8 matrix of floats
%struct.source_data=source data             1 by up to 6 vector of floats
%struct.reciever_data=reciever data         1 by 4 vector of floats
%struct.velocity=velocity data              1 by 2 vector of floats
%struct.kspace=k space data                 1 by 3 vector of floats
%struct.range_axis                          1 by 4 vector of floats
%struct.tl_axis                             1 by 4 vector of floats

```

```

%an example as seen on page 87 of the safari hand book

% struct.title='SAFARI-FIP case 1';
% struct.options = 'N I T';
% struct.freq= 5.0;
% struct.layers=[0 0 0 0 0 0 0 0;
%               0 1500 0 0 0 1 0 0;
%               100 1600 400 0.2 0.5 1.8 0 0;
%               120 1800 600 0.1 0.2 2.0 0 0];
%
% struct.source_data=95;
% struct.reciever_data=[100 100 1 1];
% struct.velocity=[100 1e8];
% struct.kspace=[2048 1 1000];
% struct.range_axis=[0.0 5.0 20 1.0];
% struct.tl_axis=[20 80 12 10];

%note the number of layers input is not required... it is determined by the
%program.

for ii=1:profiles.n
%open the output file:
fod=fopen(strcat(filename,num2str(ii),'.dat'),'w');

%construct layers from karaken data
layers=zeros(1,8); %the top layer in safari is PR
for jj=1:profiles.Nmedia(ii);
% SSP % water
Nssp = size( eval(strcat('profiles.',char(profiles.cofz(ii,jj))))), 1 );
krak_prof=(eval(strcat('profiles.',char(profiles.cofz(ii,jj)))));
sigma=zeros(Nssp,1);
sigma(1,1)=profiles.sigma(ii,jj);
%in kraken, only the interface layers can have roughness.
%In safari, any part of the ssp can
%kraken layer info is z cp cs rho ap as with sigma in a different variable and cl not used.
%safari layer info is z cp cs ac as rho sigma cl
%cl=zeros(Nssp,1); %cl is not used in kraken.
cl=zeros(Nssp,1); %cl is not used in kraken.
cl(1)=profiles.CL(ii,jj);
new_layer=[krak_prof(:,1:3) krak_prof(:,5:6) krak_prof(:,4) sigma cl];
layers=[layers; new_layer];
end
%add on the bottom
bottom_depth=layers(end,1);
layers=[layers; bottom_depth profiles.cpb profiles.csb profiles.apb profiles.asb profiles.rhob...
profiles.bot_sig 0];
%now put in the linear interpolation for the ssp.
[a b]=size(layers);
for jj=6:a-1
if layers(jj,2)~=layers(jj+1,2);
layers(jj,3)=-layers(jj+1,2);
end
end

%now eliminate repeated depths
for jj=2:a-1
if layers(jj,1)==layers(jj+1,1); %repeated depths
layers(jj+1,1)=layers(jj+1,1)+0.001; %add a millimeter
end
end

%now assemble the source data from the kraken source data.

```

```

%we will not use option L so we will use a single source
%depth
source_data=profiles.sd;

%kraken structure just uses a vector rd with all of the reciever depths.
%Safari requires [rdmin rdmax nr ir]
reciever_data=[min(profiles.rd) max(profiles.rd) length(profiles.rd) 1];

%kraken and safari use the same data for min and max phase speed
velocity = [profiles.cmin_s profiles.cmax_s];

%k-data is included in the modified kraken structure
kspace=profiles.k;

%kraken uses r_min, r_max the other two variables are really dummy
range_axis=[profiles.rmin profiles.rmax 20 1.0];

%put in a dummy tl axis
tl_axis=[20 80 12 10];
%now write the data:
fprintf(fod,[profiles.title '\r\n']);
fprintf(fod,[profiles.options '\r\n']);
fprintf(fod,'%4.1f 0',profiles.freq);fprintf(fod,'\r\n');
[a b]=size(layers);
fprintf(fod,'%d \r\n',a);
fprintf(fod,'%g %g %g %g %g %g %g %g \r\n',layers');
fprintf(fod,'%g ',source_data); fprintf(fod,'\r\n');
fprintf(fod,'%g ',reciever_data); fprintf(fod,'\r\n');
fprintf(fod,'%10.0f %10.0f',velocity); fprintf(fod,'\r\n');
fprintf(fod,'%g ',kspace); fprintf(fod,'\r\n');
fprintf(fod,'%g ',range_axis); fprintf(fod,'\r\n');
fprintf(fod,'%g ',tl_axis); fprintf(fod,'\r\n');
fclose(fod);
end

```

writeenv_ns.m

```

%function writeenv_NS(matfile)
%the load command has been taken out... make sure you load the structure!!
% writeenv
% Uses the workspace variables to write out an envfil for use with KRAKEN

%this has been modified by J. Holmes to allow for easy implementation of
%range dependence. A structure 'profiles' must be made which has the following data
%in it

% %range independent
% profiles.envfil = name of envfil
% .title= plot title
% .freq = frequency
% .sd = source depths
% .rd = reciever depths
% .rr = reciever displacements (models slope / curve in array)
% .rmax = maximum range
%
% %range dependent (n) is the number of profiles in range
% .Nmedia(n) = Nmedia = m
% .topopt(n) = top options
% .Npts(n,m) = number of points to use in the mth media
% .sigma(n,m) = rms roughness of mth interface
% .Depth(n,m) = depth of the mth media
% .cofz(n,m) = the string containing the name of the variable

```

```

% with the mth layer profile for the nth profile
%. cofz variables = variables defined above.
%. botopt(n) = Bottom options
%. bot_sig(n)%bottom roughness
%.cpb(n)      = pressure wave speed in the bottom
%.csb(n)      = shear wave speed in the bottom
%.rhob(n)     = density in the bottom
%.apb(n)      = pressure attenuation in the bottom.
%.asb(n)      = shear attenuation in the bottom.
%.cmin(n)     = minimum sound speed.
%.cmax(n)     =maximum sound speed.
% %used by field
%.ranges(n)   = profile ranges
%.n           = number for profiles
%load(matfile); %matfile should be the name of a mat file which contains the above structure.

fid = fopen(profiles.envfil, 'w' );

for ii=1:profiles.n
fprintf( fid, '%s \r\n', profiles.title );
fprintf( fid, '%f \r\n', profiles.freq );
fprintf( fid, '%i \r\n', profiles.Nmedia(ii));
fprintf( fid, '%s \r\n', char(profiles.topopt(ii)) );

for jj=1:profiles.Nmedia(ii);
% SSP % water
Nssp = size(eval(strcat('profiles.',char(profiles.cofz(ii,jj)))), 1)
fprintf( fid, '%i %f %f \r\n', profiles.Npts(ii,jj), profiles.sigma(ii,jj),profiles.Depth(ii,jj));
fprintf(fid,'%f %f %f %f %f %f \r\n', (eval(strcat('profiles.',char(profiles.cofz(ii,jj))))))' );
end

% lower halfspace
fprintf( fid, '%s ', %g\n',char(profiles.botopt(ii)),profiles.bot_sig(ii))
fprintf( fid, '%f %f %f %f %f ! lower halfspace/ \r\n', profiles.Depth(ii,end),...
profiles.cpb(ii), profiles.csb(ii), profiles.rhob(ii), profiles.apb(ii), profiles.asb(ii) );

fprintf( fid, '%f %f \r\n', profiles.cmin(ii), profiles.cmax(ii) );
fprintf( fid, '%g ! RMAX (km) \r\n',profiles.rmax);

fprintf( fid, '%i ! NSD \r\n', length(profiles.sd) );
fprintf( fid, '%f ', profiles.sd );
fprintf( fid, '! SD(1) ... \r\n' );

fprintf( fid, '%i / ! NRD \r\n', length(profiles.rd) );
fprintf( fid, '%f ', profiles.rd );
fprintf( fid, '/ ! RD(1) ... \r\n' );

fprintf( fid, '%i / ! NRR \r\n', length(profiles.rr) );
fprintf( fid, '%f ', profiles.rr );
fprintf( fid, '/ ! RR(1) ... \r\n' );

%fprintf( fid, '%s \r\n', runtyp );
%fprintf( fid, '%i \r\n', Nbeams );
%fprintf( fid, '%f %f / \r\n', alpha );
%fprintf( fid, '%f %f %f', step, zbox, rbox );
fprintf(fid,'\n\n\n');
end

fclose( fid );

```

Codes Used in Appendices

Main Matlab code for TBL pressure spectrum - pspec.m

```
%this m-file is an attempt to find the pressure spectrum at the
% wall of a cylinder due to the turbulent boundary layer.

%%%%%%%%%%%%%%%%%%%%%%%%%%%%%%%%%%%%%%%%%%%%%%%%%%%%%%%%%%%%%%%%%%%%%%%%
%constants
delta=.0014;          %m
h=.011;              %m
nk=300;
nw=40;
k=linspace(10,16000,nk); %1/m
w=linspace(2*pi*100,2000*2*pi,nw); %rad /s
U=1.5;              %m/s
rho=1000;           %kg/m^3
[W,K]=meshgrid(w,k); %defines w-k plane
%%%%%%%%%%%%%%%%%%%%%%%%%%%%%%%%%%%%%%%%%%%%%%%%%%%%%%%%%%%%%%%%%%%%%%%%
%evaluate the integral over R for all w,k in the w-k plane
I=zeros(nk,nw);
for ii=1:nk
    for jj=1:nw
        I(ii,jj)=eval_int(U,delta,h,K(ii,jj),W(ii,jj));
    end
end
alpha=besseli(1,K*h)./besselk(1,K*h).*besselk(0,K*h)+besseli(0,K*h);
P=rho*K.*alpha.*I;

%find the maximum of the spectrum and the index of the maximum
[pmax imax]=max(log10(P), [], 1);

%plot the w-k spectrum
figure
surf(w,k,20*log10(abs(P)));
view(2)
shading interp
xlabel('w');
xlabel('w');
ylabel('k');
title('P(k,w)');
axis([0 12000 0 16000]);
%now plot the convection velocity from the peak data and
%overlay the data from the Carey paper

fc=[0 300 650 1200 2600 5000 10000];
ubyu=[.1 .955 .766 .69 .671 .646 .637];
Uconv=U*ubyu;
kc=2*pi*fc./Uconv;
%hold on
%plot3(2*pi*fc,kc,ones(size(fc))*max(max(abs(P))), 'k');

figure
plot(w/(2*pi),w./k(imax)/U);
xlabel('frequency (Hz)');
ylabel('U_c/U_{\infty}');
title('Frequency Dependent Convection Velocity');
hold on
plot(fc,ubyu,'ro');
grid
axis([0 2000 .5 1]);
```

Integral evaluation function - eval_int.m

```
function I=eval_int(U,delta,h,k,w);

%this function is for use with the project evaluating the
%turbulent boundary layer flow noise wall pressure
%fluctuations. It evaluates the integral of
%gamma(R,k,w)*R*K_1(kR) given U,delta,k,w,h

%first, set up the points in R
R=linspace(h,5*h,5000);
R=logspace(log10(h),log10(2*h),10000);
dR=diff(R);
dR=[dR dR(end)];

%%%%%%%%%%%%%%%%%%%%%%%%%%%%%%%%%%%%%%%%%%%%%%%%%%%%%%%%%%%%%%%%%%%%%%%%
%constants
rho=1000;          %kg/m^3
nu=1e-6;
l=20;
vofR=U*((R-h)/delta).^(1/6);
%power law approximation... From Wilcox.
%%%%%%%%%%%%%%%%%%%%%%%%%%%%%%%%%%%%%%%%%%%%%%%%%%%%%%%%%%%%%%%%%%%%%%%%

%now find a vector of the integrand at R
integrand_num=l*sqrt(2)*U/delta*.302*...
exp(-.0160*sqrt(U/(delta*nu))*(R-h)).*R.*vofR;
integrand_den=(pi*(l^2 +(k-w./vofR).^2));
integrand=integrand_num./integrand_den.*besselk(1,k*R);
%find integral by Riemann sum
I=cumsum(integrand(2:end).*dR(2:end)); %avoids inf at 0
I=I(end);
```

Appendix B - Linear Array Theory

Gain

Consider a linear array of sensors with a plane wave of angular frequency ω propagating from a direction θ relative to the normal (i.e. “broadside”) as seen in figure B.1

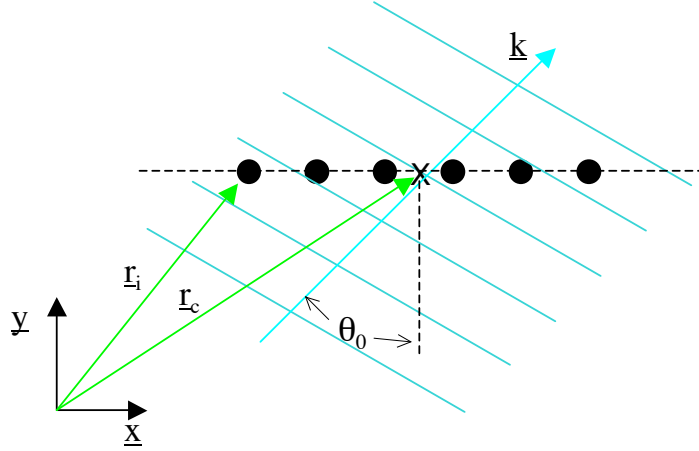


Figure B.1: Geometry of a plane wave incident on a linear array

Further, let each sensor have a location \mathbf{r}_i and the center of the array have a location \mathbf{r}_c . Define a relative position vector by

$$\mathbf{x}_i = \mathbf{r}_i - \mathbf{r}_c. \quad (\text{B.1})$$

The signal recieved on each channel is then

$$y_i(t) = P_0 \exp [i(\omega t - \mathbf{k} \cdot \mathbf{x}_i)] = P_0 \exp \left[i\omega \left(t - \frac{x_i}{c} \sin \theta_0 \right) \right] \quad (\text{B.2})$$

since $k = \omega/c$ where c is the speed of sound. The time delay beamformer output is given by

$$b(t, \Delta t_i) = \sum_m y_m(t - \Delta t_m) \quad (\text{B.3})$$

where Δt_m is a channel dependent time delay. If Δt_m is chosen such that

$$\Delta t_m = -\frac{x_m}{c} \sin \theta_s \quad (\text{B.4})$$

the array will preferentially look for a plane wave in the θ_s direction. To see this, consider the response to the plane wave above,

$$b(t, \theta_s, \theta_0) = \sum_m y_m(t - \Delta t_m(\theta_s)) = \sum_m P_0 \exp \left[i\omega \left(t - \frac{x_i}{c} (\sin \theta_0 - \sin \theta_s) \right) \right]. \quad (\text{B.5})$$

This is a maximum for $\theta_s = \theta_0$. Thus, for a receiving line array with N sensors,

$$b(\theta_s) = \sum_1^N y_n(\omega, t) e^{i \frac{x_i}{c} \sin \theta_s}. \quad (\text{B.6})$$

The power in the beam of the output is proportional to $|b(\theta_s)|^2$ and

$$|b(\theta_s)|^2 = bb^* = \sum_{n=1}^N \sum_{m=1}^N y_n y_m^*. \quad (\text{B.7})$$

If y is a signal with amplitude P and ρ_{nm} is the cross correlation between sensors,

$$|b(\theta_s)|^2 = bb^* = P^2 \sum_{n=1}^N \sum_{m=1}^N \rho_{nm}. \quad (\text{B.8})$$

For a plane wave of amplitude P_0 and perfect steering, the signal is coherent and $\rho_{nm} = 1$, which gives

$$\sum_{n=1}^N \sum_{m=1}^N \rho_{nm} = N^2; \quad |b(\theta_s)|^2 = P_0^2 N^2. \quad (\text{B.9})$$

If the signal is instead incoherent white noise with an rms pressure of P_N then

$$\rho_{nm} = \begin{cases} 1 & n = m \\ 0 & n \neq m \end{cases} \quad (\text{B.10})$$

and

$$\sum_{n=1}^N \sum_{m=1}^N \rho_{nm} = N; \quad |b(\theta_s)|^2 = P_N^2 N. \quad (\text{B.11})$$

Thus, for a plane wave signal of intensity P_0^2 on each channel, the beamformer output intensity is $P_0^2 N^2$ and the array signal gain is

$$ASG = 10 \log_{10}(P_0^2 N^2) - 10 \log_{10}(P_0^2) = 20 \log_{10}(N). \quad (\text{B.12})$$

For an uncorrelated signal with intensity P_N^2 on each channel, the beamformer output intensity is $P_N^2 N$ and the array noise gain is

$$ANG = 10 \log_{10}(P_N^2 N) - 10 \log_{10}(P_N^2) = 10 \log_{10}(N). \quad (\text{B.13})$$

By the product theorem of arrays [2], this analysis holds true for an array of N sub-arrays. That is, the relative array signal gain (gain of using N_{sub} sub-arrays compared to a single sub-array) is given by

$$RASG = 20 \log_{10} N_{sub} \quad (\text{B.14})$$

and similarly for the relative array noise gain,

$$RANG = 10 \log_{10} N_{sub}. \quad (\text{B.15})$$

Beam Widths

Sullivan *et al.* [75] presented a convenient method to determine linear array beamformer beam widths. For a plane wave arriving at an angle of θ relative to broadside of the line of the array, the output of a summing (not delay and sum) beamformer is

$$V(\theta) = \sum_{n=1}^N e^{inkd \sin \theta}. \quad (\text{B.16})$$

This assumes a uniform sensor spacing of d and k is the wavenumber $k = 2\pi/\lambda$. If the array is Nyquist sampled ($d = \lambda/2$)

$$V(\theta) \approx \text{sinc}[(N/2)kd \sin \theta]. \quad (\text{B.17})$$

The first zero of which appears at

$$(N/2)kd \sin \theta = \pi. \quad (\text{B.18})$$

By definition of the beam width as twice the angle of half power, the beam width at broadside is given approximately as

$$\Delta\theta \approx \frac{\lambda}{Nd}. \quad (\text{B.19})$$

For large N , $Nd \approx L$ where L is the length of the array. ($L = (N - 1)d$). Through half power arguments, Carey [96] gives the beam widths as

$$\begin{aligned} \Delta\theta &= 0.886 \sec \theta_0 \frac{\lambda}{L}, & \text{Near Broadside;} \\ \Delta\theta &= 2(0.886)^{1/2} \left(\frac{\lambda}{L}\right)^{1/2}, & \text{Near Endfire.} \end{aligned} \quad (\text{B.20})$$

In all cases the beam width is proportional to L^{-1} to $L^{-1/2}$ and a longer aperture gives a smaller beam width and hence a better spatial resolution. This is directly analogous to the increased frequency resolution in a Fourier transform of a time signal when the time length of the signal is increased.

General Beamformer

Given the time delay beamformer above, the general frequency domain beamformer is now derived. Let $Y_m(\omega)$ be the Fourier transform of the signal y_m and let $Z(\omega)$ be the Fourier transform of $z(t) = b(t, \theta)$. Then,

$$Z(\omega) = \sum_m Y_m(\omega) e^{i\omega \Delta t_m(\theta)}. \quad (\text{B.21})$$

Let

$$\mathbf{Y} = \begin{bmatrix} Y_1(\omega) \\ Y_2(\omega) \\ \vdots \\ Y_m(\omega) \end{bmatrix} \quad (\text{B.22})$$

and define a shading matrix \widetilde{W} such that¹

$$\begin{bmatrix} W_1 & 0 & \cdots & 0 \\ 0 & W_2 & & \\ \vdots & & \ddots & \\ 0 & & & W_m \end{bmatrix} \quad (\text{B.23})$$

where W_i is the weight (shading) of the i^{th} sensor. Now introduce a steering vector

$$\mathbf{c} = \begin{bmatrix} e^{-ik_1 \cdot x_1} \\ \vdots \\ e^{-ik_m \cdot x_m} \end{bmatrix} \quad (\text{B.24})$$

where $\mathbf{k}_i = \frac{\omega}{c} \mathbf{n}_i$ and \mathbf{n}_i is a unit vector in the direction of propagation of the wave at sensor i . x_i is the relative position of the i^{th} sensor as before. For a plane wave, the steering vector becomes

$$\mathbf{c} = \begin{bmatrix} e^{-i\frac{\omega}{c}|x_1|\sin\theta} \\ \vdots \\ e^{-i\frac{\omega}{c}|x_m|\sin\theta} \end{bmatrix}. \quad (\text{B.25})$$

Then

$$Z(\omega) = \mathbf{c} \cdot \widetilde{W} \mathbf{Y} = \mathbf{c}^H(\omega, \theta) \widetilde{W} \mathbf{Y}(\omega). \quad (\text{B.26})$$

The power in the beam is given by integrating over the frequencies

$$B(\theta)^2 = \int_{-\infty}^{\infty} Z Z^* d\omega = \int_{-\infty}^{\infty} \mathbf{c}^H \widetilde{W} \mathbf{Y} \mathbf{Y}^H \widetilde{W}^H \mathbf{c} d\omega \quad (\text{B.27})$$

but $\mathbf{Y}(\omega) \mathbf{Y}(\omega)^H \equiv \widetilde{R}$ is the correlation matrix. So, if

$$\boldsymbol{\theta} = [\theta_1 \quad \cdots \quad \theta_M] \quad (\text{B.28})$$

and

$$\widetilde{C} = [\mathbf{c}(\theta_1) \quad \cdots \quad \mathbf{c}(\theta_M)] \quad (\text{B.29})$$

where each θ_j is a beam direction, then the beamformer output as a function of direction is

$$[B(\theta_1)^2 \quad \cdots \quad B(\theta_M)^2] = \int_{-\infty}^{\infty} \text{diag} [\widetilde{C}^H \widetilde{W} \widetilde{R} \widetilde{W}^H \widetilde{C}] d\omega. \quad (\text{B.30})$$

¹The author chooses here to use a tilde ($\widetilde{}$) over a quantity to designate that quantity as a matrix rather than a vector.

Appendix C - Noise on an Array

Sources of Noise on an Array

Hydrophones convert a pressure signal into an electric signal. A simple point hydrophone does not have the ability to distinguish between pressures due to flow noise, bubble oscillations, mechanical vibrations, or acoustic fields. Because of this, care must be taken in designing a towed array to insure that the desired pressure, acoustic pressure, is sensed without corruption from unwanted pressure fields. Figure C.1 shows a schematic of a typical, long, ship-towed array including a vibration isolation module (VIM) and drogue. The shown towed array construction is reminiscent of the early work by Chesapeake Instrument Corporation [72] and consists of components designed to solve the problems experienced with towed acoustic sensors. Early towed arrays with exposed transducers exhibited high noise due to the turbulent boundary layer (TBL) noise experienced by any body moving through a fluid. To solve this, the hydrophones were mounted in an oil filled tube which separated the hydrophones from the TBL. This, however, introduced amplification of noises that excited bulge waves in the hose.

Since early arrays were towed at high speeds from tow ships, the tow cable and drogue, which is required to keep the array straight, would vibrate due to vortex shedding at frequencies characterized by the Strouhal number. Vibration isolation modules were incorporated to alleviate some of the vibration problems by including a mechanical damper in between the source of vibration and the hydrophones.

Since construction of a long array was not feasible in one section, they were constructed in modules. Mechanical couplers were required to join the modules, and each coupler could scatter noise and excite bulge waves.

At high tow speeds, arrays stretch due to drag and thus robust mechanical supports were required to keep each hydrophone centered in the array tube and at its correct position along the array. These supports could also scatter sound and potentially excite modes in the array tube.

The use of a long tow cable was included to alleviate several problems. First, a long tow cable separated the sensors from the ship noise providing noise reduction proportional to $\log_{10}(R)$ by spreading loss. Second, the arrays towed from ships were often made to tow in deep water below the surface layers and the thermocline to decrease ambient noise [73]. This deep tow also removed the array from the ship wake, an area characterized by large, highly dispersive bubble populations and thus high noise.

Bubbles also could create a problem if they form inside the array. Since bubbles are extremely efficient radiators and scatterers at their resonant frequencies, a bubble in the fill oil of the array could greatly degrade the performance.

For an AUV towed hydrophone array, many of the problems associated with a ship based array do not apply. Small AUVs are capable of speeds up to about 5 or 6 knots. Ship based arrays are often towed at 15-20 knots. Thus, for an AUV based array vortex shedding and drogue instabilities are not of primary concern. Robust hydrophone supports are also not required since the tow speeds are low and stretching of the array is unimportant. Careful design of a less scatter prone support can thus eliminate this problem. Since an AUV towed array is towed directly behind the vehicle, the tow cable catenary which allows for strum is eliminated. This means that a VIM is no longer needed. Further, an AUV towed array must be short and can be constructed in one piece, thus eliminating coupler vibrations. This leaves the following problems that are still pertinent to an AUV towed hydrophone array:

1. Tow vehicle noise,
2. Ambient noise,
3. TBL flow noise,
4. Bulge wave amplification,
5. Bubbles.

Ambient noise is inherent in the ocean and can not be avoided. In fact, if the other noise issues can be resolved, an AUV towed array could be used to measure variations in ambient noise. Tow vehicle noise is always a problem. The noise experienced by hull mounted sensors on an AUV partially motivated the development of an AUV towed array and this problem is best alleviated by the two standard means of a long tow cable and efforts to quiet the vehicle. Bubble noise is a problem by design of the array to be oil filled but is avoided by careful construction. This leaves bulge wave enhancement of noise and TBL flow noise which must be analyzed in order to control. The following sections include an analysis of the nature and effects of flow noise and the dynamics of the array hose.

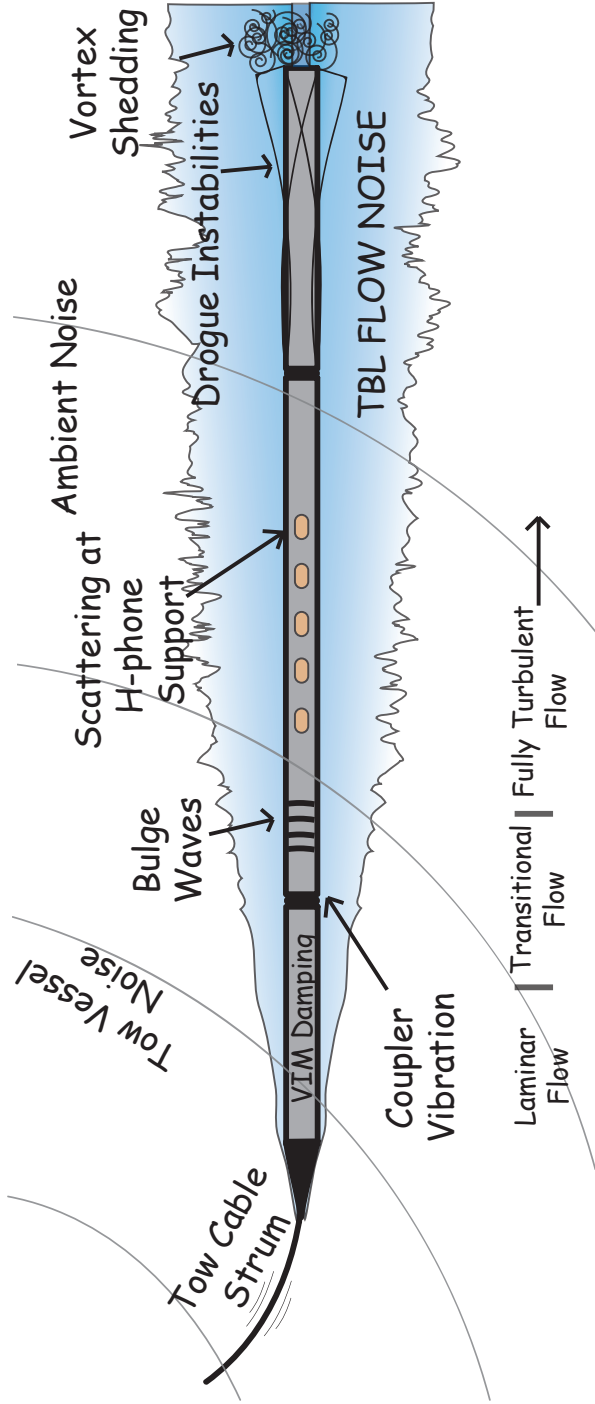


Figure C.1: Sources of noise on a ship towed array adapted from [119].

Source of Flow Noise

When a viscous fluid is caused to flow over a body, a boundary layer is formed which, at a high enough Reynolds number, becomes turbulent. That turbulence can be characterized by large and small scale eddies propagating in the fluid with some velocity. As these eddies pass by the surface of the body, they cause a local pressure disturbance on the surface. If the body in question is an acoustic transducer, these pressure disturbances generate a signal on the transducer which is often considered to be noise.

It is known from previous work that the turbulent eddies that are responsible for flow noise are convected along with a speed that is a fraction of the free stream velocity, ([120–122])

$$U_c \approx (0.6 - 0.8)U_\infty. \quad (\text{C.1})$$

There are two possible explanations for this:

1. The eddies are convected at the local v_x for a given r where $v_x \rightarrow 0$ near the wall and $v_x \rightarrow U_\infty$ as $r \rightarrow \infty$. [123]
2. Vortex interaction with the wall causes a small negative velocity of the eddies relative to the mean flow.

Since the second explanation is a non-linear affect and is only applicable very close to surface, the first explanation is assumed predominant.

All previous work on the turbulent boundary layer noise problem has shown that the strongest pressure fluctuations occur at the “convective ridge” centered on $k = \omega/U_c$. Further, the root mean square pressure fluctuations are proportional to the mean stream velocity squared [124]. Many quasi-empirical² models exist for the frequency-wavenumber spectrum. In 1980 Chase published a model for the pressure spectrum at low Mach numbers

²The term “quasi” is used here because the models are often based on fluid dynamic theory with parameters fit empirically.

for flow over a flat plate in the hydrodynamic domain ($k \gg k_{acoustic}$) given by [124,121]

$$\frac{P(k, \omega)}{\rho_0^2 v_*^3 \delta^3} = \frac{1}{[(k_+ \delta)^2 + 1/b^2]^{5/2}} \left(C_M (k_1 \delta)^2 + C_T (k \delta)^2 \frac{(k_+ \delta)^2 + 1/b^2}{(k \delta)^2 + 1/b^2} \right),$$

$$k_+^2 = (\omega - U_c k_1)^2 / (h v_*)^2 + k^2,$$

$$M = U/c_0 \ll 1,$$

$$\frac{\omega \delta}{U} > 1,$$

$$b \approx 0.75, \quad C_M \approx 0.1553, \quad C_T \approx 0.0047, \quad h \approx 3.$$
(C.2)

For this and other flat plate models, \mathbf{k} has components in the x and z directions when y is taken as the height. In 1962 (i.e. before Chase), Corcos had presented a much simpler model given by [120,124]

$$P(k, \omega) = \Phi_{pp}(\omega) \frac{l_1}{\pi [1 + l_1^2 (k_1 - \omega/U_c)^2]} \frac{l_3}{\pi [1 + l_3^2 k_3^2]},$$

$$l_1 \approx 9U_c/\omega, \quad l_3 \approx 1.4U_c/\omega$$
(C.3)

where l_1 and l_3 are experimental turbulence correlation lengths in the x and z directions. Φ_{pp} is the point pressure spectrum and may be approximated by

$$\frac{(U/\delta_*) \Phi_{pp}(\omega)}{(\rho_0 v_*^2)^2} = \frac{(\omega \delta_*/U)^2}{[(\omega \delta_*/U)^2 + (0.12)^2]^{3/2}}$$
(C.4)

where δ_* is the boundary layer displacement and for practical purposes can be approximated by $\delta/8$. v_* is the friction velocity and is typically of the order of 0.03U-0.04U. [124] For a rigid cylinder, rather than a flat plate, Knight [125] gives an empirical spectrum as

$$P_{rigid}(r = a, k_z, \omega) = C^2 \rho_0 \nu_*^3 a^2 \left[(k_z a)^2 + \frac{1}{12} \right] \left[\frac{(\omega a - u_c k_z a)^2}{h^2 \nu_*^2} + (k_z a)^2 + b^2 \right]^{-2.5}$$
(C.5)

where $C = 0.063$, $h = 3.7$, $b = 1.08$, $\nu_* = 0.04U$, $u_c = 0.68U$, and U is the tow speed.

While these models have assumed a constant convection velocity, it is known that the

eddy convection velocity along a rigid cylinder is actually slightly frequency dependent. Figure C.2 shows the ratio of convection velocity to mean stream velocity from a compilation of sources. The frequency dependence can be explained theoretically by first assuming

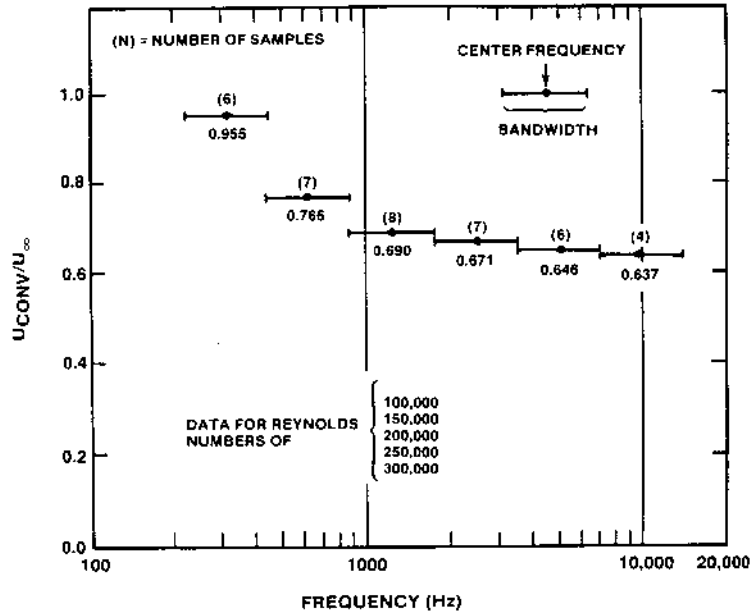


Figure C.2: Frequency dependence of measured convection velocity reprinted from [122]

the geometry of the problem as shown in figure C.3. Centered on the origin is a long, rigid cylinder of radius h that extends to infinity in the x direction. A cylindrical vortex sheet of infinitesimal core size is located a distance R from the x -axis that propagates in the x -direction at the mean local velocity. This vortex sheet has a strength Γ which is a function of wavenumber, k , and frequency, ω (or frequency and propagation velocity). It is assumed that the presence of the cylinder only effects the mean velocity via a boundary layer, and does not otherwise effect the motion of any discrete vortices. Also, discrete components of vorticity do not affect the motion of other bits of vorticity. With this,

$$\boldsymbol{\omega} = \Gamma e^{kx - \omega t} \delta(r - R) \hat{\boldsymbol{\theta}}. \quad (\text{C.6})$$

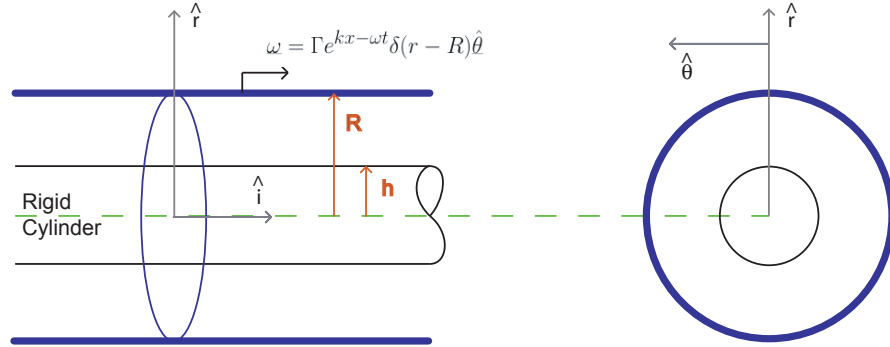


Figure C.3: Geometry of the Problem

$$\mathbf{v} = V\hat{\mathbf{i}}. \quad (\text{C.7})$$

Thus,

$$\boldsymbol{\omega} \times \mathbf{v} = \Gamma V e^{kx - \omega t} \delta(r - R) \hat{\mathbf{r}}. \quad (\text{C.8})$$

Since cylindrical hydrophones produce a voltage proportional to the circumferentially averaged pressure, cylindrical coordinates with no θ dependence can be assumed,

$$\nabla \cdot \mathbf{z} = \frac{1}{r} \frac{\partial}{\partial r} (r z_r) + \frac{\partial z_x}{\partial x}. \quad (\text{C.9})$$

So,

$$\nabla \cdot (\boldsymbol{\omega} \times \mathbf{v}) = \Gamma V e^{kx - \omega t} \delta'(r - R) + \frac{\Gamma V e^{kx - \omega t} \delta(r - R)}{R}. \quad (\text{C.10})$$

Crocco's equation for incompressible flow as derived from the Navier-Stokes equation is

$$\frac{\partial \mathbf{v}}{\partial t} + \boldsymbol{\omega} \times \mathbf{v} + \nabla B = -\frac{\eta}{\rho} \text{curl}(\boldsymbol{\omega}) + \frac{1}{\rho} \left(\eta' + \frac{4}{3}\eta \right) \nabla(\text{div}(\mathbf{v})) \quad (\text{C.11})$$

where

$$B = \int \frac{\partial P}{\rho} + \frac{1}{2} v^2. \quad (\text{C.12})$$

For steady, incompressible flow, (C.11) becomes

$$\boldsymbol{\omega} \times \mathbf{v} + \nabla B = -\frac{\eta}{\rho} \text{curl}(\boldsymbol{\omega}). \quad (\text{C.13})$$

Taking the divergence of both sides of (C.13) yields the ‘‘B-equation’’

$$\nabla^2 B = -\nabla \cdot (\boldsymbol{\omega} \times \mathbf{v}). \quad (\text{C.14})$$

Using (C.10) in (C.14), gives

$$\left[\frac{1}{r} \frac{\partial}{\partial r} \left(r \frac{\partial}{\partial r} \right) + \frac{\partial^2}{\partial x^2} \right] B = -\Gamma V e^{kx-\omega t} \delta'(r-R) - \frac{\Gamma V e^{kx-\omega t} \delta(r-R)}{R}. \quad (\text{C.15})$$

Now, assuming B has the form $\hat{B}e^{kx-\omega t}$,

$$\frac{\partial^2 \hat{B}}{\partial r^2} + \frac{1}{r} \frac{\partial \hat{B}}{\partial r} - k^2 \hat{B} = -\Gamma V \delta'(r-R) - \frac{\Gamma V}{R} \delta(r-R). \quad (\text{C.16})$$

In general, there would be a constant term in B added on, but this corresponds to the mean flow properties, which are unimportant to noise. One should keep in mind that $\Gamma = \Gamma(k, \omega)$ where explicitly writing the frequency and wavenumber dependence each time is omitted for brevity. Further, k and ω are related by some convection velocity V (which is a function of frequency) by $k = \omega/V(\omega)$.

Equation (C.16) is a Bessel Equation with $\lambda = -k^2$, so the general solution in terms of modified Bessel functions is

$$\hat{B} = aK_0(kr) + bI_0(kr). \quad (\text{C.17})$$

A bounded solution for $r > R$, requires

$$\hat{B} = aK_0(kr); \quad r > R. \quad (\text{C.18})$$

There is a discontinuity at $r = R$, namely the vortex sheet. Also, the flow for $r < h$ need

not be defined since the cylinder occupies that space. So,

$$\hat{B} = bK_0(kr) + cI_0(kr); \quad r > R. \quad (\text{C.19})$$

Where a,b, and c are constants with respect to r. Except at $r = R$,

$$B \equiv -\frac{\partial \phi}{\partial t}. \quad (\text{C.20})$$

For a hard walled cylinder, the boundary condition is

$$\frac{\partial B}{\partial r} = 0 \quad \text{at} \quad r = h. \quad (\text{C.21})$$

The equations for B given in (C.18) and (C.19) can be represented by one equation using the Heaviside function

$$\hat{B} = aK_0(kr)H(r - R) + bK_0(kr)H(R - r) + cI_0(kr)H(R - r). \quad (\text{C.22})$$

Use of (C.16) and the boundary conditions yields the constants

$$a = \Gamma V k R \left[\frac{K_1(kR) I_1(kh) - I_1(kR) K_1(kh)}{K_1(kh)} \right], \quad (\text{C.23})$$

$$b = \Gamma V k R \frac{K_1(kR) I_1(kh)}{K_1(kh)}, \quad (\text{C.24})$$

$$c = \Gamma V k R K_1(kR). \quad (\text{C.25})$$

Knowing a,b, and c, \hat{B} can be expressed in terms of $\Gamma(k, \omega, R)$, $V_c(R)$, R , $k = \omega/V_c(R)$, and h . The c in the subscript of the velocity term is adopted to denote that it is a convection velocity. The convection velocity is on the order of the tow speed (U_∞) and is much smaller than the acoustic velocity. This is why the flow noise is often referred to as psuedo-sound.

For an incompressible flow,

$$B = \frac{P}{\rho} + \frac{1}{2}v^2. \quad (\text{C.26})$$

By looking back at the derivation thus far, it is clear that it was never assumed that the fluid was inviscid. That being said, it is fair to assume that there will be a viscous boundary layer formed around the cylinder. This requires the no-slip boundary condition at the cylinder wall,

$$\mathbf{v}(h) = \mathbf{0}. \quad (\text{C.27})$$

Thus, at the cylinder wall, by (C.26)

$$B = \frac{P}{\rho} \quad \text{or} \quad \hat{P} = \rho \hat{B}. \quad (\text{C.28})$$

Thus far, the contribution to the surface pressure spectrum due to an infinitesimally thin cylindrical vortex sheet at a distance R from the center has been derived. To find the pressure spectrum at the surface of the cylinder due to a real flow, the contributions from vorticity at all R must be considered. Between the wall and R

$$\hat{B} = \left[\frac{\Gamma V k R K_1(kR) I_1(kh)}{K_1(kh)} K_0(kr) + \Gamma V k R K_1(kR) I_0(kr) \right]. \quad (\text{C.29})$$

So, from a single layer of vorticity the contribution to the pressure is

$$\Delta \hat{P}|_{r=h} = \rho \Gamma V_c k R K_1(kR) \left[\frac{I_1(kh)}{K_1(kh)} K_0(kh) + I_0(kh) \right]. \quad (\text{C.30})$$

The last term on the right of (C.30) is only a function of kh . This term is thus designated $\alpha(kh)$ for ease in writing. Integrating over the contributions from all of the layers of vorticity, gives

$$\hat{P}|_{r=h} = \rho k \alpha(kh) \int_{R=0}^{\infty} \Gamma(k, \omega, R) V_c(R) R K_1(kR) dR. \quad (\text{C.31})$$

The power spectrum of the pressure seen at the surface is given by

$$\mathbb{P} = \left(\hat{P}|_{r=h} \right) \left(\hat{P}^*|_{r=h} \right) \quad (\text{C.32})$$

where the * denotes the complex conjugate.

In order to compare this model to the measurements that have been made, the turbulent boundary layer pressure spectrum at the wall is calculated numerically using equations (C.31) and (C.32). In order to evaluate the integral, models for $\Gamma(k, \omega, R)$ and $V_c(R)$ are needed. First, to approximate the velocity distribution in the boundary layer, it is assumed that the Reynolds number is high and a boundary layer thickness δ is approximated. From Wilcox [101], the mean boundary layer velocity can be modeled by

$$V_c(R) = \left(\frac{R-h}{\delta} \right)^{1/6}. \quad (\text{C.33})$$

Further, in an ideal case, all of the eddies at a particular radius will propagate at exactly one speed. This would mean that $\Gamma(k, \omega, R)$ would have a very sharp peak around $k = \omega/V_c(R)$. To this end, it is assumed

$$\Gamma(k, \omega, R) = \delta_{f_{unc}} \left(k - \frac{\omega}{V_c(R)} \right) f(R). \quad (\text{C.34})$$

Where $f(R)$ is a function describing the rms value of Γ at a particular R and $\delta_{f_{unc}}$, the delta function, should not be confused with δ , the boundary layer thickness. Approximate fitting of one experimental measurement on a flat plate by Ong and Wallace [126] gives

$$\frac{\omega'_z \nu}{u\tau^2} \approx .302e^{-0.0160y^+} \quad (\text{C.35})$$

where τ is the wall shear stress, ν is the kinematic viscosity ($1 \times 10^{-6} m^2/s$ for water), ω'_z the rms vorticity in the z -direction, and y^+ is the non-dimensional height. Using the definition

of each of these and assuming this applies for the cylinder gives

$$\Gamma(k, \omega, R) = \sqrt{2} \frac{U_\infty}{\delta} (0.302) \delta_{func} \left(k - \frac{\omega}{V_c(R)} \right) e^{-0.0160 \left(\frac{U_\infty}{\delta \nu} \right)^{1/2} R}. \quad (\text{C.36})$$

Using a generalized function for δ_{func} ,

$$\Gamma(k, \omega, R) = \frac{l \sqrt{2} \frac{U_\infty}{\delta} (0.302) e^{-0.0160 \left(\frac{U_\infty}{\delta \nu} \right)^{1/2} R}}{\pi \left(l^2 + \left(k - \frac{\omega}{V_c(R)} \right)^2 \right)} \quad (\text{C.37})$$

where $l \rightarrow 0$. However, computationally speaking, in order to get a smooth curve answer, as $l \rightarrow 0$, the number of sample points in $R, k,$ and ω must become very large. Thus, l must not be too small in order to keep the problem computationally tractable. In this case, l was taken as approximately the total number of samples in either k or ω (which ever was lower) divided by 2 and the problem was modeled in Matlab. The codes used were *pspec.m* and *eval_int.m* from appendix A and the parameters used in the model were consistent with a 1.1 inch towed hydrophone array in sea water.

The MATLAB code produces a surface plot of the power spectrum on the ωk plane and a plot of the estimated measured convection velocity. These plots are shown in figures C.4 and C.5. A comparison can be made between the frequency dependent apparent convection velocity calculated from the theory here in figure C.5 and the compilation of measurements shown in figure C.2. It should be noted that the plateau on the left side of figure C.5 as well as the spotty nature of the figure C.4 are artifacts of the discrete method of the computation and do not represent the actual physics involved. These results agree with Knight [125] as well as VonWinkle [122] but the derivation provides insight into the nature of flow noise.

Effects of Flow Noise

In the preceding section it was shown that flow noise is caused by eddies convecting along the array surface due to viscous effects. The noise due to turbulent boundary layer flow

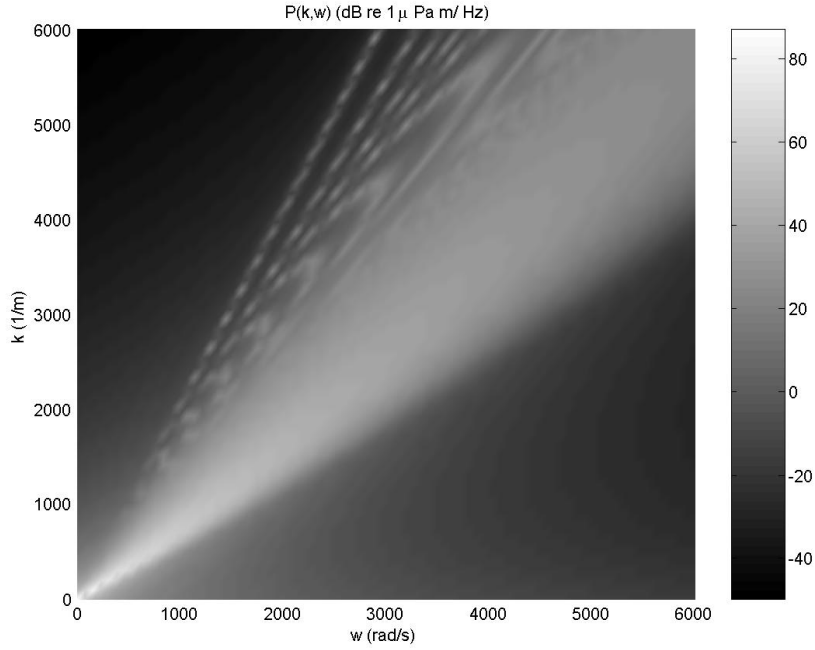


Figure C.4: Calculated $k - \omega$ plane spectrum of flow noise on a rigid cylinder

was shown to be characterized by a convective ridge in the frequency-wavenumber space. Equation (C.3) also showed that the turbulence has a characteristic correlation length. Considering these characteristics, the intent is to design a transducer to minimize flow noise effects.

The correlation length is the easiest characteristic of flow noise to take advantage of. From (C.3), it is known that

$$l \approx \frac{U_c}{\omega} \ll \lambda = \frac{2\pi c}{\omega}. \quad (\text{C.38})$$

Thus, if hydrophones are given a spatial extent which is large compared to the correlation length but short compared to an acoustic wavelength, noise will be averaged out while acoustic signals will not.

If the hydrophone can be separated from the fluid in such a way that the transfer function of the TBL to the hydrophone is small while the transfer function of the acoustic signal to the hydrophone is near unity, the the signal to noise ratio will be further enhanced.

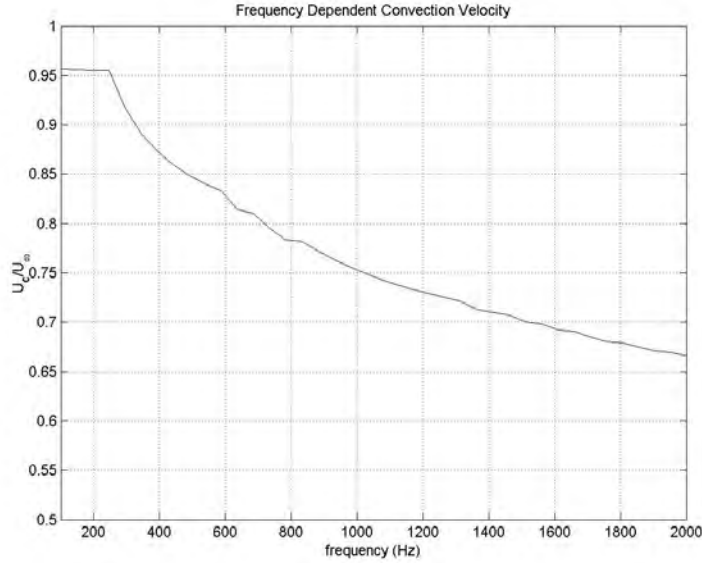


Figure C.5: Calculated frequency dependence of convection velocity

Since the convective ridge nature of TBL noise reveals that the difference between TBL noise and an acoustic signal at a given frequency is the wave number, it is clear that the design must effectively be a wave number filter.

A fluid filled flexible cylinder with a hydrophone in the center, the standard towed array design, acts as such a wave number filter. Markowitz [127] showed that for an orthotropic circular cylinder with fluid fill, the transfer function to the hydrophones is characterized by a resonant ridge in the $k - \omega$ space at the bulge wave velocity given by

$$c_b = \sqrt{\frac{\alpha^2 E h}{2 \rho_i R}} \quad (\text{C.39})$$

where ρ_i is the density of the fill fluid, R is the un-displaced cylinder radius, h is the cylinder wall thickness. $\alpha^2 E$ is the circumferential elastic modulus where α is defined so that E is the longitudinal elastic modulus. This allows for the orthotropic nature. Markowitz also showed that longitudinal waves are unimportant to the transfer function and that radiating supersonic waves do not occur until well above the frequency range of interest.

Dowling [128] gives the transfer function between the TBL and the hydrophones as approximately

$$T_h(k, \omega) = \frac{\omega^2}{\omega^2 I_0(|k|R) - \frac{\rho_0 \omega^2}{\rho_i} \frac{K_0(|k|R)}{K'_0(|k|R)} I'_0(|k|R) - 2 \frac{c_b^2 k}{R} (1 - i\delta_n) \left[1 + \frac{R^2 h^2 k^4}{12(1-\nu_h^2)} \right] I'_0(|k|R)} \quad (\text{C.40})$$

where I and K are the modified Bessel functions, ρ_0 is the density of the hose material, δ_h is the hose damping constant assumed to be approximately 0.15, and ν_h is the Poisson's ratio for the hose. This formulation assumes the internal fluid is incompressible and reduces at small ka to

$$T_h(k, \omega) = \frac{\omega^2}{\omega^2 - c_b^2 k^2 (1 - i\delta_n)}. \quad (\text{C.41})$$

The assumption of incompressibility is only valid at very low frequencies, so a correction can be made by considering the dynamics of a cylinder forced with wave propagating in the internal fluid. This gives

$$T_h(k, \omega) = \frac{\omega^2}{\omega^2 I_0(k_c R) - \frac{\rho_0 \omega^2}{\rho_i} \frac{k_c}{k} \frac{K_0(|k|R)}{K'_0(|k|R)} I'_0(k_c R) - 2 \frac{c_b^2 k_c}{R} (1 - i\delta_n) \left[1 + \frac{R^2 h^2 k^4}{12(1-\nu_h^2)} \right] I'_0(k_c R)} \quad (\text{C.42})$$

where $k_c = \sqrt{k^2 - \omega^2/c_{in}^2}$ and c_{in} is the speed of sound for the fill fluid. Combining this theory along with the TBL theory and wave propagation theory leads to the $k - \omega$ space shown schematically in figure C.6. The grayscale surface depicted in the figure is the transfer function from the surface to the center of a 1.1 inch towed hydrophone hose using (C.42). This is the hose used in the constructed array and described in the next appendix. The hatched regions of the figure indicate the region where the TBL convective ridge and acoustic signals would be on the $k - \omega$ plane. The solid line in the curve indicates the bulge wave resonance if the simplified model were used and the bulge wave was non-dispersive. The white peak in the calculated spectrum clearly shows the dispersive nature of the bulge wave. This figure also shows that TBL noise will be effectively filtered out at all but the lowest frequencies. Further, the acoustic signals are transmitted unaltered at almost all

frequencies.

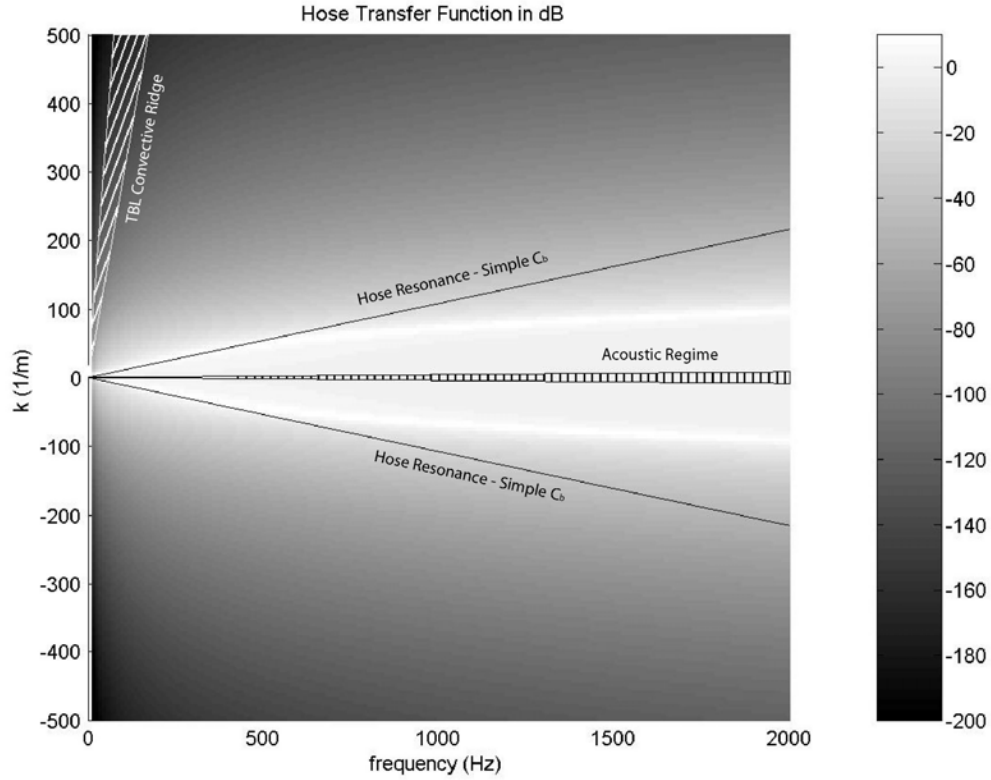


Figure C.6: Transfer function for the towed array hose on the $k - \omega$ plane. The TBL convective ridge region and acoustic regimes are shown as is the simplified bulge wave approximation.

The proper filtering of TBL noise of course assumes that the TBL noise is directly transmitted through the hose transfer function. Rigid couplers at the ends of array sections effectively impose a boundary constraint on the array hose. This gives a force described by a delta function, $\delta(x)$, at the bulkhead position. Since the transform of $\delta(x)$ is identically 1, this gives an excitation at the bulkhead due to the TBL, or any other vibration, which is wave number white. The bulge wave is thus excited which amplifies the noise [127]. Rigid hydrophone supports can cause a similar such constraint and noise contamination, especially if they fully block the flow of fluid around the hydrophone.

Appendix D - Details of Experimental Apparatus

By considering the noise effects presented in appendix C, an AUV towed hydrophone array system was carefully designed and constructed to eliminate sources of noise. The entire experimental apparatus consists of a vehicle, a towed array and a system to record the data from the array. Figure D.1 shows a diagram of the complete system with the recording system attached to the bottom of the vehicle. The design and construction of the subsystems are here described.

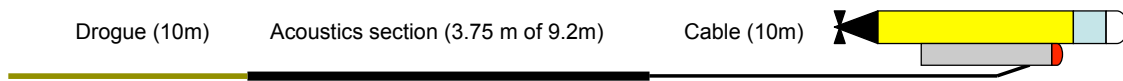


Figure D.1: Diagram of the subsystems of the towed array system. The vehicle is shown towing the array with the recording canister strapped to the bottom.

Vehicle

The vehicle chosen for this system was the REMUS vehicle designed by the Woods Hole Oceanographic Institution and commercially available from Hydroid Inc. Since the vehicle is a commercially available platform, little design work was required on the vehicle subsystem. Table D.1 gives a description of the off the shelf characteristics of a standard REMUS 100 vehicle [129]. In addition to the specifications listed, the following standard sensors are also included on a REMUS 100:

- Acoustic Doppler Current Profiler
- Side Scan Sonar
- Conductivity, Temperature, and Depth Probe

A global positioning system (GPS) and acoustic communications modem are optional transducers that were also included on the vehicle used.

Table D.1: Summary of off the shelf REMUS 100 specifications

Item	Specification
Vehicle Diameter	19 cm
Vehicle Length	160 cm
Weight in Air	363 N
Trim Weight	10 N
Max Operating Depth	100 m
Energy Source	1 kw-hr internal Lithium Ion Battery
Endurance	22 Hours at 3 knots, >8 hours at 5 knots
Drive System	Direct drive with brushless motor
Propeller Diameter	14 cm
Propeller RPM Max	1525 RPM
Propeller Blades	3
Nominal Speed	3 knots
Max Speed	5 knots
Control Method	Coupled yaw and pitch fins
Navigation	Long baseline; Ultra short baseline; Doppler -assisted dead reckoning

Since the vehicle was not originally designed to tow a hydrophone array, some modifications were required. In order to hold the recording system, a water-tight canister was clamped to the vehicle using rubber coated stainless steel hose clamps. A molded fiberglass nose cone was included on the front of this canister to minimize drag. In order to protect the towed array cable from the propeller and the vehicle control surfaces from the cable, an aluminum propeller shroud was attached to the tail section of the vehicle. This required the modification of the rear hull and also served well as an attachment point for the towed array. Also, deployment of the vehicle from a ship necessitated the inclusion of a lifting bail on the top of the vehicle which also was attached to the hull with hose clamps. The side scan sonar transducers were removed since they were not used and risked breaking from the hose clamps. The vehicle used in this work is seen in figure D.2.

After returning from a mission, the on board sensor data from the vehicle can be downloaded through a network connection. Data is written about every second during the mission and includes velocity, heading, depth, altitude above bottom, speed, latitude, and longitude. This data is available for post-processing and is synchronized to acoustic data



Figure D.2: Photograph of the REMUS 100 AUV used in the experiments. Here the vehicle rests on the deck of R/V Tioga in its cradle. The propellor shroud, recording canister, and lifting bail are all clearly visible.

by considering the time at which the thruster is first heard on the acoustic data.

Towed Array

Summarizing the major points from appendix C:

- Robust hydrophone supports that scatter sound are not needed.
- Construction of the array in one section reduces coupler vibration.
- Tow cable strum and drogue vortex shedding are not of significant concern and thus VIMs are not needed.
- A fluid filled flexible hose design acts as a wave number filter of noise.
- Bubbles must be avoided in construction.
- Hydrophones that are larger than the correlation scale of the noise field will minimize flow noise.

Based on these points the design solution chosen was to use a typical fluid filled flexible hose array construction with simplifications. The array consists of a tow cable, an acoustic oil filled hose section and the drogue. Details of the mechanical construction of the acoustic section array are given in figure D.3. It is constructed from a 9.2 m long Kevlar reinforced tube with an outer diameter of 2.8 cm (1.1 inches). A sample of the array tube was tested in a tensile test machine to have a longitudinal modulus of elasticity of 212 MPa and a circumferential modulus of elasticity of 15.1 MPa. This is a result of the fact that all Kevlar reinforcement fibers in the tube are longitudinal. With light mineral oils as the fill fluid, the estimated bulge wave speed is approximately 40 m/s. The hose transfer function shown in figure C.6 was calculated using this hose with a mineral oil fill as was the TBL convective ridge. From the figure it is clear that this construction is expected to work well as a wave number filter.

The hydrophones used in the towed array are Benthos³ AQ-2000 hydrophones. These hydrophones are acceleration canceling piezo-ceramic transducers which are 4.56 cm long and 1.32 cm in diameter with a sensitivity of -201 dB re $1V/\mu Pa$ up to 10 kHz. From equation (C.38), it is expected that at maximum tow speed of 2.5 m/s (about 5 knots) the longest correlation length of the flow noise will be on the order of 1 cm or less. At 5 kHz the wavelength is expected to be 30 cm long. Given the length of an AQ-2000, using a single hydrophone per channel will give a sensor that is $\lambda/6$ long. This satisfies the requirement for a quiet system that the sensor length be longer than the correlation length but shorter than a wavelength. At 2 kHz the wavelength is 0.75 m and the use of two hydrophones wired in parallel and placed one after the other in a group will make the hydrophone group longer than 10 correlation lengths but shorter than $\lambda/8$. This enhances the signal to noise ratio and thus the six channels of the array are constructed with two hydrophones each wired in parallel and placed end to end. In this configuration the acoustic center of the hydrophone group is in between the two hydrophones.

³Benthos, Inc., 49 Edgerton Dr., North Falmouth, MA 02556

Expected voltage outputs from an AQ-2000 hydrophone due to a signal of 100 dB re μPa (as is expected in a long-range transmission loss experiment with a reasonable source) are on the order of microvolts. Transmission of such signals over several meters to a recorder outside of the acoustic section of the array would be subject to large electromagnetic noise problems. Each channel thus includes a 26 dB gain pre-amplifier, a Benthos AQ-202, to amplify the signals to more reasonable recording levels.

For the wave number filtering properties of the array hose to be realized, the hydrophones must be centered in the array tube. Scattering of acoustic signals is avoided if the support has properties very similar to the fill fluid. By wrapping the hydrophones and preamplifiers in polyester wool batting material, they are held in the center of the tube when the array is assembled and the fill oil saturates the batting, giving it acoustic properties very near the oil. In order to maintain hydrophone group spacing without hindering the scattering properties of the support, all of the wired and batting wrapped components of the array are inserted into a slightly elastic polyethylene mesh sleeve that contracts under longitudinal tension, reminiscent of a Chinese finger trap toy. A photograph of a wired hydrophone group is shown in figure D.4 and the group inserted into the mesh sleeve is shown in figure D.5. To ensure the components do not shift, the sleeve is tied off around the components with nylon cord. This is shown in figure D.6. A wiring schematic for the internal components is shown in figure D.8.

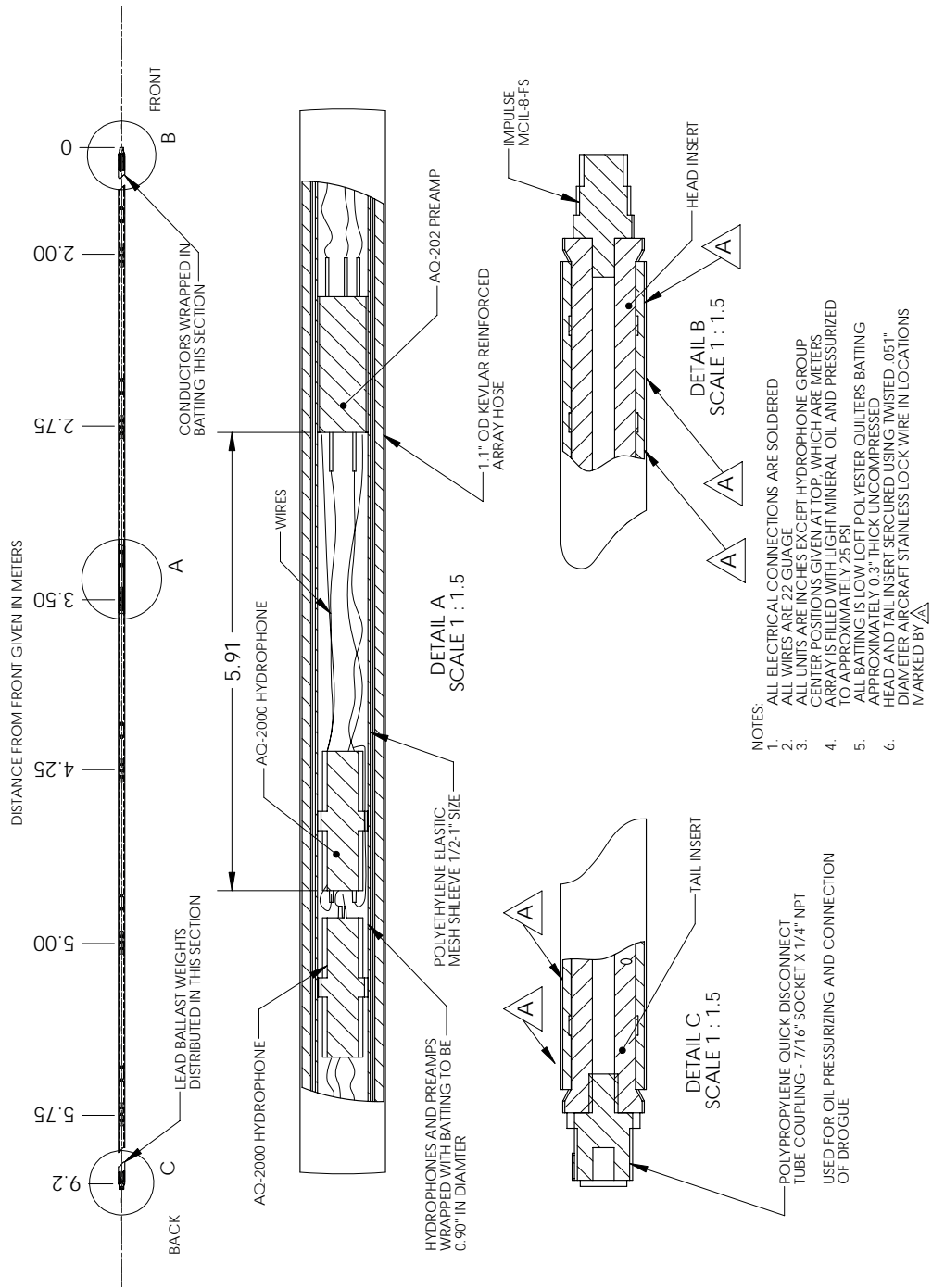
The array is constructed in one section with an acetal termination at each end as shown in figure D.3. The front termination, the head insert, has an electrical connector to connect the acoustic section to the tow cable. Figure D.9 shows the engineering details of this insert. The rear termination, the tail insert, has a standard polypropylene quick disconnect pressure fitting on it. This pressure fitting serves two purposes. During construction, the array is filled and pressurized through this port. When in use, the drogue has a drogue connector adhered to it with epoxy which mates with the retaining ring of the quick disconnect port without engaging the valve inside the port. The engineering details of this insert are shown in figure D.10 and the mating drogue connector is shown in figure

D.11. Stainless steel aircraft wire is twisted around the array hose and inserts to clamp the ends shut. Wire clamp locations are indicated in figure D.3 and a photograph of a wire clamp at the front end of the connector is shown in figure D.7

Since hydrophones only populate 3.75 m of the 9.2 m hose, lead weights are distributed through out the rest of the acoustic section to achieve neutral buoyancy. The distribution of these weights is such that the array lays nearly flat when still in sea water and was determined empirically.

During the construction process, all bubbles must be removed from the inside of the array tube. This is done by careful construction. First, the mineral oil fill fluid is degassed under vacuum. The acoustic section is assembled without fully inserting the front termination and supported on an incline such that the still open front of the array is immersed in a supply of degassed oil and the end of the array is approximately 2.5 m high. An empty plenum is then attached to the quick disconnect valve on the raised end and a vacuum drawn on it with an aspirator. This draws the oil up through the array. Once oil enters the plenum with no bubbles coming out, the front termination on the array is inserted and clamped. The section is then pressurized to 25 psi by attaching a pressurized air line to the plenum, forcing some oil in the plenum back into the array. After pressurization the plenum is disconnected which closes the valve on the array.

The drogue, which gets attached to the quick release port, is 10 m long and made from 1.25 cm diameter twisted nylon rope epoxied to the drogue connector shown in figure D.11. The tow cable is 10m long and has 8 conductors in a waterproof monomer rubber insulation . To achieve neutral buoyancy sealed sections of air filled tubing is attached to the tow cable. One end of the cable connects to the front of the acoustic section and the other to the recording system.



- NOTES:
1. ALL ELECTRICAL CONNECTIONS ARE SOLDERED
 2. ALL WIRES ARE 22 GAUGE
 3. ALL UNITS ARE INCHES EXCEPT HYDROPHONE GROUP CENTER POSITIONS GIVEN AT TOP, WHICH ARE METERS
 4. ARRAY IS FILLED WITH LIGHT MINERAL OIL AND PRESSURIZED TO APPROXIMATELY 25 PSI
 5. ALL BATTING IS LOW LOFT POLYESTER QUILTERS BATTING APPROXIMATELY 0.3" THICK UNCOMPRESSED
 6. HEAD AND TAIL INSERT SECURED USING TWISTED .051" DIAMETER AIRCRAFT STAINLESS LOCK WIRE IN LOCATIONS MARKED BY Δ

Figure D.3: Details of construction of the towed hydrophone array

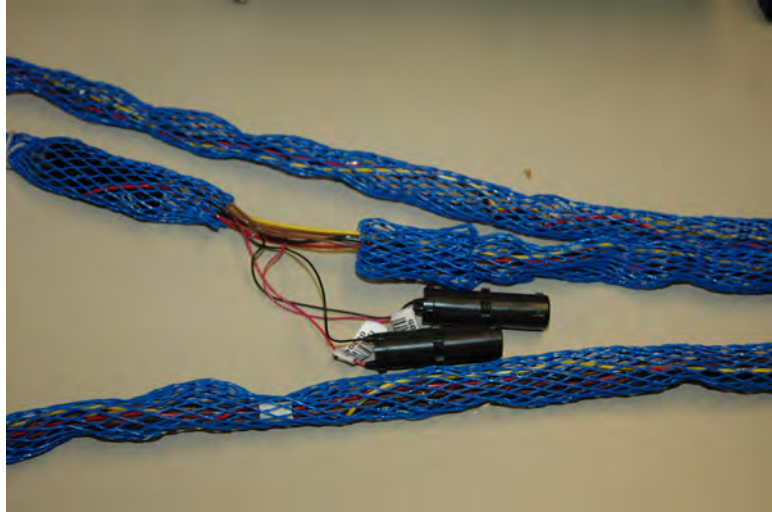


Figure D.4: Photograph of wired hydrophone group



Figure D.5: Photograph of hydrophone group wrapped in batting material and inserted in the mesh sleeve



Figure D.6: Photograph of a tie off used on the mesh sleeve to keep array components in place



Figure D.7: Photograph of the connector, termination, and wire clamp on the front of the acoustic section of the array

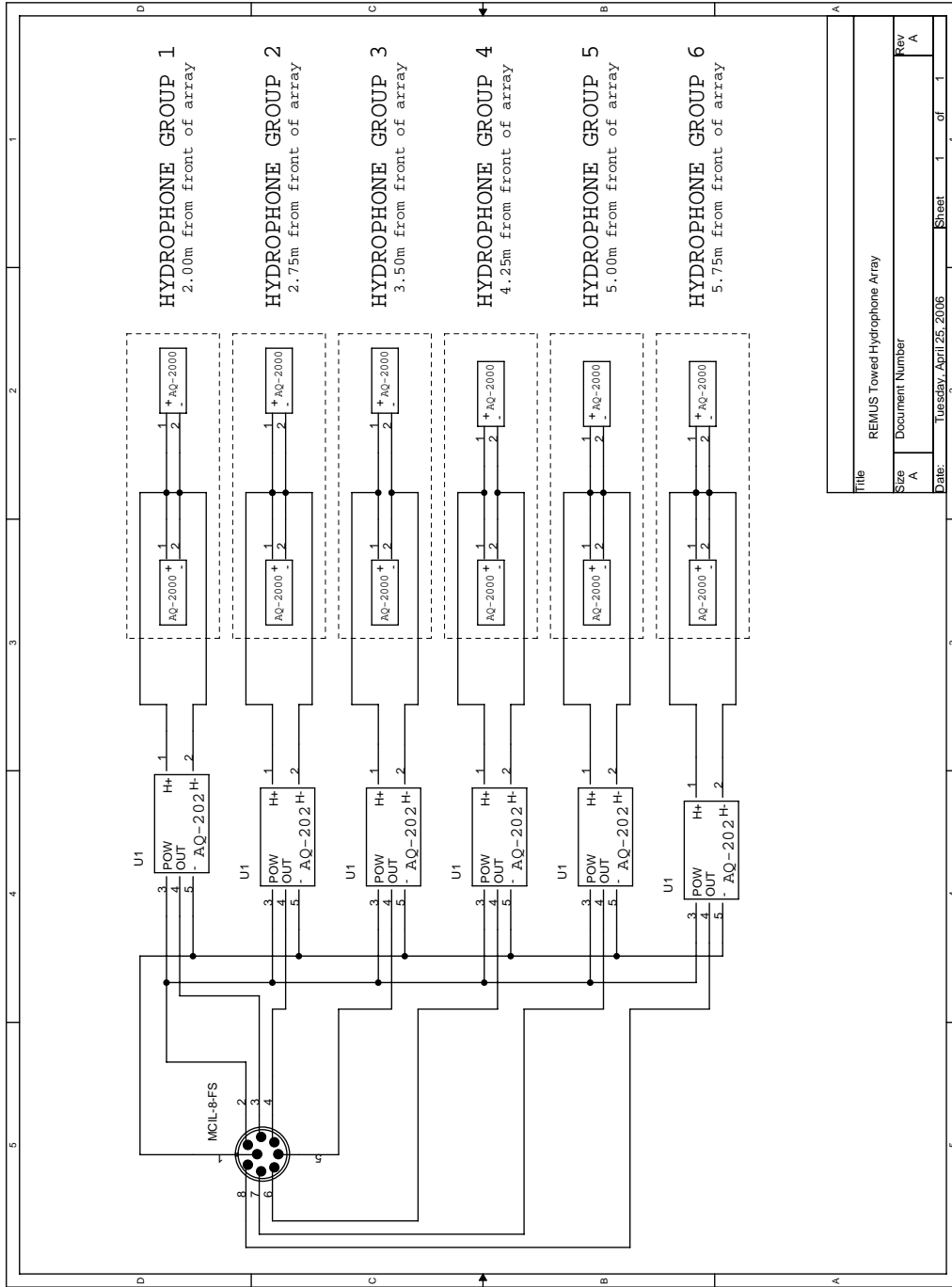


Figure D.8: Wiring schematic for internal array components

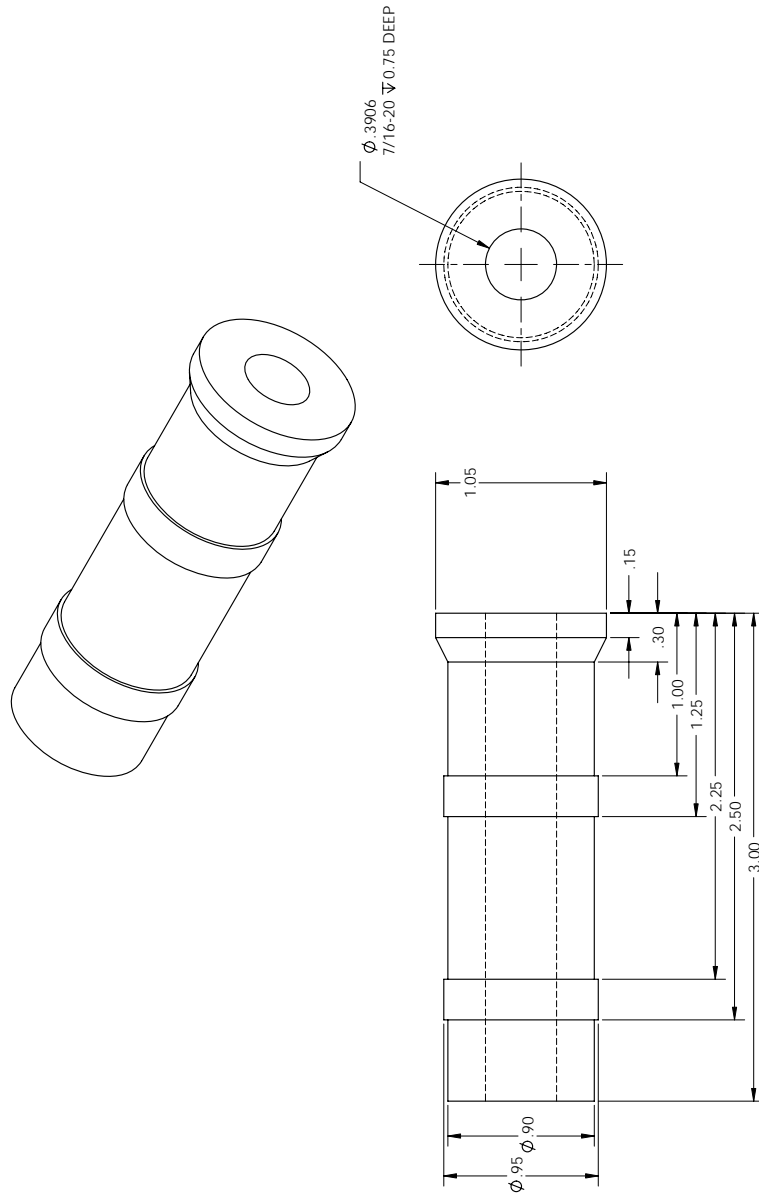


Figure D.9: Engineering drawing of the head insert which terminates the front of the array

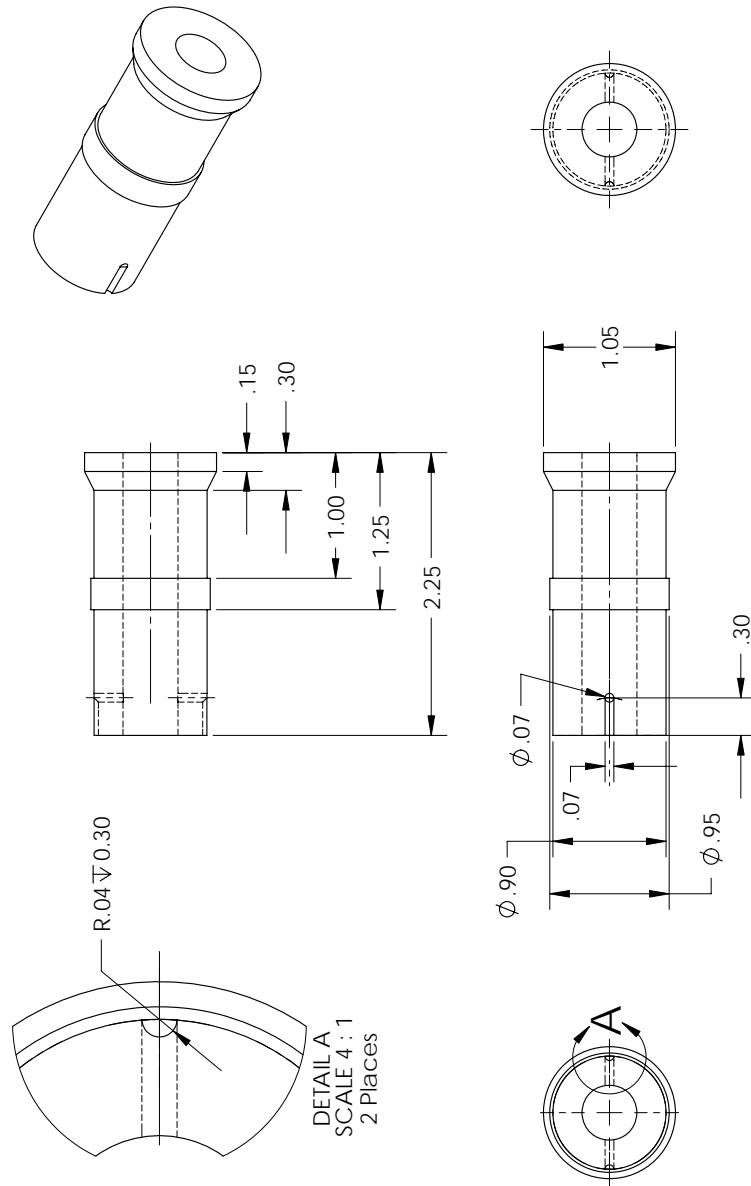


Figure D.10: Engineering drawing of the tail insert which terminates the back of the array

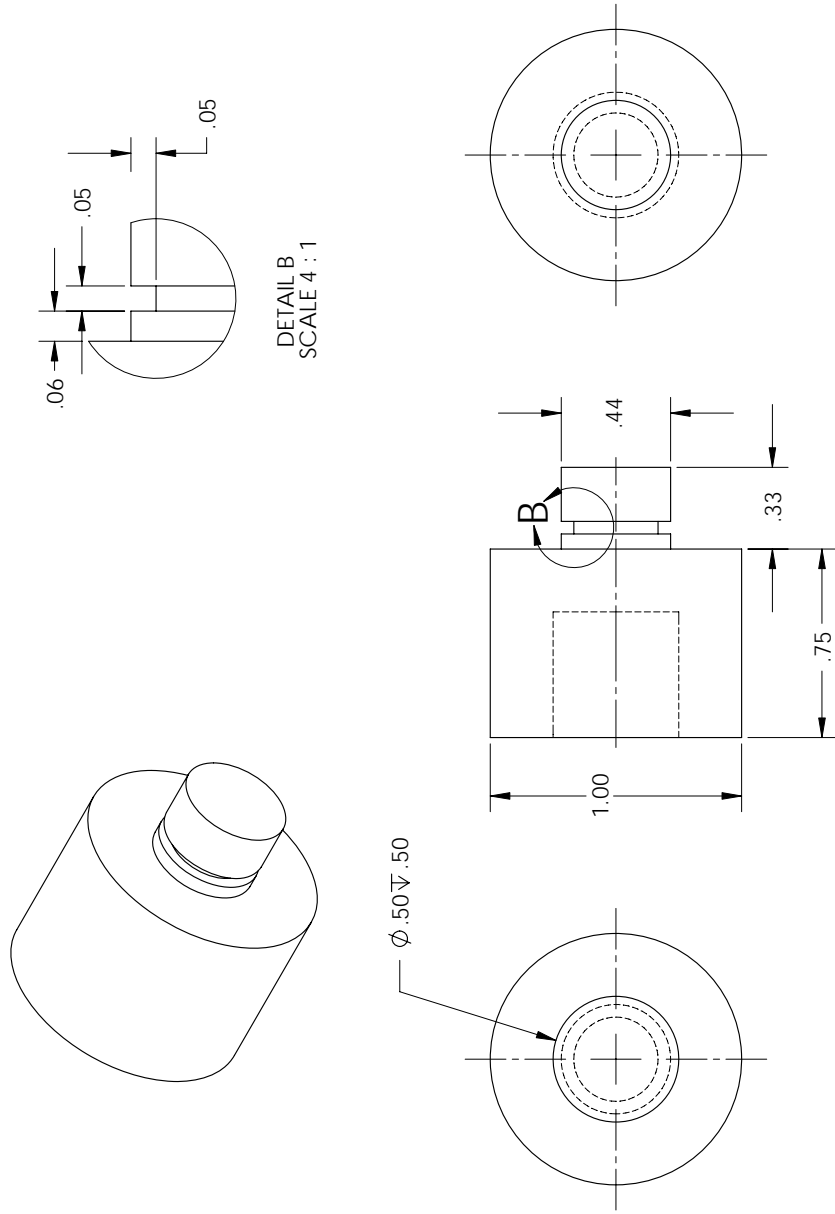


Figure D.11: Engineering drawing of the drogue connector which mates the drogue to the acoustic section at the quick disconnect connector without engaging the valve.

Recording System

Rapid implementation and ease of use lead to the development of a recording system consisting of off the shelf components. Since the array only has six channels, three Sony NHF-800 Hi-MD mini-disc recorders are used which can each record a left and right channel. A sampling rate of 44.1 kss at 16 bits limits recording times on 1 giga-byte mini-discs to 90 minutes of uncompressed data on each recorder.

A conditioning and timing board is used to mate the recorders to the array as well as provide synchronization between the three recorders. The schematic for this board is shown in figure D.12 and the schematic for the entire system is shown in figure D.13. A timing integrated circuit followed by a binary counter cascade which is reset when its first and last bits are both positive provide a milli-second scale pulse every 10-15 minutes. This pulse is simultaneously distributed to each channel through an octal buffer integrated circuit and isolating diodes so that the timing circuit will not corrupt hydrophone signals. This also minimizes channel cross talk. RC high pass filters on each channel remove the 5 V DC carrier signal coming from the array preamplifiers and a shunt capacitor on the supply voltage ensures low noise on the array power.

Data can be downloaded from the mini-disc recorders using Sony supplied software and a universal serial bus on a computer and then imported into MATLAB or other signal analysis software for analysis. If the units of the signal imported into MATLAB are termed wav units⁴ the the recorders are calibrated to 0.125 *wav/volt* at the most sensitive recorder setting with the automatic gain control turned off.

The entire recording system is housed in a 10 cm diameter water-tight cylinder strapped to the bottom of the vehicle. This includes three mini-disc recorders, the 9V batteries which power the array, four 1.5 V batteries which power the timing circuit, and the conditioning and timing board. A photograph of the recorder system is shown in figure D.14.

⁴This unit is so named because the file extension on the downloaded data is “wav”.

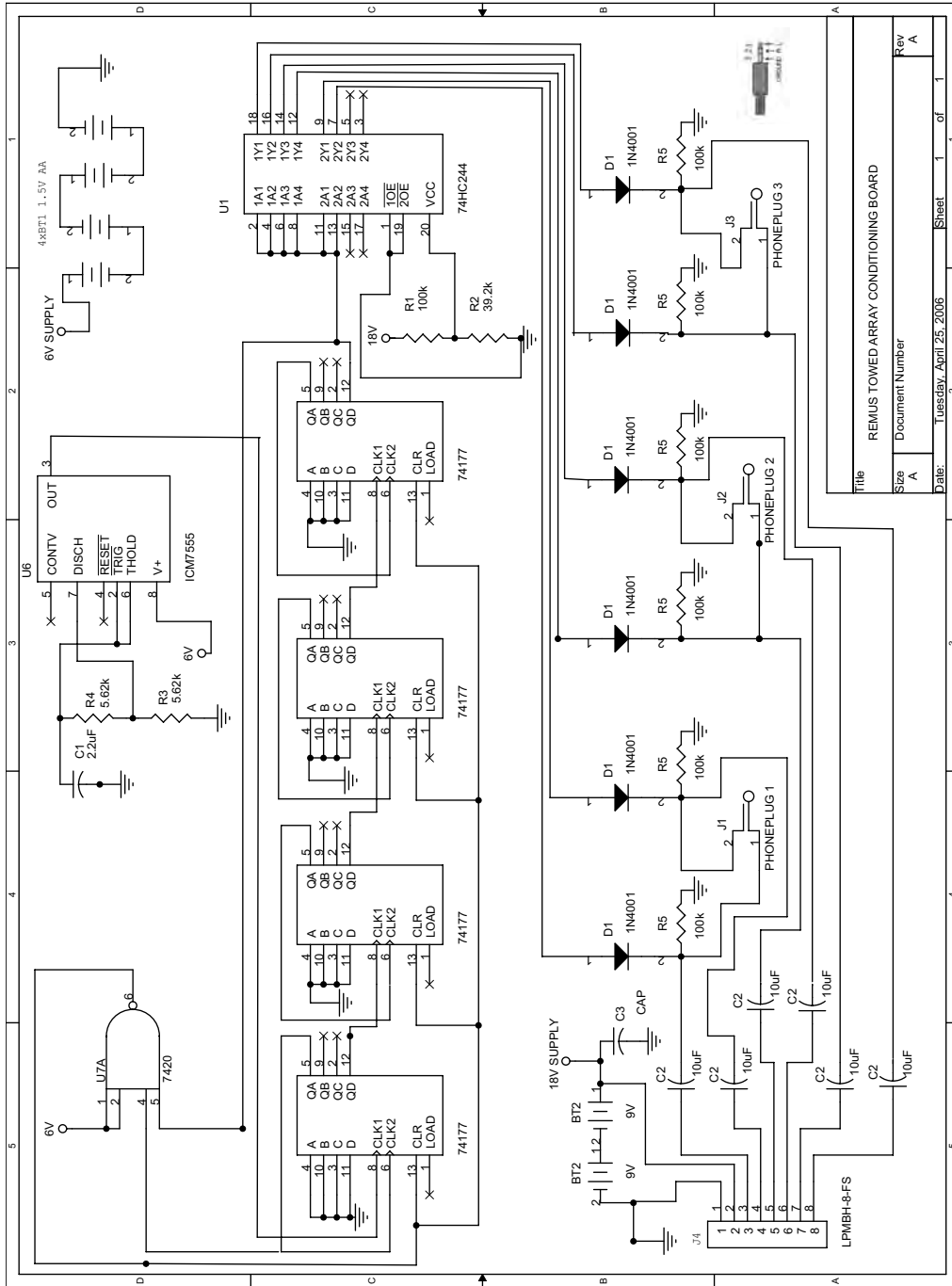


Figure D.12: Schematic of recording system conditioning and timing board

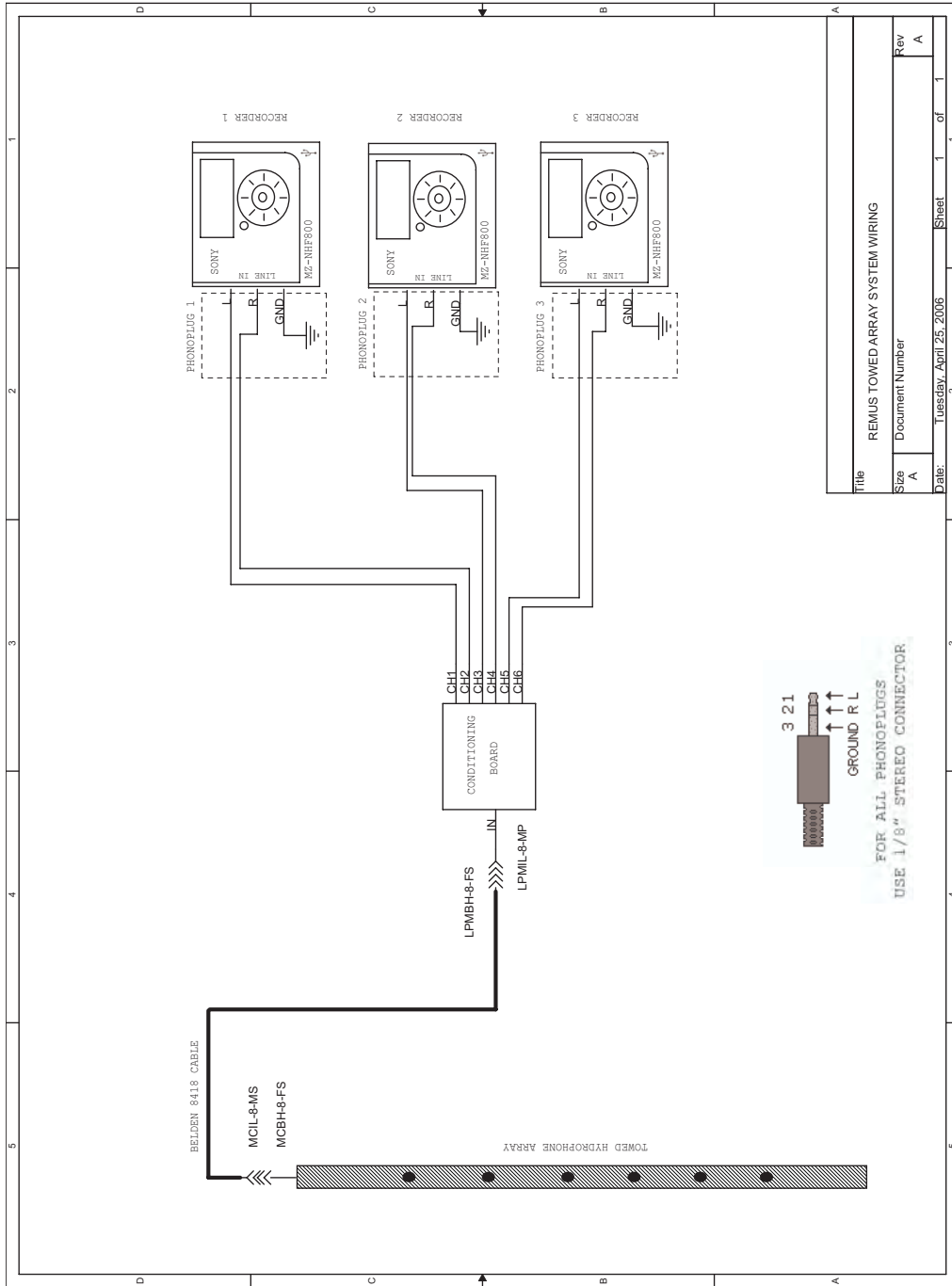


Figure D.13: Schematic of recording system conditioning and timing board



Figure D.14: Photograph of recording system including its location when strapped to the AUV

Appendix E - Pressure, range and time

The vehicle used in the Nantucket Sound experiments reports position and speed, among other data, approximately every second. The overlap sampling scheme detailed in section 2.3.2, however, requires that acoustic samples be taken for every advance d of the array. The recording system samples at 44.1 kss and is synchronized to the vehicle data by considering the acoustic modem start ping and the start of the vehicle thruster, which are recorded acoustically and indicated in the vehicle data.

For post processing a method must be determined to find the correct t_i for each sample on the array such that the array moves a distance d between samples $i - 1$ and i . To do this, the vehicle's navigation data is used. When the vehicle is on the surface at the beginning of the mission, it's GPS determines it latitude and longitude. When submerged, electromagnetic waves do propagate far in the water and thus the latitude and longitude are determined by another navigation means, in this case dead reckoning. Dead reckoning determines the vehicle position by integrating the vehicle velocity which is here determined by speed-over-ground estimated from the acoustic doppler current profiler.

The vehicle navigation data can be put into a local Cartesian coordinate system by considering the local variation of latitude and longitude. In Nantucket Sound a good estimate is

$$\frac{\text{meters}}{\text{degree latitude}} = 111061, \quad (\text{E.1})$$

$$\frac{\text{meters}}{\text{degree longitude}} = 83668. \quad (\text{E.2})$$

The latitude and longitude of the source, as determined by GPS, are taken as the origin of the Cartesian coordinate system.

Since the distance between each navigation data point is known versus time, the time to advance each d meters can be found. The first time sample of acoustic data is taken at the exact time of a navigation data point. Figure E.1 show the problem schematically

where tick marks indicate navigation data and i 's indicate acoustic data. The time at which

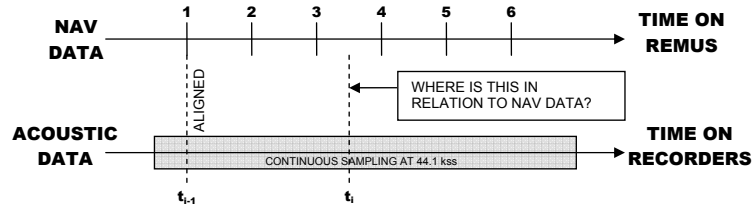


Figure E.1: Schematic of the problem of different acoustic and navigation time scales

the next acoustic sample is to be started is found by interpolating the range from point 1 to each other point vs. time

$$R_{1 \rightarrow j} = \sqrt{(x_1 - x_j)^2 + (y_1 - y_j)^2} \quad (\text{E.3})$$

as shown in figure E.2 where j 's represent navigation data . Once t_i is determined, x and

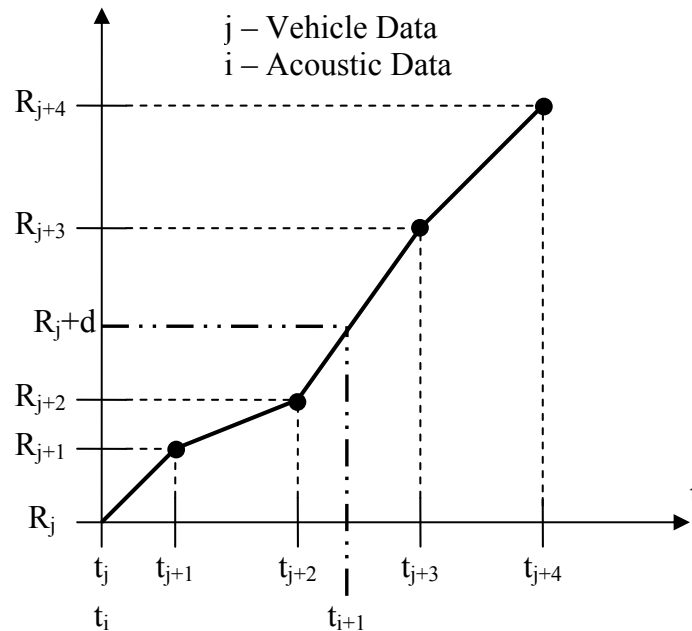


Figure E.2: Schematic of range and time interpolation between navigation data and acoustic data.

y on the Cartesian coordinates are found by interpolation versus time. Then the range to the i^{th} data point from the source is

$$R_i = \sqrt{x_i^2 + y_i^2}. \quad (\text{E.4})$$

This is then repeated for each successive sample by considering the range to the sample before it.

Once the time at which a sample is determined, the complex pressure is found at each known experimental frequency by taking a time interval $t = (t_i, t_i + \Delta t)$ where Δt is the length of the time interval used for Fourier analysis. Quadrature integration is used to find the real and imaginary parts by making use of the known frequency and the orthogonality of sine and cosine.

$$\text{Real}(p_{ij}) = \sum_{k:t_k \in (t_i, t_i + \Delta t)} \frac{p_{kj} \cos(2\pi f_{dop} t_k)}{\cos^2(2\pi f_{dop} t_k)}; \quad (\text{E.5})$$

$$\text{Imaginary}(p_{ij}) = \sum_{k:t_k \in (t_i, t_i + \Delta t)} \frac{p_{kj} \sin(2\pi f_{dop} t_k)}{\sin^2(2\pi f_{dop} t_k)} \quad (\text{E.6})$$

where the second index on p indicates the hydrophone number and the first a sample number. The frequency f_{dop} is found by considering the vehicle velocity at time t_i and

$$f_{dop-max} = f \left(1 + \frac{v}{c}\right), \quad (\text{E.7})$$

$$f_{dop-min} = f \left(1 - \frac{v}{c}\right). \quad (\text{E.8})$$

f_{dop} is then the frequency in $(f_{dop-min}, f_{dop-max})$ that gives the maximum pressure amplitude in the Fourier quadrature routine.

The pressures found by the quadrature routine at each t_i can then be used in the overlap processing routine. Since interpolation is used on time, the average range and

average complex pressure at each position is given by

$$|\bar{p}_i| = \sum_i^N |p_{i,i}|, \quad (\text{E.9})$$

$$\angle \bar{p}_i = \sum_i^N \angle p_{i,i}, \quad (\text{E.10})$$

$$\bar{R}_i = \sum_i^N R_{i,i}. \quad (\text{E.11})$$

Averaging over the ranges is used since the operations are discrete and thus the range at each position for different sub-apertures are slightly different.

Finally, the pressure versus time and range output of the array is given by

$$p(r, t) = p(R(t), t) \quad (\text{E.12})$$

Appendix F - Acoustic Sources

This appendix includes information on the sources used in the Nantucket Sound Experiments. Figure F.1 shows how the source was used in conjunction with a signal generator, amplifier, reference hydrophone, and signal analyzer to monitor the source levels during the experiment. The signal generator used was a Hewlett Packard 8904 Multi-Function Synthesizer with an external rubidium clock capable of synthesizing four separate continuous wave sinusoidal signals with 0.1 Hz resolution. This synthesizer can simultaneously generate four signals and the output can be set to add the contributions from each signal to form a complex signal [130]. Doing so allowed multiple continuous wave tones to be used at any given time during the experiment.

The output of the synthesizer was limited to 10 volts peak-to-peak, so a McIntosh MC2500 amplifier was used to drive the high impedance sources. The important characteristics of the amplifier were that it had a maximum channel power of 500 W, was calibrated flat from 20 Hz to 20 kHz with less than 0.25 dB gain variation, had distortion less than 2%, and the input level was limited to 2.50V rms [131].

The output of the signal generator as well as the reference hydrophone were monitored by a Hewlett Packard 35670A signal analyzer. This signal analyzer performs 200, 400, 800, or 1600 point fast Fourier transforms on input signals and can report the measured frequency domain spectrum in band corrected and non-band corrected units [132]. This enabled the determination of the level of each tone out of the signal generator as well as the received signal level at the hydrophone 1 m away from the source. The hydrophone used was an ITC-8180⁵ with a calibrated voltage sensitivity of -176 dB re $1V/\mu Pa$ and a 20 dB pre-amplifier. The digital audio tape (DAT) recorder was not critical to monitoring the system, but was included in case play-back of the source was necessary.

Figure F.2 shows the XF-4 flex-tensional source that was deployed in the September 2005 Nantucket sound experiment. This source was broken during the experiment and

⁵International Transducer Corporation, 869 Ward Drive, Santa Barbara, CA 93111

the expected source levels were higher than the source levels determined by matching transmission loss data to calculations. Figure F.3 shows the HX-188 omni-directional sound source that was used in the December 2005 Nantucket Sound experiment. While the maximum sound pressure levels are reported, they are related to the transmit voltage response by the maximum driving voltage.

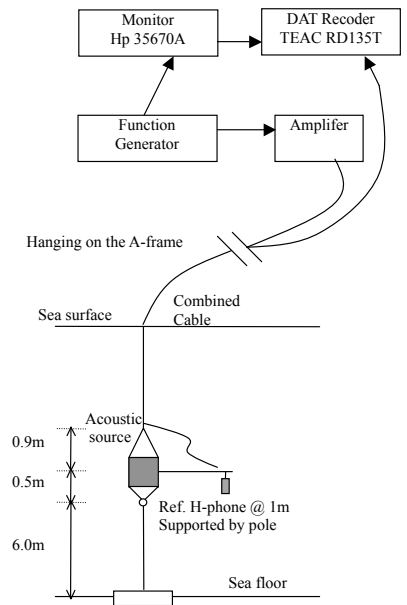
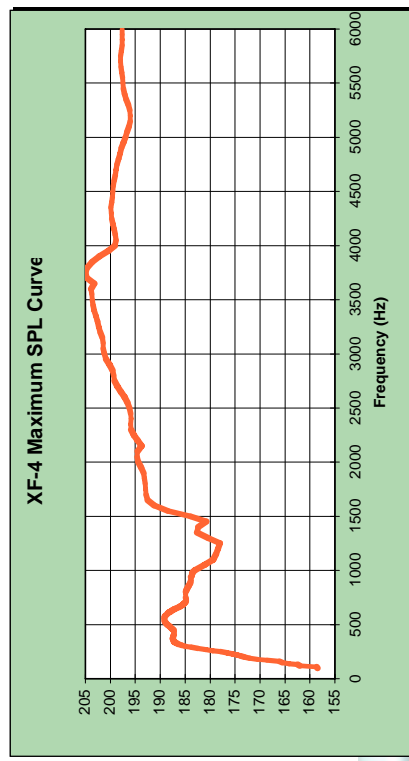


Figure F.1: Wiring diagram for the source on the ship. In this case the source is attached to a heavy anchor to prevent sway. Later the anchor was removed and the weight of the source alone was found sufficient to prevent sway.

**XF-4
FLEX TENSION**

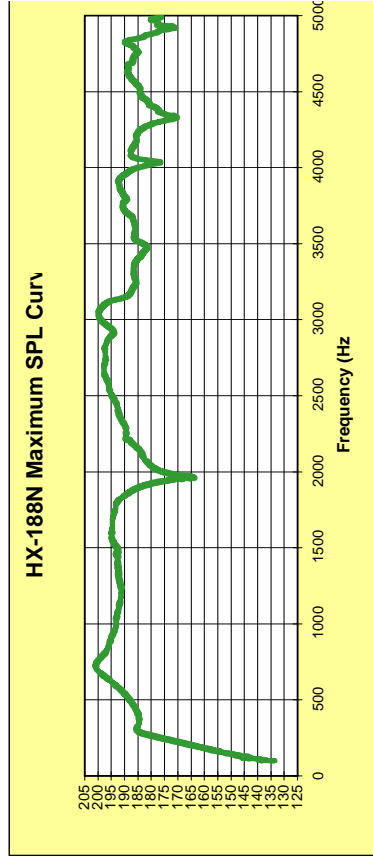


TRANSDUCER SPECIFICATIONS	
Frequency Range	100 - 6000 Hz
Resonant Frequency	3750 Hz
Maximum Drive Voltage	600 Vrms
Maximum Source Level	204.9 dB/μPa/m
Max Operating Depth	1300 ft
Weight in Air	180 lbs
Dimension (LxWxD)	19.5 x 7.5 x 22.0



Figure F.2: Properties of the XF-4 Flex-tensional source used in the September 2005 Nantucket Sound Experiment. [133]

**HX-188N
OMNIDIRECTIONAL
PROJECTOR**



TRANSDUCER SPECIFICATIONS	
Frequency Range	100 - 5000 Hz
Resonant Frequency	720 Hz
Maximum Drive Voltage	600 Vrms
Maximum Source Level	200.9 dB/ μ Pa/m
Maximum Input Power	1590 VA @ 720 Hz
Max Operating Depth	2500 ft
Weight in Air	200 lbs
Dimensions	12.0-inch diameter by 15.0-inch length

Figure F.3: Properties of the HX-188 Omnidirectional source used in the December 2005 Nantucket Sound Experiment. [133]

Bibliography

- [1] Andrew George, *The Epic of Gilgamesh, a new translation*, Allen Lane, The Penguin Press, London, England, 1999
- [2] Robert J. Urick, *Principles of underwater sound for engineers*, McGraw Hill, New York, 1967
- [3] Naval Historical Center, Department of the Navy, PHOTO# NH46757, photograph (circa 1919)
- [4] Stanley G. Lemon, Towed Array History, 1917-2003, *IEEE Journal of Oceanic Engineering* **29**(2), 365–373 (2004)
- [5] M.Grant Gross, *Oceanography, a view of the earth*, Prentice-Hall, Englewood Cliffs, New Jersey, 1972
- [6] F.B. Jensen, W.A. Kuperman, M.B. Porter and H. Schmidt, *Computational ocean acoustics*, American Institute of Physics, New York, 1994
- [7] Alick C. Kibblewhite, Attenuation of sound in marine sediments: A review with emphasis on new low-frequency data, *The Journal of the Acoustical Society of America* **86**(2), 716–738 (1989)
- [8] Maurice A. Biot, General Theory of Three-Dimensional Consolidation, *Journal of Applied Physics* **12**(2), 155–164 (1941)
- [9] M. A. Biot, Consolidation Settlement Under a Rectangular Load Distribution, *Journal of Applied Physics* **12**(5), 426–430 (1941)
- [10] M. A. Biot and F. M. Clingan, Consolidation Settlement of a Soil with an Impervious Top Surface, *Journal of Applied Physics* **12**(7), 578–581 (1941)
- [11] M. A. Biot, Theory of Elasticity and Consolidation for a Porous Anisotropic Solid, *Journal of Applied Physics* **26**(2), 182–185 (1955)
- [12] M.A. Biot, General Solutions of the Equations of Elasticity and Consolidation for a Porous Material, *Journal of Applied Mechanics* **78**, 91–96 (1956)
- [13] M. A. Biot, Theory of Deformation of a Porous Viscoelastic Anisotropic Solid, *Journal of Applied Physics* **27**(5), 459–467 (1956)

- [14] M. A. Biot, Mechanics of Deformation and Acoustic Propagation in Porous Media, *Journal of Applied Physics* **33**(4), 1482–1498 (1962)
- [15] M. A. Biot, Generalized Theory of Acoustic Propagation in Porous Dissipative Media, *The Journal of the Acoustical Society of America* **34**(9A), 1254–1264 (1962)
- [16] M.A. Biot, Nonlinear and Semilinear Rheology of Porous Solids, *Journal of Geophysical Research* **78**(23), 4924–4937 (1973)
- [17] M.A. Biot, Theory of propagation of elastic waves in a fluid saturated porous solid. I. Low frequency range., *The Journal of the Acoustical Society of America* **28**(2), 168–178 (1956)
- [18] M. A. Biot, Theory of Propagation of Elastic Waves in a Fluid-Saturated Porous Solid. II. Higher Frequency Range, *The Journal of the Acoustical Society of America* **28**(2), 179–191 (1956)
- [19] R.D. Stoll, *Sediment Acoustics*, Springer Verlag, New York, NY, 1989
- [20] Edwin L. Hamilton, Compressional-wave attenuation in marine sediments, *Geophysics* **37**(4), 620–646 (August 1972)
- [21] E. L. Hamilton, George Shumway, H. W. Menard and C. J. Shipek, Acoustic and Other Physical Properties of Shallow-Water Sediments off San Diego, *The Journal of the Acoustical Society of America* **27**(5), 1007–1007 (1955)
- [22] E. L. Hamilton, George Shumway, H. W. Menard and C. J. Shipek, Acoustic and Other Physical Properties of Shallow-Water Sediments off San Diego, *The Journal of the Acoustical Society of America* **28**(1), 1–1 (1956)
- [23] Edwin L. Hamilton, Sound Channels in Surficial Marine Sediments, *The Journal of the Acoustical Society of America* **48**(5B), 1296–1298 (1970)
- [24] Edwin L. Hamilton, Sound attenuation as a function of depth in the sea floor, *The Journal of the Acoustical Society of America* **59**(3), 528–535 (1976)
- [25] Edwin L. Hamilton, Attenuation of shear waves in marine sediments, *The Journal of the Acoustical Society of America* **60**(2), 334–338 (1976)
- [26] Edwin L. Hamilton, Sound velocity–density relations in sea-floor sediments and rocks, *The Journal of the Acoustical Society of America* **63**(2), 366–377 (1978)
- [27] E. L. Hamilton, Compressional and shear wave gradients in marine sediments, *The Journal of the Acoustical Society of America* **64**(S1), S141–S141 (1978)
- [28] Edwin L. Hamilton, Sound velocity gradients in marine sediments, *The Journal of the Acoustical Society of America* **65**(4), 909–922 (1979)
- [29] Edwin L. Hamilton, V_p/V_s and Poisson’s ratios in marine sediments and rocks, *The Journal of the Acoustical Society of America* **66**(4), 1093–1101 (1979)

- [30] Edwin L. Hamilton, Geoacoustic modeling of the sea floor, *The Journal of the Acoustical Society of America* **68**(5), 1313–1340 (1980)
- [31] Edwin L. Hamilton and Richard T. Bachman, Sound velocity and related properties of marine sediments, *The Journal of the Acoustical Society of America* **72**(6), 1891–1904 (1982)
- [32] Edwin L. Hamilton, Sound velocity as a function of depth in marine sediments, *The Journal of the Acoustical Society of America* **78**(4), 1348–1355 (1985)
- [33] R.D. Stoll, Marine sediment acoustics, *The Journal of the Acoustical Society of America* **77**(5), 1789–1799 (1985)
- [34] J.M. Hovem. A note on attenuation and dispersion in marine sediments. memorandum SM-218, Saclant Undersea Research Centre, April 1989.
- [35] Klaus C. Leurer, Attenuation in fine-grained marine sediments: Extension of the Biot-Stoll model by the “effective grain model” (EGM), *Geophysics* **62**(5), 1465–1479 (1997)
- [36] Kevin L. Williams, An effective density fluid model for acoustic propagation in sediments derived from Biot theory, *The Journal of the Acoustical Society of America* **110**(5), 2276–2281 (2001)
- [37] Michael J. Buckingham, Wave propagation, stress relaxation, and grain-to-grain shearing in saturated, unconsolidated marine sediments, *The Journal of the Acoustical Society of America* **108**(6), 2796–2815 (2000)
- [38] Nicholas P. Chotiros and Marcia J. Isakson, A broadband model of sandy ocean sediments: Biot–Stoll with contact squirt flow and shear drag, *The Journal of the Acoustical Society of America* **116**(4), 2011–2022 (2004)
- [39] I. Rozenfeld, W.M. Carey, P.G. Cable and W.L. Siegmann, Modeling and analysis of sound transmission in the Strait of Korea, *Journal of Oceanic Engineering* **26**(4), 809–820 (2001)
- [40] Jason D. Holmes, Simona Dediu and William M. Carey. Nonlinear frequency dependent attenuation in sandy sediments. Technical Report AM-05-006, Boston University Department of Aerospace and Mechanical Engineering, March 2005.
- [41] Ji-Xun Zhou and Xue-Zhen Zhang, Nonlinear frequency dependence of the effective seabottom acoustic attenuation from low-frequency field measurements in shallow water, *The Journal of the Acoustical Society of America* **117**(4), 2494–2494 (2005)
- [42] Frank Ingenito, Measurements of mode attenuation coefficients in shallow water, *The Journal of the Acoustical Society of America* **53**(3), 858–863 (1973)
- [43] J. H. Beebe, S. T. McDaniel and L. A. Rubano, Shallow-water transmission loss prediction using the Biot sediment model, *The Journal of the Acoustical Society of America* **71**(6), 1417–1426 (1982)

- [44] W.M. Carey and R.B. Evans, Frequency dependence of sediment attenuation in two low-frequency shallow-water acoustic experimental data sets, *Journal of Oceanic Engineering* **23**(4), 439–447 (1998)
- [45] P.H. Rogers, J.X. Zhou, X. Z. Zhang, F. Li et al. Seabottom acoustic parameters from inversion of Yellow Sea experimental data. in A. Caiti et al., Herausgeber, *Experimental Acoustic Inversion Methods for Exploration of the Shallow Water Environment*, Seiten 219–234. Kluwer, Norwell, MA 2000.
- [46] B.F. Cole, Marine sediment attenuation and ocean-bottom-reflected sound, *The Journal of the Acoustical Society of America* **38**(2), 291–297 (1965)
- [47] Michael J. Buckingham and Eric M. Giddens, Inversion of underwater sound from a high-Doppler airborne source (a light aircraft) for the geoacoustic properties of the sea bed, *The Journal of the Acoustical Society of America* **118**(3), 1845–1845 (2005)
- [48] Dajun Tang, Inverting for sandy sediment sound speed in very shallow water using boat noise, *The Journal of the Acoustical Society of America* **117**(4), 2503–2503 (2005)
- [49] Harry J. Simpson and Brian H. Houston, Synthetic array measurements of acoustical waves propagating into a water-saturated sandy bottom for a smoothed and a roughened interface, *The Journal of the Acoustical Society of America* **107**(5), 2329–2337 (2000)
- [50] Preston S. Wilson, Ronald A. Roy and William M. Carey, Development of an impedance tube technique for in-situ classification of marine sediments, *The Journal of the Acoustical Society of America* **113**(4), 2318–2318 (2003)
- [51] Preston S. Wilson, Eun-Joo Park, Ronald A. Roy and William M. Carey, The measurement of acoustic dispersion in loosely consolidated, saturated sediments using a water-filled impedance tube, *The Journal of the Acoustical Society of America* **112**(5), 2363–2363 (2002)
- [52] Preston S. Wilson et al., Evidence of Dispersion in a Water-Saturated Granular Sediment, in *Proceedings of Oceans 2005, Brest, France*. IEEE, 2005
- [53] E.W. Lane, Report of the Subcommittee on Sediment Terminology, *Transactions, American Geophysical Union* **28**(6), 936–938 (1947)
- [54] United States Army Corp of Engineers. *Engineering and Design - Sedimentation Investigations of Rivers and Reservoirs*, 1995. Publication Number: EM 1110-2-4000.
- [55] F.P. Shepard, Nomenclature based on sand-silt-clay ratios, *Journal of Sedimentary Petrology* **24**, 151–158 (1954)
- [56] Ji xun Zhou, Xue zhen Zhang, Peter H. Rogers and Jacek Jarzynski, Geoacoustic parameters in a stratified sea bottom from shallow-water acoustic propagation, *The Journal of the Acoustical Society of America* **82**(6), 2068–2074 (1987)

- [57] J.X. Zhou, X.Z. Zhang et al., Reverberation vertical coherence and sea-bottom geoaoustic inversion in shallow water, *Journal of Oceanic Engineering* **29**(4), 988–999 (2004)
- [58] Fredrick Tappert. Analysis of ACT1 data using the UMPE model. from correspondence, 1993.
- [59] J. Matthew Tatarsall and Dmitry Chizhik. Application of Biot theory to the study of acoustic reflection from sediments. Technical Report NUWC-NL-TR-10-115, Naval Undersea Warfare Center - New London, 1992. "DTIC ADA255651".
- [60] J. Matthew Tatarsall, Dmitry Chizhik, Bernard F. Cole and F. R. DiNapoli, The effect of frequency-dependent bottom reflectivity on transmission loss in shallow water over a sandy bottom, *The Journal of the Acoustical Society of America* **93**(4), 2395–2395 (1993)
- [61] Z. Peng, J.X. Zhou, P.H. Dahl and R. Zhang, Sea-bed acoustic parameters from dispersion analysis and transmission loss in the East China Sea, *Journal of Oceanic Engineering* **29**(4), 1038–1045 (2004)
- [62] David P. Knobles, Robert A. Koch, James H. Miller and Gopu R. Potty, Evidence for nonlinear frequency dependence of attenuation in an East China Sea environment, *The Journal of the Acoustical Society of America* **115**(5), 2551–2551 (2004)
- [63] Ji xun Zhou, Normal mode measurements and remote sensing of sea-bottom sound velocity and attenuation in shallow water, *The Journal of the Acoustical Society of America* **78**(3), 1003–1009 (1985)
- [64] D.P. Knobles, T.W. Yudichak, R.A. Koch, P.G. Cable, J.H. Miller and G.R. Potty. Inference on seabed attenuation in the East China Sea from distributed acoustic measurements. Manuscript to be published.
- [65] D. Richard Blidberg. The Development of Autonomous Underwater Vehicles(AUV); A brief summary. Technical report, Autonomous Undersea Systems Institute, 2001.
- [66] W.L. Greer. Exploration of potential future fleet architectures. Technical report, Institute for Defense Analysis, 2005. DTIC ADA 442435.
- [67] Lee Frietag et al., A bidirectional coherent acoustic communications system for underwater vehicles, in *Proceedings of Oceans 98, Nice, France*. IEEE, 1998
- [68] Kevin D. LePage and Henrik Schmidt, Bistatic Synthetic Aperture Imaging of Proud and Buried Targets from an AUV, *IEEE Journal of Oceanic Engineering* **27**(3), 471–483 (2002)
- [69] Joseph R. Edwards, Henrik Schmidt and Kevin D. LePage, Bistatic Synthetic Aperture Target Detection and Imaging with and AUV, *IEEE Journal of Oceanic Engineering* **26**(4), 690–699 (2001)

- [70] Stewart A. L. Glegg et al., A passive sonar system based on an autonomous underwater vehicle, *IEEE Journal of Oceanic Engineering* **26**(4), 700–710 (2001)
- [71] Gerald L. D'Spain, Eric Terrill, C. David Chadwell, Jerome A. Smith and Richard Zimmerman, Passive acoustic localization with an AUV-mounted hydrophone array, *The Journal of the Acoustical Society of America* **115**(5), 2615–2615 (2004)
- [72] James W. Fitzgerald, Richard D. Doolittle and Robert F. Greenwell, Chesapeake Instrument Corporation Project Toad: Principles and Applications of Towflex Hydrophones, *IEEE Journal of Oceanic Engineering* **29**(2), 388–406 (2004)
- [73] M. Laskey, R.D. Doolittle, B.D. Simmons and S.G. Lemon, Recent progress in towed hydrophone array research, *IEEE Journal of Oceanic Engineering* **29**(2), 374–387 (2004)
- [74] Nai-Chyuan Yen and William Carey, Application of synthetic-aperture processing to towed-array data, *The Journal of the Acoustical Society of America* **86**(2), 754–765 (1989)
- [75] Edmund J. Sullivan, William M. Carey and Stergios Stergiopoulos, Editorial - Synthetic Aperture Processing, *IEEE Journal of Oceanic Engineering* **17**(1), 1–7 (1992)
- [76] John R. Potter, Eric Delory, Socol Constantin and Sorin Badiu, The 'Thinarray'; A lightweight, ultra-thin(8 mm OD) towed array for use from small vehicles of opportunity, in *Proceedings of the IEEE Underwater Technology Conference 2000*. IEEE, 2000
- [77] Roger T. Richards and Philip V. Duckett. Piezocrystal vector-sensor towed line array. Technical report, NUWC, 2004. Presented at Joint Undersea Warfare Technology Fall Conference.
- [78] J.E. White, *Seismic Waves: Radiation, Transmission, and Attenuation*, McGraw-Hill, New York, 1965
- [79] Ajit K. Mal and Sarva Jit Singh, *Deformation of Elastic Solids*, Prentice Hall, Englewood Cliffs, New Jersey 07632, 1991
- [80] Allan D. Pierce, William M. Carey and Mario Zampolli, Low-frequency attenuation of sound in marine sediments, in *Proceedings of Oceans 2005, Brest, France*. IEEE, 2005
- [81] William M. Carey, Jason D. Holmes, Allan D. Pierce and James F. Lynch, Attenuation characteristics of sandy-sediments - A simplified Biot approach, in *Proceedings, Underwater Acoustic Measurements technologies and results conference - Crete 2005*, 2005
- [82] Allan D. Pierce. *Handbook of Acoustics*, Kapitel Chapter 3, Basic Linear Acoustics. Springer-Verlag, New York, 2006. To be published August of 2006, Edited by Thomas Rossing.

- [83] Robert D. Stoll and T. K. Kan, Reflection of acoustic waves at a water–sediment interface, *The Journal of the Acoustical Society of America* **70**(1), 149–156 (1981)
- [84] C. L. Pekeris. Thoery of propagation of explosive sound in shallow water. Technical Report Memoir 27, The Geological Society of America, 1948.
- [85] Jason D. Holmes, William M. Carey, Allan D. Pierce and James F. Lynch, Attenuation Characteristics of Sandy Sediments - A Simplified Biot Approach, in *Proceedings of the boundary influences in high frequency, shallow water acoustics conference*. University of Bath, UK, 2005
- [86] R. E. Sheriff, Factors affecting seismic amplitudes, *Geophysics-Prospecting* **23**, 125–138 (1975)
- [87] W. A. Kuperman and F. Ingenito, Attenuation of the coherent component of sound propagating in shallow water with rough boundaries, *The Journal of the Acoustical Society of America* **61**(5), 1178–1187 (1977)
- [88] V.A. Grigor’ev, B.G. Katsnel’son and V.G. Petnikov, Determination of the absorbing and scattering properties of the sea floor in a shallow water environment by the spectra of wide band signals, *Acoustical Physics* **47**(3), 330–335 (2001)
- [89] James F. Lynch, Subramaniam D. Rajan and George V. Frisk, A comparison of broadband and narrow-band modal inversions for bottom geoacoustic properties at a site near Corpus Christi, Texas, *The Journal of the Acoustical Society of America* **89**(2), 648–665 (1991)
- [90] George V. Frisk, *Ocean and Seabed Acoustics: A theory of Wave Propagation*, PTR Prentice Hall, Upper Saddle River, NJ, 1994
- [91] George V. Frisk, James F. Lynch and Subramaniam D. Rajan, Determination of compressional wave speed profiles using modal inverse techniques in a range-dependent environment in Nantucket Sound, *The Journal of the Acoustical Society of America* **86**(5), 1928–1939 (1989)
- [92] J. Doutt, R. Cederberg, R. Evans, W. Carey and W. Siegmann. Experimental Horizontal wavenumber spectra and implications for full field processing. in O. Diachok et al., Herausgeber, *Full Field Inversion Methods in Ocean and Seismo-Acoustics*, Seiten 341–346. Kluwer Academic Pub, Dordrecht, Netherlands 1995.
- [93] Subramaniam D. Rajan, James F. Lynch and George V. Frisk, Perturbative inversion methods for obtaining bottom geoacoustic parameters in shallow water, *The Journal of the Acoustical Society of America* **82**(3), 998–1017 (1987)
- [94] Gopu R. Potty, James H. Miller and James F. Lynch, Inversion for sediment geoacoustic properties at the New England Bight, *The Journal of the Acoustical Society of America* **114**(4), 1874–1887 (2003)

- [95] Karl Crawford Focke. Acoustic attenuation in ocean sediments found in shallow water regions. Technical Report ARL-TRT-84-6, Applied Research Laboratories, University of Texas at Austin, 1984. DTIC AD-A140 869.
- [96] William M. Carey and William B. Moseley, Space-Time Processing, Environmental-Acoustic Effects, *IEEE Journal of Oceanic Engineering* **16**(3), 285–301 (1991)
- [97] Edmund J. Sullivan and Geoffrey S. Edelson, Model-based broadband towed-array processing, *The Journal of the Acoustical Society of America* **115**(5), 2577–2577 (2004)
- [98] George V. Frisk and James F. Lynch, Shallow water waveguide characterization using the Hankel transform, *The Journal of the Acoustical Society of America* **76**(1), 205–216 (1984)
- [99] Anonymous. Underwater electroacoustic standard transducers catalogue. Technical report, USRD, Naval Research Laboratory, 1982.
- [100] Donald Ross, *Mechanics of Underwater Noise*, Peninsula Publishing, Los Altos, CA, 1987
- [101] David C. Wilcox, *Basic Fluid Mechanics*, DCW Industries, La Cañada, CA, 2000
- [102] Kimberly M. Cipolla and Michael R. Williams, Drag Measurements of Long Cylinders in Axial Tow, in *Proceedings, Undersea Defense Technology Conference, Hawaii*. Naval Undersea Warfare Center, Submarine Sonar Department, Code 214, 2001
- [103] National Oceanic and Atmospheric Administration, Nautical Chart, United States, East Coast, Massachusetts, Nantucket Island (1992)
- [104] Robert N. Oldale, *Cape Cod and the Islands: The Geologic Story*, Parnassus Press, 1992
- [105] Brian L. Howes et al. Ecology of Buzzards Bay: An estuarine profile. Technical Report Biological Report 31, U.S. Department of the Interior, National Biological Service, 1996.
- [106] John A. Goff et al., Detailed investigation of sorted bedforms, or “ripple scour depressions” within the Martha’s Vineyard Coastal Observatory, Massachusetts, *Continental Shelf Research* **25** (2005)
- [107] LLC Cape Wind Associates. Cape Wind Energy Project Draft Environmental Impact Statement. Technical report, U.S. Army Corp of Engineers, 2005. Submitted for approval of the Cape Wind off shore wind park in Nantucket Sound, available online.
- [108] Charles J. O’Hara and Robert N. Oldale. Geology, Shallow Structure and Bedform Morphology, Nantucket Sound Massachusetts. 1:125,000. Technical Report MF 1911, United States Geological Survey, 1987.

- [109] John C. Hathaway. Data file: Continental margin program Atlantic Coast of the United States Vol:2 samples collection and analytical data. Technical Report Ref. No. 71-15, Woods Hole Oceanographic Institution, 1971.
- [110] R. J. Cederberg, W. L. Siegmann and W. M. Carey, Influence of geoacoustic modeling on predictability of low-frequency propagation in range-dependent, shallow-water environments, *The Journal of the Acoustical Society of America* **97**(5), 2754–2766 (1995)
- [111] Subramaniam D. Rajan. *An Inverse Method for Obtaining the Attenuation Profile and Small Variations in the Sound Speed and Density Profiles of the Ocean Bottom*. PhD thesis, Woods Hole Oceanographic Institution and Massachusetts Institute of Technology, 1985.
- [112] M. B. Porter. The KRAKEN normal mode program. Technical report, SACLANT Undersea Research Center, 1992.
- [113] Michael D. Collins. User’s guide for RAM versions 1.0 and 1.0p. Technical report, Naval Research Laboratory, 1995.
- [114] Michael D. Collins, A split-step Padé solution for the parabolic equation method, *The Journal of the Acoustical Society of America* **93**(4), 1736–1742 (1993)
- [115] Henrik Schmidt. SAFARI Seismo-Acoustic Fast field Algorithm for Range-Independent environments, user’s guide. Technical Report SR-133, SACLANT ASW Research Centre, La Spezia, Italy, 1988.
- [116] William M. Carey, The determination of signal coherence length based on signal coherence and gain measurements in deep and shallow water, *The Journal of the Acoustical Society of America* **104**(2), 831–837 (1998)
- [117] M. Stern, A. Bedford and H. R. Millwater, Wave reflection from a sediment layer with depth-dependent properties, *The Journal of the Acoustical Society of America* **77**(5), 1781–1788 (1985)
- [118] Ira Dyer, Statistics of Sound Propagation in the Ocean, *The Journal of the Acoustical Society of America* **48**(1B), 337–345 (1970)
- [119] Lowell W. Brooks and Dominic Fraioli. Requirements for the low wavenumber experiment by the NUSC towed array exploratory development team. Technical Report TM No. 811185, Naval Underwater Systems Center: New London Laboratory, 1982.
- [120] G.M. Corcos, The structure of the turbulent pressure field in boundary layer flows, *Journal of Fluid Mechanics* **18**, 353–378 (1964)
- [121] D.M. Chase, Modeling the wavevector-frequency spectrum of turbulent boundary layer wall pressure, *Journal of Sound and Vibration* **70**, 29–67 (1980)

- [122] W.A. Von Winkle, J. Fitzgerald, W. M. Carey and H. P. Bakewell. Hydrodynamic noise and surface compliance. Technical Report NUSC TD 6607, Naval Underwater Systems Center, Newport, RI, 1982.
- [123] M.S. Howe, On the Generation of Sound by Turbulent Boundary Layer Flow Over a Rough Wall, *Proceedings of the Royal Society of London* **395 A**(1809), 247–263 (1984)
- [124] M.S. Howe, *Acoustics of fluid-structure interaction*, Cambridge University Press, New York, NY, 1998
- [125] Andrew Knight, Flow noise calculations for extended hydrophones in fluid- and solid-filled towed arrays, *The Journal of the Acoustical Society of America* **100**(1), 245–251 (1996)
- [126] Lawrence Ong and James M. Wallace, Joint probability density analysis of the structure and dynamics of the vorticity field of a turbulent boundary layer, *J. Fluid Mech.* **367**, 291–328 (1998)
- [127] Alan Edward Markowitz. *An investigation into the self-noise properties of a long, flexible wall, fluid filled cylinder towed at sea*. Engineering, mechanical, University of Rhode Island, 1976.
- [128] A.P. Dowling, Underwater flow noise, *Theoretical and Computational Fluid Dynamics* **10**, 135–153 (1998)
- [129] Hydroid, LLC. REMUS 100 autonomous underwater vehicle. brochure, Falmouth, MA, 2006.
- [130] Hewlett Packard. *Hewlett Packard 8904A Multifunction Synthesizer DC-600 kHz User's Manual*.
- [131] McIntosh. *McIntosh MC2500 Stereo Power Amplifier Owner's Manual*.
- [132] Hewlett Packard. *Hewlett Packard 35670A Dynamic Signal Analyzer User's Manual*.
- [133] Joseph Kaminski, Obtained by personal communication with Joseph Kaminski, Naval Undersea Warfare Center, code 1511 (2005)

Born: 1980**Address:** 173 Bay State Rd. Boston, MA 02215**E-mail:** jholmes@bu.edu**Work:** 617-353-4854

Education:

Ph.D., Mechanical Engineering, Boston University (2007).

B.S. Mechanical Engineering, Boston University (2003).

Fellowships

2003–2004 Dean’s Fellow, Department of Aerospace and Mechanical Engineering, Boston University

2004-2006 National Defense Science and Engineering Graduate Fellowship, through the American Society for Engineering Education and supported by the Office of Naval Research

Appointments

2003-2006 Guest student investigator, the Woods Hole Oceanographic Institution, Woods Hole, MA.

Work Experience

2001-2003 Engineering Standards Department and Electric Systems Department, Ametek Aerospace, Wilmington, MA.

Awards and Activities

Boston University College of Engineering Class of 2003 Valedictorian

. ASA student paper award in UW - OCT 2005.

Member, Tau Beta Pi, Engineering Honor Society

Member, Pi Tau Sigma, Mechanical Engineering Honor Society

Member, National Society of Collegiate Scholars

Member, American Society of Mechanical Engineers

Member, Acoustical Society of America

Eagle Scout

Contributions to conferences :

Shallow-water waveguide characterization using an autonomous underwater vehicle-towed hydrophone array Jason D. Holmes, William M. Carey, and James F. Lynch, J. Acoust. Soc. Am. 119, 3346 (2006)

Low-frequency sound reflection and conversion to Darcy-type type diffusion waves at bottom interfaces with marine sediments Jason D. Holmes, Allan D. Pierce, William M. Carey, and James F. Lynch, J. Acoust. Soc. Am. 119, 3253 (2006)

An autonomous underwater vehicle technique for in situ waveguide characterization
Jason D. Holmes, William M. Carey, and James F. Lynch, *J. Acoust. Soc. Am.* 118, 2042 (2005)

An autonomous underwater vehicle towed hydrophone array for ocean acoustic measurements
Jason D. Holmes, William M. Carey, James F. Lynch, Arthur E. Newhall, and Amy Kukulya, *J. Acoust. Soc. Am.* 117, 2624 (2005)

An acoustic array to be towed behind an autonomous underwater vehicle
Jason D. Holmes, William M. Carey, and James F. Lynch, *J. Acoust. Soc. Am.* 115, 2621 (2004)

Development of a submersible, baffled impedance tube for characterization of bubbly liquids
Jed C. Wilbur, Jason Holmes, Michael Canney, William M. Carey, and Ronald A. Roy, *J. Acoust. Soc. Am.* 115, 2473 (2004)

13th International Congress of Sound and Vibration, Vienna Austria, 2006. *Contributed Talk* Broadband Passive Synthetic Aperture Towed Array Processing.

Non-Linear Statistical Signal Processing Workshop 2006, Cambridge, UK, 2006. *Contributed Talk* Model Based Processing For a Short Towed Array.

Research papers (refereed journals and invited papers):

1. Jason D. Holmes and William M. Carey. Array Measurements and Characterizations with Relative Velocity as a Parameter. Proceedings of the International Conference “Underwater Acoustic Measurements: Technologies & Results”, Heraklion, Crete, Greece. July 2005.
2. Jason D. Holmes, William M. Carey, Allan D. Pierce, James F. Lynch. Attenuation Characteristics of Sandy Sediments- A simplified Biot approach. Proceedings of the boundary influences in high frequency, shallow water acoustics meeting. University of Bath, UK. Sept. 2005.
3. Jason D. Holmes, William M. Carey, and James F. Lynch, Results from an autonomous underwater vehicle towed hydrophone array experiment in Nantucket Sound. Accepted to The Journal of the Acoustical Society of America, Express Letters May 2006.
4. Edmund J. Sullivan, Jason D. Holmes, William M. Carey, James F. Lynch, Broadband passive synthetic aperture: experimental results. Submitted to The Journal of the Acoustical Society of America, Express Letters May 2006.

Research papers (review articles and conference proceedings):

1. An Autonomous Underwater Vehicle Towed Array for Ocean Acoustic Measurements and Inversions. Proceedings IEEE Oceanic Engineering Society’s OCEANS ’05 Europe conference. Jason D. Holmes,